MICRO/NANOSTRUCTURED SURFACES THROUGH THIN FILM STENCIL LIFT-OFF: APPLICATIONS TO PATTERNING AND SENSING

MICRO/NANOSTRUCTURED SURFACES THROUGH THIN FILM STENCIL LIFT-OFF: APPLICATIONS TO PATTERNING AND SENSING

By

YUJIE ZHU, B. ENG.

A Thesis

Submitted to the School of Graduate Studies

In Partial Fulfillment of the Requirements for the Degree

Doctor of Philosophy

Doctor of Philosophy (2016)

McMaster University (Chemistry), Hamilton, Ontario

TITLE:	Micro/Nanostructured Surfaces through Thin Film Stencil Lift-Off: Applications to Patterning and Sensing
AUTHOR:	Yujie Zhu
	B. Eng. (East China University of Science and Technology)
SUPERVISOR:	Dr. Jose Moran-Mirabal
NUMBER OF PAGES:	xiii, 199

Abstract

The rapid development of micro/nanofabrication techniques have enabled engineering of material interfacial properties. Micro/nanostructures with unique electrical, mechanical, thermal, magnetic, optical, and biological properties, have found applications in a wide range of fields such as electronics, photonics, biological/chemical sensing, tissue engineering, and diagnostics, etc. As such, numerous strategies have been developed for structuring materials into micro/nano- scale. However, the challenge still lies in the high cost, low throughput, complexity in fabrication, and difficulty in scaling up. This thesis aims to explore fabrication strategies for micro/nanostructured surfaces that are versatile, simple, and inexpensive. The thin film stencil lift-off technique with both Parylene and self-adhesive vinyl has been explored for this purpose. Further applications of the resulted micro/nanostructured surfaces are also presented in this thesis.

Through improved Parylene stencil fabrication process, both spontaneously phase-segregated and arbitrary binary supported lipid bilayer patterns have been achieved. Also, the microstructured Parylene surfaces have been ddemonstrated for patterning stacked SLBs that are either homogeneous or phase-segregated. Without any lithography technique involved, vinyl stencil lift-off offers as a facile and inexpensive benchtop method for patterning thin films such as metal and glassy films. Combining the thermal shrinking of shape memory polymer, the patterned feature sizes are further decreased by 60% in both x and y dimensions, pushing the patterning resolution to down to sub-100 μm range. In addition, the shrinking process induces micro/nanostructures onto the deposited thin film, and the structure sizes are easily tunable with film thickness deposited. Further applications of such patterned micro/nanostructured surfaces has also been explored. The structured gold films have served as high-surface-area electrodes for electrochemical sensing. By introducing photoresist as a sacrificial layer, the structured gold thin films can be lifted off and

transferred onto elastomeric substrate, and serve stretchable and flexible sensors. Such sensing devices exhibit great stability and reproducibility even when working under external strain. Finally, the micro/nanostructured glassy surfaces have been employed as substrate for cell growth to study topographical effect on cell morphology. It has been concluded that rougher surfaces lead to cell elongation, and finer structures promote filopodia generation.

These results underscore the strength and suitability of thin film stencil lift-off as a powerful technique for creating micro- and nanostructured surfaces. These structured surfaces could find applications in many other areas, due to their great properties such as tunable structure size, high surface area, flexibility, and long-term stability.

Acknowledgements

First of all, I wold like thank to my advisor, Dr. Jose Moran-Mirabal, without whose continuous support I would not be where I am now. He guided me through my graduate study with his immense knowledge, inspiring advices, and great patience. I would never forget the time when he showed me every technique from scratch, and the days we stayed late to set up new instruments. It has been my great honor to be his first graduate student and be exposed such interesting research. I would also like to express my sincere gratitude to my committee members Dr. Harold Stover and Dr. An-Chang Shi for their insightful comments and encouragement, and for inspiring me to think more about my research from polymer chemistry and physics perspectives.

I am very grateful to all my collaborators from inside and outside Chemistry department. I would like to thank Dr. Leyla Soleymani and Christine Gabardo from Physics Engineering department, with whom we accomplished the first work for micro/nanostructured surfaces and laid the foundation for many later projects. Dr. Adam Hitchcock and Jonathan West in Chemistry department were instrumental in the lipid characterization work with scanning transmission X-ray microscopy. I would like also to thank Dr. Jason Slinker and Dimithree Kahanda from University of Texas at Dallas, for their guidance and input in the DNA work, and for giving me access to the laboratory and research facilities. My collaboration inside Moran-Mirabal group with Kevin Saem on all-PDMS microfluidics fabrication were very enjoyable and fruitful.

I would like to acknowledge Dr. Todd Hoare, Fei Xu and Emilia Bakaic in Chemical engineering for giving us access to their cell culture facility and helping with fibroblast work, Dr. Daniel Chen for his training and suggestions in silicone related work, Dr. Zhilin Peng, Doris Stevanovic, and Dr. Shahram Tavakoli for their help in relation to various microfabrication facilities in the Center of Emerging Device Technology, and staff members from the Canadian

Center of Electron Microscopy and Biointerfaces Institute for their help with electron microscopy and atomic force microscopy. I would also like to thank CREATE IDEM for funding me and providing me with opportunities to communicate with researcher locally and internationally.

My lovely lab mates deserve my heartfelt gratitude for making the lab such a wonderful place to work in. I would like to thank Saeid Rahim for sharing thoughts and time with me as my first lab mate, Ayodele Fatona for all the scientific or random conversations, Kevin Saem for every effort in helping me moving my and our projects forward, Mohanad Babi for helping me with image processing, and all others for their help and moral support through both smooth and rough times. My special thanks also go to the brilliant undergraduate students who I have worked closely with, Justin Boyle, Katija Bonin, and Ahmed Negmi for the excellent jobs they have done.

I would also like to thank all my friends in Hamilton who have made the past five years such enjoyable and memorable time: Jason and Winnie, Meng and Xiaohui, Minha and Sean, Fei and Judy, Michelle and Mai, Juan and Xiuping. Special thanks to Xiaohui Zhu, for his understanding, accompany, and support.

Lastly, I would like to thank my parents and my brother for their love and support throughout my study and my life. You are the greatest families that I am so lucky to have. 感谢父母给我生命，感谢父母养育教导，因为你们的爱护和支持，无论情感或物质，我的生活未曾贫瘠。感谢弟弟同我成长，伴我前行, 你是揪掉我玩偶鼻子的小男孩，也是我引以为傲的帅小伙。I am deeply grateful to all my beloved families and friends, thank you for being in my life.

Table of Contents

List of Figures

Chapter 1

Chapter 2

Chapter 3

Chapter 4

Chapter 5

Chapter 6

List of Tables

List of Abbreviations and Symbols

AFM	Atomic force microscopy
CA	Chronoamerprometry
CV	Cyclic voltammetry
DHPE-LR	Lissamin Rhodamine B 1,2-Dihexadecanoyl-sn-Glycero-3-Phosphoethanolamine
DHPE-OG	Oregon Green 488 1,2-Dihexadecanoyl-sn-Glycero-3-Phosphoethanolamine
DMPS	1,2-dimyristoyl-sn-glycero-3-phospho-L-serine
DOPC	1,2-dioleoyl-sn-glycero-3-phosphocholine
DOTAP	1,2-dioleoyl-3-trimethylammonium-propane
DSPC	1,2-distearoyl-sn-glycero-3-phosphocholine
l_d	Liquid-disordered
l_o	Liquid-ordered
MTT	3-(4,5-dimethylthiazol-2-yl)-2,5-diphenyltetrazolium bromide
PDMS	Polydimethylsiloxane
PSLO	Polymer stencil lift-off
PS	Polystryrene
RIE	Reactive ion etching
R_s	Sheet resistance
SLB	Supported lipid bilayer
SUV	Small unilamellar vesicle
SEM	Scanning electron microscope
T_g	Glass-transition temperature
WLIM	White light interferometry microscopy

Chapter 1 Introduction

Microfabrication refers to the process of manipulating structures of micrometer scales and smaller, and nanofabrication is the manipulation of materials with at least one dimension in the 1-100 nanometer size.[1] The rapid development of micro/nanofabrication techniques have enabled engineering of material interfacial properties. Micro/nanostructured surfaces and films have been designed to control mechanical,[2] thermal,[3–5] magnetic,[6,7] electrical,[8,9] and optical[10–12] properties, as well as to influence biological processes such as protein adsorption and conformation,[13] cell behavior,[14] bacterial adhesion,[16] etc. Combined with various surface modification and functionalization approaches, these structured surfaces are becoming increasingly important in a variety of applications, such as electronics,[17] photonics,[18,19] sensing devices,[20] tissue engineering,[14,21] biodiagnostics[22,23], among many others.

Micro- and nanostructured surfaces have been targeted as powerful tools to investigate biomolecular interactions because they yield high-density arrays of biomaterials at biologically relevant scales. The ability to control, monitor and study biomolecular interactions, such as recognition, binding, catalysis and signal transduction, is critical not only for understanding fundamental cell biology but also for the design of efficient high-throughput biosensing and diagnostic methods. Biomolecular micropatterns can produce motifs that can be used as simplified surrogates for the complex cellular microenvironment. The successful fabrication of DNA, protein, and biomembrane patterns have enabled the study of targeted biomolecular interactions in vitro, which would be hard or impossible to study in vivo. Moreover, the demand for efficient detection of proteomic and genomic biomarkers, as well as the need for rapid detection of pathogenic threats has placed great emphasis on the production of biofunctional micro/nanostructured materials. Such materials can act as recognition elements in high-throughput biosensing platforms, and enable the

specific binding and sensing of target biomolecules in complex mixtures with hig8h sensitivity and low noise.

Micro- and nanomaterials are also attractive candidates for high surface area electrodes, which can be achieved by either structuring thin films or conducting polymers into micro/nano scales, or by using high-surface-area nanomaterials such as graphene, carbon nanotubes, metal nanoparticles, etc. On one hand, high surface area electrodes are very important components in the development of electrochemical energy conversion and storage technologies such as batteries, fuel cells, and electrochemical supercapacitors.[24–26] As electrodes with high surface area provide a higher capability for charge accumulation and storage, they can increase the device energy density.[27] On the other hand, such electrodes could increase the sensitivity of electrochemical sensors and lower the detection limit for the quantitative detection of chemical and biological species.[28,29] High packing density of electrode materials can more effectively support a large number of electroactive species, and thereby greatly enhance the mass and electron transfer efficient.[25,30]

In addition, micro- and nano-sized topography has been intensively explored to mimic the cellular microenvironment for cell and tissue engineering, and to study the extracellular matrix (ECM) effect on cell behavior.[31] The ECM provides cells and tissues their unique microenvironment in vivo, with certain geometry, architecture, composition, as well as many mechanical and dynamic properties (Figure 1-1).[32] These factors can direct cell behavior by providing spatial and mechanical cues to which cells respond. However, in traditional culturing conditions, cells are grown in a very different environment from their ECM, on polystyrene or glass petri dishes that are rigid, uniform, and static. Therefore, micro/nano- topographies have been explored, and it has been shown that they can provide cues to stimulate cells and lead to changes in cell properties such as morphology, architecture and contractility, as well as changes in cell

behavior such as adhesion,[16] proliferation,[33] and differentiation.[34] The ability to control cell morphology and function through structured materials would lead to more accurate prediction and better interpretation of cell behavior *in vitro*.

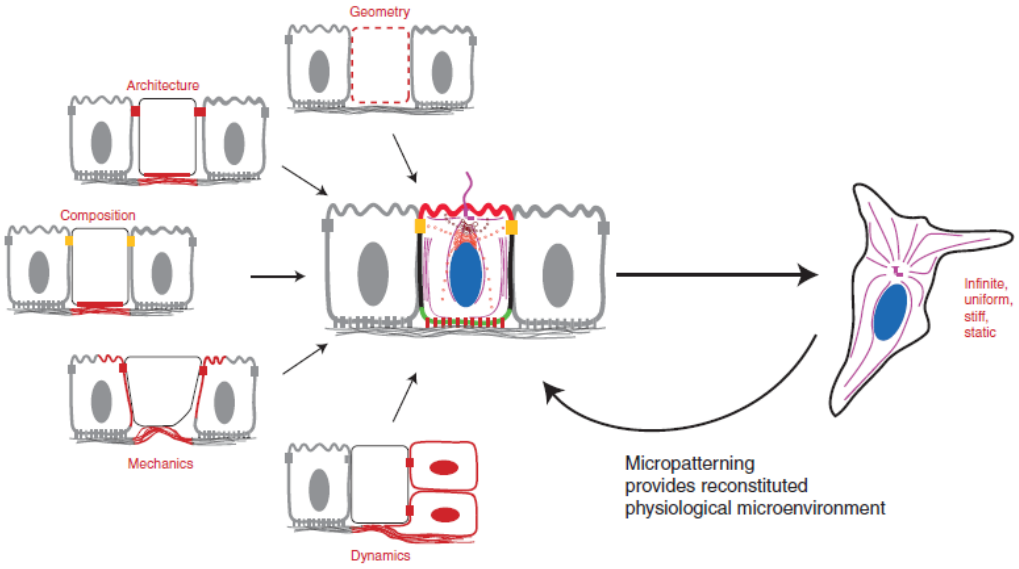

Figure 1-1 Schematic illustration of various types of physical cues that ECM can provide for cell growth in vivo, and comparison with conventional in vitro culturing environment. (Reprinted from reference [32])

1.1 Micro/Nanofabrication Strategies

Due to the unique properties and various applications that micro/nanostructured surfaces can provide, numerous approaches have been explored to produce a broad range of surface structures with desired functions. According to the way how materials are treated, we can categorize the fabrication strategies into the following three types: 1) adding materials in micro/nano scales, 2) removing materials within chemically or physically defined boundaries, and 3) direct structuring of bulk materials or thin films.

1.1.1 Material Addition

Adding materials onto a substrate in a controlled manner at micro/nano scales is one of the strategies for micro/nanostructure construction. To control material addition accurately, a mask is often used during the process (e.g. photoresists, polymer films, and metal masks). In the lift-off approach, the mask is removed after material deposition or growth. Alternatively, direct transfer of material could be used to move an existing pattern onto another substrate (microcontact printing), or to write out patterns with automated control system or computer-aided design -driven techniques (e.g. inkjet printing, pin microspotting, etc.).

1.1.1.1 Vapor Deposition

Deposition refers to the process creating a thin layer of a specific, solid-state material with structural or functional properties on the surface of a substrate.[35] Vapor deposition techniques are based on physical or chemical processes, or a combination of both. In a physical vapor deposition process, a physical force is applied to remove atoms from the target source (either solid or liquid) and transform them into a gaseous phase, which are then deposited onto sample surfaces. The driving force to remove source atoms could be a thermal process or a plasma. The former evaporates the source material into gaseous phase, while the later ejects the atoms off a solid target due to collision and thermal spike.[36] The plasma driven deposition is also called sputtering, very commonly applied in semiconductor fabrication involving materials such as Au, Pt, Cr, Ti, TiO_2, ITO, Si_3N_4, etc. Chemical vapor deposition (CVD) is a method for depositing a thin solid material from the gas phase by a chemical reaction (e.g. pyrolysis, reduction, oxidation, nitridation, and carbidization, etc.). CVD is capable of providing uniform, conformal surface coverage over large areas, which is one of the major advantages over physical vapor deposition. It is a very versatile technique that can be used to deposit materials with high degree of purity and control in amorphous,

epitaxial, polycrystalline, and monocrystalline forms. Materials that can be deposited by CVD include silicon and carbon-based materials, fluorocarbons, filaments, tungsten, titanium nitride and various high- κ dielectrics.[36]

Polymerization by CVD has significantly increased the capabilities of designing and fabricating polymeric surfaces. In CVD polymerization, the thin films are formed through polymerization of vapor-phase monomers, which enables insoluble polymer coating and eliminates solvent damage to the underlying substrates.[37] Poly-xylylene (also known as Parylene) thin film deposition is a commercially available CVD process for microelectromechanical system and medical device fabrication. Parylene is the generic name for a polymer series including Parylene N (poly-para-xylylene), Parylene C (with one chlorine atom in each unit), Parylene D (with two chlorine atoms in each unit), Parylene F (perfluorinated), and Parylene AF4 (fluorination of the four aromatic positions), etc. Among them, Parylene N, Parylene C and Parylene D are widely used as coating materials, with structures shown in Figure 1-2. The Parylene N exhibits high dielectric strength and very low dissipation factor, but it has too weak strength for some applications. With the chlorinated Parylenes, higher film density can be achieved, due to their higher molecular weight. While Parylene D suffers from poor film uniformity across large area, Parylene C maintains the balance of good electric and physical properties, allowing the formation of highly conformal film with very low permeability to moisture or other corrosive gases.[38,39]

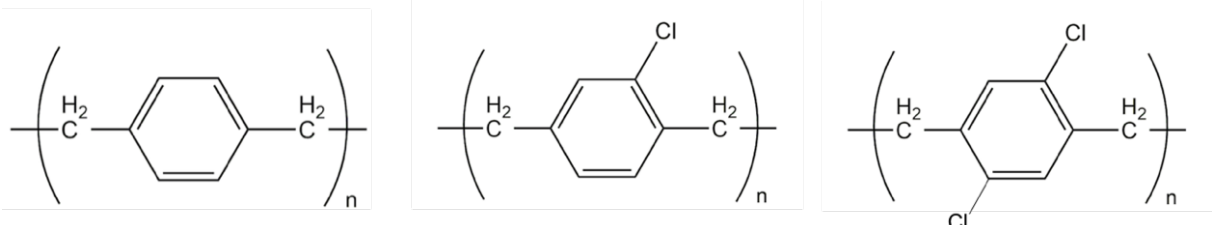

Figure 1-2 The chemical structures of Parylene N, Parylene C, and Parylene D.

Vapor phase deposition of the Parylene polymer allows the formation of a continuous film which is pin-hole free and truly conformal to the substrate surface. The deposition process through gaseous processors was first discovered as a product of the pyrolysis of para-xylene, by Szwarc in 1947.[40] Later in the 1960s, Gorham improved the Parylene deposition method and it has since become commercialized and widely used.[41] This method starts with the sublimation of Parylene dimer (di-para-xylylene) at 150-200 °C, followed by its pyrolysis at 550-650 °C into para-xylylene monomers (Figure 1-3). The monomers are then physisorbed onto a substrate surface (25-30 °C), and polymerize through surface migration and possibly bulk diffusion.[42] The resulting Parylene film thickness is usually controlled by the amount of solid-phase dimer that is loaded into the system, which can be from tens of nanometers to several micro meters in thickness.[43]

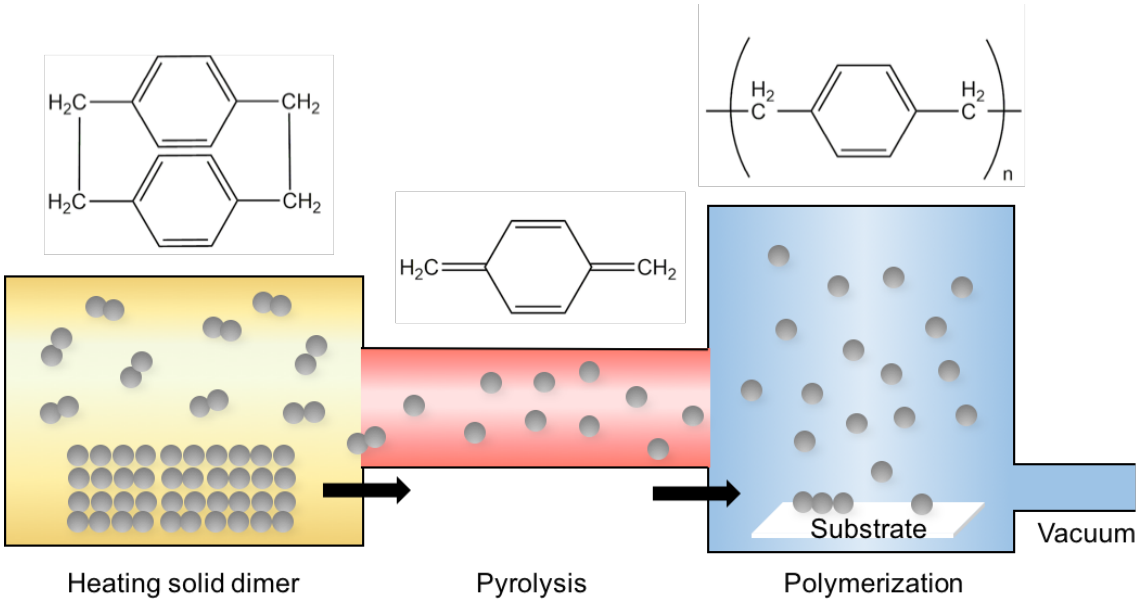

Figure 1-3 The mechanism for Parylene thin film formation using chemical vapor deposition. The Parylene dimers go through vaporization and pyrolysis, and the resulting monomers are then physisorbed onto substrate surfaces and polymerize into uniform coating.

1.1.1.2 Growth

Guided and controlled nucleation and material growth have also been used to fabricate micro/nanostructured surfaces. These fabrication techniques are bottom-up processes such as self-assembly and electrodeposition. Self-assembly forms well-defined and functional micro/nano-geometries through the local interaction and organization of pre-existing components including atoms, molecules or nanoparticles.[44,45] Various fundamental interaction forces can govern self-assembly processes, such as Van der Waals forces, electrostatic forces, hydrophobic effect, steric and depletion forces, hydrogen bonding, etc. Electrodeposition creates micro/nano structures via electrochemical reactions, and is used widely for growing metal, alloy, and polymer structures. These bottom-up approaches are versatile and cost-effective, and practically realizable.[44]

Electrodeposition has been highlighted as an attractive approach for growing nanostructured materials. Different from physical and chemical etching in a dry environment, in electrodeposition the substrate is submerged in liquid, an electrolyte solution. Figure 1-4 (A) shows the setup for electrodeposition process, where an external source is applied to generate an electrochemical reaction to achieve deposition.[35] As the electrochemical process involves electron transfer, the substrates are required to be conductive. The deposited film thickness can be accurately controlled by monitoring the charge involved in the reaction, and deposition rates on the order of tens of microns per hour can be routinely achieved.[46] The formation of nanostructures is greatly affected by nucleation and growth modes of metal or polymer electrodeposits, which depends on the binding energy between the reduced atom and deposited substrate. With simple equipment and low cost, electrodeposition can aid in the preparation of nanostructures from various materials, including metals, alloys, ceramics, polymers and composites.[47–50] These nanomaterials can be formed either as coatings or as freestanding structures in desired shapes (e.g. foils, wires, nanorods,

etc.). Figure 1-4 (B) presents an example of triangular Pd nanorod structures fabricated by electrodeposition.

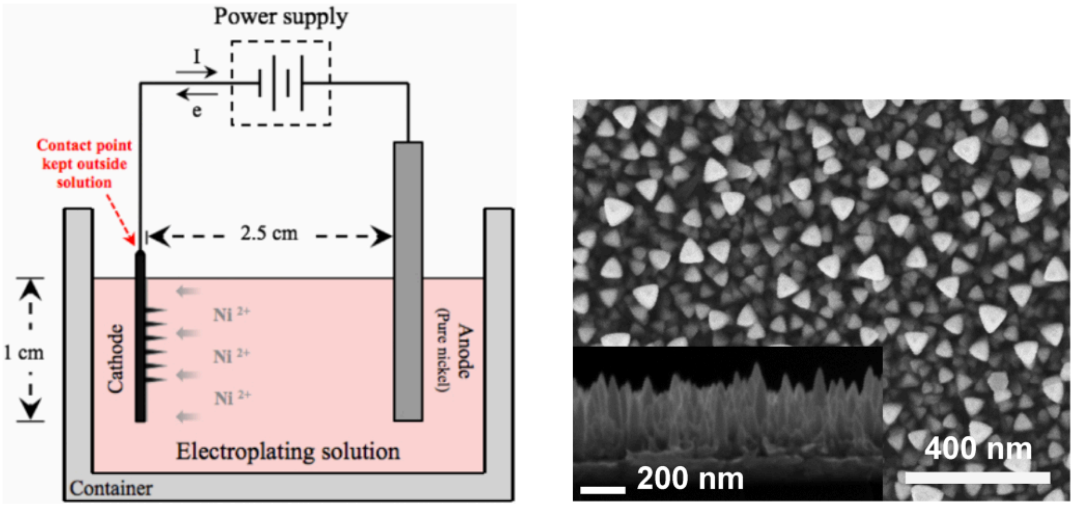

Figure 1-4 Electrodeposition process and an example of nanostructured surfaces created with this technique. (A) Schematics depiction of the electrochemical setup for the electrodeposition process (reprinted form reference [51]). (B) SEM image of triangular Pd rod structures electrodeposited, and the inset shows a cross-sectional image (reprinted from reference [49]).

1.1.1.3 Transfer

Micro/nanostructures can also be created by transferring materials as pre-existing patterns or as printable ink. Example for such techniques include microcontact printing (μCP), inkjet printing, pin microspotting, and screen printing. Direct-writing techniques with printable ink are flexible, inexpensive, and convenient for design customization, but they suffer from low resolution and are not the best option for mass production.[52] In contrast, pattern-transfer through μCP is well suited for large scale production in a cost-efficient manner, and is very popular technique for micropatterning.[53]

μCP is a relatively new soft lithography technique, which was first proposed by Whitesides and Kumar in 1994.[54,55] As illustrated in Figure 1-5, in μCP, an elastomer and hardener mixture is

cast onto a master mould and cured to form a structured surface. The cured elastomer (e.g PDMS) can then be used as a tool to stamp an "ink" containing the molecules to be transferred to a solid surface. Due to the patterned structure of the stamp, only the areas with protrusions are able to contact the substrate surface, and the target molecules are area-selectively transferred according to the pattern of the template, with a reproducible resolution of down to 500 nm.[53] Major problems with this technique is the shrinking and deformation of stamp which leads to unfaithful transfer of the designed pattern and limits the pattern resolution. By modifying PDMS stamp or employing new stamp materials, the capacity of μCP has been greatly improved to form patterns within sub-100 nm range.[56–58] μCP achieves high throughput with relatively low cost, via the use of reproducible and reusable elastomer stamps with easily adjustable stamping area. However, this technique could cause sample contamination, as uncured siloxane oligomers can potentially be left and transferred from the stamp to the sample, decreasing the pattern quality.[59]

In the initial implementation of μCP, such a stamp was used to transfer patterns of self-assembled monolayers of thiolated molecules onto a gold surface. With the improvement of printing methods and stamp materials, μCP is becoming an increasingly reproducible surface-patterning technique with higher pattern resolution,[53] , and has been utilized for patterning a variety of other materials, such as nanoparticles,[60] thin metal layers,[61] conducting polymers,[62] proteins,[63] and cells.[64]

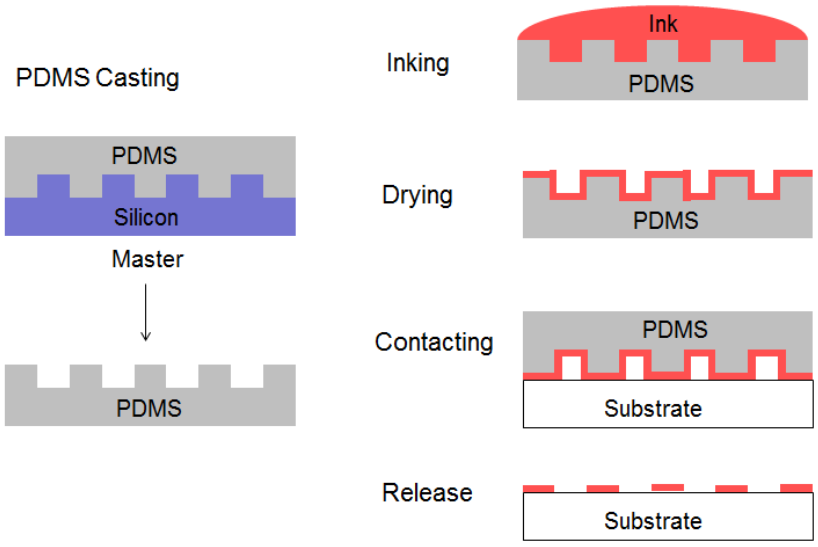

Figure 1-5 A schematic representation of microcontact printing technique

1.1.2 Material Removal

Another way of creating micro/nanostructured surfaces is to selectively remove some materials from a thin film or from the surface of a bulk material. To manipulate the position where materials should be removed, the processes mostly involve using a mask to expose the desired area either optically or physically. Nevertheless, with some techniques, direct writing is feasible and no mask is required (e.g., electron beam lithography, focused ion beam). Lithography and etching are two common methods for micro/nanofabrication involving material removal, and due to the importance to the research presented in this thesis they will be discussed respectively.

1.1.2.1 Lithography

Lithography is a conventional and classical technology for micro/nano patterning which removes part of the resist layer through masking or controlled writing by energy source of photons, electrons, X-rays, and ions, etc. Standard techniques include optical lithography, electron beam lithography, soft X-ray lithography, and ion beam lithography. Novel lithography techniques

include nanoimprint lithography, scanning probe lithography, and two-photon lithography.[65] Table 1-1 compares the throughput and resolution of standard lithographical techniques.

Table 0-1 Comparison between standard lithography techniques of their resolution and throughput. (The table is adapted and modified form [66])

Lithography Technique	**Resolution**	**Throughput**
Photolithography (Contact and Proximity Printing)	2-3 μm	Very High
Photolithography (Projection Printing)	37 nm	High- Very High
Electron Beam Lithography	5 nm	Very Low
X-Ray Lithography	15 nm	Low
Ion Beam Lithography	50-300 nm[67]	Low

Photolithography is one of the most important technologies in the microelectronics industry. It is based on the ultraviolet (UV) light radiation of photoresist to create desired patterns. A photolithography system consists of a light source, a photo mask, and an optical projection system. The resolution of photolithography is not only limited by the wavelength of UV, but also affected by the printing method. Contact and proximity printing have a resolution of 2-3 μm, and projection printing possesses a higher resolution. By implementing extreme UV which possesses a smaller wavelength, the resolution down to 37 nm could be achieved. Photoresists is a mixture of photoactive compounds, polymeric backbones (e.g. resin), and suitable solvent. There are two types of photoresist: positive tone resists are ones that becomes more soluble after being exposed to radiation, while negative tone resists show decreased solubility upon exposure. Most positive photoresists use diazoquinone (DQ) or diazonaphthoquinone (DNQ) as photosensitive compounds, which is not soluble in the base developer solution. However, DQ or DNQ undergoes molecular rearrangement forming a ketone under UV radiation. During development, OH^- group from the basic developer solution attaches to the carbon atom of the ketone, forming an acid, and then dissolves in the basic solution.[68] On the other hand, negative resists form highly cross-linked, chemically resistant polymers (e.g. styrene, maleic acid polymer) upon radiation, where the

initiator absorbs photons forming radicals, and initiates polymerization process.[69] As shown in Figure 1-6 photolithography starts with the spin coating of photoresist with controlled thickness. When the resist exposed to UV through a photo mask, the exposed areas become either soluble (positive resist) or insoluble (negative resist) in the developer. The developing process removes the soluble materials, leaving defined patterns on the substrate. Photolithography is common lab technique, but the process is relatively time consuming and is not ideal for scaling up.

Compared to photolithography and X-ray lithography, electron beam lithography has a much higher resolution of ~5 nm, achieved by using electron beam which has a shorter wavelength than UV or X-ray. The process for E-beam lithography, similar to photolithography, involves spin coating of e-beam resist, exposure to the beam, and development, as shown in figure 1-6. Instead of using projection masks, a scanning system is mostly used for pattern generating with electron beam. In this mode, a highly focused electron beam is scanned over the surface of the resist with the diameter as small as sub-10 nanometers. Since electron beam lithography has ultra-high resolution, and ease of prototyping, it is usually used at the very beginning of a multiple technique and a multiple step process in a top down approach in order to transfer the nanostructure into the substrate or subsequently build up a device in a layer by layer fashion. The disadvantages of this techniques are low throughput, high cost, and complex operation.

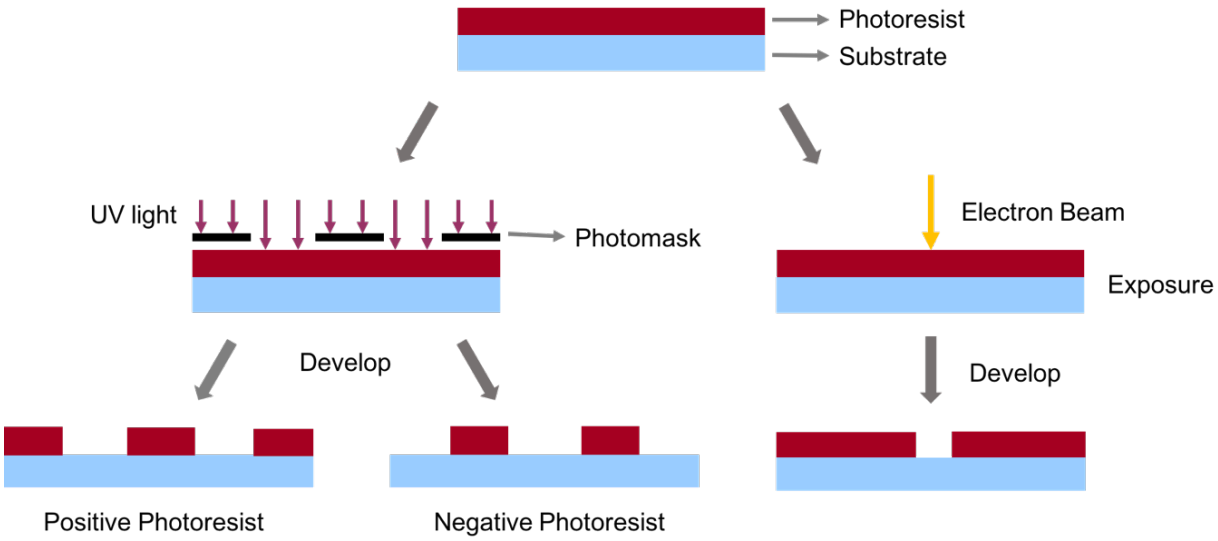

Figure 1-6 The schematic presentation of photolithography (left) and electron beam lithography processes (right).

1.1.2.2 Etching

Etching refers to the techniques that remove materials from a substrate, by dissolving it with liquid or gaseous chemically active compounds or by electrochemical processes. To create micro and nano-patterned surfaces, a mask layer (e.g. photoresist and thin metal film) is used to protect areas that are not to be etched. The protective layer is usually removed after the process is completed. Etching can be achieved through either a wet or a dry process.

Wet etching utilizes a liquid etchant and requires the target material to be reactive with or soluble in the etchant solution. The reaction products must also be soluble in the liquid or can be removed from the system by other methods. Moreover, neither the masking material nor the substrate should be insoluble in the etchant solution. Table 1-2 shows some examples of thin film materials and their etchants as well the etching conditions. Some etchants show different reaction rate for different crystal faces of a material, thus making anisotropic etching possible. For conductive films, electrochemical etching could also be used, where the target film is employed as an electrode in an electrolytic cell, and the electrically driven reaction would lead to film

consumption. The biggest limitation of wet chemistry etching is the low resolution compared to dry etching, due to the isotropic nature of the etching which leads to the undercutting of the mask film, as illustrated in figure 1-7.

Table 0-2 Examples of thin film materials and their liquid etchant in wet chemical etching. (Adapted from references [36,70])

Film	Etchant	Temperature of Etch Bath (℃)
SiO_2	HF	20-25
Si_3N_4	H_3PO_4	160-180
Si	HNO_3+HF KOH Ethylenediamine Pyrocatechol	20-25 50 110
Pt	HNO_3 + HCl	108
Au	HNO_3 + HCl I_2+KI	108 20-25
Al	H_3PO_4+HNO_3+CH_3COOH	40-50
ITO	HCl+HNO3	40

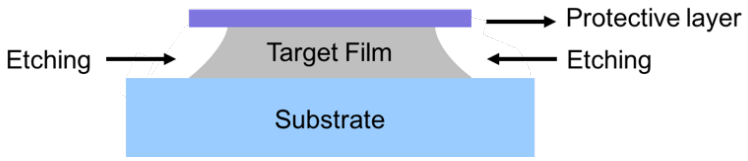

Figure 1-7 The schematic illustration shows the undercutting effect of protective layer in wet chemical etching.

In dry etching, typical etchants are vapor, plasma and ions. The target materials can either be removed chemically (vapor phase etching and reactive ion etching) or physically (sputter etching). Vapor phase etching uses one or more type of gases to dissolve the target material through chemical reactions. For example, silicon dioxide can be etched using hydrogen fluoride (HF) and silicon can be etched with xenon diflouride (XeF_2). In sputter etching, an ion beam is directed onto the surface of target material and remove it by bombardment, very similar to sputtering deposition which was introduced in section 1.2.1.1. The selection of substrates and resist layers should be based on relative sputter rate of the materials. However, the fact that sputter rate of most materials does not differ much, limits the choices and applications of this technique.

In contrast to sputter etching, reactive ion etching (RIE) can remove materials more selectively using plasma of a reactive gas. Ions in the plasma are not as energetic as in sputtering, so the reactive components do not bombard the surface, but just adhere to it and undergo chemical reactions. The reaction products are desorbed and released from the system by constant pumping. Another advantage of RIE compared to wet etching is that it can etch into depths of several hundred microns without undercutting the resist layer, because the higher etching rate on the horizontal surface than the side walls. RIE was first used to strip photoresist in integrated circuit fabrication,[71] and has matured and used for numerous applications over the past decades.

1.1.3 Direct Material Structuring

The third strategy to create micro/nanostructures is to change the shape or morphology of a material directly through applying external force, such as molding, compressing, and electrical force, etc. Here, micro hot embossing, soft lithography, and polymer compressing methods will be introduced in details.

1.1.3.1 Micro Hot Embossing

Micro hot embossing is a very inexpensive replication technology to transfer microstructure patterns from a master mold onto thermoplastic polymer substrates under appropriate pressure and temperature.[72] This technology has over 40-year history, and has been partially applied in industrial production,[73] as one of the most promising techniques to fabricate high-precision and high-quality features at the micro/nano scale in academia and industry. Briefly, the micro hot embossing technique involves four major steps (Figure 1-8): (1) heating of the mold and substrate to molding temperature; (2) isothermal molding by embossing through either velocity control or force control; (3) cooling the mold and substrate to demolding temperature, with the pressing force

being maintained; (4) Demolding of the embossed material from the mold. Steps (1) and (2) is a stress application and strain hardening stage, while steps (3) and (4) is a stress relaxation and deformation recovery stage.[74] Molding temperature, pressing force and holding time are the most important factors that affect the micro hot embossing process.

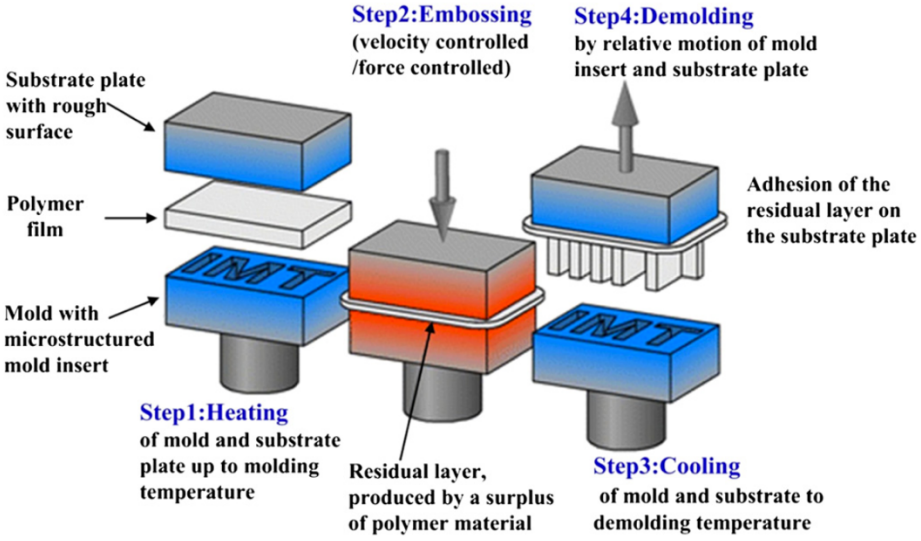

Figure 1-8 Schematic representation of a typical micro hot embossing process with four major steps: heating, molding, cooling and demolding. (Reprinted form reference [75])

Thermoplastic polymers are the most used materials in micro hot embossing, due to their low cost, light weight, and low molding temperature.[73] The process temperature is critical to the local fidelity and global uniformity of microstructure formation with such polymers. With the increase of temperature, thermoplastic polymers go through three phase states: glassy state, rubbery state and flow state (figure 1-9).[76] When the thermoplastic polymers are pressed in the glassy state, the deformation is elastic and is majorly contributed by the increase of atomic distance. When pressed in rubbery state, the thermoplastic polymers act like an incompressible or approximately incompressible rubber, because chain segments begin to move but are still fixed by the temporary

network of entanglements. When polymers reach the viscous liquid flow state, the entire polymer chains are mobile and the polymer flows by chain sliding, so deformation at this stage is irreversible.[73] At this state, the polymer flow have relative easy access into the corners of the embossing mold, and thus results in microstructures with high fidelity.[77] Although high process temperature (above T_g) is important for faithful transfer of microstructures, it introduces difficulty in demolding and bending or distortion of embossed devices on large scale due to excessive heat. especially for large area and high aspect embossing. [78] With low temperature micro hot embossing (lower or near T_g), the global flatness can be significantly improved, but both instantaneous and retarded recovery after becomes an issue.[77] Therefore, the molding temperature needs to be optimized according to the material properties and the fabrication requirements.

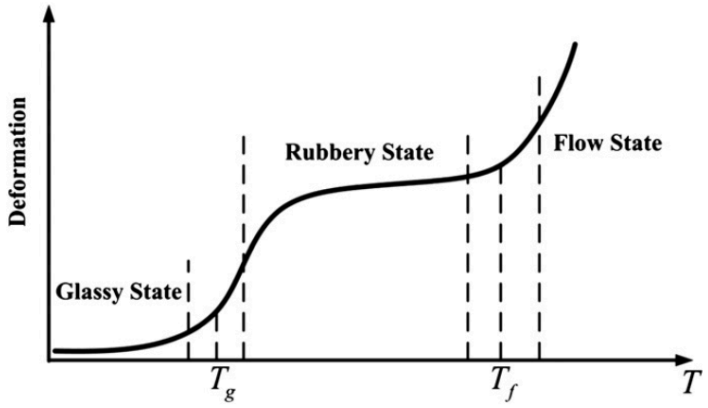

Figure 1-9 Thermoplastic polymers deformation versus temperature in three states: glassy, rubbery, and glow state. (Reprinted from reference[76])

1.1.3.2 Soft Lithography

Soft lithography refers to a family of low cost non-photolithographic techniques first introduced by Bain and Whitesides in early 1990s.[79] This strategy is based on self-assembly and replica molding of organic molecules and polymeric materials for carrying out micro- and nanofabrication.[80,81] Many techniques have been developed using this concept: microcontact

printing (μCP), replica molding, micromolding in capillaries, solvent assisted micromolding (SAMIM), microtransfer molding (μTM), phase-shifting edge lithography, nanotransfer printing, decal transfer lithography, and nanoskiving. Although with different approaches, they are all in principle based on printing, molding and embossing processes. μCP has been introduced in the previous section *1.2.1.3* as a technique to transfer patterned materials. Here we will briefly introduce two other methods which can directly structure materials into micro/nano sized features.

Fabrication of elastomeric stamps is the basis for all the soft lithography techniques, as shown in Figure 1-10. Typically, the stamps are created by mixing elastomer precursors and curing agent and cured the mixture in the mold with desired shape. The molds for stamp casting can be made of various materials, such as photoresist, Si_3N_4, and metals, etc. Figure 1-11 illustrates the fabrication processes of μTM, replica molding, and SAMIM. In μTM, the stamp is filled with a pre-polymer, placed on a substrate and cured, while in replica molding, the prepolymer is applied onto the substrate, and the stamp is pressed against it. When the stamp is removed, the patterned structure is left on the substrate. In SAMIM, the surface of the elastomeric stamp is wetted with a solvent and pressed against the polymer film deposited on the substrate at ambient conditions. The polymer is softened by the solvent, and conforms to the shape of the stamp. The main problem associated with this technique is that the solvent can swell the elastomer mold, and thus decrease the accuracy of pattern transfer. Both μTM and SAMIM can be used to form isolated nanostructures.

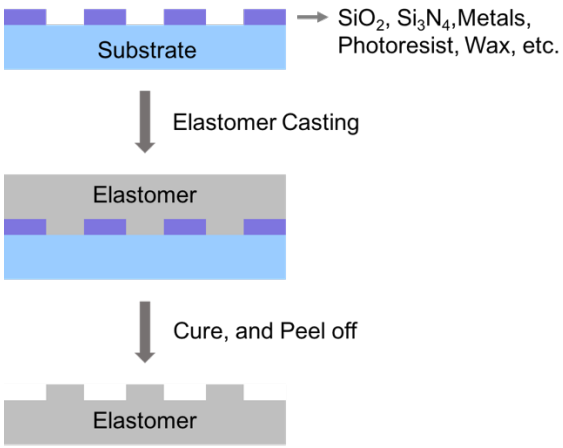

Figure 1-10 A schematic illustration of the elastomeric stamp fabrication in soft lithography.

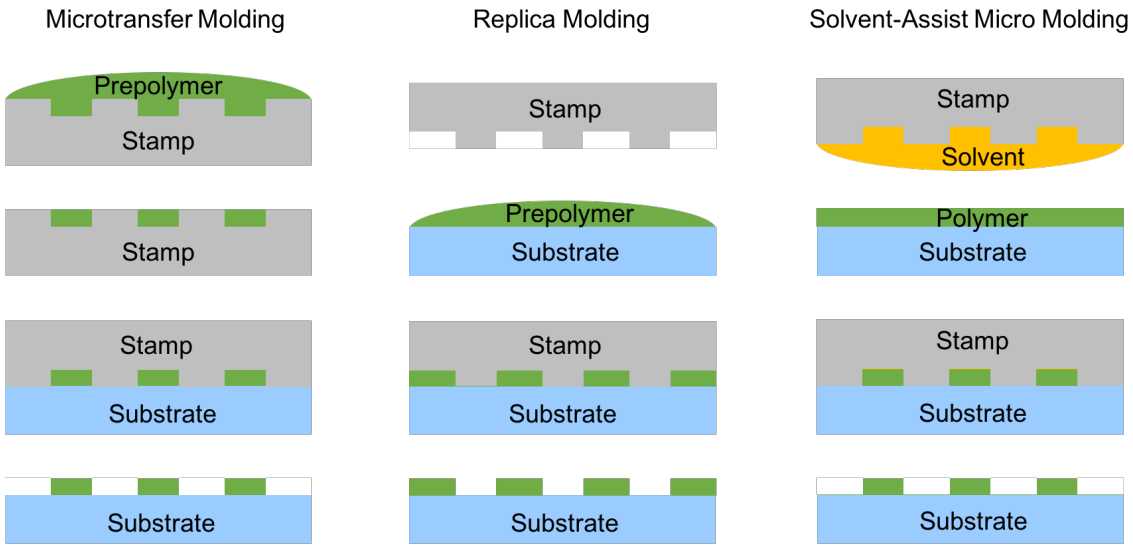

Figure 1-11 Schematic illustration of three major soft lithographic techniques: microtransfer molding, replica molding, and solvent-assist micro molding.

1.1.3.3 Pre-stressed Polymer-Based Structuring

By pre-stressing a polymer substrate and releasing the tension, a material film deposited on top can be structured. There are generally two ways to achieve this: (1) Mechanically pre-stress the stretchable elastomer within its elastic recovery range, deposit thin films, and then release the

external force; (2) Pre-stress and mold a shape memory polymer under high temperature, deposit thin films, and reheat to retract. Both methods apply a compressive force on the deposited thin film, which cause the surface to wrinkle and buckle either on one axis or both axes, depending on where the strain was applied.

Polydimethylsiloxane (PDMS) is probably the most widely used elastic substrate for wrinkling thin films, a phenomenon that was first reported by Martin et al. in the early 1980s.[82] Later, Whitesides et al. studied ordered structures on PDMS and further developed a model that relates the stresses to the wave patterns.[83] Figure 1-12 depicts the wrinkle formation process, where the mismatch of the mechanical properties of the thin film and the elastomer substrate leads to the buckling. The wavelength of uniaxial wrinkling can be determined by equation (1), where λ is the wrinkle wavelength, h is the film thickness, v_s and v_f are the Poisson's ratios of substrate and thin film, respectively, E_s and E_f are their Young's modulus.

$$\lambda = 2\pi h \left[\frac{(1-{v_s}^2)E_f}{(1-{v_f}^2)E_s}\right]^{1/3} \quad (1)$$

As, the wavelength λ is proportional to the thin film thickness *h*, for the same material, the wrinkle sizes increase with increasing film thickness. λ also increases with the increase of thin film rigidity and the decrease in substrate rigidity (described by the Young's Modulus E_f and E_s). The amplitude of the wrinkles is also linearly proportional to film thickness, and can be quantitatively evaluated by equation (2):[84,85]

$$\mathrm{A} = \mathrm{h}\left(\frac{\epsilon}{\epsilon_c} - 1\right)^{1/2} \quad (2)$$

Where A is amplitude, ϵ and ϵ_c are the buckling strain and the critical buckling strain, respectively. The critical buckling strain must be exceeded for wrinkling to happen.

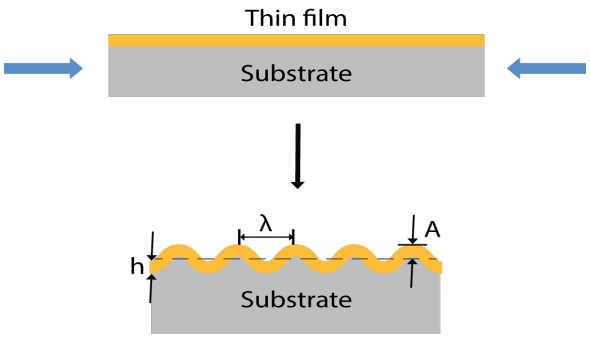

Figure 1-12 Schematic presentation of the wrinkle formation of a thin film on elastomeric substrate, where h represents thin film thickness, λ is wavelength, and A is amplitude.

When larger strain is applied, the film can buckle in multiple scales to release the excess strain. After the first generation of wrinkles saturates, a secondary wrinkling appears on much larger wavelength, forming hierarchical structures.[86] The secondary winkle wavelength can be determined similarly as the first generation using equation (1), using the effective height (h_{eff}) of the first generation wrinkled film and the effective Young's moduli of the film (E_{feff}) and substrate (E_{seff}) at the corresponding buckled condition.[87] The wrinkled structures are not only useful as a component in functional devices, but can also be used to transfer patterned materials onto other planar surfaces such as glass, or Si wafers. For example, colloidal particles can be patterned with this method, which is then accessible for studying their optical, electronic, and physical properties.[88]

1.2 Thin film Structuring Techniques Used in This Thesis

In this section, three patterning and structuring techniques that our group has developed are introduced in detail: Parylene stencil lift-off, vinyl stencil lift-off, and shape-memory polymer thermal shrinking. All the techniques we use aim at decreasing fabrication cost and simplifying fabrication processes.

1.2.1 Parylene Stencil Lift-Off

Parylene stencil lift-off (PSLO) is utilized for in this thesis work for micropatterning, due to its good biocompatibility, pattern transfer fidelity, and its applicability to patterning under aqueous conditions. PSLO is a relatively new patterning method that enables the formation of arrays of micro- to nanometre-sized biomaterial domains over large surface areas. In this approach, Parylene C (dichloro-[2,2]-paracyclophane) is the most commonly used polymer because it produces chemically inert, pinhole-free, thin polymer films. Furthermore, these films do not swell in the many solvent and can be mechanically peeled off from the surface under aqueous conditions, which makes them excellent templates for patterning biomaterials that need to be kept in hydrated environments (e.g. lipid membranes and cells).

The principle behind PSLO is illustrated in Figure 1-13. First, a thin conformal polymer film is deposited onto the solid surface through chemical vapor deposition. A photoresist layer is then coated on the polymer and patterned using photolithography. With the patterned photoresist as a mask, the sample is subjected to a controlled oxygen plasma reactive ion etching process that removes the exposed polymer, thus effectively creating a polymer stencil. The materials of interest can then be applied and bound onto the exposed substrate, while the polymer stencil keeps all the covered areas protected. After the excess materials are washed away, the stencil can be mechanically peeled off due to its weak adhesion to the substrate, leaving the micropatterns on the surface.

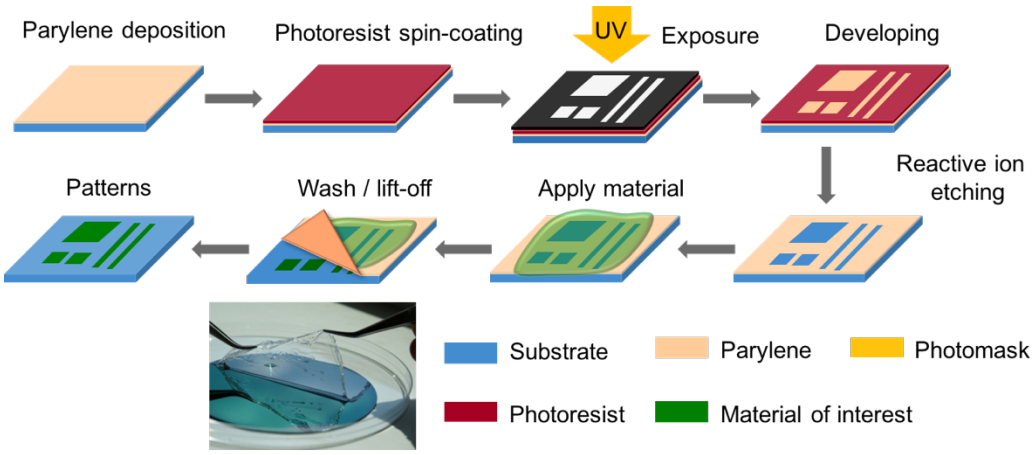

Figure 1-13 Schematic of Parylene stencil lift-off technique. Inset is a photo showing the lift-off process of a ~600 nm Parylene thin film on a SiO_2 wafer.

1.2.2 Vinyl Stencil Lift-Off

Adhesive films, such as self-adhesive vinyl, can also be used as simple and cost-effective stencils. A pattern on the vinyl film is cut out through a computer-aided design (CAD)-driving cutter, where cutter motor and cutting step size are the determining factors of the resolution (100-200 µm).[50] After application of the vinyl mask on the solid substrate (e.g. polystyrene, glass, Si wafer, etc.), thin film material can be deposited by various techniques, such as sputtering, dip coating, spin coating, and blade casting, etc. This method is a truly lithography-free, bench top patterning strategy, which is great for prototyping of preliminary device design, and for fabricating low-cost, disposable devices for sensing, bioprocessing, tissue engineering and photovoltaic devices. In combination with shape-memory polymers, the pattern size can be further decreased to sub-100 µm scale, which could replace photolithography for some purposes. The limitation regarding to the use of polystyrene shrinking process is that the material must be heat resistant, since thermal shrinking of polystyrene occurs above 100°C.

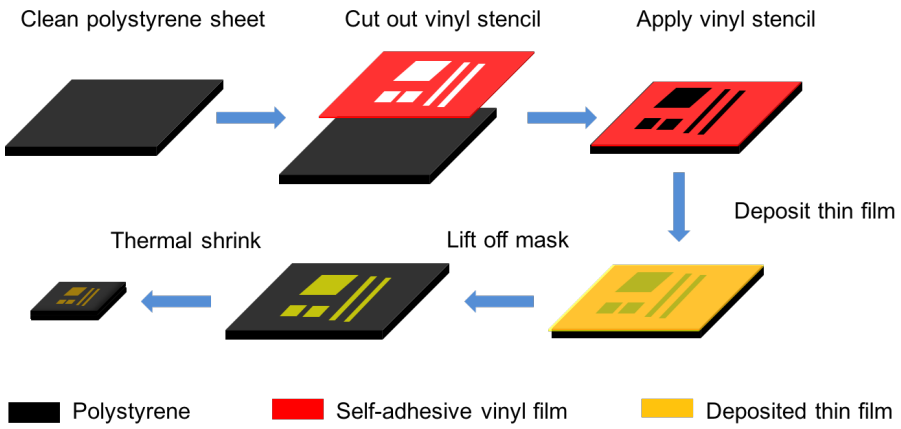

Figure 1-14 Schematic of vinyl film stencil lift-off technique. Inset is a photo showing the lift-off process of a cut-out vinyl from a polystyrene sheet.

1.2.3 Thermal Shrinking of Shape-Memory Polymer

Very recently, the thermal shrinking of shape-memory polymers was proposed as a facile and quick approach developed to form micro/nanostructured surfaces. Shape-memory effect refers to the ability that a material can gain back its original shape when activated with suitable stimulation (photo, chemical, or heat). The Whitesides group was the first to report the use of a shape-memory polymer for microfabrication purposes in the late 1990s.[83,89] For thermoplastic polymers, the glass transition temperature is usually a range where polymer transit from glass state to rubbery state (Figure 1-9). Below this temperature, polymer molecules are in glassy state with limited chain mobility and flexibility. Above T_g, the bonds between the polymer chains become weak and the macromolecules become mobile. Figure 1-14 illustrates the molecular mechanism of programming the temporary shape and recovering the permanent shape for a linear thermoplastic polymer. Under no external strain, the polymer chains mostly form compact random coils as this conformation is entropically favored, compared to the elongated conformation. When proper external force is applied under heat, the polymer chains tend to disentangle and to stretch along the direction of

external force. The decrease in temperature can freeze the chain mobility in a stretched state even after stress is released. When the temperature is brought back to above T_g, the polymer chain can relax back to an entropically favored state, recovering its original configuration.[90]

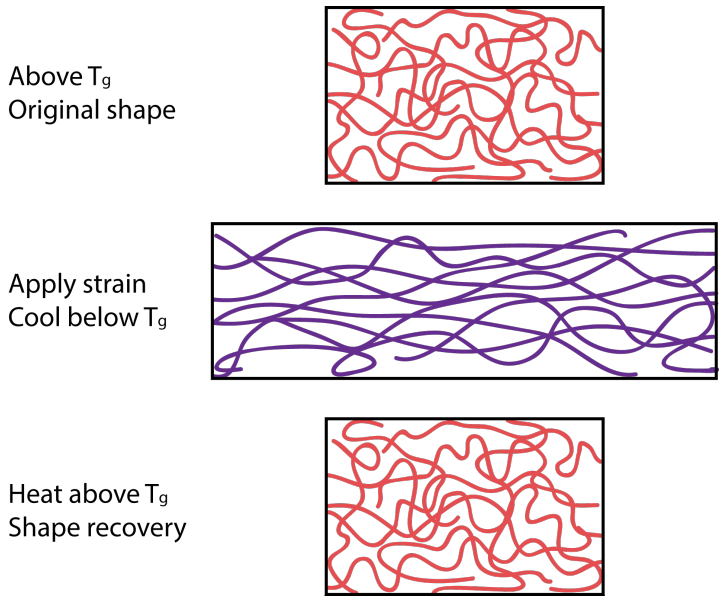

Figure 1-15 Schematic illustrations of shape-memory effect a linear thermoplastic polymer.

The shrinking process of a shape-memory polymer exerts compressive stress on the deposited thin film material causing it to wrinkle and form the micro/nanostructured surfaces in a controllable and reproducible fashion. The surface structure sizes and roughness are tunable by varying thin film thickness. The general fabrication process involves just three major steps: (1) Cleaning the shape memory polymer, (2) depositing a thin film of the desired material onto polystyrene surfaces, with adhesive masks applied if necessary, and (3) heating above the glass transition temperature of the polymer to shrink it. Many shape-memory polymers have been explored for structuring thin films including polystyrene,[91] polyolefin,[92] and polyethylene.[93,94] Polystyrene (T_g round 100°C) is the most widely used material, as it is commercially available at very low cost. The shape-memory polystyrene sheets are produced by Shrinky Dinks® for making

plastic arts and crafts, but has very recently find its application in micro/nanofabrication for scientific research. The industrial fabrication of Shrinky Dinks follows a roll-to-roll process where the polystyrene is pre-stressed under heat, and cooled down to below its glass transition temperature to maintain in the stressed state. The films shrink uniformly with a decrease of 60% in size in both x and y dimensions, and an increase in film thickness (z axis) to 600% to 700% of its original. The Khine group at the University of California, Irvine, was the first to report the use of such material for microfluidic device fabrication in 2008,[91] and later many other applications.

1.3 Applications of the Thin Film Structuring Techniques

1.3.1 Micropatterning of Supported Lipid Bilayer

The biological membrane is arguably the most important structural component of cells because it not only provides a protective container for the cell and its sub-cellular compartments, but it also mediates cellular communication, the transport of ions and molecules, and participates in a variety of biological processes.[95] Specific recognition and binding activities associated with biomembrane components form the basis of many biosensing assays, where robust patterning techniques can help reduce cross-contamination between patterned species and improve signal-to-noise ratio. As a supported lipid bilayer (SLB) retains a number of the structural and dynamic properties of cellular membranes, SLB micropatterns have been employed in biosensor design[96,97] and biophysical studies for cell membrane behavior.[98] Moreover, the easy integration of SLB patterns with miniaturized platforms such as microfluidics and lab-on-a-chip, has provided a powerful tool for studying biomolecule interactions with low sample consumption in an automated and high throughput manner.[99,100]

1.3.1.1 Supported Lipid Bilayer and its Formation

In cellular membranes, lipid molecules are held together by hydrophobic/hydrophilic interactions and self-assemble into a continuous bilayer, and various proteins are embedded within cellular membranes or transiently associated with them. Since the lipid bilayer was recognized four decades ago as the basic unit to design lipid models, various model lipid bilayer systems have been developed to investigate biomembrane structure and biological processes at the cellular level. Large multilamellar liposomes, as well as small and large unilamellar vesicles were applied in the early characterization of lipid bilayer structure and thermodynamic properties[101,102] as well as in protein insertion and binding studies.[103,104] Black lipid membranes, single unsupported planar bilayers, have also been applied to study the formation of ion channels in phospholipid bilayers by peptides, proteins and antibiotics.[105,106] In early 1980s, Tamm and McConnell first introduced the SLB system which is a fluid but highly ordered planar lipid bilayer structure formed on a solid support.[107,108] Compared to liposomes and monolayer models, SLBs have the advantage of easy access to a wide variety of high-resolution analytical techniques such as fluorescence microscopy,[109,110] atomic force microscopy,[111] and surface plasmon resonance.[112] The SLB is also a more stable system that allows changes in their properties and environment for specific applications. To date, SLBs have been used for chemical and biological sensing,[95,113,114] drug screening and delivery,[115,116] membrane-associated compound separation,[117,118] protein purification,[119] and fabrication of matrices for cell and tissue engineering.[120–122]

Supported lipid bilayers are typically ~5 nm in height, with ~1 nm water layer in between the bilayer and the substrate.[123] The hydrophobic tails of the lipids point toward each other and hydrophilic head groups point toward the water, as illustrated in Figure 1-15 (B). The thin water layer is crucial in maintaining the mobility of the lipid molecules on a solid substrate. SLBs are

mostly created through two techniques. One is the Langmuir deposition technique which involves two processes, Langmuir-Blodgett and Langmuir-Schaffer (Figure 1-15 (A)).[124] In Langmuir-Blodgett step, a lipid monolayer is first spread at the air-water interface of a Langmuir trough, and transferred onto a solid substrate. Then in the Langmuir-Schaffer step, the monolayer is transferred horizontally onto the monolayer at air-water surface by Langmuir-Schaffer pushing. This method is particularly useful for the formation of asymmetric bilayers, but is not suitable for incorporating proteins into the bilayer because some portions of the proteins would be exposed to air and may denature during the process. The other method is vesicle fusion where SLBs are formed on solid substrates directly through the fusion of small unilamellar vesicles (SUVs),[125] as illustrated in Figure 1-15 (B). SUVs can be created through either vesicle extrusion or sonication. The SLB formation involves the adhesion and rupture of vesicles on the support and the evolution of supported bilayer patches. A continuous SLB grows by successive vesicle fusion and lateral bilayer patch mobility.[126] The process depends on a number of environmental parameters, including substrate roughness and hydrophilicity, lipid-substrate electrostatic interactions and incubation conditions.[127,128] These parameters affect the integrity and the fluidity of the SLBs, so appropriate conditions are required to form homogeneous and fluid SLBs with little defects and high mobility.

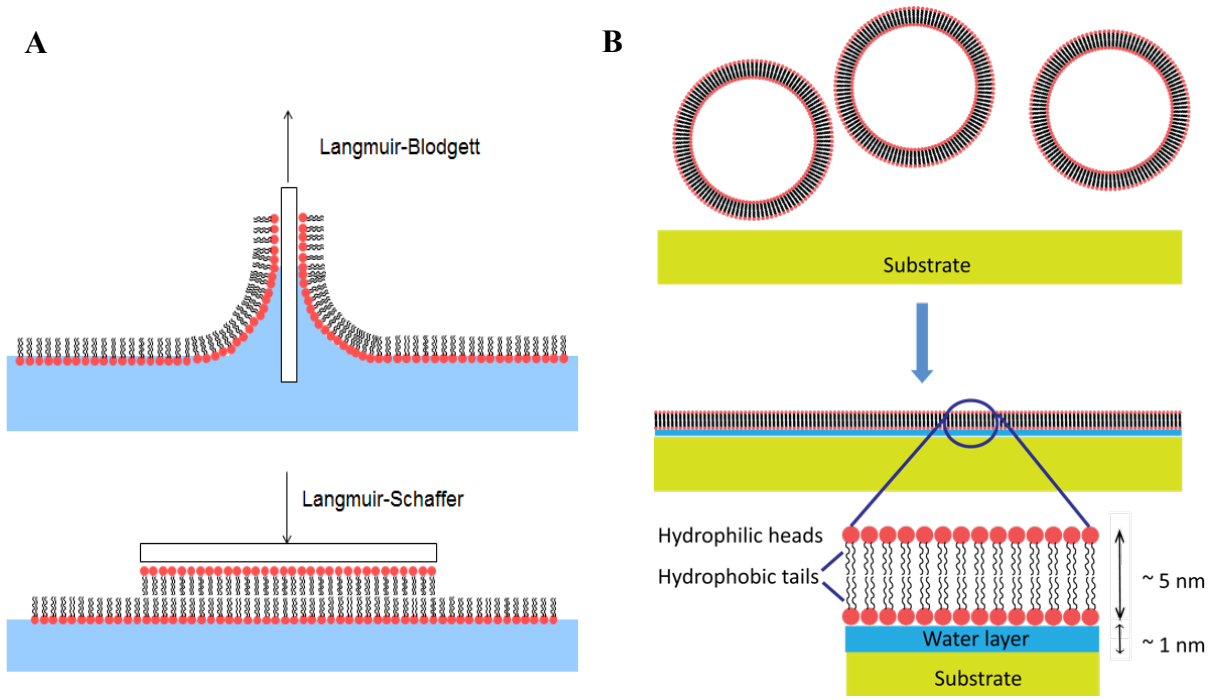

Figure 1-16 Two techniques for SLB formation: (A) Langmuir-Blodgett pulling for the bottom layer and Langmuir-Schaffer pushing for the top layer and (B) vesicle fusion to form SLB directly on the substrate.

1.3.1.2 Phase Segregation in SLBs

The study of phase segregation in lipid membranes has attracted much attention because it provides useful information about lipid-lipid interactions and can shed light into the formation of important cellular membrane structures. Phase segregation of lipid membranes into liquid-disordered (l_d) and liquid-ordered (l_o) domains (so called lipid rafts) has been recognized as a fundamental principle for the functional organization of proteins and lipids within the plasma membrane.[129,130] The description of which membrane molecules are clustered together and which are kept separated, helps us to understand more complex systems such as cell membranes. SLB is one of the most popular model systems that can mimic the key features of plasma membrane domains for such studies. The ease of integration of proteins into SLB allows the exploration of protein functions in the context of lipid phase segregation under controlled conditions in vitro.[131] Moreover, fluorescent probes with different partition coefficients make it easy to observe and

characterize individual phases of lipid molecules, as well as labeled proteins. AFM is also a robust tool for this purpose by probing the height differences between lipid phases.[111,132]

The phase segregation in a lipid bilayer is a spontaneous process, which is stochastic, time and lipid composition dependent. Changes in temperature, cholesterol concentration, ionic strength, and lipid components during vesicle fusion are factors that can trigger the segregation of different lipid components in membranes.[133,134] Figure 1-16 depicts the phase separation process of two types of lipids with different transition temperatures. In this thesis, we have used DOPC with T_g of -20 °C and DSPC with T_g of 55 °C. With the same carbon chain length, saturated lipids (e.g. DSPC) have higher transition temperature than unsaturated lipids (e.g. DOPC). When the temperature decreases to below the higher T_g, saturated lipids decrease in their mobility and form gel phase domains, while unsaturated lipid remain fluid, forming liquid disordered phase.

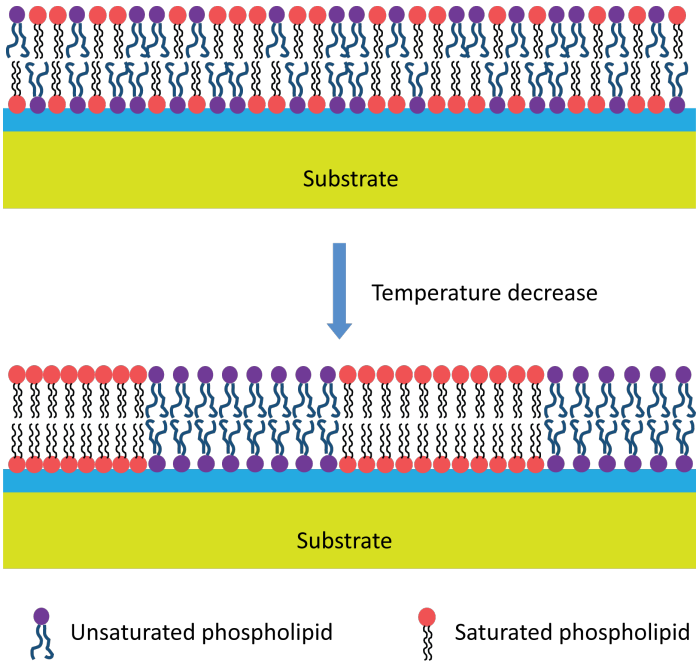

Figure 1-17 Schematic presentation of SLB phase separation. When the ambient temperature decrease from above to below saturated lipid transition temperature, the unsaturated and saturated lipids separate into two phases.

1.3.1.3 SLB Patterning through PSLO

Different from DNA and protein patterning, supported lipid bilayer (SLB) and cellular patterning are more challenging because they require the materials to remain in 'never-dry' condition which is not as easily achievable. A host of techniques have been used for SLB patterning including barrier separation,[135,136] quill-pin spotting,[137] micro-contact printing,[138,139] polymer stencil lift-off,[140,141] nanoshaving lighography,[142] and micro-fluidic networks,[143,144] etc. However, shortcoming of the current techniques lies in the ability to deposit a multiplicity of biomaterials to form intricate patterns. Techniques that could create complex SLB patterns will enhance our ability to study membrane and cell behavior under controlled environmental conditions. Furthermore, such techniques should also expand the range of platforms available for diagnostics based on membrane-binding analytes, and for the screening of drugs that target membrane associated proteins.[115] Polymer stencil lift-off is a robust technique for patterning in aqueous condition, which we utilized and improved to create complex SLB patterns. In chapter 2, we present the use of PSLO technique to create micropatterned SLB arrays, and use them as models to study the effect of domain size and environmental factors on the lipid mixture behavior. In chapter 3, PSLO is demonstrated for patterning stacked SLBs that are either homogeneous or phase-segregated. Through these simplified model systems, we aim at understanding more complex systems such as the plasma membrane and its interaction with other biological systems.

1.3.2 Micro/Nanostructuring of Thin Films

Thermal shrinking of shape-memory polymer has been recently used as a simple and low-cost micro/nanofabrication method for structuring thin films. Various materials have been structured with this technique, such as metal thin films,[92,145] hydrogels,[146] and silica.[147,148] Due to the high surface area, and the tunable micro/nanotopography, such structured surfaces have found broad

applications in chemical and biological sensing, flexible electronics, tissue engineering, and cell lysis. Here, we introduce a few specific application areas that relates to the work presented in Chapter 4, 5, and 6.

1.3.2.1 High Surface Area Electrode for Sensing and Flexible Electronics

The micro/nanostructured thin films are excellent candidates for the implementation of high surface area electrodes that can be applied in electrochemical sensing for increased sensitivity or photonic devices for higher energy conversion efficiency. In our pioneering work, we combined the thermal shrinking of a patterned gold film with subsequent electrodeposition, and fabricated hierarchical high-surface-area gold electrodes which demonstrate up to 1000% enhancements in electroactive surface area. In chapter 4, the development of this benchtop fabrication method is described in detail, as well as the electrode surface characterization and electrochemical sensing ability. Sonny et al. has later incorporate this high surface area electrodes into microfluidic devices for sensing.[149] The Soleymani group has also applied the wrinkled gold electrode for building a proof-of-concept electrocatalytic DNA biosensor which can distinguish between complementary and noncomplementary oligonucleotides.[150] They have also used the structured gold electrode for bacteria lysis, and achieved lower voltage lysis with high efficiency.[151] Zhang et al. employed the structured Pt/ITO film as photocathode in the dye-sensitized solar cells, demonstrating an energy conversion efficiency enhancement of 34%.[152]

In addition to high surface area, the shrink induced micro/nanostructures also contribute to the stretchability and bendability of the thin metal films. Taking advantage of this property, we fabricated stretchable and flexible electrodes that have shown high stretchability and reproducibility. In chapter 5, we describe the structured film lift-off and transfer techniques for creating the stretchable and bendable devices which have shown great stability as flexible

electrochemical sensor. Some other recent work has also demonstrated the suitability of the wrinkled metal films to serve as electrode component in flexible electronics. Khine group reported the use of wrinkled metallic films as stretchable wires, which have been demonstrated to have robust conductive performance in excess of 200% strain.[153]

1.3.2.2 Tunable Nanotopography for Tissue Engineering

How cells respond to external guidance cues from their microenvironment has been an interesting question, as the understanding of cell responses to the stimulations is key in tissue engineering and regenerative medicine. Engineered topographical substrates which mimic natural topographies can help reconstruct tissue like environment in vitro, and allow us to accurately predict and control cell behaviour. Various geometrical features have been fabricated for this purpose, including grooves, gratings, nanofibers, and nanopillars, etc. Table 1-3 summarizes the studies that have been carried out with various topographical feature designs. Very recently, the shrink induced structure has also been used for macrophage phenotype study, where the wrinkled PDMS surfaces promote macrophage alternative activation.[154]

In chapter 6, we present the use of micro/nanostructured glassy film for fibroblast morphology study, where we have shown that rougher surfaces lead to cell elongation, and finer structures promote filopodia generation. This finding is in good agreement with previously reported trends and suggest the possibility of using the structured surfaces as platforms for the polarization and differentiation of specific cell lineages.

Table 1-3 Summary of the effects of sizes of the micro/nano- topography on cell morphology and alignment. (Reprinted from reference [14])

Feature type	Sizes			Materials	Cell type	Effect on cell behavior
	Width/ diameter	Gap/ spacing	Depth/ height			
Nano-islands[155]	N.A.	N.A.	13, 35, 95 nm	Demixed Polymer	Fibroblasts	Cells showed increased length, width, and area on the 13 nm high islands
Gratings[156]	150- 800 nm	50- 800 nm	200- 500 nm	PEG hydrogel	Rat ventricular myocytes	Cells showed increased area and perimeter on the biggest gratings (800× 800 × 500 nm)
TiO_2 nanotube arrays[157]	30- 100 nm	N.A.	N.A.	TiO2	hMSCs	Cell elongation was increased up to 10 folds on larger nanotubes of 70-100 nm as compared to on small nanotubes (30 nm) and flat surface
Gratings[158]	20-1000 nm	20-1000 nm	5- 350 nm	Polystyrene	Fibroblasts	Gratings of 100 nm width and 35 nm depth was the smallest nanotopgraphy which significantly influence cell alignment
Aligned electrospun nanofibers[159]	80- 760 nm	N.A.	N.A.	poly(D,L-lactic-co-glycolic acid)	Fibroblasts	Cells were strongly aligned to electrically aligned nanofibers and nanoimprinted gratings with feature sizes larger than 100 nm
Gratings[160]	0.25-10 μm	0.25- 10 μm	0.25- 10 μm	PDMS	hMSCs	Cell focal adhesions were significantly smaller and more elongated on nanoscale gratings (< 1 μm) than on microscale gratings (1-10 μm)
Electrospun fibers[161]	0.16-8.64 μm	N.A.	N.A.	PMMA	Fibroblasts	Cells aligned closely and elongated along the fiber axis when the fiber diameter is > 1 μm
Electrospun fibers[162]	0.14- 3.6 μm	N.A.	N.A.	PLGA	Fibroblasts	Cell area, aspect ration, and length of the long axis were decreased on smaller fibers (< 1 μm) as compared to these on bigger fibers (3.6 μm) and smooth surface
Gratings[163]	70- 1900 nm	330-2100 nm	600 nm	Silicon	Human corneal epithelial cell	Cells aligned parallel on 4 μm-pitch gratings and perpendicularly on 400 nm-pitch gratings and perpendicularly on 400 nm-pitch gratings
Gratings[164]	Aspect ratio (depth: width) 0.05-1			polystyrene; silicone	Human foreskin fibroblasts; Smooth muscle cells; endothelial cells	Cell alignment increased with aspect ratio

1.4 References

(1) Venugopal, G.; Kim, S. Nanolithography. In *Advances in Micro/Nano Electromechanical Systems and Fabrication Technologies*; 2013.

(2) Cheng, Y. T.; Rodak, D. E.; Wong, C. A.; Hayden, C. A. Effects of Micro- and Nano-Structures on the Self-Cleaning Behaviour of Lotus Leaves. *Nanotechnology* **2006**, *17*, 1359–1362.

(3) Guo, P.; Zheng, Y.; Wen, M.; Song, C.; Lin, Y.; Jiang, L. Icephobic/anti-Icing Properties of Micro/nanostructured Surfaces. *Adv. Mater.* **2012**, *24* (19), 2642–2648.

(4) McCarthy, M.; Gerasopoulos, K.; Maroo, S. C.; Hart, a. J. Materials, Fabrication, and Manufacturing of Micro/Nanostructured Surfaces for Phase-Change Heat Transfer Enhancement. *Nanoscale Microscale Thermophys. Eng.* **2014**, *18* (3), 288–310.

(5) Kim, P.; Wong, T.-S.; Alvarenga, J.; Kreder, M. J.; Adorno-martinez, W. E.; Aizenberg, J.; Al, K. I. M. E. T. Liquid-Infused Nanostructured Surfaces with Extreme Anti-Ice and Anti-Frost Performance. *ACS Nano* **2012**, *6* (8), 6569–6577.

(6) Ghost, A.; Fischer, P. Controlled Propulsion of Artificial Magnetic Nanostructured Propellers. *Nano Lett.* **2009**, *9* (6), 2243–2245.

(7) Moroni, R.; Sekiba, D.; Buatier de Mongeot, F.; Gonella, G.; Boragno, C.; Mattera, L.; Valbusa, U. Uniaxial Magnetic Anisotropy in Nanostructured Co/Cu(001): From Surface Ripples to Nanowires. *Phys. Rev. Lett.* **2003**, *91* (16), 167207.

(8) Park, J.; Lee, Y.; Ha, M.; Cho, S.; Ko, H. Micro/Nanostructured Surfaces for Self-Powered and Multifunctional Electronic Skins. *J. Mater. Chem. B* **2016**, *4*, 2999–3018.

(9) Wang, J.; Xu, Y.; Yan, F.; Zhu, J.; Wang, J. Template-Free Prepared Micro/nanostructured Polypyrrole with Ultrafast Charging/discharging Rate and Long Cycle Life. *J. Power Sources* **2011**, *196* (4), 2373–2379.

(10) Acuna, G. P.; Möller, F. M.; Holzmeister, P.; Beater, S.; Lalkens, B.; Tinnefeld, P. Fluorescence Enhancement at Docking Sites of DNA-Directed Self-Assembled Nanoantennas. *Science (80-.).* **2012**, *338* (2012), 506–510.

(11) Amezcua-Correa, A.; Yang, J.; Finlayson, C. E.; Peacock, A. C.; Hayes, J. R.; Sazio, P. J. a.; Baumberg, J. J.; Howdle, S. M. Surface-Enhanced Raman Scattering Using Microstructured Optical Fiber Substrates. *Adv. Funct. Mater.* **2007**, *17* (13), 2024–2030.

(12) Corcoran, C. J.; Kang, S.; Li, L.; Guo, X.; Chanda, D.; Nuzzo, R. G. Mechanisms of Enhanced Optical Absorption for Ultrathin Silicon Solar Microcells with an Integrated Nanostructured Backside Reflector. *ACS Appl. Mater. Interfaces* **2013**, *5* (10), 4239–4246.

(13) Arima, Y.; Iwata, H. Effect of Wettability and Surface Functional Groups on Protein Adsorption and Cell Adhesion Using Well-Defined Mixed Self-Assembled Monolayers. *Biomaterials* **2007**, *28* (20), 3074–3082.

(14) Nguyen, A. T.; Sathe, S. R.; Yim, E. K. F. From Nano to Micro: Topographical Scale and Its Impact on Cell Adhesion, Morphology and Contact Guidance. *J. Phys. Condens. Matter* **2016**, *28* (18), 183001.

(15) Xiaoxue Zhang; Wang, L.; Levänen, E. Superhydrophobic Surfaces for Reduction of Bacterial Adhesion. *RCS Adv.* **2013**, No. MARCH 2013, 1–53.

(16) Truong, V. K.; Lapovok, R.; Estrin, Y. S.; Rundell, S.; Wang, J. Y.; Fluke, C. J.; Crawford, R. J.; Ivanova, E. P. The Influence of Nano-Scale Surface Roughness on Bacterial Adhesion to Ultrafine-Grained Titanium. *Biomaterials* **2010**, *31* (13), 3674–3683.

(17) Zeng, W.; Shu, L.; Li, Q.; Chen, S.; Wang, F.; Tao, X. M. Fiber-Based Wearable Electronics: A Review of Materials, Fabrication, Devices, and Applications. *Adv. Mater.* **2014**, 5310–5336.

(18) Pessoa, R. S.; Fraga, M. A.; Santos, L. V.; Massi, M.; Maciel, H. S. Nanostructured Thin Films Based on TiO2 And/or SiC for Use in Photoelectrochemical Cells: A Review of the Material Characteristics, Synthesis and Recent Applications. *Mater. Sci. Semicond. Process.* **2015**, *29*, 56–68.

(19) Tachibana, Y.; Vayssieres, L.; Durrant, J. R. Artificial Photosynthesis for Solar Water-Splitting. *Nat. Photonics* **2012**, *6* (8), 511–518.

(20) Zhu, C.; Yang, G.; Li, H.; Du, D.; Lin, Y. Electrochemical Sensors and Biosensors Based on Nanomaterials and Nanostructures. *Anal. Chem.* **2015**, *87* (1), 230–249.

(21) Stratakis, E.; Ranella, A.; Fotakis, C. Biomimetic Micro/nanostructured Functional Surfaces for Microfluidic and Tissue Engineering Applications. *Biomicrofluidics* **2011**, *5* (1).

(22) Rosi N.L., M. C. a. Nanostrucutres in Biodiagnostics. *Chem. Rev.* **2005**, *105*, 1547–1562.

(23) Kolusheva, S.; Yossef, R.; Kugel, A.; Katz, M.; Volinsky, R.; Welt, M.; Hadad, U.; Drory, V.; Kliger, M.; Rubin, E.; et al. Array-Based Disease Diagnostics Using Lipid/polydiacetylene Vesicles Encapsulated in a Sol-Gel Matrix. *Anal. Chem.* **2012**, *84* (14), 5925–5931.

(24) Zheng, C.; Zhou, X.; Cao, H.; Wang, G.; Liu, Z. Synthesis of Porous Graphene/activated Carbon Composite with High Packing Density and Large Specific Surface Area for Supercapacitor Electrode Material. *J. Power Sources* **2014**, *258*, 290–296.

(25) Saravanan, K.; Ananthanarayanan, K.; Balaya, P. Mesoporous TiO2 with High Packing Density for Superior Lithium Storage. *Energy Environ. Sci.* **2010**, *3*, 939.

(26) Hu, Y.; Yella, A.; Guldin, S.; Schreier, M.; Stellacci, F.; Gr??tzel, M.; Stefik, M. High-Surface-Area Porous Platinum Electrodes for Enhanced Charge Transfer. *Adv. Energy Mater.* **2014**, *4* (14), 1–8.

(27) Wang, G.; Lei, Z.; Jiujun, Z. A Review of Electrode Materials for Electrochemical

Supercapacitors. *ChemsucChem* **2012**, *5*, 797.

(28) Paulus, U. A.; Schmidt, T. J.; Gasteiger, H. A.; Behm, R. J. Oxygen Reduction on a High-Surface Area Pt / Vulcan Carbon Catalyst : A Thin-Film Rotating Ring-Disk Electrode Study. **2001**, *495*, 134–145.

(29) Mayrhofer, K. J. J.; Strmcnik, D.; Blizanac, B. B.; Stamenkovic, V.; Arenz, M.; Markovic, N. M. Measurement of Oxygen Reduction Activities via the Rotating Disc Electrode Method: From Pt Model Surfaces to Carbon-Supported High Surface Area Catalysts. *Electrochim. Acta* **2008**, *53* (7), 3181–3188.

(30) Mei, L. P.; Feng, J. J.; Wu, L.; Chen, J. R.; Shen, L.; Xie, Y.; Wang, A. J. A Glassy Carbon Electrode Modified with Porous Cu2O Nanospheres on Reduced Graphene Oxide Support for Simultaneous Sensing of Uric Acid and Dopamine with High Selectivity over Ascorbic Acid. *Microchim. Acta* **2016**, 1–8.

(31) Gattazzo, F.; Urciuolo, A.; Bonaldo, P. Extracellular Matrix: A Dynamic Microenvironment for Stem Cell Niche. *Biochim. Biophys. Acta - Gen. Subj.* **2014**, *1840* (8), 2506–2519.

(32) Théry, M. Micropatterning as a Tool to Decipher Cell Morphogenesis and Functions. *J. Cell Sci.* **2010**, *123* (Pt 24), 4201–4213.

(33) Chaudhuri, P. K.; Pan, C. Q.; Low, B. C.; Lim, C. T. Topography Induces Differential Sensitivity on Cancer Cell Proliferation via Rho-ROCK-Myosin Contractility. *Sci. Rep.* **2016**, *6*, 19672.

(34) Pan, F.; Zhang, M.; Wu, G.; Lai, Y.; Greber, B.; Sch??ler, H. R.; Chi, L. Topographic Effect on Human Induced Pluripotent Stem Cells Differentiation towards Neuronal Lineage. *Biomaterials* **2013**, *34* (33), 8131–8139.

(35) Gatzen, H. H.; Saile, V.; Leuthold, J. *Micro and Nano Fabrication: Tools and Processes*; Springer, 2014.

(36) Brodie, I.; Muray, J. J. *The Physics of Micro/Nano-Fabrication*; Plenum Press: New York and London, 1992.

(37) Asatekin, A.; Barr, M. C.; Baxamusa, S. H.; Lau, K. K. S.; Tenhaeff, W.; Xu, J.; Gleason, K. K. Designing Polymer Surfaces via Vapor Deposition. *Mater. Today* **2010**, *13* (5), 26–33.

(38) Song, J. S.; Lee, S.; Jung, S. H.; Cha, G. C.; Mun, M. S. Improved Biocompatibility of Parylene-C Films Prepared by Chemical Vapor Deposition and the Subsequent Plasma Treatment. *J. ofAppliedPolymer Sci.* **2009**, *112*, 3677–3685.

(39) Wahjudi, P. N.; Oh, J. H.; Salman, S. O.; Seabold, J. A.; Rodger, D. C.; Tai, Y. C.; Thompson, M. E. Improvement of Metal and Tissue Adhesion on Surface-Modified Parylene C. *J. Biomed. Mater. Res. - Part A* **2009**, *89* (1), 206–214.

(40) M. SZWAR. Some Remarks on the P-XYLYL RADICAL Molecule. *Discuss. Faraday*

Soc **1947**, *2*, 46–49.

(41) Gorham, W. F. Para-Xylylene Polymers. 3,342,754.

(42) Fortin, J. B.; Lu, T.-M. A Model for the Chemical Vapor Deposition of Poly(Para - Xylylene) (Parylene) Thin Films. *Chem. Mater.* **2002**, *14* (5), 1945–1949.

(43) Huang, H.; Xu, Y.; Low, H. Y. Effects of Film Thickness on Moisture Sorption, Glass Transition Temperature and Morphology of Poly(chloro-P-Xylylene) Film. *Polymer (Guildf).* **2005**, *46* (16), 5949–5955.

(44) Thiruvengadathan, R.; Korampally, V.; Ghosh, A.; Chanda, N.; Gangopadhyay, K.; Gangopadhyay, S. Nanomaterial Processing Using Self-Assembly-Bottom-up Chemical and Biological Approaches. *Rep. Prog. Phys.* **2013**, *76* (6), 066501.

(45) Ariga, K.; Hill, J. P.; Lee, M. V; Vinu, A.; Charvet, R.; Acharya, S. Challenges and Breakthroughs in Recent Research on Self-Assembly. *Sci. Technol. Adv. Mater.* **2008**, *9* (1), 014109.

(46) Gurrappa, I.; Binder, L. Electrodeposition of Nanostructured Coatings and Their Characterization—a Review. *Sci. Technol. Adv. Mater.* **2008**, *9* (4), 043001.

(47) Tang, Q.; Cai, H.; Yuan, S.; Wang, X. Counter Electrodes from Double-Layered Polyaniline Nanostructures for Dye-Sensitized Solar Cell Applications. *J. Mater. Chem. A* **2013**, *1* (2), 317–323.

(48) Shu, H.; Cao, L.; Chang, G.; He, H.; Zhang, Y.; He, Y. Direct Electrodeposition of Gold Nanostructures onto Glassy Carbon Electrodes for Non-Enzymatic Detection of Glucose. *Electrochim. Acta* **2014**, *132*, 524–532.

(49) Choi, S.; Jeong, H.; Choi, K. H.; Song, J. Y.; Kim, J. Electrodeposition of Triangular Pd Rod Nanostructures and Their Electrocatalytic and Sers Activities. *ACS Appl. Mater. Interfaces* **2014**, *6* (4), 3002–3007.

(50) Gabardo, C. M.; Zhu, Y.; Soleymani, L.; Moran-Mirabal, J. M. Bench-Top Fabrication of Hierarchically Structured High-Surface-Area Electrodes. *Adv. Funct. Mater.* **2013**, *23* (24), 3030–3039.

(51) Mansoor, I.; Liu, Y.; Hafeli, U. O.; Stoeber, B. Fabrication of Hollow Microneedle Arrays Using Electrodeposition of Metal onto Solvent Cast Conductive Polymer Structures. *2013 Transducers Eurosensors XXVII 17th Int. Conf. Solid-State Sensors, Actuators Microsystems, TRANSDUCERS EUROSENSORS 2013* **2013**, *085011*, 373–376.

(52) Calvert, P. Inkjet Printing for Materials and Devices. *Chem. Mater.* **2001**, *13*, 3299–3305.

(53) Perl, A.; Reinhoudt, D. N.; Huskens, J. Microcontact Printing: Limitations and Achievements. *Adv. Mater.* **2009**, *21* (22), 2257–2268.

(54) Wilbur, J. L.; Kumar, A.; Kim, E.; Whitesides, G. M. Microfabrication by Microcontact Printing of Self-assembled Monolayers. *Adv. Mater.* **1994**, No. 718, 600–604.

(55) Xia, Y.; Mrksich, M.; Kim, E.; Whitesides, G. M. Microcontact Printing of Octadecylsiloxane on the Surface of Silicon Dioxide and Its Application in Microfabrication. *J. Am. Chem. Soc.* **1995**, 5–6.

(56) Yoo, P. J.; Choi, S.-J.; Kim, J. H.; Suh, D.; Baek, S. J.; Kim, T. W.; Lee, H. H. Unconventional Patterning with A Modulus-Tunable Mold: From Imprinting to Microcontact Printing. *Chem. Mater.* **2004**, *16* (24), 5000–5005.

(57) Schmid, H.; Michel, B. Siloxane Polymers for High-Resolution, High-Accuracy Soft Lithography. *Macromolecules* **2000**, *33* (8), 3042–3049.

(58) Coyer, S. R.; Garcia, A. J.; Delamarche, E. Facile Preparation of Complex Protein Architectures with Sub-100-Nm Resolution on Surfaces. *Angew. Chemie - Int. Ed.* **2007**, *46* (36), 6837–6840.

(59) Thibault, C.; Séverac, C.; Mingotaud, A. F.; Vieu, C.; Mauzac, M. Poly(dimethylsiloxane) Contamination in Microcontact Printing and Its Influence on Patterning Oligonucleotides. *Langmuir* **2007**, *23* (21), 10706–10714.

(60) Han, S. T.; Zhou, Y.; Xu, Z. X.; Huang, L. B.; Yang, X. B.; Roy, V. A. L. Microcontact Printing of Ultrahigh Density Gold Nanoparticle Monolayer for Flexible Flash Memories. *Adv. Mater.* **2012**, *24* (26), 3556–3561.

(61) Kim, T. Il; Kim, M. J.; Jung, Y. H.; Jang, H.; Dagdeviren, C.; Pao, H. A.; Cho, S. J.; Carlson, A.; Yu, K. J.; Ameen, A.; et al. Thin Film Receiver Materials for Deterministic Assembly by Transfer Printing. *Chem. Mater.* **2014**, *26* (11), 3502–3507.

(62) Wang, Z.; Zhang, P.; Kirkland, B.; Liu, Y.; Guan, J. Microcontact Printing of Polyelectrolytes on PEG Using an Unmodified PDMS Stamp for Micropatterning Nanoparticles, DNA, Proteins and Cells. *Soft Matter* **2012**, *8* (29), 7630.

(63) Bernard, A.; Bernard, B. A.; Renault, J. P.; Michel, B.; Bosshard, H. R.; Delamarche, E. Microcontact Printing of Proteins. *Adv. Mater.* **2011**, *4095* (JULY), 1123574.

(64) Mendelsohn, A. D.; Bernards, D. a; Lowe, R. D.; Desai, T. a. Patterning of Mono- and Multilayered Pancreatic Beta-Cell Clusters. *Langmuir* **2010**, *26* (12), 9943–9949.

(65) *Nanofabrication Handbook*; Stefano Cabrini, S. K., Ed.; Boca Raton, 2012.

(66) Srivastava, R.; Yadav, B. C. Nanolithography : Processing Methods for Nanofabrication Development. **2016**, No. 6, 275–284.

(67) Beam, I.; Ciba, A. ION BEAM LITHOGRAPHY AND NANOFABRICATION : Next Generation Lithographies (NGLs) Are Being Actively Developed to Take over from the Highly Successful Optical Lithography . As Feature Sizes Shrink Well below 100 Nm , Several Key Challenges for Optical Lit. **2005**, *4* (3), 269–286.

(68) Meyerhofer, D. Photosolubility of Diazoquinone Resists. *IEEE Trans. Electron Devices* **1980**, *27* (5), 921–926.

(69) Shaw, J. M.; Gelorme, J. D.; LaBianca, N. C.; Conley, W. E.; Holmes, S. J. Negative Photoresists for Optical Lithography. *IBM J. Res. Dev.* **1997**, *41* (1.2), 81–94.

(70) Gupta. Silicon Processing for the VLSI Era. Lattice Press 1986, pp 157–160.

(71) Poulsen, R. G. Plasma Etching in Integrated Circuit manufacture—A Review. *J. Vac. Sci. Technol.* **1977**, *14* (1), 266.

(72) Heckele, M.; Bacher, W.; Muller, K. D. Hot Embossing - The Molding Technique for Plastic Microstructures. *Microsyst. Technol.* **1998**, *4* (3), 122–124.

(73) Peng, L.; Deng, Y.; Yi, P.; Lai, X. Micro Hot Embossing of Thermoplastic Polymers: A Review. *J. Micromechanics Microengineering* **2014**, *24* (1), 13001.

(74) Liu, C.; Li, J. M.; Liu, J. S.; Wang, L. D. Deformation Behavior of Solid Polymer during Hot Embossing Process. *Microelectron. Eng.* **2010**, *87* (2), 200–207.

(75) Worgull, M.; Hétu, J. F.; Kabanemi, K. K.; Heckele, M. Hot Embossing of Microstructures: Characterization of Friction during Demolding. *Microsyst. Technol.* **2008**, *14* (6), 767–773.

(76) Lan, S.; Lee, H. J.; Lee, S. H.; Ni, J.; Lai, X.; Lee, H. W.; Song, J. H.; Lee, M. G. Experimental and Numerical Study on the Viscoelastic Property of Polycarbonate near Glass Transition Temperature for Micro Thermal Imprint Process. *Mater. Des.* **2009**, *30* (9), 3879–3884.

(77) Shan, X. C.; Liu, Y. C.; Lu, H. J.; Wang, Z. F.; Lam, Y. C. Studies of Polymer Deformation and Recovery in Hot Embossing. *DTIP Mems Moems* **2007**, No. April, 25–27.

(78) Shan, X. C.; Ikehara, T.; Murakoshi, Y.; Maeda, R. Applications of Micro Hot Embossing for Optical Switch Formation. *Sensors Actuators, A Phys.* **2005**, *119* (2), 433–440.

(79) Biebuyck, H. A.; Bain, C. D.; Whitesides, G. M. Comparison of Self-Assembled Monolayers on Gold---Coadsorption of Thiols and Disulfides. *Langmuir* **1989**, *5*, 723–727.

(80) Xia, Y.; Whitesides, G. M. SOFT LITHOGRAPHY. *Annu. Rev. Mater. Sci.* **1998**, *28*, 153–184.

(81) Zhao, X.-M.; Xia, Y.; Whitesides, G. M. Soft Lithographic Methods for Nano-Fabrication. *J. Mater. Chem.* **1997**, *7* (7), 1069–1074.

(82) Martin, G. C.; Su, T. T.; Loh, I. H.; Balizer, E.; Kowel, S. T.; Kornreich, P. The Metallization of Silicone Polymers in the Rubbery and the Glassy State. *J. Appl. Phys.* **1982**, *53* (1), 797–799.

(83) Bowden, N.; Brittain, S.; Evans, A.; Hutchinson, John W. Whitesides, G. M. Spontaneous Formation of Ordered Structures in Thin Films of Metals Supported on an Elastomeric Polymer. *Nature* **1998**, *393* (May), 146–149.

(84) Huang, R. Kinetic Wrinkling of an Elastic Film on a Viscoelastic Substrate. *J. Mech. Phys. Solids* **2005**, *53* (1), 63–89.

(85) Jiang, H.; Khang, D.-Y.; Song, J.; Sun, Y.; Huang, Y.; Rogers, J. a. Finite Deformation Mechanics in Buckled Thin Films on Compliant Supports. *Proc. Natl. Acad. Sci.* **2007**, *104* (40), 15607–15612.

(86) Efimenko, K.; Rackaitis, M.; Manias, E.; Vaziri, A.; Mahadevan, L.; Genzer, J. Nested Self-Similar Wrinkling Patterns in Skins. *Nat. Mater.* **2005**, *4* (4), 293–297.

(87) Gabardo, C. M.; Hosseini, A.; Soleymani, L. A New Wrinkle in Biosensors. *IEEE Nanotechnol. Mag.* **2016**, No. June, 6–18.

(88) Schweikart, A.; Horn, A.; Böker, A.; Fery, A. Controlled Wrinkling as a Novel Method for the Fabrication of Patterned Surfaces Alexandra. *Adv. Polym. Sci.* **2012**, No. May 2012, 1–34.

(89) Zhao, X.-M.; Xia, Y.; Qin, D.; Whiteside, G. M. Fabrication of Polymeric Microstructures with High Aspect Ratios Using Shrinkable Polystyrene Films. *Adv. Mater.* **1997**, *9* (3), 251–254.

(90) Lendlein, A.; Kelch, S. Shape-Memory Effect From Permanent Shape. *Angew. Chemie* **2002**, *41* (12), 2034–2057.

(91) Grimes, A.; Breslauer, D. N.; Long, M.; Pegan, J.; Lee, L. P.; Khine, M. Shrinky-Dink Microfluidics: Rapid Generation of Deep and Rounded Patterns. *Lab Chip* **2008**, *8* (1), 170–172.

(92) Nguyen, D.; Taylor, D.; Qian, K.; Norouzi, N.; Rasmussen, J.; Botzet, S.; Lehmann, M.; Halverson, K.; Khine, M. Better Shrinkage than Shrinky-Dinks. *Lab Chip* **2010**, *10* (12), 1623–1626.

(93) Scalet, G.; Auricchio, F.; Bonetti, E.; Castellani, L.; Ferri, D.; Pachera, M.; Scavello, F. An Experimental, Theoretical and Numerical Investigation of Shape Memory Polymers. *Int. J. Plast.* **2015**, *67*, 127–147.

(94) Chen, A.; Lieu, D. K.; Freschauf, L.; Lew, V.; Sharma, H.; Wang, J.; Nguyen, D.; Karakikes, I.; Hajjar, R. J.; Gopinathan, A.; et al. Shrink-Film Configurable Multiscale Wrinkles for Functional Alignment of Human Embryonic Stem Cells and Their Cardiac Derivatives. *Adv. Mater.* **2011**, *23* (48), 5785–5791.

(95) Castellana, E. T.; Cremer, P. S. Solid Supported Lipid Bilayers: From Biophysical Studies to Sensor Design. *Surf. Sci. Rep.* **2006**, *61* (10), 429–444.

(96) Zhou, X.; Moran-Mirabal, J. M.; Craighead, H. G.; McEuen, P. L. Supported Lipid Bilayer/carbon Nanotube Hybrids. *Nat Nano* **2007**, *2* (3), 185–190.

(97) Magliulo, M.; Mallardi, A.; Mulla, M. Y.; Cotrone, S.; Pistillo, B. R.; Favia, P.; Vikholm-Lundin, I.; Palazzo, G.; Torsi, L. Electrolyte-Gated Organic Field-Effect Transistor Sensors Based on Supported Biotinylated Phospholipid Bilayer. *Adv. Mater.* **2013**, *25*

(14), 2090–2094.

(98) Tanaka, M.; Sackmann, E. Polymer-Supported Membranes as Models of the Cell Surface. *Nature* **2005**, *437* (7059), 656–663.

(99) Bomer, J. G.; Prokofyev, A. V; van den Berg, A.; Le Gac, S. Wafer-Scale Fabrication of Glass-FEP-Glass Microfluidic Devices for Lipid Bilayer Experiments. *Lab Chip* **2014**, *14*, 5–8.

(100) Zagnoni, M. Miniaturised Technologies for the Development of Artificial Lipid Bilayer Systems. *Lab Chip* **2012**, *12* (6), 1026–1039.

(101) Lentz, B. R.; Barenholz, Y.; Thompson, T. E. Fluorescence Depolarization Studies of Phase Transitions and Fluidity in Phospholipid Bilayers. 2 Two-Component Phosphatidylcholine Liposomes. *Biochemistry* **1976**, *15* (20), 4529–4537.

(102) Vemuri, S.; Rhodes, C. T. Preparation and Characterization of Liposomes as Therapeutic Delivery Systems: A Review. *Pharm. Acta Helv.* **1995**, *70* (2), 95–111.

(103) Paternostre, M. T.; Roux, M.; Rigaud, J. L. Mechanisms of Membrane Protein Insertion into Liposomes during Reconstitution Procedures Involving the Use of Detergents. 1. Solubilization of Large Unilamellar Liposomes (Prepared by Reverse-Phase Evaporation) by Triton X-100, Octyl Glucoside, and Sodium. *Biochemistry* **1988**, *27* (8), 2668–2677.

(104) Murray, D. H.; Tamm, L. K.; Kiessling, V. Supported Double Membranes. *J. Struct. Biol.* **2009**, *168* (1), 183–189.

(105) Bamberg, E.; Alpes, H.; Apell, H. J.; Bradley, R.; Härter, B.; Quelle, M. J.; Urry, D. W. Formation of Ionic Channels in Black Lipid Membranes by Succinic Derivatives of Gramicidin A. *J. Membr. Biol.* **1979**, *50* (3-4), 257–270.

(106) Penia, A.; Lievano, A.; Darszont, A.; Culberston, M. R.; Kung, C.; Gómez-Lagunas, F.; Peña, A.; Liévano, A.; Darszon, A. Incorporation of Ionic Channels from Yeast Plasma Membranes into Black Lipid Membranes. *Biophys. J.* **1989**, *56* (1), 115–119.

(107) Brian, a a; McConnell, H. M. Allogeneic Stimulation of Cytotoxic T Cells by Supported Planar Membranes. *Proc. Natl. Acad. Sci. U. S. A.* **1984**, *81* (19), 6159–6163.

(108) Tamm, L. K.; McConnell, H. M. Supported Phospholipid Bilayers. *Biophys. J.* **1985**, *47* (1), 105–113.

(109) Baumgart, T.; Hunt, G.; Farkas, E. R.; Webb, W. W.; Feigenson, G. W. Fluorescence Probe Partitioning between Lo Membranes /Ld Phases in Lipid. *Biochim. Biophys. Acta* **2007**, *1768* (9), 2182–2194.

(110) Shaw, J. E.; Epand, R. F.; Epand, R. M.; Li, Z.; Bittman, R.; Yip, C. M. Correlated Fluorescence-Atomic Force Microscopy of Membrane Domains: Structure of Fluorescence Probes Determines Lipid Localization. *Biophys. J.* **2006**, *90* (6), 2170–2178.

(111) Burns, A. R.; Frankel, D. J.; Buranda, T. Local Mobility in Lipid Domains of Supported

Bilayers Characterized by Atomic Force Microscopy and Fluorescence Correlation Spectroscopy. *Biophys. J.* **2005**, *89* (2), 1081–1093.

(112) Lambertz, C.; Martos, A.; Henkel, A.; Neiser, A.; Kliesch, T.-T.; Janshoff, A.; Schwille, P.; Sönnichsen, C. Single Particle Plasmon Sensors as Label-Free Technique To Monitor MinDE Protein Wave Propagation on Membranes. *Nano Lett.* **2016**, acs.nanolett.6b00507.

(113) Bally, M.; Bailey, K.; Sugihara, K.; Grieshaber, D.; Vörös, J.; Ståler, B. Liposome and Lipid Bilayer Arrays towards Biosensing Applications. *Small* **2010**, *6* (22), 2481–2497.

(114) Liu, L.; Yang, C.; Zhao, K.; Li, J.; Wu, H.-C. Ultrashort Single-Walled Carbon Nanotubes in a Lipid Bilayer as a New Nanopore Sensor. *Nat. Commun.* **2013**, *4*, 2989.

(115) Nguyen, T. T.; Conboy, J. C. High-Throughput Screening of Drug-Lipid Membrane Interactions via Counter-Propagating Second Harmonic Generation Imaging. *Anal. Chem.* **2011**, *83* (15), 5979–5988.

(116) Ashley, C. E.; Carnes, E. C.; Phillips, G. K.; Padilla, D.; Durfee, P. N.; Brown, P. a; Hanna, T. N.; Liu, J.; Phillips, B.; Carter, M. B.; et al. The Targeted Delivery of Multicomponent Cargos to Cancer Cells by Nanoporous Particle-Supported Lipid Bilayers. *Nat. Mater.* **2011**, *10* (5), 389–397.

(117) Jönsson, P.; Gunnarsson, A.; Höök, F. Accumulation and Separation of Membrane-Bound Proteins Using Hydrodynamic Forces. *Anal. Chem.* **2011**, *83* (2), 604–611.

(118) Liu, C.; Monson, C. F.; Yang, T.; Pace, H.; Cremer, P. S. Protein Separation by Electrophoretic À Electroosmotic Focusing on Supported Lipid Bilayers. *Anal. Chem.* **2011**, *83* (2), 7876–7880.

(119) Loidl-Stahlhofen, A.; Kaufmann, S.; Braunschweig, T.; Bayerl, T. M. The Thermodynamic Control of Protein Binding to Lipid Bilayers for Protein Chromatography. *Nat. Biotechnol.* **1996**, *14* (8), 999–1002.

(120) Choi, S.-E.; Greben, K.; Wördenweber, R.; Offenhäusser, A. Positively Charged Supported Lipid Bilayer Formation on Gold Surfaces for Neuronal Cell Culture. *Biointerphases* **2016**, *11*, 021003.

(121) van Weerd, J.; Sankaran, S.; Roling, O.; Sukas, S.; Krabbenborg, S.; Huskens, J.; le Gac, S.; Ravoo, B. J.; Karperien, M.; Jonkheijm, P. A Microfluidic Device with Continuous Ligand Gradients in Supported Lipid Bilayers to Probe Effects of Ligand Surface Density and Solution Shear Stress on Pathogen Adhesion. *Adv. Mater. Interfaces* **2016**, *3* (9), 1600055.

(122) Lautscham, L. a.; Lin, C. Y.; Auernheimer, V.; Naumann, C. a.; Goldmann, W. H.; Fabry, B. Biomembrane-Mimicking Lipid Bilayer System as a Mechanically Tunable Cell Substrate. *Biomaterials* **2014**, *35* (10), 3198–3207.

(123) Cremer, P. S.; Boxer, S. G. Formation and Spreading of Lipid Bilayers on Planar Glass Supports. *J. Phys. Chem. B* **1999**, *103* (13), 2554–2559.

(124) Korenbrot, J. I.; Pramik, M. J. Formation, Structure, and Spectrophotometry of Air-Water Interface Films Containing Rhodopsin. *J. Membr. Biol.* **1977**, *37*, 235–262.

(125) Kalb, E.; Frey, S.; Tamm, L. K. Formation of Supported Planar Bilayers by Fusion of Vesicles to Supported Phospholipid Monolayers. *BBA - Biomembr.* **1992**, *1103* (2), 307–316.

(126) Jass, J.; Tjärnhage, T.; Puu, G. From Liposomes to Supported, Planar Bilayer Structures on Hydrophilic and Hydrophobic Surfaces: An Atomic Force Microscopy Study. *Biophys. J.* **2000**, *79* (6), 3153–3163.

(127) Erik Reimhult, *; Fredrik Höök, and; Kasemo, B. Intact Vesicle Adsorption and Supported Biomembrane Formation from Vesicles in Solution: Influence of Surface Chemistry, Vesicle Size, Temperature, and Osmotic Pressure†. *Langmuir* **2002**, *19* (5), 1681–1691.

(128) Richter, R. P.; Bérat, R.; Brisson, A. R. Formation of Solid-Supported Lipid Bilayers: An Integrated View. *Langmuir* **2006**, *22* (8), 3497–3505.

(129) van Meer, G.; Voelker, D. R.; Feigenson, G. W. Membrane Lipids: Where They Are and How They Behave. *Nat. Rev. Mol. Cell Biol.* **2008**, *9* (2), 112–124.

(130) Milovanovic, D.; Honigmann, A.; Koike, S.; Göttfert, F.; Pähler, G.; Junius, M.; Müllar, S.; Diederichsen, U.; Janshoff, A.; Grubmüller, H.; et al. Hydrophobic Mismatch Sorts SNARE Proteins into Distinct Membrane Domains. *Nat. Commun.* **2015**, *6*, 5984.

(131) Khan, M. S.; Dosoky, N. S.; Williams, J. D. Engineering Lipid Bilayer Membranes for Protein Studies. *Int. J. Mol. Sci.* **2013**, *14* (11), 21561–21597.

(132) Bhatia, T.; Husen, P.; Ipsen, J. H.; Bagatolli, L. a.; Simonsen, A. C. Fluid Domain Patterns in Free-Standing Membranes Captured on a Solid Support. *Biochim. Biophys. Acta - Biomembr.* **2014**, *1838* (10), 2503–2510.

(133) Jørgensen, K.; Mouritsen, O. G. Phase Separation Dynamics and Lateral Organization of Two-Component Lipid Membranes. *Biophys. J.* **1995**, *69* (3), 942–954.

(134) Shimshick, E. J.; McConnell, H. M. Lateral Phase Separation in Phospholipid Membranes. *Biochemistry* **1973**, *12* (12), 2351–2360.

(135) Groves, J. T.; Ulman, N.; Boxer, S. G. Micropatterning Fluid Lipid Bilayers on Solid Support. *Science (80-.).* **1997**, *275*, 651–653.

(136) Kung, L. a.; Kam, L.; Hovis, J. S.; Boxer, S. G. Patterning Hybrid Surfaces of Proteins and Supported Lipid Bilayers. *Langmuir* **2000**, *16* (17), 6773–6776.

(137) Fang, Y.; Frutos, A. G.; Lahiri, J. Ganglioside Microarrays for Toxin Detection. *Langmuir* **2003**, *19* (5), 1500–1505.

(138) Hovis, J. S.; Boxer, S. G. Patterning and Composition Arrays of Supported Lipid Bilayers by Microcontact Printing. *Langmuir* **2001**, *17* (11), 3400–3405.

(139) Nafday, O. a.; Lowry, T. W.; Lenhert, S. Multifunctional Lipid Multilayer Stamping. *Small* **2012**, *8* (7), 1021–1028.

(140) Moran-Mirabal, J. M.; Tan, C. P.; Orth, R. N.; Williams, E. O.; Craighead, H. G.; Lin, D. M. Controlling Microarray Spot Morphology with Polymer Liftoff Arrays. *Anal. Chem.* **2007**, *79* (3), 1109–1114.

(141) Orth, R. N.; Kameoka, J.; Zipfel, W. R.; Ilic, B.; Webb, W. W.; Clark, T. G.; Craighead, H. G. Creating Biological Membranes on the Micron Scale: Forming Patterned Lipid Bilayers Using a Polymer Lift-off Technique. *Biophys. J.* **2003**, *85* (5), 3066–3073.

(142) Shi, J.; Chen, J.; Cremer, P. S. Sub-100 Nm Patterning of Supported Bilayers by Nanoshaving Lithography. *J. Am. Chem. Soc.* **2008**, *130* (9), 2718–2719.

(143) Burridge, K. a.; Figa, M. a.; Wong, J. Y. Patterning Adjacent Supported Lipid Bilayers of Desired Composition to Investigate Receptor-Ligand Binding under Shear Flow. *Langmuir* **2004**, *20* (23), 10252–10259.

(144) Shi, J.; Yang, T.; Cremer, P. S. Multiplexing Ligand-Receptor Binding Measurements by Chemically Patterning Microfluidic Channels. *Anal. Chem.* **2008**, *80* (15), 6078–6084.

(145) Pegan, J. D.; Ho, A. Y.; Bachman, M.; Khine, M. Flexible Shrink-Induced High Surface Area Electrodes for Electrochemiluminescent Sensing. *Lab Chip* **2013**, *13* (21), 4205–4209.

(146) Le Goff, G. C.; Blum, L. J.; Marquette, C. A. Shrinking Hydrogel-DNA Spots Generates 3D Microdots Arrays. *Macromol. Biosci.* **2013**, *13* (2), 227–233.

(147) Sharma, H.; Wood, J. B.; Lin, S.; Corn, R. M.; Khine, M. Shrink-Induced Silica Multiscale Structures for Enhanced Fluorescence from DNA Microarrays. *Langmuir* **2014**, *30* (37), 10979–10983.

(148) Lin, S.; Hedde, P. N.; Venugopalan, V.; Gratton, E.; Khine, M. Multi-Scale Silica Structures for Improved HIV-1 Capsid (p24) Antigen Detection. *Analyst* **2016**, 1–8.

(149) Sonney, S.; Shek, N.; Moran-Mirabal, J. M. Rapid Bench-Top Fabrication of Poly(dimethylsiloxane)/polystyrene Microfluidic Devices Incorporating High-Surface-Area Sensing Electrodes. *Biomicrofluidics* **2015**, *9* (2), 026501.

(150) Woo, S. M.; Gabardo, C. M.; Soleymani, L. Prototyping of Wrinkled Nano-/microstructured Electrodes for Electrochemical DNA Detection. *Anal. Chem.* **2014**, *86* (24), 12341–12347.

(151) Gabardo, C. M.; Kwong, A. M.; Soleymani, L. Rapidly Prototyped Multi-Scale Electrodes to Minimize the Voltage Requirements for Bacterial Cell Lysis. *Analyst* **2015**, *140* (5), 1599–1608.

(152) Zhang, B.; Zhang, M.; Song, K.; Li, Q.; Cui, T. Shrink Induced Nanostructures for Energy Conversion Efficiency Enhancement in Photovoltaic Devices. *Appl. Phys. Lett.* **2013**, *103* (2).

(153) Kim, J.; Park, S. J.; Nguyen, T.; Chu, M.; Pegan, J. D.; Khine, M. Highly Stretchable Wrinkled Gold Thin Film Wires. *Appl. Phys. Lett.* **2016**, *108* (6).

(154) Wang, T.; Luu, T. U.; Chen, A.; Khine, M.; Liu, W. F. Topographical Modulation of Macrophage Phenotype by Shrink-Film Multi-Scale Wrinkles. *Biomater. Sci.* **2016**, 0–4.

(155) Dalby, M. J.; Riehle, M. O.; Johnstone, H. J. H.; Affrossman, S.; Curtis, A. S. G. Polymer-Demixed Nanotopography: Control of Fibroblast Spreading and Proliferation. *Tissue Eng.* **2002**, *8* (6), 1099–1108.

(156) Kim, D.-H.; Lipke, E. A.; Kim, P.; Cheong, R.; Thompson, S.; Delannoy, M.; Suh, K.-Y.; Tung, L.; Levchenko, A. Nanoscale Cues Regulate the Structure and Function of Macroscopic Cardiac Tissue Constructs. *Proc. Natl. Acad. Sci. U. S. A.* **2010**, *107* (2), 565–570.

(157) Oh, S.; Brammer, K. S.; Li, Y. S.; Teng, D.; Engler, A. J.; Chien, S.; Jin, S. Stem Cell Fate Dictated Solely by Altered Nanotube Dimension. *Proc. Natl. Acad. Sci. U. S. A.* **2009**, *106* (7), 2130–2135.

(158) Loesberg, W. A.; te Riet, J.; van Delft, F. C. M. J. M.; Schön, P.; Figdor, C. G.; Speller, S.; van Loon, J. J. W. A.; Walboomers, X. F.; Jansen, J. A. The Threshold at Which Substrate Nanogroove Dimensions May Influence Fibroblast Alignment and Adhesion. *Biomaterials* **2007**, *28* (27), 3944–3951.

(159) Chaurey, V.; Block, F.; Su, Y. H.; Chiang, P. C.; Botchwey, E.; Chou, C. F.; Swami, N. S. Nanofiber Size-Dependent Sensitivity of Fibroblast Directionality to the Methodology for Scaffold Alignment. *Acta Biomater.* **2012**, *8* (11), 3982–3990.

(160) Teo, B. K. K.; Wong, S. T.; Lim, C. K.; Kung, T. Y. S.; Yap, C. H.; Ramagopal, Y.; Romer, L. H.; Yim, E. K. F.; Ramgopal, Y. Nanotopography Modulates Mechanotransduction of Stem Cells and Induces Differentiation through Focal Adhesion Kinase. *ACS Nano* **2013**, *7* (6), 4785–4798.

(161) Tsimbouri, P.; Gadegaard, N.; Burgess, K.; White, K.; Reynolds, P.; Herzyk, P.; Oreffo, R.; Dalby, M. J. Nanotopographical Effects on Mesenchymal Stem Cell Morphology and Phenotype. *J. Cell. Biochem.* **2014**, *115* (2), 380–390.

(162) Bashur, C. A.; Dahlgren, L. A.; Goldstein, A. S. Effect of Fiber Diameter and Orientation on Fibroblast Morphology and Proliferation on Electrospun Poly(d,l-Lactic-Co-Glycolic Acid) Meshes. *Biomaterials* **2006**, *27* (33), 5681–5688.

(163) Teixeira, A. I.; McKie, G. A.; Foley, J. D.; Bertics, P. J.; Nealey, P. F.; Murphy, C. J. The Effect of Environmental Factors on the Response of Human Corneal Epithelial Cells to Nanoscale Substrate Topography. *Biomaterials* **2006**, *27* (21), 3945–3954.

(164) Crouch, A. S.; Miller, D.; Luebke, K. J.; Hu, W. Correlation of Anisotropic Cell Behaviors with Topographic Aspect Ratio. *Biomaterials* **2009**, *30* (8), 1560–1567.

Chapter 2 Micropatterning of Phase-Segregated Supported Lipid Bilayers and Binary Lipid Phases through Polymer Stencil Lift-Off

Yujie Zhu and Jose M. Moran-Mirabal designed the experiments. Yujie Zhu optimized the Parylene stencil fabrication and cleaning process, and conducted the SLB patterning and characterization experiments. Yujie Zhu and Jose M. Moran-Mirabal analyzed the data and wrote the manuscript.

2.1 Abstract

Supported lipid bilayers (SLBs) provide an excellent model system for studying structural and functional characteristics of biomembranes. Patterning model membranes on solid supports has elicited much interest because lipid bilayer arrays at cellular or sub-cellular scales provide attractive platforms for reconstituting tissue-like conditions for cell culture, and for creating simplified physiological environments to study biological processes. Phase-segregated SLB patterns can be especially useful for such studies, as the selective functionalization of the lipid phases with different lipids, receptors or proteins can be achieved to mimic the key features of plasma membrane. However, it remains challenging to pattern phase-segregated lipid bilayers and to spatially control the lipid phases at the micron scale. Current methods to achieve this involve multiple surface modification and patterning steps, elaborate techniques such as microfluidic, microcontact printing, or electrochemical control, among others. To overcome the complexity in producing phase-segregated patterns, we have developed simple and rapid strategies to pattern SLBs with phase separation utilizing the polymer stencil lift-off (PSLO) technique. PSLO is a

powerful technique for SLB patterning, since it allows the faithful pattern transfer of micron-sized lipid domains onto solid surfaces under aqueous conditions, which eliminates the need for controlled humidity and reduces the risk of bilayer disruption through drying. By integrating post-etching substrate cleaning and a blocking treatment, well-defined homogeneous and phase-segregated SLB patterns were achieved with lipid mobility that matches that of SLBs formed on clean SiO_2 wafer substrates. A two-step incubation method was also developed for patterning binary lipid phases, which allowed precise control of their position and geometries. The created phase-segregated SLB patterns were used to study lipid phase behavior within confined areas, and quantitative analysis showed that smaller pattern sizes resulted in smaller gel phase domains, which also covered a smaller fraction of the total patterned SLB area. This was attributed to the decreased mobility of the bottom leaflet of the SLB which lies in close proximity to the substrate, and the resulting hindered exchange of lipid molecules between the bottom and upper leaflets through the SLB boundary. By further integration with functional groups, the phase-segregated lipid bilayer patterns might find relevant application in tissue engineering, biophysical studies of biomolecular and cellular interactions, and biosensing platforms.

2.2 Introduction

The membrane is one of the most important structural components of cells, and the study of its structure and organization is key to understanding cellular responses to the environment. The supported lipid bilayer (SLB) system provides an excellent experimental model for *in vitro* studies, as it retains a number of the structural and dynamic properties of cellular membranes.[1,2] The ability to control the chemical composition of SLBs on the micrometer scale allows the creation of engineered physiological environments for the study of membrane properties,[3] biomolecular interactions,[4,5] or cell behavior.[6,7] For example, SLBs have been used to study the receptor

segregation patterns that arise from the interaction between T-cells and antigen presenting cell receptors.[8] Patterned membranes can also serve as the basis for biosensor design with enhanced detection signal.[9] Especial interest lies in developing micropatterning strategies for the precise spatial control of lipid phase geometries, since lipid bilayer phase segregation is known as a fundamental principle for the functional organization of lipids and proteins within the biological membrane.[10,11]

A host of techniques have been used for SLB pattering including physical or diffusion barrier separation,[12,13,14] micro-contact printing (μCP),[15] non-contact printing,[16] polymer stencil lift-off (PSLO),[4,17,18] 2D or 3D micro-fluidic networks,[19,20] pre-patterned functionalized substrates,[21] and pattern-guided self-spreading.[22] Despite the success with these micropatterning techniques, most of them created single-component or single-composition SLB patterns. Recent efforts have focused on patterning multiple lipid components: Smith *et al.* created micropatterned lipid bilayer arrays with spatially addressed compositions on a glass substrate using a continuous flow microspotter,[23] Roder *et al.* used fatty acid functionalized PEG polymer patterns as tethers to anchor two different lipid phases and achieved the controlled spatial organization of polymer-supported membranes,[24] Adams *et al.* exploited the destabilization effect of lipopolysaccharide, combined with soft lithography, to generate voids and then backfilled them to introduce different membrane components,[25] and Yamada *et al.* used inkjet printing of lipid bilayers onto pre-patterned polymeric bilayers to make bilayer microarrays.[26] While SLB micropatterns with different compositions can be obtained through these methods, they either suffer from low resolution or involve multiple patterning steps and technically elaborate microfluidic, spotting, or electrochemical techniques.

To provide an alternative to these techniques, we report a simple and direct approach to pattern phase-segregated domains in spatially controlled geometries with micron-scale resolution using the PSLO technique. PSLO, first introduced by Ilic and Craighead,[27] is an efficient and robust patterning technique that employs microfabricated polymer coatings as stencils and has been used with biomaterials such as nucleic acids,[28] lipids,[17] proteins,[29] and cells.[30] Individual micron-sized SLB domains can be formed without using permanent barriers or substrate surface modification, which allows the lipid molecules to diffuse freely across all patterned areas. The use of a micropatterned polymer coating in the PSLO technique means that large surfaces (*e.g.* whole wafers) can be patterned with smaller and more uniform features, something that could not be achieved with the μCP technique, where PDMS deformation can be a significant problem. In addition, the fact that the polymer coating can be lifted-off while the substrates are immersed in aqueous buffers translates into the ability of patterning SLBs without the requirement of strict humidity control or the risk of disrupting the bilayer through drying. In the present study, we have improved the PSLO process, as applied to lipid bilayer patterning, through post-etch cleaning and BSA treatment after lift-off to achieve well-defined and highly fluid lipid bilayer patterns that retain the patterned shapes over several days of storage. Such improvement allowed phase-segregated SLB patterns to form within micron-scale patterns, and the effects of pattern size and cooling rate on lipid phase segregation were studied. It was found that smaller patterns and higher cooling rate led to smaller gel phase domains, and that the phase segregation was strongly influenced by the patterned feature boundaries. Moreover, we established a simple two-step incubation approach for patterning two contiguous lipid phases in sequence, which allowed us to further control the distribution of lipid phases. The proposed micropatterning strategies for phase-segregated and binary SLBs could open up new possibilities to localize membrane-associated

proteins or other biomolecules within the sub-cellular sized domains and further study the effects of lipid bilayer confinement on phase-segregation dynamics. Such platforms are also attractive for *in-vitro* studies of biomolecular interactions and cell behavior, such as cell signaling, ligand-receptor interactions, pathogen attack, and enzymatic reactions occurring at the cell surface.

2.3 Experimental Section

2.3.1 Materials

1,2-dioleoyl-sn-glycero-3-phosphocholine (DOPC) and 1,2-distearoyl-sn-glycero-3-phosphocholine (DSPC) were purchased from Avanti Polar Lipids (Alabaster, AL), and were suspended in chloroform at a concentration of 10 mg/ml. Lissamine rhodamine-labeled 1,2-dihexadecanoyl-sn-glycero-3-phosphoethanolamine (DHPE-LR) and Oregon green-labeled 1,2-dihexadecanoyl-sn-glycero-3-phosphoethanolamine (DHPE-OG) were purchased from Molecular Probes-Invitrogen (Eugene, OR), and were suspended in chloroform at 1 mg/ml concentration. Sodium hydroxide, 10× phosphate buffered saline (PBS, pH 7.5) solution, L-ascorbic acid, bovine serum albumin (BSA) and sodium hydroxide (NaOH) were obtained from Sigma-Aldrich (Oakville, ON, Canada). Sulfuric acid (H_2SO_4, 98%) was purchased from Caledon Laboratories (Georgetown, ON, Canada). All reagents were of analytical grade and were used without further purification. Parylene-C was obtained from Specialty Coating Systems (Indianapolis, IN). Deionized water was obtained from a Milli-Q Reference A+ Purification System (Millipore, Billerica, MA) with a resistance of 18.2 MΩ·cm. Single side polished four inch ⟨100⟩ Si wafers with 100 nm thermal oxide layer were purchased from University Wafer (Boston, MA) and were used as substrates for forming SLBs.

2.3.2 Formation of SLB

Small unilamellar vesicle (SUV) solutions were prepared by the vesicle extrusion method. Briefly, lipids dissolved in chloroform were mixed in the appropriate molar ratios to obtain the desired lipid bilayer compositions. The chloroform in the mixture was evaporated under a dry nitrogen stream. After desiccation under vacuum overnight, the dry lipids were rehydrated with 1× PBS, until the lipid film completely resuspended, forming a cloudy solution containing large multilamellar vesicles (LMV) of various sizes. The LMV solution was pre-filtered through a 0.45 μm pore polyethersulfone membrane to reduce the vesicle size and was then extruded ten times through a 100 nm pore polycarbonate membrane (Whatman, Maidstone, UK) at a temperature above the highest transition temperature of the lipids in the mixture. This resulted in a clear solution containing ~100 nm diameter SUVs.

SLBs were formed by applying the SUV solution onto the substrate surface and incubating under the appropriate conditions. To form homogeneous SLBs, 0.1 mM DOPC:DHPE-LR (99:1) mixture was incubated for 1 hr at room temperature, or 0.1 mM DSPC:DHPE-OG (99:1) was incubated for 30 min at 60°C in a moisture-saturated box. To remove excess vesicles after incubation, the samples were washed 5 times with 1× PBS supplemented with 5 mM ascorbic acid (used as oxygen scavenging agent to reduce fluorophore photobleaching). For phase-segregated SLB formation, 0.1 mM SUVs with DOPC:DSPC:DHPE-LR (49.5:49.5:1) composition were incubated at 60°C for 30 min on hydrophilic substrates. After incubation, the samples were washed 5 times with 60°C warm 1× PBS buffer to remove excess vesicles. The formed SLBs were cooled down to room temperature to allow the lipids to phase segregate.

2.3.3 Fabrication of polymer stencils

SiO_2 wafers were cleaned in piranha solution (sulfuric acid: hydrogen peroxide in a volume ratio of 3:1, 100°C) for 10 min, followed by two successive 5 min rinses in deionized water, and then dried under a nitrogen stream. A Parylene-C film of ~700 nm thickness was then deposited onto the clean SiO_2 wafer substrates through chemical vapor deposition (CVD) in a Labcoater2000 Parylene deposition system (SCS, Indianapolis, IN). S1808 positive photoresist (Shipley, Marlborough, MA) was spin-coated on the polymer-coated coverslips at 2500 RPM for 30 seconds and pre-baked at 90°C for 2 min to obtain a nominal resist thickness of 1.1 μm. A chrome photo mask with 2-200 μm features fabricated by Fineline Imaging Company (Colorado Springs, CO) was used in the patterning process. Photolithography was performed in soft contact mode using a Karl Suss MJB3 contact aligner (UV wavelength 365 nm, Suss MicroTec, Garching, Germany), with an exposure of 30 mJ. The samples were developed in Microposit 351 developer (Shipley, Malborough, MA) for 25 s to remove the exposed photoresist, followed by deionized water rinsing and drying under a nitrogen stream. Exposed regions of the polymer film were reactive ion etched in an oxygen plasma chamber (Technics, Series 800, Pleasanton, CA) for 7 min (30 sccm O_2, 100 W). Residual photoresist was removed by washing successively with acetone, isopropanol and deionized water. To remove any remaining polymer residue within the etched openings, the etched substrates were treated in a UV/O_3 cleaner and further cleaned in an alkaline solution. A series UV/O_3 and base treatment conditions were tested, from which it was determined that 1 min exposure (10 mW/cm^2, UV 254 nm), followed by 1 min soaking in 100 mM NaOH solution provided the optimal surfaces for SLB formation. Substrates were soaked in deionized water for 1 min and dried under nitrogen stream after UV/O_3 and base treatment.

2.3.4 Patterning homogeneous SLB with PSLO

Prior to use in lipid bilayer patterning, all the polymer-coated SiO_2 wafers were cleaned in a plasma chamber (Harrick, Ithaca, NY) for 60 s at high power (30 W) and using a partial air pressure of 600 mTorr. The SUV solution of interest was then applied over the surface of the patterned substrate and incubated under appropriate conditions until a uniform SLB formed. Excess vesicles were removed by washing the surface five times with 1× PBS (supplemented with 5 mM ascorbic acid). After washing, the polymer stencil was mechanically lifted-off under aqueous conditions, leaving behind patterned SLBs. BSA solution was used as a blocking agent to prevent fluid lipid bilayers from spreading. 10 mg/mL BSA in 1× PBS was used to wash off the vesicles after incubation and during the stencil lift-off step instead of pure buffer. Excess BSA was washed off after the lift-off using 5 rinses with 1× PBS.

2.3.5 Patterning binary SLBs

The binary SLB patterns were achieved using the backfilling method. Homogeneous DSPC patterns were first formed using PSLO as described above. After the polymer stencil was lifted-off, concentrated DOPC SUV solution was added to the buffer solution containing the substrate to reach a lipid vesicle concentration of 0.1 mM. The sample was then incubated for 1 hr at room temperature, and washed five times with 1× PBS buffer.

2.3.6 Fluorescence microscopy and image analysis

SLB patterns were imaged using a Nikon Eclipse LV100N POL epifluorescence microscope (Nikon Instruments, Mississauga, ON, Canada) equipped with excitation and emission filters for FITC and Rhodamine dyes, and a UMPLNFL 60×/1.00NA physiological objective. Images were acquired with a Retiga 2000R cooled CCD camera (QImaging, Surrey, BC, Canada) and recorded

with NIS-Elements AR software (Nikon Instruments, Mississauga, ON, Canada). Fluorescence recovery after photobleaching (FRAP) was used for quantitative SLB mobility tests. An image of the sample was acquired at low illumination intensity before photobleaching, after which the illumination intensity was increased and focused onto a small area of the SLB. This caused the fluorophores on the SLB to bleach quickly, leaving a partially darkened region behind. For SLBs with good mobility on the substrate, fluorescent lipid molecules would diffuse into the bleached region, and the fluorescence could recover. The fluorescence recovery was followed by acquiring successive images every 2 seconds over a total of 12 minutes. The recovery kinetics were analyzed using the simFRAP plugin of ImageJ,[31] where the experimental recovery kinetics are fitted to a simulated fluorescence recovery. The analysis algorithm allows the accurate determination of diffusion coefficients of bleached areas of arbitrary shape contained within bounded domains (*e.g.*, cells or in the case of this manuscript patterned SLBs).

Fluorescence images of spontaneously phase segregated SLB patterns with features sizes of 10- 100 μm were analyzed using Image J.[32] The fluorescence images were first converted into binary images, and then the areas of gel phase domains were measured (*cf.* Figure 4A). Through calculation, the average gel phase domain size and fractional area covered by gel phase domains in the SLB pattern were obtained, and compared for different patterned feature sizes. A minimum of three replicate sample images (containing multiple replicate features) was analyzed for each feature size, and statistical analysis of the differences between the phase segregated domains was performed using the statistical program Prism (GraphPad Software Inc., La Jolla, CA).

2.4. Results and Discussion

The polymer stencils used for SLB patterning were fabricated on SiO_2 wafers thorough photolithography and reactive ion etching (Figure 1). The fabrication process consisted on first depositing thin Parylene-C films onto clean SiO_2 wafer substrates. The films were subsequently etched through a photoresist mask to define the openings in the polymer stencil. The stencil fabrication process was accomplished within a day, yielding a number of wafers containing patterned stencils which could be stored indefinitely for future experiments. After cleaning the patterned substrates with acetone and air plasma, an SUV solution was incubated under appropriate conditions to promote vesicle fusion and SLB formation. The polymer stencil was then lifted off, leaving behind intact SLB patterns. Homogeneous micron-scale SLB patterns were easily achieved using this procedure. In addition to the simplicity of patterning by just mechanically lifting-off the polymer coating, a key advantage of the PSLO lift-off procedure is the ability to pattern the lipid bilayers under fully hydrated conditions, as the polymer lift-off process can be done in aqueous media. This eliminates the need for controlled humidity conditions during the patterning step and avoids the risk of lipid bilayer disruption due to drying. Initial FRAP tests performed on patterned bilayers in the L_α (liquid disordered) phase showed complete fluorescence recovery at room temperature (Figure S1), while those in the L_β (gel) phase showed the anticipated lack in recovery (Figure S2). However, it was noted that the diffusion coefficients obtained for the L_α SLBs patterned with the etched stencils were only *ca.* 33% of those obtained for bilayers prepared on clean SiO_2 surfaces (Figure S3), indicating that while the patterned lipid bilayers retained their integrity, their mobility was compromised. Methods to improve the quality of the patterned lipid bilayers were explored and are discussed in detail further below.

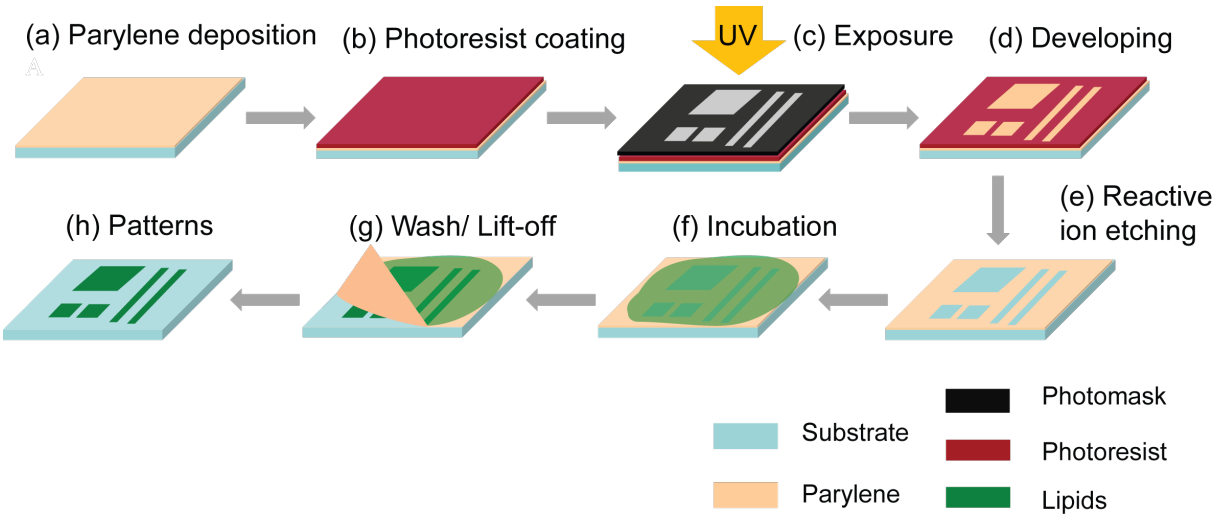

Figure 2-1 Schematic illustration of the polymer stencil lift-off for patterning supported lipid bilayers. (a) Polymer film is deposited on a SiO_2 substrate. (b) Photoresist is spin-coated onto the substrate and (c) exposed to UV light through a photomask. (d) Photoresist is developed and areas that have been exposed are removed. (e) Exposed polymer is removed by oxygen plasma reactive ion etching, yielding a stencil with micron-sized features of exposed SiO_2. (f) Lipid vesicle solution is applied onto the substrate, and incubated to form bilayers in the stencil openings. (g) Polymer stencil is lifted-off and (h) lipid bilayer patterns are left behind.

The temporal stability of patterned SLBs was studied for lipids in the L_α and L_β phases. DSPC SLBs that were patterned in the L_β phase showed uniform and stable patterned shapes after the polymer stencil lift-off step (Figure 2A) and for several weeks of storage at 4°C. On the other hand, DOPC SLBs patterned in the L_α phase showed pattern deformation due to bilayer spreading at the edges after the stencil was removed (Figure 2B). The pattern deformation was followed over a period of 24 hours and it was observed that after the initial spread following the stencil lift-off, the domains equilibrated over a time span between 6 and 12 hours (Figure S4). The spreading of the SLBs was thus limited by the amount of material contained within the patterned stencil and the area that this material could cover on the SiO_2 surface after the stencil was removed. Similar spreading behavior has been previously reported by Burridge *et al.*[33] for SLBs patterned using microfluidic channels after the PDMS template was removed. To prevent the DOPC SLB from

spreading and maintain the patterned feature shape fidelity, we performed the polymer stencil lift-off in 1× PBS buffer containing BSA, and subsequently washed away the excess BSA. Using this approach, the resulting SLB patterns had better defined edges compared to the ones without BSA treatment and the SLB did nor spread over time (Figures 2C and S4). The proposed mechanism for the observed effect is that BSA physically adsorbs onto the exposed bare SiO_2 surfaces once the stencil is lifted-off and effectively competes with lipid bilayer spreading. This was corroborated by imaging surfaces where the BSA treatment contained a small fraction (0.1%) of fluorescently-tagged BSA, which was seen to absorb preferentially on the spaces devoid of lipids (Figure S5). Furthermore, the addition of the BSA treatment did not alter the mobility of the patterned lipid bilayers, as evidenced by quantitative FRAP experiments (Figure S3). An additional benefit of the BSA treatment is that after lift-off, the SLB patterns had cleaner surfaces due to the blockage of non-specific binding of lipid vesicles during the washing steps. Thus, the use of a blocking agent during the polymer stencil lift-off step allowed us to produce well-defined homogeneous, and fluid SLB patterns with different shapes and sizes ranging from 2 to 200 μm (Figure S6).

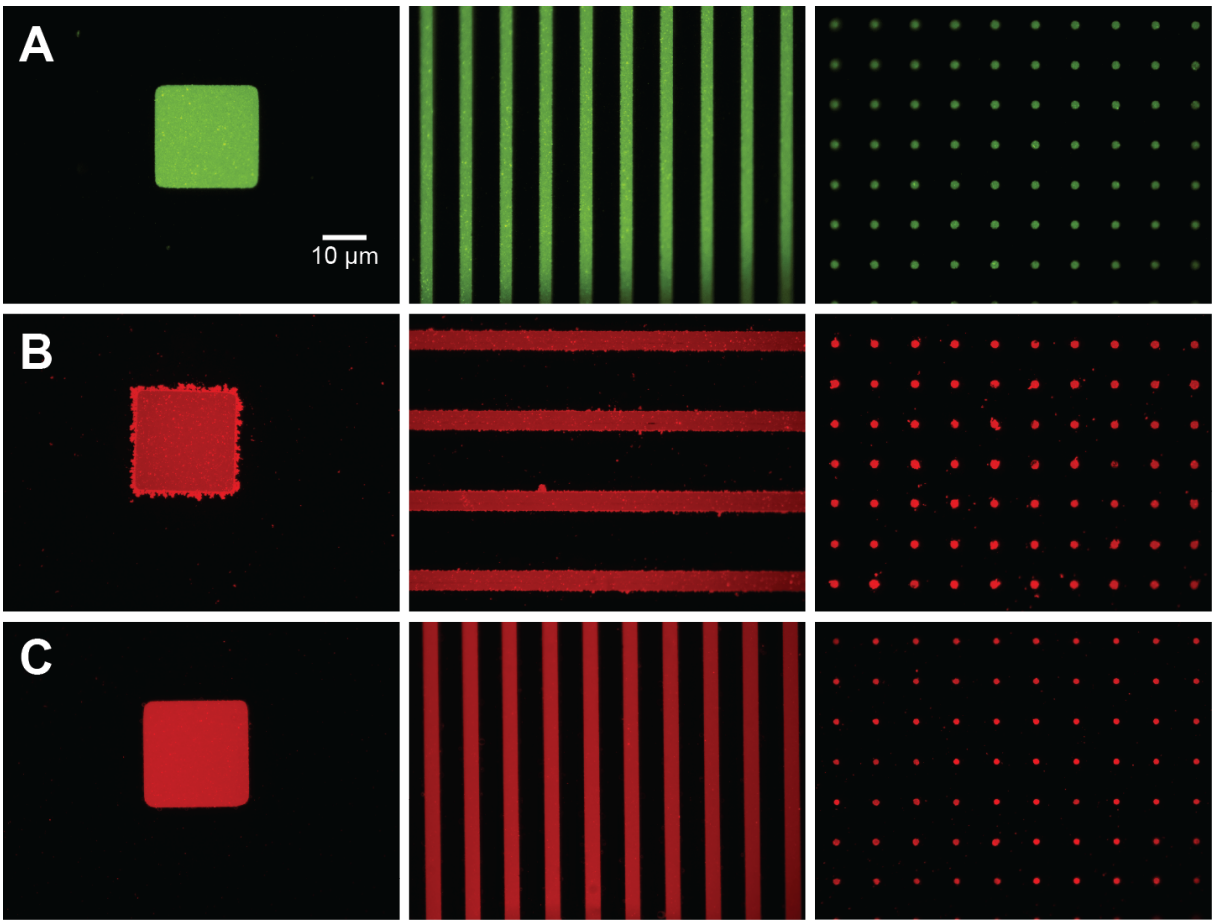

Figure 2-2 Epifluorescence images of homogeneous SLB patterns with and without incubation with BSA as a blocking agent. (A) DSPC:DHPE-OG (99:1) patterns exhibit no spreading, due to the DSPC bilayers existing in the L_β phase at room temperature. (B) Images of DOPC patterns without BSA treatment show lipid bilayer spreading beyond the patterned boundaries after the polymer stencil was lifted-off, as DOPC remained in the L_α phase at room temperature. (C) Images of DOPC SLB patterns with BSA treatment to prevent spreading. Better-defined pattern edges and cleaner bilayer surfaces were obtained. All images were obtained at the same magnification.

Next, we aimed to pattern phase-segregated SLBs from equimolar DOPC:DSPC mixtures doped with 1% DHPE-LR. On clean SiO_2 substrates, SLBs that were formed at 60°C showed spontaneous phase segregation after the bilayers were cooled down below the mixture's transition temperature (Figure S7). At room temperature, DSPC molecules with T_m = 55°C become more

ordered and coalesce into L_β phase domains, while DOPC molecules remain in the L_α phase due to their low transition temperature (T_m = -20°C). Initial attempts to form phase-segregated SLB patterns were unsuccessful and it was observed that although vesicles had adsorbed onto the substrate surface, no continuous bilayer was formed. This was further confirmed by qualitative bleaching experiments, where little or no recovery was observed (Figure S7). We hypothesized that the lack of SLB formation could be due to polymer residue inside the patterned openings, which increased surface roughness and prevented vesicle fusion. This assumption was verified through scanning electron micrographs that showed polymer residue left along the edges and within the etched openings after the stencil was lifted off (Figure S8). SLB formation could not be improved through over-etching, indicating that the residual polymer could not be efficiently degraded through oxygen plasma reactive ion etching alone. Polymer contamination left behind after etching has been previously observed by Goddard *et al.*,[34] who reported a UV/O_3 and base treatment to remove polymer residues from silicon sensor surfaces after etching. The treatment utilizes UV/O_3 to partially decompose organic residues and the base to clean the oxide surface by etching into it. A key consideration for SLB formation after the cleaning treatment is that the etch step should be strong enough to remove the polymer residue without significantly roughening the surface. Thus, a range of UV/O_3 cleaning times (1-10 min) and NaOH concentrations (0.01-1 M) were tested for the cleaning protocol. By assessing the quality of the SLBs formed on the cleaned substrates through fluorescence imaging (Figure S9), it was determined that the optimal cleaning procedure was 1 min UV/O_3 followed by a 1 min 100 mM base treatment. The improvement in the quality of the patterned SLBs after the optimized cleaning procedure was further validated by a marked improvement in FRAP recovery kinetics. DOPC SLBs patterned on etched and cleaned stencil openings had excellent mobilities, where the diffusion coefficients for the full bilayer

(Figure S3) and for the lower leaflet (Figure S10) matched those of the SLBs formed on clean SiO_2 substrates. Using the optimized substrate preparation conditions and BSA blocking treatment led to high quality, fully mobile SLBs that enabled the formation of well-defined patterned arrays of phase-segregating DOPC:DSPC SLBs through the polymer stencil lift-off technique (Figure 3).

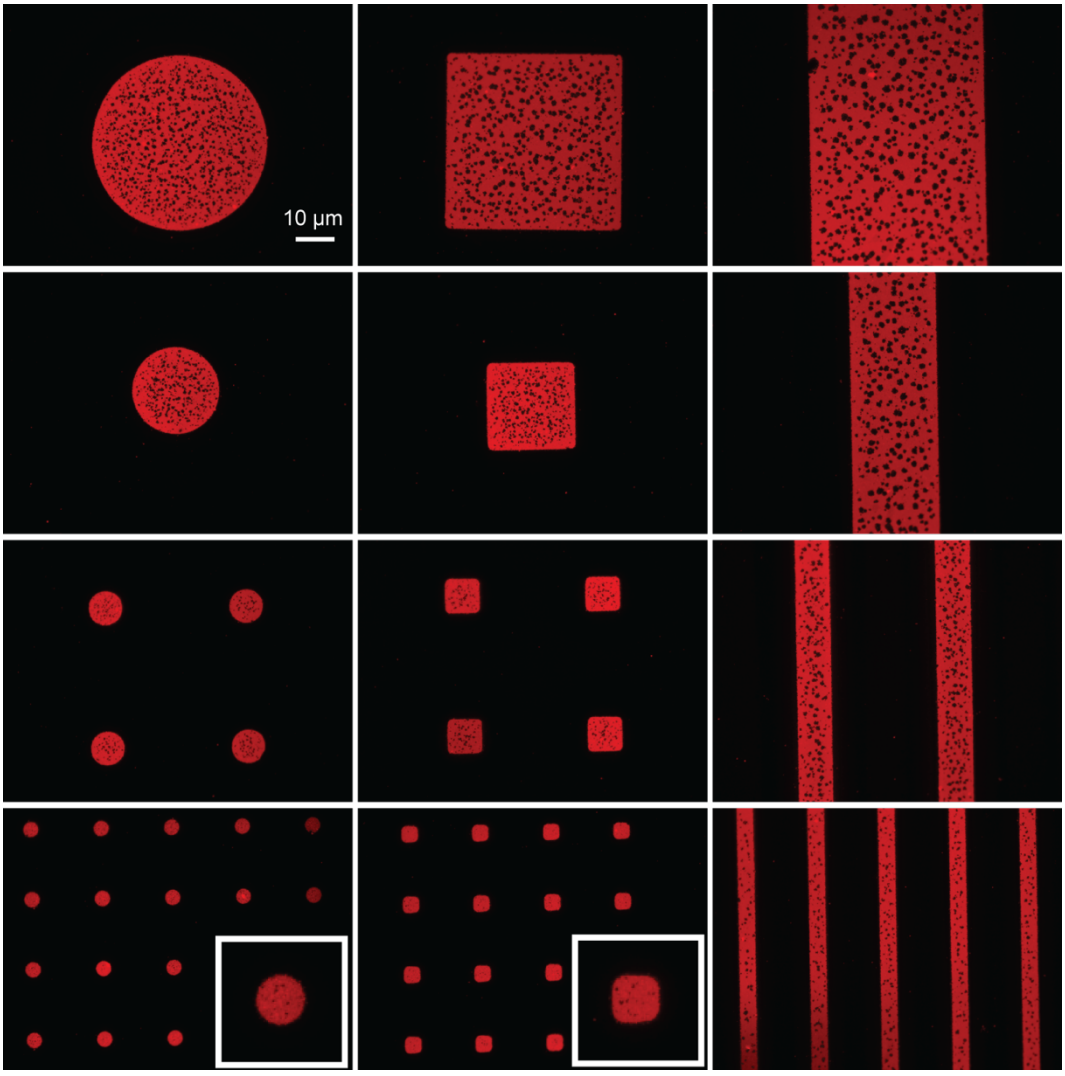

Figure 2-3 Epifluorescence images show phase-segregating DOPC:DSPC SLB patterns of various shapes and sizes produced through the polymer stencil lift-off technique. 1% DHPE-LR (red) partitioned preferentially with DOPC (L_α phase), rendering the DSPC (L_β phase) domains dark. All images were obtained at the same magnification. The insets are magnified images of the small circular and square patterns.

Given the high quality of the patterned SLBs, the gel phase domain sizes within the micropatterns could be adjusted by varying the cooling rate. Lower cooling rates led to larger gel phase domain formation, a well-known effect. Using the phase segregated patterns we studied the cooling rate effect in confined lipid bilayer patches. In a fast cooling process, the temperature was decreased directly from 60°C to room temperature, while a slower cooling process was to reduce the temperature in the incubator from 60°C to 25°C in 5°C steps with equilibration times of 5 minutes. When comparing the two cooling conditions, much larger gel phase domains were formed when the SLBs were cooled down slowly (Figure S11), as the slower cooling process allowed enough time for DSPC molecules to diffuse and coalesce to form larger gel domains before the mobility of DSPC molecules was drastically reduced.

It was also observed that in the SLB patterns formed through the slow cooling protocol, the smaller SLB patterns led to smaller gel phase domains. To study the effect of patterned feature size on lipid phase behavior, fluorescence image analysis was used to determine the average domain size and the percent area occupied by the gel phase within the patterned areas. The analysis algorithm separated the gel domains from the liquid disordered phase based on a fluorescence intensity threshold. Representative fluorescence and binary images of this process are shown in Figure 4A. The bar graphs in Figures 4B and 4C show a positive correlation between the average gel domain size and the patterned feature size, which is also observed in the percent area occupied by the gel phase. Similar trends were observed in the circular and square patterns. While the larger patterned features exhibited higher variability in the gel phase domain size and the fractional area occupied by the gel phase, the differences with the smaller patterned features were statistically significant, evidencing a clear effect of patterned domain size on the phase segregation kinetics in the SLB patches.

The observed trends were attributed to the strong influence of the boundary conditions, as a strong depletion of domains near the edges of the bilayer patch was observed. If diffusion is hindered near the boundary of the SLB pattern, because a) there are obstacles (polymer residue) associated with the fabrication process, b) the diffusion of the lower leaflet of the lipid bilayer (in close contact with the SiO_2 surface) is significantly lower, or c) the boundary is not perfectly reflective (due to a curved edge of the bilayer), we expect that the ability of DSPC molecules to coalesce near the boundary would decrease and the formation of gel phase domains would be diminished. FRAP experiments performed on the center versus the edge of large patterned domains did not show any appreciable mobility difference (Figure S3), arguing against scenario (a). On the other hand, FRAP experiments conducted on the patterned bilayers in presence of 100 mM $CoCl_2$ showed that the diffusion coefficient of the bottom leaflet of the patterned bilayer is only 68% of that measured for the full bilayer (Figures S3 and S10). This observation supports scenario (b), which can explain the depletion of gel phase domains near the boundary and the reduction in the size of the gel phase domains throughout the SLB patch. For this scenario, the smaller patterns with a larger perimeter to area ratio experience more pronounced effects, which is in good agreement with the experimental observation (Figures 3 and 4). To the best of our knowledge, this is the first observation on pattern size and boundary effect on lipid phase behavior.

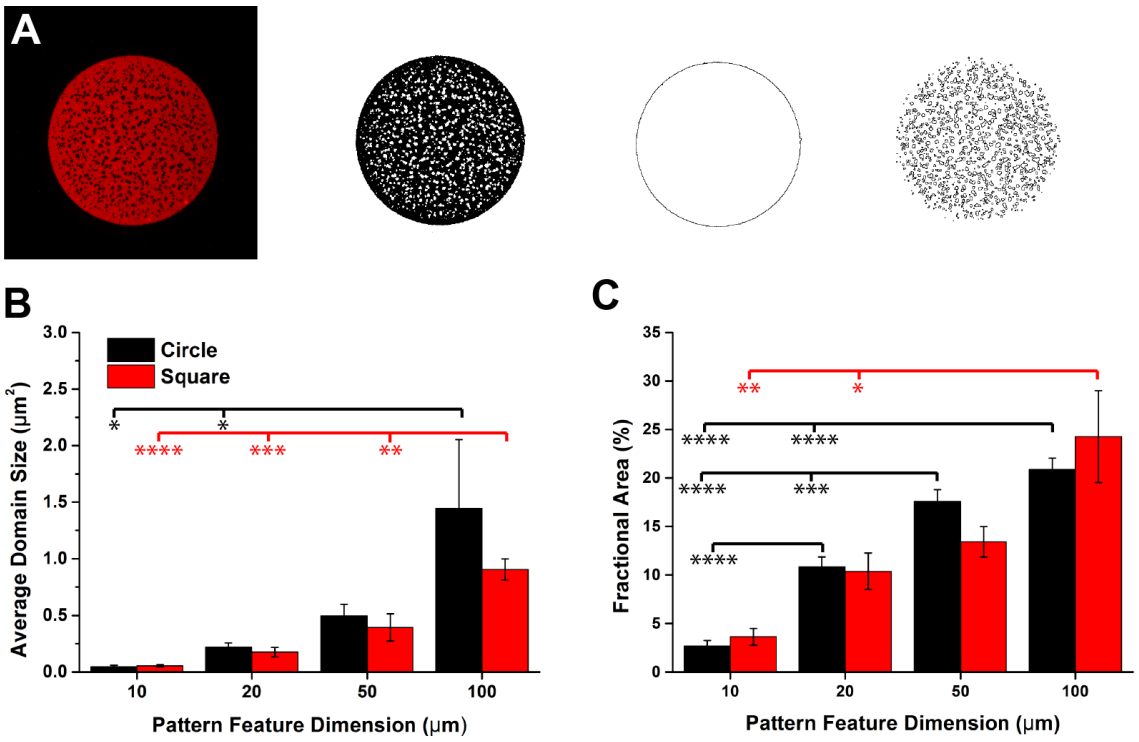

Figure 2-4 Quantitative analysis of lipid phase behaviour in micropatterns (A) Typical image processing steps including converting fluorescence image to binary, measuring the patterned feature size, and measuring the average gel phase domain sizes. (B) Average gel domain size in circular (black) and square (red) SLB patterns increases with the increase of the patterned feature size. (C) Percent area of gel phase increases with the increase of patterned feature size for circular (black) and square (red) SLB patterns. Error bars represent the standard error of the mean of replicate measurements performed on the patterned SLBs ($n \geq 3$). Statistical significance evaluated through ANOVA: *$p<0.05$, **$p<0.01$, ***$p<0.001$, ****$p<0.0001$.

Employing the established UV/O_3 and base treatment, L_β phase lipid bilayer patterns were also successfully fabricated. DSPC doped with 1% DHPE-OG vesicle solutions were incubated on patterned substrates at 60°C, and formed homogeneous SLB patterns as small as 2 μm, shown in Figure 2C. In contrast to DOPC bilayers, no spreading of lipids happened after lift-off, since DSPC lipid bilayers were in the gel phase with very limited mobility at room temperature, therefore obviating the need for BSA blocking treatment. For the same reason, no recovery was observed

after bleaching with the patterned DSPC bilayers (Figure S2). With the ability of patterning L_β phase SLBs, we further investigated the strategy for patterning binary arrays containing two lipid phases. A two-step incubation method was implemented (Figure 5A). DSPC SLBs were first patterned at 60 °C, followed by polymer lift-off and DOPC incubation at room temperature, which formed a continuous liquid disordered phase surrounding the DSPC patterns. With this simple and quick method involving only the mechanical lift-off of the polymer coating and successive SLB formation, well-defined binary SLB patterns were produced and visualized using two different fluorescent probes (Figure 5B). Recovery after photobleaching was observed in the DOPC liquid disordered phase but not in the DSPC gel phase (Figure S12), which was the expected behavior at room temperature but shows that even the SLBs formed on the substrate that was under the polymer coating exhibit excellent mobility (Figure S3). After being heated up to 60 °C and cooled down again, the two phases mixed together and spontaneous phase segregation occurred (Figure S13), which demonstrates that the binary patterns were connected and could exchange lipids under the appropriate environmental conditions.

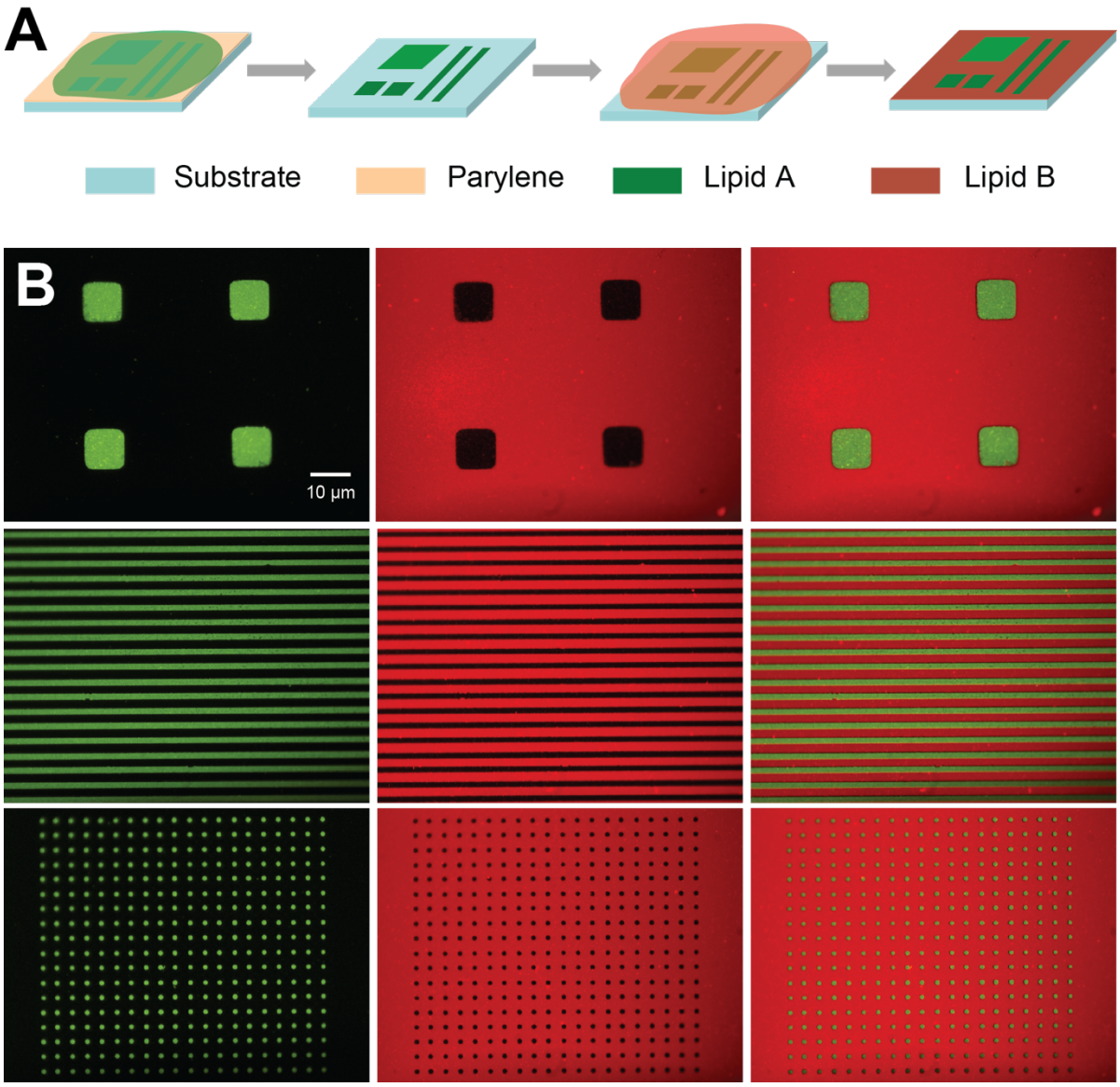

Figure 2-5 Binary lipid patterning process and fluorescence images. (A) Schematic illustration of the two-step incubation method for patterning binary lipid arrays. Lipid A vesicle solution is incubated to form lipid bilayer gel phase within the opening areas. Lipid B is then incubated to form fluid disordered phase after the stencil is lifted off. (B) Epifluorescence images of binary lipid bilayer patterns with DSPC (green) and DOPC (red) using DHPC-OG and DHPE-LR fluorescent probes, respectively. An overlay image is shown to demonstrate the perfect registration of the two lipid phases. All images were obtained at the same magnification.

2.5 Conclusions

In conclusion, we have improved the fidelity and quality of SLB patterns produced through the polymer stencil lift-off technique through a combination of a UV/O_3 and NaOH cleaning procedure and BSA blocking treatment, and achieved uniform 2-100 μm patterned SLB features. The use of BSA as blocking agent effectively prevented lipids in the liquid disordered phase from spreading and resulted in cleaner SLB surfaces by reducing non-specific binding. The use of the UV/O_3 and base cleaning procedure improved the quality of the patterned lipid bilayers, which exhibited mobilities comparable to those of SLBs formed on clean SiO_2 wafer substrates. This allowed us to produce SLBs with enough mobility to spontaneously phase-segregate. Using the phase-segregating SLB patterns, we studied the effect of cooling rate and pattern size on lipid phase behavior. Control over the cooling rate translated into the ability to control the gel phase domain sizes within the micropatterned SLBs, with slower cooling rates producing larger L_β phase domains. Smaller patterned feature sizes also led to smaller L_β phase domains and fractional area covered by the L_β phase, which is attributed to diffusion hindrance in the bottom leaflet of the SLB, which impacts the exchange rate of lipids from the top to the bottom leaflet at the SLB boundaries. In addition, a precise control over the spatial organization of binary lipid phases was achieved by patterning two lipid components with the two-step incubation method. The presented patterning strategies based on the PSLO technique are simple, quick and robust, since they rely on microfabricated stencils that can be produced at large scales and stored indefinitely until needed, the patterning of the SLBs can then be done by mechanically peeling the stencil under aqueous conditions without need of strict humidity or environmental control (similar to how it would be done on mica or any other hydrophilic flat surface), and the patterns are stable over weeks of storage under refrigerated conditions. While the peeling of a continuous sheet of polymer imposes

some limitations on the type of patterns that can be achieved and the number of bilayers with different compositions that can be deposited, the PSLO technique is also compatible with quill pin, microcontact, or inkjet printing and combinations of such techniques could be exploited to provide complementary technique strengths and benefits. We anticipate that the developed patterning strategies could be used to develop surfaces that can serve as useful tools for biophysical studies of membrane and membrane-associated biomolecules, as well as platforms for biosensing applications.

2.6 Acknowledgements

This work was supported through the Natural Sciences and Engineering Research Council (RGPIN/418326) and the Canada Foundation for Innovation Leaders Opportunity Fund. Jose Moran-Mirabal is the recipient of an Early Researcher Award through the Ontario Ministry of Research and Innovation. Yujie Zhu was partially supported by the Interdisciplinary Development of Extracellular Matrices Collaborative Research Training Program. This research made use of facilities at the Centre for Emerging Device Technology and the Canadian Centre for Electron microscopy at McMaster University.

2.7 References

(1) Brian, A. A; McConnell, H. M. Allogeneic Stimulation of Cytotoxic T Cells by Supported Planar Membranes. *Proc. Natl. Acad. Sci. U. S. A.* **1984**, *81* (19), 6159–6163.

(2) Castellana, E. T.; Cremer, P. S. Solid Supported Lipid Bilayers: From Biophysical Studies to Sensor Design. *Surf. Sci. Rep.* **2006**, *61* (10), 429–444.

(3) Wu, M.; Holowka, D.; Craighead, H. G.; Baird, B. Visualization of Plasma Membrane Compartmentalization with Patterned Lipid Bilayers. *Proc. Natl. Acad. Sci. U. S. A.* **2004**, *101* (38), 13798–13803.

(4) Moran-Mirabal, J. M.; Edel, J. B.; Meyer, G. D.; Throckmorton, D.; Singh, A. K.; Craighead, H. G. Micrometer-Sized Supported Lipid Bilayer Arrays for Bacterial Toxin Binding Studies through Total Internal Reflection Fluorescence Microscopy. *Biophys. J.*

2005, *89* (1), 296–305.

(5) Nguyen, T. T.; Conboy, J. C. High-Throughput Screening of Drug-Lipid Membrane Interactions via Counter-Propagating Second Harmonic Generation Imaging. *Anal. Chem.* **2011**, *83* (15), 5979–5988.

(6) Hwang, S. Y.; Kwon, K. W.; Jang, K.-J.; Park, M. C.; Lee, J. S.; Suh, K. Y. Adhesion Assays of Endothelial Cells on Nanopatterned Surfaces within a Microfluidic Channel. *Anal. Chem.* **2010**, *82* (7), 3016–3022.

(7) Torres, A. J.; Contento, R. L.; Gordo, S.; Wucherpfennig, K. W.; Love, J. C. Functional Single-Cell Analysis of T-Cell Activation by Supported Lipid Bilayer-Tethered Ligands on Arrays of Nanowells. *Lab Chip* **2012**, No. 207890, 90–99.

(8) Mossman, K. D.; Campi, G.; Groves, J. T.; Dustin, M. L. Altered TCR Signaling from Geometrically Repatterned Immunological Synapses. *Science (80-.).* **2005**, *310* (5751), 1191–1193.

(9) Bally, M.; Bailey, K.; Sugihara, K.; Grieshaber, D.; Vörös, J.; Ståler, B. Liposome and Lipid Bilayer Arrays towards Biosensing Applications. *Small* **2010**, *6* (22), 2481–2497.

(10) van Meer, G.; Voelker, D. R.; Feigenson, G. W. Membrane Lipids: Where They Are and How They Behave. *Nat. Rev. Mol. Cell Biol.* **2008**, *9* (2), 112–124.

(11) Simons, K.; Sampaio, J. Membrane Organization and Lipid Rafts. *Cold Spring Harb. Perspect. Biol.* **2011**, *3* (10), a004697.

(12) Kung, L. A.; Kam, L.; Hovis, J. S.; Boxer, S. G. Patterning Hybrid Surfaces of Proteins and Supported Lipid Bilayers. *Langmuir* **2000**, *16* (17), 6773–6776.

(13) Jung, M.; Vogel, N.; Köper, I. Nanoscale Patterning of Solid-Supported Membranes by Integrated Diffusion Barriers. *Langmuir* **2011**, *27* (11), 7008–7015.

(14) Nakai, K.; Morigaki, K.; Iwasashi, Y. Molecular Recognition on Fluidic Lipid Bilayer Microarray Corralled by Well-Defined Polymer Brushe. *Soft Matter* **2010**, *6*, 5937–5943.

(15) Hovis, J. S.; Boxer, S. G. Patterning and Composition Arrays of Supported Lipid Bilayers by Microcontact Printing. *Langmuir* **2001**, *17* (11), 3400–3405.

(16) Kaufmann, S.; Sobek, J.; Textor, M.; Reimhult, E. Supported Lipid Bilayer Microarrays Created by Non-Contact Printing. *Lab Chip* **2011**, *11* (14), 2403–2410.

(17) Orth, R. N.; Kameoka, J.; Zipfel, W. R.; Ilic, B.; Webb, W. W.; Clark, T. G.; Craighead, H. G. Creating Biological Membranes on the Micron Scale: Forming Patterned Lipid Bilayers Using a Polymer Lift-off Technique. *Biophys. J.* **2003**, *85* (5), 3066–3073.

(18) Zhu, Y.; Negmi, A.; Moran-Mirabal, J. Multi-Stacked Supported Lipid Bilayer Micropatterning through Polymer Stencil Lift-Off. *Membranes (Basel).* **2015**, *5* (3), 385–398.

(19) Zagnoni, M. Miniaturised Technologies for the Development of Artificial Lipid Bilayer

Systems. *Lab Chip* **2012**, *12* (6), 1026–1039.

(20) Malmstadt, N.; Nash, M. a.; Purnell, R. F.; Schmidt, J. J. Automated Formation of Lipid-Bilayer Membranes in a Microfluidic Device. *Nano Lett.* **2006**, *6* (9), 1961–1965.

(21) Spycher, P. R.; Hall, H.; Vogel, V.; Reimhult, E. Patterning of Supported Lipid Bilayers and Proteins Using Material Selective Nitrodopamine-mPEG. *Biomater. Sci.* **2015**, *3* (1), 94–102.

(22) Furukawa, K.; Aiba, T. Supported Lipid Bilayer Composition Microarray Fabricated by Pattern-Guided Self-Spreading. *Langmuir* **2011**, *27* (12), 7341–7344.

(23) Smith, K. A; Gale, B. K.; Conboy, J. C. Micropatterned Fluid Lipid Bilayer Arrays Created Using a Continuous Flow Microspotter Micropatterned Fluid Lipid Bilayer Arrays Created Using a Continuous Flow Microspotter. *Anal. Chem.* **2008**, *80* (21), 7980–7987.

(24) Roder, F.; Birkholz, O.; Beutel, O.; Paterok, D.; Piehler, J. Spatial Organization of Lipid Phases in Micro- Patterned Polymer-Supported Membranes. *J. Am. Chem. Soc.* **2013**, 647–650.

(25) Adams, P. G.; Swingle, K. L.; Paxton, W. F.; Nogan, J. J.; Stromberg, L. R.; Firestone, M. A.; Mukundan, H.; Montaño, G. A. Exploiting Lipopolysaccharide-Induced Deformation of Lipid Bilayers to Modify Membrane Composition and Generate Two-Dimensional Geometric Membrane Array Patterns. *Sci. Rep.* **2015**, *5*, 10331.

(26) Yamada, M.; Imaishi, H.; Morigaki, K. Microarrays of Phospholipid Bilayers Generated by Inkjet Printing. *Langmuir* **2013**, *29*, 6404–6408.

(27) Ilic, B.; Craighead, H. G. Topographical Patterning of Chemically Sensitive Biological Materials Using a Polymer-Based Dry Lift Off. *Biomed. Microdevices* **2000**, *2* (4), 317–322.

(28) Moran-Mirabal, J. M.; Tan, C. P.; Orth, R. N.; Williams, E. O.; Craighead, H. G.; Lin, D. M. Controlling Microarray Spot Morphology with Polymer Liftoff Arrays. *Anal. Chem.* **2007**, *79* (3), 1109–1114.

(29) Atsuta, K.; Suzuki, H.; Takeuchi, S. A Parylene Lift-off Process with Microfluidic Channels for Selective Protein Patterning. *J. Micromechanics Microengineering* **2007**, *17* (3), 496–500.

(30) Tan, C. P.; Seo, B. R.; Brooks, D. J.; Chandler, E. M.; Craighead, H. G.; Fischbach, C. Parylene Peel-off Arrays to Probe the Role of Cell-Cell Interactions in Tumour Angiogenesis. *Integr. Biol.* **2009**, *1* (10), 587–594.

(31) Blumenthal, D.; Goldstien, L.; Edidin, M.; Gheber, L. A. Universal Approach to FRAP Analysis of Arbitrary Bleaching Patterns. *Sci. Rep.* **2015**, *5*, 11655.

(32) Schneider, C. a; Rasband, W. S.; Eliceiri, K. W. NIH Image to ImageJ: 25 Years of Image Analysis. *Nat. Methods* **2012**, *9* (7), 671–675.

(33) Burridge, K. A.; Figa, M. A.; Wong, J. Y. Patterning Adjacent Supported Lipid Bilayers of Desired Composition to Investigate Receptor-Ligand Binding under Shear Flow. *Langmuir* **2004**, *20* (23), 10252–10259.

(34) Goddard, J. M.; Mandal, S.; Nugen, S. R.; Baeumner, A. J.; Erickson, D. Biopatterning for Label-Free Detection. *Colloids Surf. B. Biointerfaces* **2010**, *76* (1), 375–380.

Chapter 3 Multi-Stacked Supported Lipid Bilayer Micropatterning through Polymer Stencil Lift-Off

Yujie Zhu and Jose M. Moran-Mirabal designed the experiments; Yujie Zhu fabricated the Parylene stencils and optimized the supported lipid bilayer patterning and imaging conditions; Ahmed Negmi performed most of the patterning and imaging. Yujie Zhu, Ahmed Negmi, and Jose Moran-Mirabal analyzed the data; and Yujie Zhu and Jose M. Moran-Mirabal wrote the manuscript.

3.1 Abstract

Complex multi-lamellar structures play a critical role in biological systems, where they are present as lamellar bodies, and as part of biological assemblies that control energy transduction processes. Multi-lamellar lipid layers not only provide interesting systems for fundamental research on membrane structure and bilayer-associated polypeptides, but can also serve as components in bioinspired materials or devices. Although the ability to pattern stacked lipid bilayers at the micron scale is of importance for these purposes, limited work has been done in developing such patterning techniques. Here, we present a simple and direct approach to pattern stacked supported lipid bilayers (SLBs) using polymer stencil lift-off and the electrostatic interactions between cationic and anionic lipids. Both homogeneous and phase-segregated stacked SLB patterns were produced, demonstrating that the stacked lipid bilayers retain lateral diffusivity. We demonstrate patterned SLB stacks of up to four bilayers, where fluorescence resonance energy transfer (FRET) and

quenching was used to probe the interactions between lipid bilayers. Furthermore, the study of lipid phase behaviour showed that gel phase domains align between adjacent layers. The proposed stacked SLB pattern platform provides a robust model for studying lipid behavior with a controlled number of bilayers, and an attractive means towards building functional bioinspired materials or devices.

3.2 Introduction

In living systems, multilamellar membranous structures are present as lamellar bodies and as key elements in many active biological assemblies that control energy transduction processes[1]. *In vitro* models of lipid multilayers that can mimic these natural systems are important tools for biophysical studies of membranes. Such stacked lipid bilayer systems have been previously used to study interactions between neighboring bilayers, such as membrane fusion[2] and anomalous swelling[3], as well as the structure of membranes as they interact with polypeptides[4]. Stacked bilayers are also of interest for practical applications such as cell sensing[5], drug delivery[6] and disease diagnosis[7]. For example, it has been recently reported that stacked SLBs can be used as a tunable substrate to study dynamic, mechano-regulated cell linkages and cellular mechano-sensing[58]. Therefore, methods for reconstructing lipid multilayer structures at the nano- or microscale *in vitro* need to be developed for better mimicking the complexity of natural biomembranes.

A number of strategies have been developed for building stacked SLBs from the bottom-up *in vitro*. Electrostatic interactions between cationic and anionic lipid bilayers[9] and between phospholipids and silica templates[10] have been used to form double stacked bilayers and highly ordered hybrid multilamellar assemblies respectively. In addition, specific biological interactions involving biotin-streptavidin coupling[11] and DNA hybridization[12], as well as covalent bonds

involving inter-bilayer maleimide-thiol coupling[13] have been used to form double bilayer systems with variable stability. Despite the efforts made in building stacked bilayers, to date there are no reported techniques that can easily pattern them at the micron scale and in large array format. A key limitation for the in-situ patterning of stacked lipid bilayers is the need to conduct the formation of the bilayer stack and the selective patterning under aqueous conditions. Thus, the majority of techniques reported have been limited to patterning of a single SLB. Microcontact printing has been used for patterning multiple lipid bilayers, but with poor control of lipid organization and stack thickness[14]. Similarly, capillary assembly and dip-pen nanolithography (DPN) and have been successfully used to pattern multi-stacked SLB through the use of microstructured surfaces[15] and by direct writing of arbitrary patterns[1617], respectively. Moreover, a method combining microcontact printing, nanoimprint lithography and dip-pen nanolithography, has been developed to create nanostructured lipid multilayer arrays[18]. However, these techniques are resource intensive, are not able to control the number of bilayers accurately or have difficulty in patterning phase-segregated SLBs. Therefore, new techniques that allow simple patterning of lipid multilayers in large areas with accurate stack thickness control and which can pattern phase segregated bilayers are needed.

Polymer stencil lift-off (PSLO) is a robust technique that uses a microfabricated Parylene stencil[19] to pattern a wide range of biomaterials, such as proteins[20], DNA[21], cellulose fibrils[22], or cells[23], at the micron scale (its patterning resolution only limited by the lithographic technique used to define the stencil openings). The PSLO technique has also been successfully applied in functional SLB patterning[24], which allows faithful transfer of uniform SLB patterns in aqueous condition with sub-micron resolution[25]. Here, we report the extension of the PSLO technique as a simple and direct approach to pattern a controlled number of stacked SLBs under aqueous

conditions. SLB stacks were formed by electrostatic interactions between cationic and anionic lipids. This strategy allows patterning large areas of SLB stacks of micrometer dimensions, with accurately controlled number of layers and compositions. Both homogeneous and phase-segregated stacked SLB patterns were achieved. To our knowledge, this is the first report of patterned SLB stacks that are built form the bottom-up with controlled distributions of lipids, which opens up possibilities for new biophysical studies on interactions between membranes and between membranes and membrane associated proteins, as well as future applications in cell culture and drug screening.

3.3. Results and Discussion

3.3.1 Supported Lipid Bilayer Micropatterning

Supported Lipid Bilayer stacks were deposited into micron-sized patterns through the use of Polymer Stencil Lift-Off (PSLO, Figure 3-1). In this process, Parylene was first deposited through chemical vapor deposition onto SiO_2 surfaces to form a 500-1000 nm thick, conformal, pinhole-free film. Parylene films were then patterned thorough standard photolithography and reactive ion etching processes. This resulted in polymer stencils with arrays of features with 2-200 μm critical dimensions, which were subsequently cleaned with acetone, UV-O_3, and 100 mM sodium hydroxide solution to remove any photoresist and polymer residue in the opening areas, producing smooth surfaces suitable for SLB formation through vesicle fusion. By incubating small unilamellar lipid vesicles (SUVs) on the substrates under the appropriate temperature, SLBs formed within the Parylene stencil openings. For single lipid bilayer patterning, the stencil could be removed after the first incubation step, while for multiple SLB stack formation the stencil remained in place until after the last bilayer was deposited. The Parylene stencil served as a stable

physical barrier preventing the SLBs from spreading and remained intact during the whole SLB stacking process, which was conducted under aqueous conditions. The deposited lipids formed micron-sized single and multiple SLBs domains, demonstrating the suitability of PSLO for patterning stacked SLBs.

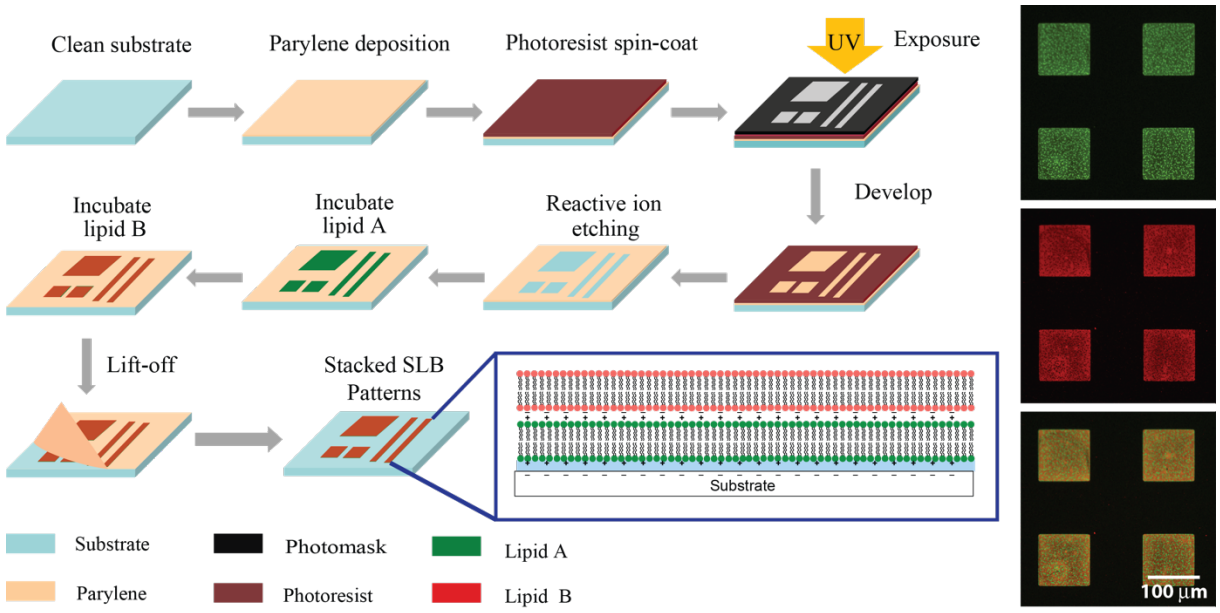

Figure 3-1 Illustration of the PSLO patterning process for stacked SLBs. Parylene film is deposited onto a clean substrate, and photoresist is patterned using photolithography. After reactive ion etching of Parylene and removal of photoresist, small unilamellar lipid vesicles are deposited on the stencils and incubated to form SLBs. The final step is to lift-off the stencil, revealing stacked SLB patterns. Inset: side view illustration of a double lipid bilayer with cationic and anionic lipids, and fluorescence images of a two-bilayer stack.

3.3.2 Homogeneous SLB Stacks

The ability to pattern SLB stacks through the PSLO technique was first tested using lipid mixtures that formed homogenous bilayers. Two kinds of 1,2-dioleoyl-sn-glycero-3-phosphocholine (DOPC) vesicle solutions were prepared: one was doped with 10% cationic lipid

1,2-dioleoyl-3-trimethylammonium-propane (DOTAP), and the other with 10% anionic lipid 1,2-dimyristoyl-sn-glycero-3-phospho-L-serine (DMPS). As the SiO_2 substrate was negatively charged under slightly basic buffer conditions, a positively charged SLB containing DOTAP was formed first by vesicle fusion directly on the substrate. With the first cationic bilayer formed, the anionic lipid vesicles were then incubated to form the second SLB. The electrostatic interactions between the oppositely charged lipids promoted the fusion of anionic vesicles on top of the underlying cationic bilayer. By alternating the charge of the subsequent layers, three- and four-bilayer stacks could be similarly formed. We demonstrated the formation of up to four homogenous SLBs with DOPC as the main component through this bilayer-by-bilayer approach. However, it must be noted that any number of bilayers is possible provided the thickness of the resulting stack does not exceed the stencil thickness. The stacked SLB patterns were visualized by fluorescence microscopy during the stack formation (Figure 3-2). Oregon Green labeled 1,2-dihexadecanoyl-sn-glycero-3-phosphoethanolamine (DHPE-OG) and Lissamine Rhodamine B 1,2-dihexadecanoyl-sn-glycero-3-phosphoethanolamine (DHPE-LR) were added to the vesicles at low concentrations (0.1% molar ratio) to label the SLBs, and were imaged in the green and red fluorescence channels respectively. The images show that fluorescence intensity of both channels changed with the addition of each new bilayer. Specifically, after the second bilayer (labeled with DHPE-LR) and third bilayers were formed, the intensity of DHPE-OG in the first bilayer and the DHPE-LR in the second bilayer greatly decreased, a change ascribed to fluorescence resonance energy transfer (FRET) or collisional quenching mechanisms respectively. On one hand in FRET, Oregon Green, as a donor chromophore, initially in its electronic excited state, transferred energy through non-radiative dipole–dipole coupling to the acceptor chromophore, Lissamine Rhodamine (LR), resulting in decreased green channel intensity; on the other hand the addition of a third

bilayer and the close proximity of DHPE-OG molecules to DHPE-LR could cause collisional quenching, leading to reduced intensities in the red channel too. Quantitative fluorescence analysis was conducted by measuring the absolute and relative fluorescence intensities of each bilayer (relative intensity normalized to the intensity of the first bilayer added in each channel), as shown in Figure 3-3. The ratio of red over the green channel raw intensities (Figure 3-3c) increases with the deposition of LR labeled SLBs, and decreases with then addition of OG-labeled SLBs. The trend for fluorescence intensity change was in good agreement with expected intensity variations based on the successive addition of fluorescent bilayers taking into account FRET and quenching effects, further confirming the formation of patterned SLB stacks. In addition, fluorescence recovery after photobleaching (FRAP) experiments were performed on each successive bilayer added (Supplemental Figure 1), where the observation of homogeneous recovery indicated that each bilayer of the stack retained good mobility at room temperature. The fluorescence background observed outside the patterns in bilayers 2 and 3 of Figure 3-3 was generated by vesicles adhered on the Parylene stencil, as the stencil was not lifted off until all four bilayers had been deposited. The fluorescence images, fluorescence intensity analysis, and FRAP tests demonstrated that fully mobile SLB stacks could be formed by layer-by layer deposition and easily patterned using the PSLO approach.

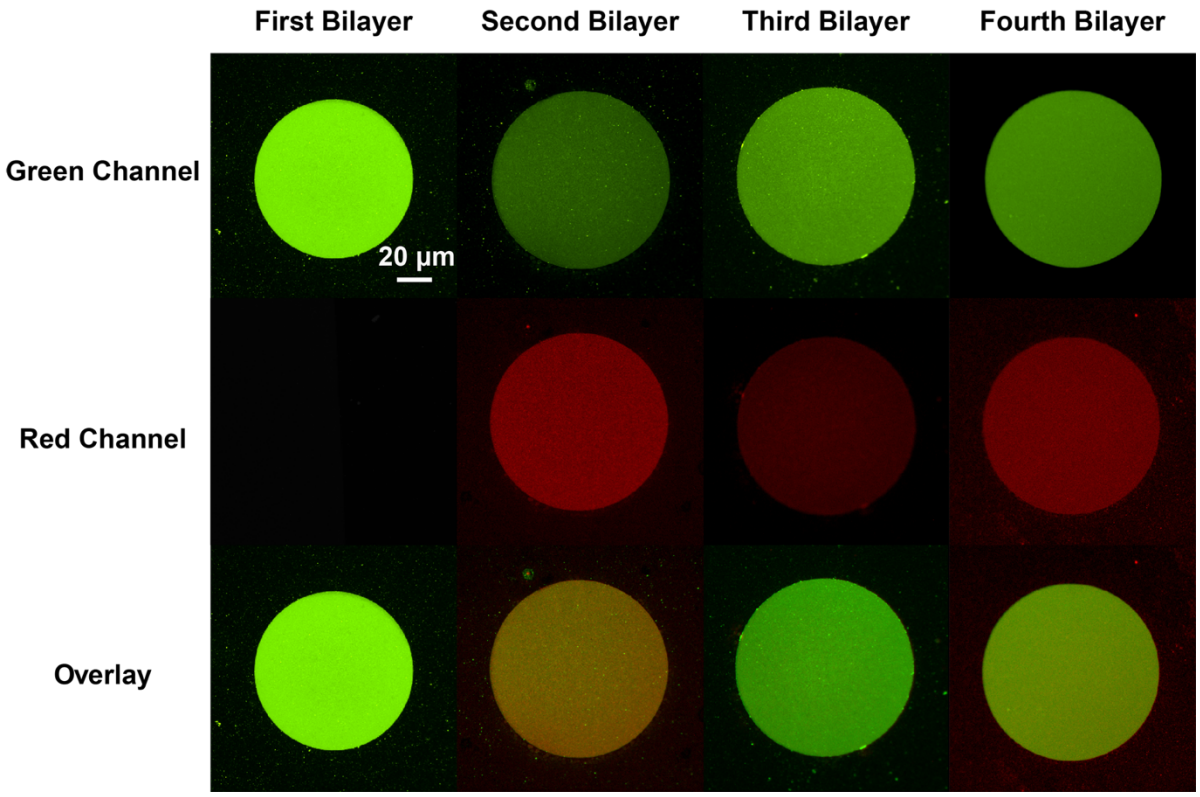

Figure 3-2 Epifluorescence images of four-bilayer homogeneous stacked SLB micropatterns. The first and third bilayers were composed of DOPC:DOTAP:DHPE-OG and can be observed in green channel. Second and fourth bilayers were composed of DOPC:DMPS:DHPE-LR, and can be observed in red channel (middle). The bottom row presents an overlay of both red and green channels. All images were acquired at the same magnification.

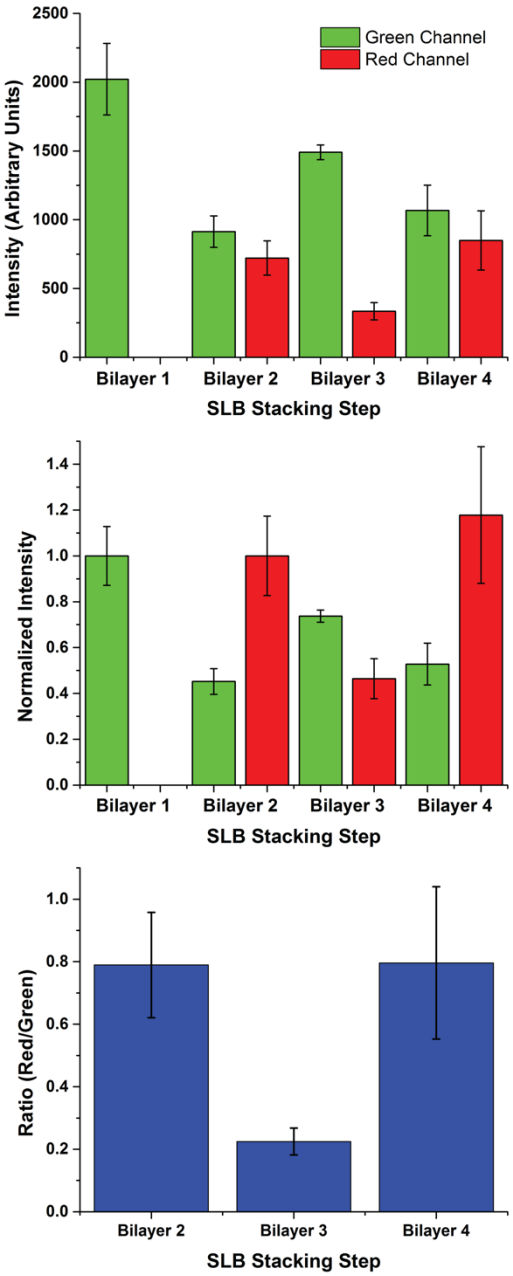

Figure 3-3 Quantitative fluorescence intensity analysis of stacked SLB formation. (a) Raw fluorescence intensity of green (DHPE-OG) and red (DHPE-LR) channels of the four-bilayer SLB patterns after each stacking step. (b) Normalized intensity of each stacking step (green channel normalized to bilayer 1 and red channel normalized to bilayer 2 values). (c) Ratio of the raw intensities of red to green channels at each stacking step.

3.3.3 Stacked SLBs containing phase-segregated domains

The same bilayer-by-bilayer deposition and PSLO approach was applied to create stacked SLB patterns containing phase-segregating lipid compositions. The anionic and cationic lipids used in these experiments (DOPS, DOTAP) partition preferentially into the liquid-disordered phase due to their unsaturated carbon chains, which result in lower transition temperatures (T_m = -11 and -11.9°C, respectively). Phase segregation was achieved by introducing 1,2-distearoyl-sn-glycero-3-phosphocholine (DSPC, a fully saturated lipid with T_m = 55°C) into the DOPC:DOPS/DOTAP:DHPE-OG/LR lipid mixtures. Homogeneous, fully mixed bilayers were successfully formed at 60°C (above the DSPC transition temperature), after which cooling to room temperature (21°C) resulted in the formation of visible phase-segregated lipid domains. Since the DHPE-OG/LR dyes preferentially partition into the liquid-disordered phase (primarily composed of DOPC), the gel phase consisting mostly of DSPC would be observed as dark domains. First, we demonstrated the ability to form two-bilayer stacks composed of a phase-segregated bilayer on top of a homogeneous one (Figure 3-4). As expected, the first lipid bilayer deposited, with composition DOPC:DOTAP:DHPE-OG, was uniformly fluorescent in the green channel. However, upon formation of a second phase-segregated SLB, with composition DOPC:DSPC:DOPS:DHPE-LR, it was observed that the green channel now showed a complementary pattern to the red channel, as shown in the overlay image of Figure 3-4. This phenomenon can be readily explained by the close proximity and interaction between the fluorescent probes in each of the bilayers within the stack, which results in FRET. Since FRET could only occur between DHPE-OG molecules (green) in the first bilayer (homogeneous) that came into close proximity with DHPE-LR molecules (red) in the second bilayer (phase-segregated), and given that the DHPE-LR molecules partitioned preferentially to the fluid phase, areas of the first bilayer overlapping the gel domains in the second

bilayer appeared brighter than the surrounding areas. This phenomenon directly probes the interactions between the two bilayers, and demonstrates that the stacked bilayers are in close proximity. Additionally, the observation of phase segregation in the second bilayer, coupled with FRAP measurements on both homogenous and phase-segregated layers in this experiment (Supplementary Figure 2), confirmed the formation of fully mobile heterogeneous SLB stacks through the PSLO technique.

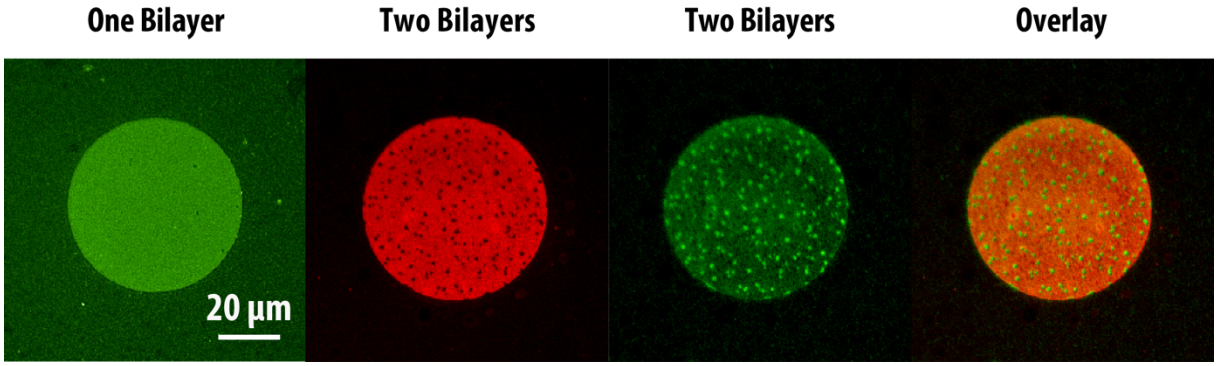

Figure 3-4 Epifluorescence images showing patterns of two-bilayer SLB stacks consisting of a homogeneous bottom bilayer and a phase-segregated top bilayer. The first lipid bilayer (composed of DOPC: DOTAP: DHPE-OG) is observed in green channel, while the second lipid bilayer (composed of DOPC: DSPC: DOPS: DHPE-LR) can be observed in red channel. The formation of the second bilayer leads to significant fluorescence intensity changes in the first bilayer. The overlaid image of the two bilayers shows the fluorescence patterns are complimentary, due to FRET.

Next, we explored the possibility of patterning two-bilayer stacks where both bilayers would phase-segregate, and investigated the phase behaviour of the stacked bilayers. Small unilamellar lipid vesicles composed of DOPC:DSPC:DOTAP:DHPE-OG were deposited and incubated at 60°C to form the first bilayer. It was observed that when the substrate was properly cleaned (i.e. the bilayer mobility was appropriate), micron-scale gel domains formed on the cationic bilayer upon slow cooling. As expected, the DHPE-OG molecules preferentially partitioned into the liquid disordered phase, leaving the gel phase dark (Figure 3-5a, green channel). A second anionic phase-

segregated bilayer (with composition DOPC:DSPC:DOPS:DHPE-LR, Figure 3-5a red channel) could then be formed on top by incubating the lipid vesicles at 60°C followed by slow cooling. The formation of this second bilayer also led to decreased fluorescence intensity from the first bilayer due to FRET. When both lipid bilayers phase-segregated, it was observed that the gel domains aligned between the two bilayers (Figure 3-5a, overlay), indicating coupling between the phase-segregation processes of both bilayers. Tayebi and collaborators[189] have previously reported the long-range alignment of phase-segregated lipid bilayer domains across hundreds of membrane lamellae. They postulated that such alignment originated from the surface tension associated with differences in the network of hydrogen-bonded water molecules at the hydrated interfaces between the domains and the surrounding phases. In our case, in addition to surface tension effects, the alignment could also be promoted by charges within the lipid bilayer, since the cationic and anionic lipids both partition preferentially into the liquid disordered phase. On the other hand, when the first cationic bilayer was not highly mobile, due to improper cleaning or cooling rate, it did not show visible phase segregation and the fluorescence intensity remained homogeneous (Figure 3-5b, green channel). Under this scenario, formation of the second anionic lipid bilayer led to phase segregation only on the second layer, where gel phase domains appeared dark (Figure 5b, red channel). In this case FRET between the two layers caused the green channel intensity from the first bilayer to show a complementary pattern to the phase segregation of the second bilayer (Figure 3-5b, overlaid image), resembling the results obtained from patterned SLB stacks where the first bilayer was homogeneous and the second one was phase segregating. These experimental results demonstrate that it is possible to pattern lipid bilayer stacks with heterogeneous lipid bilayers through the bilayer-by-bilayer and PSLO approach, and observe interactions between phase-segregating lipid mixtures across lipid lamellae. However, it must be noted that sample preparation

and substrate cleanliness are key to obtaining highly mobile lipid bilayers that enable such interactions.

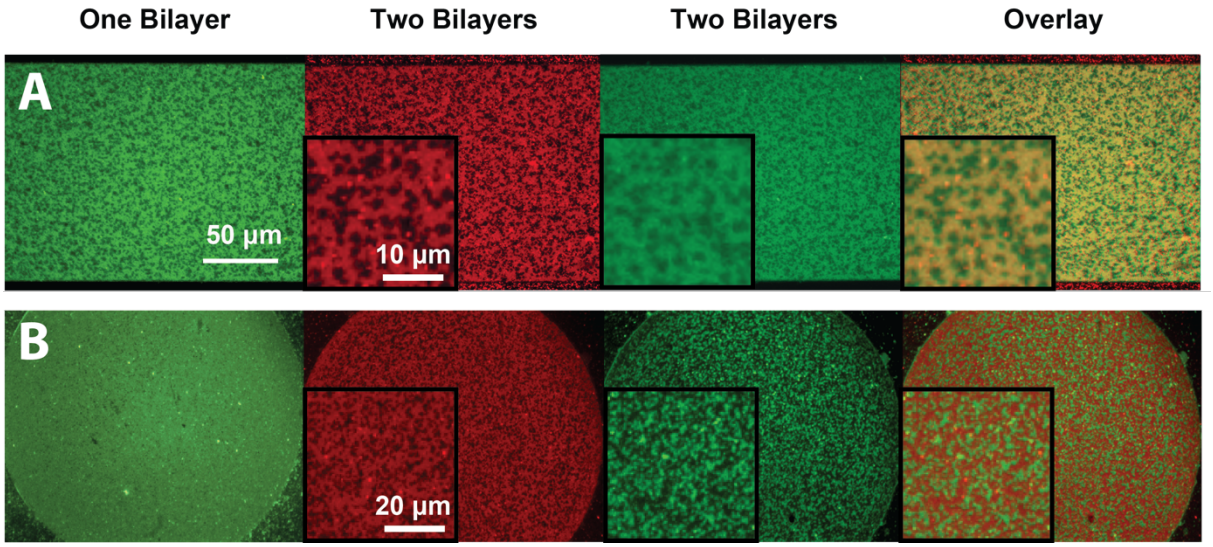

Figure 3-5 Epifluorescence images of stacked phase-segregated SLB patterns. The first lipid bilayer was composed of DOPC:DSPC:DOTAP:DHPE-OG (green channel), while the second lipid bilayer was composed of DOPC:DSPC:DOPS:DHPE-LR (red channel). Insets show zoomed-in areas of the patterned bilayers. (a) When the first bilayer showed good phase segregation (green), the second lipid bilayer would phase segregate in the same pattern (red). The fluorescence intensity of first bilayer would decrease due to FRET, and the overlaid image of the two channels showed alignment of gel phase domains in the two bilayers. (b) When the first bilayer did not phase-segregate, the second SLB would still show gel-phase domains. The first bilayer appeared dimmer in areas that overlapped with the liquid disordered phase of the second bilayer. Image contrast has been adjusted to facilitate the visualization of the overlapping patterns in the stacked lipid bilayers.

3.4 Conclusions

In conclusion, we have demonstrated a simple bottom-up approach to pattern stacked supported lipid bilayers using bilayer-by-bilayer deposition together with polymer stencil lift-off. Mobile SLBs were successfully stacked through electrostatic interactions between cationic and anionic lipids. This technique allowed patterning of both homogeneous and phase-segregated

stacked SLB with controlled number of bilayers and lipid compositions under aqueous conditions. We have demonstrated stacked SLB pattern formation with up to four bilayers consisting of all-homogeneous bilayers, phase-segregated on homogeneous bilayers, and phase-segregated on phase-segregated bilayers. The formation of patterned SLB stacks could be monitored through quantitative fluorescence microscopy. In addition, the fast fluorescence recovery in FRAP tests confirmed the good mobility of each stacked bilayer. For all patterned stacked SLBs, interactions between neighboring bilayers could be observed through fluorescence resonance energy transfer between the dye molecules embedded in each bilayer. Furthermore, a study of lipid behavior in neighboring bilayers showed that phase-segregated domains align across the stack, provided the underlying membrane is fully mobile. We anticipate that the proposed stacked SLB patterning approach will be useful tool for biophysical studies of biomembrane and membrane-associated proteins. With the ability to control the number of bilayers in a stack, the multilamellar bilayer model could be an excellent platform for integrating transmembrane proteins, as it would prevent protein denaturation. Such a system can overcome the low fluidity, which arises in single SLBs due to the close proximity to the substrate, by increasing the distance between the top lipid bilayer and the substrate without modifying the lipid or introducing additional polymer layers. The ability to pattern stacked SLBs at the micron scale could also contribute to studying cell behaviour in vitro, because the patterns can be used to mimic cell microenvironments providing tunable substrate stiffness and adjustable biological components. The micropatterned multiple lipid bilayers are expected to be further applicable in building functional lipid-based devices for cell sensing and drug screening, where changes in bilayer stack thickness or order can be explored in a controlled environment.

3.5 Experimental Section

3.5.1 Materials

1,2-dioleoyl-sn-glycero-3-phosphocholine, chloride salt, (DOPC), 1,2-dioleoyl-3-trimethylammonium-propane, chloride salt, (DOTAP), 1,2-dimyristoyl-sn-glycero-3-phospho-L-serine, sodium salt, (DMPS) 1,2-dioleoyl-sn-glycero-3-phospho-L-serine, sodium salt (DOPS) and 1,2-distearoyl-sn-glycero-3-phosphocholine (DSPC) were purchased from Avanti Polar Lipids (Alabaster, AL). Lissamine Rhodamine B 1,2-dihexadecanoyl-sn-glycero-3-phosphoethanolamine, triethylammonium Salt (DHPE-LR) and Oregon Green 488 1,2-dihexadecanoyl-sn-glycero-3-phosphoethanolamine (DHPE-OG) were purchased from Life Technologies (Carlsbad, CA). Parylene-C was obtained from Specialty Coating Systems (Indianapolis, IN). Sodium hydroxide, 10× phosphate buffered saline (PBS) solution (which was diluted to 1× for buffer use), hydrochloric acid, hydrogen peroxide (30%), sulfuric acid (40%) and ammonium hydroxide (27%) were acquired from Caledon Laboratories (Georgetown, Canada). L-ascorbic acid was obtained from Sigma-Aldrich (Saint Louis, MO). Deionized water (18.2 MΩ·cm) was obtained from a Millipore Milli-Q Purification System (Millipore, Billerica, MA).

3.5.2 Methods

3.5.2.1 Microfabrication of Parylene Stencils

SiO_2 (100 nm thermal oxide) on Si <100> wafers were cleaned in piranha solution (sulfuric acid:hydrogen peroxide 3:1 v/v) for 10 minutes, followed by two successive 5-minute rinses in Milli-Q water, and then dried under a nitrogen stream. Then an ~800nm thick Parylene film was deposited onto the clean wafers through chemical vapor deposition in a Labcoater 2000 Parylene deposition system (SCS, Indianapolis, IN). S1808 positive photoresist (Shipley, Marlborough, MA) was spin-coated on the Parylene-coated substrates at 2500 rpm for 30 seconds to obtain a

nominal resist thickness of 1.1 μm, and then baked at 90 °C for 2 minutes. A chrome photo mask with 2-200 μm features (fabricated by Fineline Imaging Company, Colorado Springs, CO) was used in the patterning process. Photolithography was performed in soft-contact mode using a Karl Suss MJB3 contact aligner (UV wavelength 365 nm, Karl Suss, Garching, Germany), with exposure energy of 30 mJ. The samples were developed in Microposit 351 developer (Shipley, Malborough, MA) for 25 seconds to remove the exposed photoresist, and then rinsed in Milli-Q water and dried under a nitrogen stream. Exposed regions of the Parylene film were reactive ion etched in an oxygen plasma chamber (Technics, Series 800, Arlington, TX) for 9 minutes at 30 sccm O_2, 100W. Residual photoresist was removed by washing successively with acetone, isopropanol and Milli-Q water. To remove any remaining Parylene residue within the etched openings, the etched substrates were treated in a UV/O_3 cleaner and further cleaned in an alkaline solution. Various UV/base conditions were tested, from which it was determined that one minute UV/O_3 cleaning (10 mW/cm^2, 254 nm), followed by 1 minute soaking in 100 mM sodium hydroxide solution provided the optimal surfaces for SLB formation. After this treatment, substrates were soaked in Milli-Q water for 1 minute and dried under a nitrogen stream. Prior to use in lipid bilayer patterning, all the substrates were cleaned in a plasma chamber (Harrick, Ithaca, NY) for 60 seconds at high power using an air flow rate of 30 sccm.

3.5.2.2 Preparation of Small Unilamellar Vesicle Solutions

Small unilamellar vesicle (SUV) solutions of different compositions were all prepared through the vesicle extrusion method. The lipids dissolved in chloroform were mixed at the desired ratios to ensure a homogeneous mixture of the lipids. Afterwards, the chloroform was removed by rotatory evaporation using a stream of nitrogen to produce dry lipid films, and then any remaining solvent was evaporated under vacuum overnight. The lipid films were hydrated with the required

volume of 1× PBS until the lipid films completely resuspended forming a cloudy solution containing large multilamellar vesicles (LMV) of various sizes. The LMV solutions were pre-filtered through a 0.45 μm pore polyethersulfone filtering membrane to remove impurities and reduce the vesicle size. Then, the solutions were then extruded 10 times through a 100 nm pore polycarbonate membrane filter (Whatman, Maidstone, UK) using a mini-extruder (Avanti Polar Lipids, Alabaster, AL). This resulted in clear solution containing SUVs of approximate 100 nm diameter. Lipid compositions are expressed as molar ratios. The solutions used for these experiments were 1 mM DOPC:DOTAP:DHPE-OG (90:10:0.1), 1mM DOPC:DMPS:DHPE-LR (90:10:0.1), 1mM DOPC:DSPC:DOPS:DHPE-LR (80:10:10:0.1) and 1mM DOPC:DSPC:DOTAP:DHPE-OG (80:10:10:0.1).

3.5.2.3 Formation of Stacked Supported Lipid Bilayers

Supported lipid bilayers were formed by applying the SUV solution onto the substrate surface. Prior to SLB formation, the wafers with Parylene stencils on top were air plasma cleaned for 1 minute using the Expanded Plasma Cleaner & PlasmaFlo (Harrick, Ithaca, NY) to remove adsorbed impurities and increase the number of silanol groups providing a more negatively charged surface for better electrostatic interactions with the charged lipids. Afterwards, 0.2 mM lipid SUV solution of interest was deposited on the micropatterned surfaces and incubated under appropriate conditions until a uniform SLB formed. The incubation temperatures were set higher than the transition temperatures of the lipids in the solution to ensure all lipids are at the liquid phase. The homogenous SLBs were prepared by incubating the appropriate SUV solutions on the patterned substrates for 60 minutes at 30°C, while phase-segregated SLBs were prepared by incubating the appropriate SUV solutions for 30 min at 60°C. In order to remove excess lipid vesicles, the surface was carefully washed three times with 1× PBS (pH=6) supplemented with 5

mM ascorbic acid, followed by another three washes with 1× PBS (pH=9) supplemented with 5 mM ascorbic acid. Both the ascorbic acid and PBS buffer at pH 9 were used to reduce the rate at which the DHPE-OG fluorophore bleaches for better imaging and analysis with the fluorescence microscope. The formed SLBs were then allowed to cool to room temperature. For both the multi-layer phase-segregated and homogeneous SLB, the Parylene stencil was removed after the formation of all the layers and right before the characterization was conducted.

3.5.2.4 Mobility and Intensity Characterization by Fluorescence Microscopy

The distinctive bilayers were imaged using a Nikon Eclipse LV100N POL epifluorescence microscope (Nikon Instruments, Mississauga, ON.) equipped with excitation and emission filters for Oregon Green or Lissamine Rhodamine dyes, and an UMPLNFL 20×/0.5NA objective. Images were acquired with a Retiga 2000R cooled CCD camera (QImaging, Surrey, BC) and recorded with software NIS-Elements AR (Nikon, Tokyo, Japan).

Fluorescence recovery after photobleaching (FRAP) was used for SLB mobility tests in all the experiments. This technique began by saving an image of the sample before photobleaching. The light source was then briefly focused onto a small area of the SLB. The fluorophores in this region received high intensity illumination and bleached quickly, leaving a dark region behind. The sample fluorescence was monitored at subsequent time intervals. As diffusion proceeded, the bright molecules diffused into the bleached region. So the fluorescence could recover after a while, demonstrating that the lipids retained their fluidity on the substrates.

The fluorescence intensity for each of the four layers in the multilamellar homogeneous SLB was measured and compared to prove the presence of each lipid bilayer. The intensity profiles were obtained for five different micropatterned areas on each layer using the NIS Elements software, and the average intensity was calculated for comparison. The parameters used for

acquiring pictures of green fluorophore (DHPE-OG) labeled layers were 3.0 gain and 100 ms exposure time; while for the bilayers containing the red fluorophore (DHPE-LR), the parameters were set to 5.0 gain and 100 ms exposure time. However for the phase-segregated layer labeled with LR dye, the exposure time was 50 ms.

3.6 Acknowledgments

This work was supported through the Natural Sciences and Engineering Research Council (RGPIN/418326) and the Canada Foundation for Innovation Leaders Opportunity Fund. JMM is the recipient of an Early Researcher Award through the Ontario Ministry of Research and Innovation. YZ was partially supported by the Interdisciplinary Development of Extracellular Matrices Collaborative Research Training Program. This research made use of facilities at the Centre for Emerging Device Technology at McMaster University.

3.7 References

(1) Tayebi, L.; Ma, Y.; Vashaee, D.; Chen, G.; Sinha, S. K.; Parikh, A. N. Long-Range Interlayer Alignment of Intralayer Domains in Stacked Lipid Bilayers. *Nat. Mater.* **2012**, *11* (12), 1074–1080.

(2) Rand, R. P.; Parsegian, V. A. Hydration Forces between Phospholipid Bilayers. *Biochim. Biophys. Acta* **1989**, *988* (3), 351–376.

(3) Chu, N.; Kučerka, N.; Liu, Y.; Tristram-Nagle, S.; Nagle, J. F. Anomalous Swelling of Lipid Bilayer Stacks Is Caused by Softening of the Bending Modulus. *Phys. Rev. E* **2005**, *71* (4), 41904.

(4) Bechinger, B.; Resende, J. M.; Aisenbrey, C. The Structural and Topological Analysis of Membrane-Associated Polypeptides by Oriented Solid-State NMR Spectroscopy: Established Concepts and Novel Developments. *Biophys. Chem.* **2011**, *153* (2-3), 115–125.

(5) Minner, D. E.; Rauch, P. Polymer-Tethered Lipid Multi-Bilayers: A Biomembrane-Mimicking Cell Substrate to Probe Cellular Mechano-Sensing. *Soft Matter* **2014**, *10*, 1189–1198.

(6) Joo, K. Il; Xiao, L.; Liu, S.; Liu, Y.; Lee, C. L.; Conti, P. S.; Wong, M. K.; Li, Z.; Wang, P. Crosslinked Multilamellar Liposomes for Controlled Delivery of Anticancer Drugs.

Biomaterials **2013**, *34* (12), 3098–3109.

(7) Sloan, C. D. K.; Marty, M. T.; Sligar, S. G.; Bailey, R. C. Interfacing Lipid Bilayer Nanodiscs and Silicon Photonic Sensor Arrays for Multiplexed Protein–Lipid and Protein–Membrane Protein Interaction Screening. *Anal. Chem.* **2013**, *85* (5), 2970–2976.

(8) Lautscham, L. a.; Lin, C. Y.; Auernheimer, V.; Naumann, C. a.; Goldmann, W. H.; Fabry, B. Biomembrane-Mimicking Lipid Bilayer System as a Mechanically Tunable Cell Substrate. *Biomaterials* **2014**, *35* (10), 3198–3207.

(9) Kaizuka, Y.; Groves, J. T. Structure and Dynamics of Supported Intermembrane Junctions. *Biophys. J.* **2004**, *86* (2), 905–912.

(10) Gupta, G.; Iyer, S.; Leasure, K.; Virdone, N.; Dattelbaum, A. M.; Atanassov, P. B.; López, G. P. Stable and Fluid Multilayer Phospholipid-Silica Thin Films: Mimicking Active Multi-Lamellar Biological Assemblies. *ACS Nano* **2013**, *7* (6), 5300–5307.

(11) Murray, D. H.; Tamm, L. K.; Kiessling, V. Supported Double Membranes. *J. Struct. Biol.* **2009**, *168* (1), 183–189.

(12) Chung, M.; Lowe, R.; Chan, Y.-H. M.; Ganesan, P. V; Boxer, S. G. DNA-Tethered Membranes Formed by Giant Vesicle Rupture. *J. Struct. Biol.* **2009**, *168* (1), 190–199.

(13) Johnson, M. A.; Naumann, C. A. Iterative Layer-by-Layer Assembly of Polymer-Tethered Multi-Bilayers Using Maleimide–thiol Coupling Chemistry. *Soft Matter* **2013**, 9643–9650.

(14) Taylor, P.; Xu, C.; Fletcher, P. D. I.; Paunov, V. N. Fabrication of 2D Arrays of Giant Liposomes on Solid Substrates by Microcontact Printing. *Phys. Chem. Chem. Phys.* **2003**, *5* (21), 4918.

(15) Berre, L.; Chen, Y.; Baigl, D.; Diguet, A. Preparation of Phospholipid Multilayer Patterns of Controlled Size and Thickness by Capillary Assembly on a Microstructured Substrate. **2009**, 1661–1666.

(16) Lenhert, S.; Sun, P.; Wang, Y.; Fuchs, H.; Mirkin, C. a. Massively Parallel Dip-Pen Nanolithography of Heterogeneous Supported Phospholipid Multilayer Patterns. *Small* **2007**, *3* (1), 71–75.

(17) Lenhert, S.; Brinkmann, F.; Laue, T.; Walheim, S.; Vannahme, C.; Klinkhammer, S.; Xu, M.; Sekula, S.; Mappes, T.; Schimmel, T.; et al. Lipid Multilayer Gratings. *Nat. Nanotechnol.* **2010**, *5* (4), 275–279.

(18) Nafday, O. a.; Lowry, T. W.; Lenhert, S. Multifunctional Lipid Multilayer Stamping. *Small* **2012**, *8* (7), 1021–1028.

(19) Ilic, B.; Craighead, H. G. Topographical Patterning of Chemically Sensitive Biological Materials Using a Polymer-Based Dry Lift Off. *Biomed. Microdevices* **2000**, *2* (4), 317–322.

(20) Meyer, G. D.; Morán-Mirabal, J. M.; Branch, D. W.; Craighead, H. G. Nonspecific Binding

Removal from Protein Microarrays Using Thickness Shear Mode Resonators. *IEEE Sens. J.* **2006**, *6* (2), 254–261.

(21) Moran-Mirabal, J. M.; Tan, C. P.; Orth, R. N.; Williams, E. O.; Craighead, H. G.; Lin, D. M. Controlling Microarray Spot Morphology with Polymer Liftoff Arrays. *Anal. Chem.* **2007**, *79* (3), 1109–1114.

(22) Luterbacher, J. S.; Moran-Mirabal, J. M.; Burkholder, E. W.; Walker, L. P. Modeling Enzymatic Hydrolysis of Lignocellulosic Substrates Using Confocal Fluorescence Microscopy I: Filter Paper Cellulose. *Biotechnol. Bioeng.* **2015**, *112* (1), 21–31.

(23) Tan, C. P.; Seo, B. R.; Brooks, D. J.; Chandler, E. M.; Craighead, H. G.; Fischbach, C. Parylene Peel-off Arrays to Probe the Role of Cell-Cell Interactions in Tumour Angiogenesis. *Integr. Biol.* **2009**, *1* (10), 587–594.

(24) Moran-Mirabal, J. M.; Edel, J. B.; Meyer, G. D.; Throckmorton, D.; Singh, A. K.; Craighead, H. G. Micrometer-Sized Supported Lipid Bilayer Arrays for Bacterial Toxin Binding Studies through Total Internal Reflection Fluorescence Microscopy. *Biophys. J.* **2005**, *89* (1), 296–305.

(25) Orth, R. N.; Kameoka, J.; Zipfel, W. R.; Ilic, B.; Webb, W. W.; Clark, T. G.; Craighead, H. G. Creating Biological Membranes on the Micron Scale: Forming Patterned Lipid Bilayers Using a Polymer Lift-off Technique. *Biophys. J.* **2003**, *85* (5), 3066–3073.

Chapter 4 Bench-Top Fabrication of Hierarchically Structured High Surface Area Electrodes

Yujie Zhu and Jose M. Moran-Mirabal developed the benchtop fabrication strategy for patterning gold films on pre-stressed polystyrene sheets using self-adhesive vinyl masks designed and created by craft cutter. They also introduced the thermal shrinking process of patterned polystyrene which resulted in sub-millimetre sized pattern features and micro/nanostructured surfaces. They optimized the fabrication conditions and characterized the surfaces roughness of gold films. Chrinstine M. Gabardo and Leyla Soleymani implemented this fabrication strategy to create high-surface-area electrodes, and further created nano-sized structures through gold electrochemical deposition. They characterized the electrical and electrochemical properties of these electrodes, and demonstrated their suitability for electrochemical sensing. Yujie Zhu optimized the vinyl stencil lift-off and polystyrene thermal shrinking process, and film surface roughness measurements. Christine M. Gabardo conducted the electrical measurements, the electrochemical measurements and electrodepostion. All the authors participated in writing the manuscript.

4.1 Abstract

Fabrication of hierarchical materials - with highly optimized features from the millimeter to the nanometer scale - is crucial to applications in diverse areas including biosensing, energy storage, photovoltaics, and tissue engineering. In the past, complex material architectures have been achieved using a combination of top-down and bottom-up fabrication approaches. A remaining challenge, however, is the rapid, inexpensive, and simple fabrication of such materials systems using bench top prototyping methods. To address this challenge, we develop and

investigate the properties of hierarchically structured electrodes by combining three bench top techniques: top-down electrode patterning using vinyl masks created by a CAD-driven cutter, thin film micro/nanostructuring using a shrinkable polymer substrate, and tunable electrodeposition of conductive materials. By combining these methods, controllable electrode arrays have been created with features in three distinct length scales: 40 μm - 1 mm, 50 nm - 10 μm, and 20 nm - 2 μm. We analyze the electrical and electrochemical properties of these electrodes and demonstrate that they are excellent candidates for next generation low-cost electrochemical and electronic devices.

4.2 Introduction

Recently, there has been increased interest in fabricating hierarchical materials with morphologies tunable in the micron to nanometer scale. Natural hierarchical materials - optimized over multiple length scales through evolution to answer specific functional demands - have inspired the synthesis of hierarchical materials with unique characteristics unparalleled by bulk materials.[1,2] The properties of such materials can be tuned for specific applications by adjusting the material composition, geometry, and size of the structured features. In photovoltaic and photo-electrochemical energy conversion devices, hierarchically branched nanowires enable considerable improvement in light absorption efficiency due to enhanced surface area and light scattering properties.[3,4] Hierarchical structures have also found wide application as tissue engineering scaffolds because they mimic the multi-scale features found in biological niches, which not only offer structural support but also provide the microenvironment needed for cell proliferation.[5–7] In drug delivery, hierarchically-structured dendrimers are tuned to provide the required geometry, size, and surface chemical functionality to entrap or transport small drug molecules.[8,9] Similarly, the integration of high surface area hierarchical structures on sensing

electrodes dramatically improves the speed and sensitivity of electrochemical biosensors.[10–13] These applications highlight the potential that hierarchically structured materials present in the development of functional devices.

Various methods for the fabrication of hierarchical materials have been developed, such as multilayer photolithography,[14] electron-beam lithography,[15] templated self assembly,[16] and soft lithography.[17] While these methods have been used to create nature-inspired hierarchical materials, they often need to be combined in order to span the entire millimeter to nanometer length scale. As a result, they rely on at least one step that requires a mask, template, or a master that cannot be rapidly fabricated in the laboratory. Thus, it remains a major challenge to develop such materials systems using simple laboratory processes and to implement the entire process - from design to fabrication - in timescales from minutes to hours.

A facile and quick approach has been recently developed to fabricate micro- and nanostructured materials, which takes advantage of the thermal shrinking of pre-stressed polymer films, such as polystyrene (PS),[18] polyolefin (PO),[19] and polyethylene.[5] Printing onto PS substrates and shrinking has been used to generate micropatterned templates, which allowed the fabrication of rounded microfluidic channels with critical dimensions as small as 65 μm.[20] Through this shrinking approach, Fu and collaborators also created uniaxial and biaxial wrinkles on gold-coated PS sheets. They demonstrated that the wrinkle wavelength could be tuned by adjusting the thickness of the metal film.[18] More recently, the shrinking approach has been applied to create micro and nanoscale structures with cross-linked PO thin films, which exhibited larger shrinking ratios (up to 95%) and greater shrinking uniformity than PS substrates.[5] These shrinking methods offer an attractive route to the fast, easy and inexpensive bench top fabrication of micro- and nanostructured devices, which can aid in the development of functional microdevices.

In this manuscript we present a method combining millimeter patterning through vinyl masking, micrometer stress-driven wrinkling, and nanometer electrodeposition for the controlled fabrication of electrodes with hierarchical structures spanning multiple length scales. This process offers speed, ease of fabrication and cost-effectiveness in producing micro- and nanostructured surfaces. In addition, we show that electrodes fabricated in this fashion display excellent conductive and electrochemical properties, and can be used to monitor charge transfer and reduction/oxidation reactions. Furthermore, the hierarchically structured electrodes exhibited electroactive surface area enhancements in excess of 1000% when compared to flat electrodes. Altogether these results show that our approach to structuring conductive surfaces produces high surface area electrodes that can be incorporated into a variety of microdevices. This newly developed method could facilitate the design and prototyping of tunable material systems applicable to the fabrication of low-cost biosensing, bioprocessing, tissue engineering and photovoltaic devices.

4.3 Results and Discussion

4.3.1 Quick Prototyping of Patterned Electrodes

Bench top fabrication techniques offer capabilities to prototype devices in a quick, facile and cost-effective manner. In particular, the ability to rapidly fabricate and test electrodes in a variety of configurations, shapes, and sizes ranging from the millimeter to the micrometer scale, could prove valuable in the development of new sensing electrode architectures for functional devices. To produce patterned electrodes with designed shapes and sizes, we have combined two bench top fabrication techniques: vinyl film masking and pre-stressed polystyrene (PS) sheet shrinking. The fabrication steps followed to produce patterned thin gold electrodes using the vinyl masking and

PS shrinking approach are depicted in Figure 4-1a. Self-adhesive vinyl film was employed as a masking material not only because of its ease of use, ability to bind to a wide range of materials, ease of removal without leaving adhesive residue behind, and adequate resistance to solvents and mild acidic conditions, but also because it can be effectively patterned using a bench top craft cutter. To produce the pattern masks, self-adhesive vinyl films (red film, Figure 4-1a) were bound to clean PS sheets (black sheet, Figure 1a) and flattened using a roller. Patterns designed in a CAD program were then scored into the vinyl film bound to the PS sheets using a craft cutter. The optimization of the force, speed and acceleration with which the blade cut into the vinyl film allowed us to obtain parallel line cuts with spacings as small as 100 μm (limited by the step size of the cutter motor) and circular features with diameters as small as 200 μm (limited by the turning radius of the blade). The optimized parameters also ensured that the blade did not cut into the underlying PS sheet, which would introduce undesired topography in the final electrodes. The cut out vinyl was peeled-off using rounded tip tweezers to avoid scratching the underlying PS surface. Peeling the vinyl with a uniform force applied parallel to the thinnest features prevented tearing of the vinyl and ensured that it was removed as a continuous film. Once the desired pattern was exposed, a thin gold coating of controlled thickness (20-200 nm) was sputtered onto the devices. Finally, the remaining vinyl mask was lifted-off to reveal a patterned electrode on the PS sheet (Figure 4-1a). Occasional tearing, similar to that obtained in resist lift-off processes, could be observed after the vinyl lift-off in SEM images taken from the edges of thick gold films (Supplemental Figure 1). This patterning approach allowed us to quickly produce electrodes with various shapes and sizes (Figure 4-1b) and with different film thicknesses (Figure 4-1c). Although for this study we report on the patterning of gold films, the same approach can be used to produce patterns of a number of different conducive, semiconductive and insulating thin films.

The size of the gold patterns was reduced through biaxial shrinking of the PS substrate to generate electrodes with features as small as 80 micrometers. When heated above their glass transition temperature of 100°C,[21] pre-stressed PS sheets have the ability to shrink to under 50% of their original size due to polymer chain relaxation. We have taken advantage of this effect to reduce the dimensions of the features on our patterned gold films. PS sheets containing patterned gold films of thicknesses ranging from 20 to 200 nanometers were heated at 130 and 160°C and their shrinking behaviors were characterized. The higher temperature shrunk the devices significantly faster (full shrinking in 2 minutes) than the lower one (full shrinking in 10 minutes). It was observed that at both temperatures the shrunken PS sheets and the patterned gold films retained their original overall shape and that shrinking was highly reproducible (Figure 4-1c) if heat transfer to the PS sheet was uniform. Yet, slight differences were noted between the devices shrunken at the two temperatures. It was noted that devices shrunk at 160°C reached transverse dimensions that were ~38% of the original size, while those shrunk at 130°C only reached ~40% (Figure 4-1d). Conversely, the devices shrunk at 160°C reached ~700% of their original thickness, while those shrunk at 130°C reached only ~650% of their original value (Figure 4-1e). These small differences are most likely due to the higher fluidity of the PS chains at higher temperatures, as well as the more rapid relaxation of the strain in the pre-stressed film during the shrinking process. Finally, it was also observed that the shrinking process induced the gold films to become more firmly attached to the PS substrates, as shrunken films could not be removed from the surface by the scotch tape peeling test (5 successive peels), but they could be partially removed in unshrunken devices. The increase in adhesive strength has been previously observed[18] and is attributed to the fact that at elevated temperatures the shrinking PS surface becomes soft enough to integrate with the metallic film. Thus, the combination of patterning gold films through vinyl masking and

shrinking of the underlying PS substrates has enabled us to quickly produce robust gold electrodes with critical dimensions as small as 80 micrometers in a reproducible fashion.

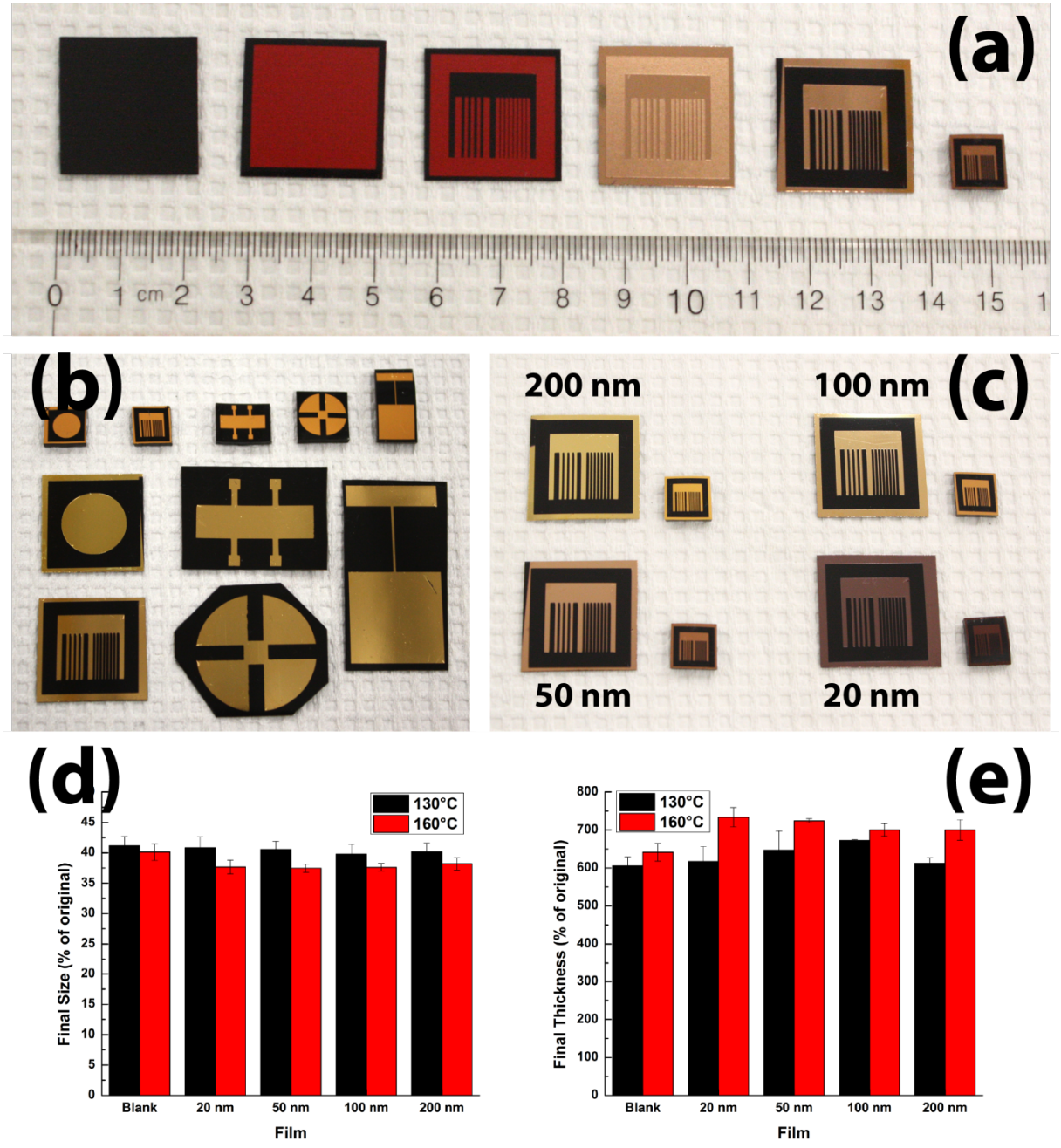

Figure 4-1 Bench top fabrication techniques can be used to produce patterned electrodes with critical dimensions < 100 μm. (a) Depiction of the fabrication of patterned electrodes through vinyl masking and pre-stressed PS substrate shrinking (from left to right: clean polystyrene, apply vinyl film, cut out designed shape, deposit gold film, lift off

vinyl stencil, thermal shrinking). (b) The bench top approach developed allows the fabrication of patterned electrodes with a wide variety of geometrical shapes. (c) Patterned electrodes were fabricated from a variety of gold film thicknesses. Shrinking of the patterned electrodes at 130 and 160°C was highly reproducible, with (d) final transverse dimensions ~40% of the original size and (e) axial dimensions ~650% of the original size.

4.3.2 Stress-Driven Micro and Nanostructuring of Gold Electrodes

The surfaces of the crumple-structured gold films were characterized through white light interferometry to assess their roughness. Interferometry is a powerful technique that allows the measurement of surface height differences based on fringes, which arise from the interference between a reference and a measuring light beam. The pixel size of the interferometer camera used to image the surfaces was equivalent to 112 nm, which meant that the best lateral resolution that could be achieved was ~200 nm. While this prevented measuring the nanoscale structure of the thinnest wrinkled films with the same resolution as that of the electron microscope, our measurements revealed significant trends. Interferometry images showed that all crumple-structured films had similar overall surface features with islands of high elevations surrounded by valleys of lower height (Figure 4-3 a-b). Although the surface structures looked similar, their heights were significantly different. As figures of merit we chose to characterize the surfaces using their root mean square (RMS) roughness, which indicates the average deviation from the baseline, and the peak-valley spread (PV), which is calculated as the height difference between the highest and the lowest points and reports on the range of height measurements.

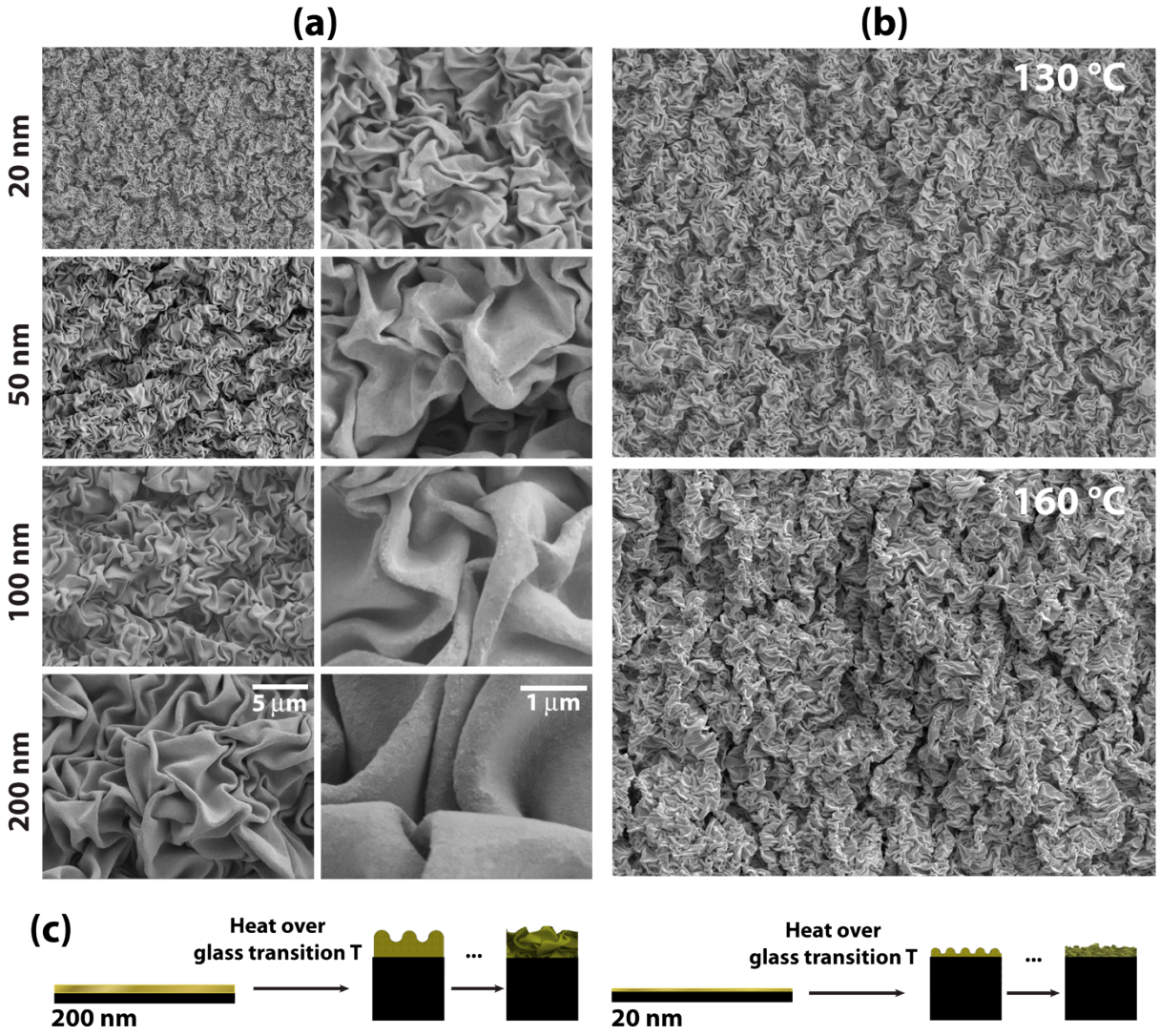

Figure 4-2 Shrinking of the polystyrene substrate causes an adhered gold film to buckle and wrinkle. (a) The size of the resulting wrinkles depends strongly on the film thickness. (b) The shrinking temperature also affects the wrinkling process, with higher temperatures producing rougher surfaces. (c) Schematic depiction of the stress-driven wrinkling of gold films.

All the crumple-structured gold surfaces exhibited RMS surface roughness values that were higher than that of the shrunken PS sheet alone (19 and 23 nm for sheets shrunken at 130 and 160°C). The RMS roughness for crumple-structured films ranged from 250 nm for 20 nm thick films shrunken at 130°C, to 1200 nm for 200 nm thick films shrunken at 160° (Figure 4-3c). The

increase in surface roughness was directly correlated with increasing film thickness. This is to be expected, as the thicker films are less pliable and do not buckle as easily during the shrinking step. In addition, we observed that the surface roughness was significantly higher for films shrunken at 160°C as compared with those shrunken at 130°C. These differences confirm our observations from SEM images, where the films shrunken at the higher temperature seemed to have deeper valleys and higher peaks. The PV values for crumple-structured films ranged from ~2 μm, for 20 nm films shrunken at 130°C, to ~12 μm, for 200 nm films shrunken at 160°C, and were also significantly higher than those for shrunken PS sheets alone (ca. 450 nm for films shrunken at both temperatures). The PV followed a similar trend to that observed for the RMS roughness, with increasing PV values for increasing films thickness and higher PV values for films shrunken at 160°C (Figure 4-3d). The characterization of the crumple-structured thin films through interferometry demonstrates that the gold electrodes fabricated through vinyl masking and PS sheet shrinking have surfaces that are significantly roughened, and that this surface roughness can be controlled by the choice of film thickness and shrinking temperature.

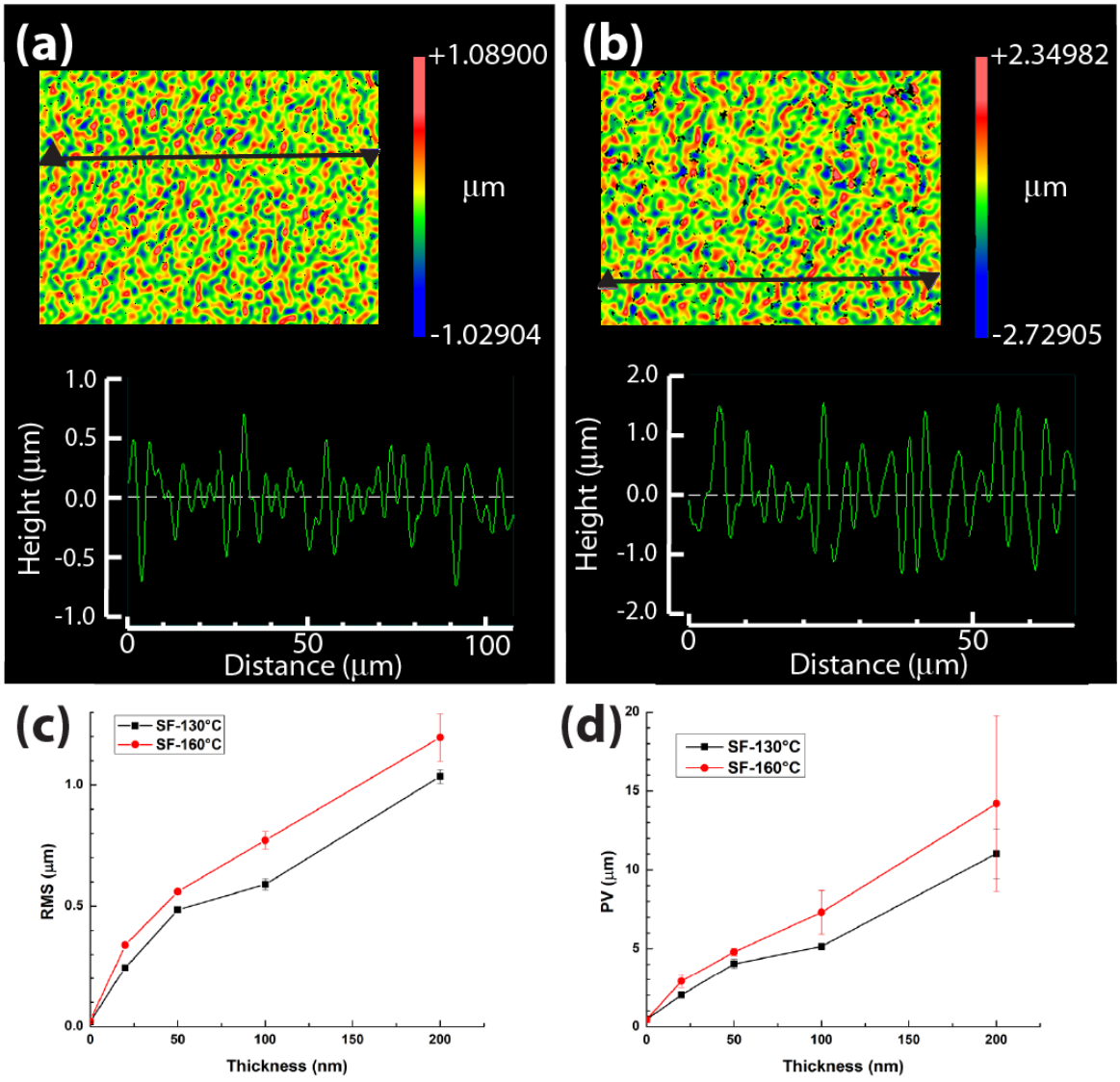

Figure 4-3 White light interferometry was used to characterize the surface roughness of crumple-structured gold films. (a) Sample interferometry image and line profile for a 20 nm thick crumpled film. (b) Sample interferometry image and line profile for a 100 nm thick crumpled film. Comparison of (c) RMS roughness and (d) PV spread for crumple-structured films fabricated at 130 and 160°C. Error bars represent the standard deviation of replicate measurements performed on the structured films (n > 3).

The increased surface roughness of the micro- and nanostructured films also influenced their wettability. To characterize the wettability of the patterned gold films we measured the contact angles of water droplets on the films before and after shrinking of the underlying PS substrate

(Supplemental Figure 3). The contact angle of unshrunken gold films of all thicknesses was statistically equal with a value ~65°, and close to that of unshrunken PS film, which was 70°. Upon shrinking, all the micro- and nanostructured films had increased contact angles, ranging from 104° for 20 nm thick shrunken films, and increasing with thickness to a plateau value close to 120° for 100 and 200 nm thick films. In comparison, the contact angle for the shrunken PS sheets was ~90°. The increase in contact angle is a direct result of the structured surface and can be understood in terms of the crevices and clefts that are inaccessible to water, resulting in a Cassie or mixed Cassie-Wenzel wetting pattern.[31] These results show that the wettability of gold surfaces can be tailored by controlling the size of the structures induced by the shrinking of the underlying PS substrate. The ability to tailor the wettability of thin film surfaces has attracted much attention, as it can lead to applications such as self-cleaning coatings. The ease with which these structured surfaces are fabricated makes them attractive for the development of multiplexed biosensors and microfluidic devices that exploit the hydrophobic nature of the structured films to integrate multiple samples on a single substrate.

4.3.3 Electrochemical Characterization of Electrodes Patterned on PS Sheets

Electrical and electronic devices created on polymeric substrates hold great potential in next generation display,[32] chemical and biological sensing,[33] and photovoltaic[34] technologies because their mechanical flexibility and light weight is complemented with rapid and cost-effective manufacturing. In addition, reproducibility in conductivity, electron transfer kinetics, surface area, and electrochemical activity are essential to material systems used in electrochemical sensing. To assess the suitability of metallic films patterned on PS sheets as functional electrodes, we used cyclic voltammetry (CV) to compare the electrochemical behavior of two sets of devices: patterned electrodes on glass substrates and patterned electrodes on unshrunken PS sheets (Supplemental

Figure 4). Self-adhesive vinyl masks with a square cutout were immobilized on the devices to ensure that the electrodes fabricated on glass and PS substrates exposed the same geometric gold surface area (Supplemental Figure 4a). CV curves of unshrunken PS devices measured in sulfuric acid solutions displayed a well-defined redox signature associated with the oxidation of gold and the subsequent reduction of gold oxide, which compared favorably to the voltammograms obtained from electrodes fabricated on glass (Supplemental Figure 4b). It was observed that the unshrunken PS devices exhibited a slightly lower electroactive surface area than their glass counterparts exposing the same geometric area, as estimated from the integrated charge contained in the reduction peak of CV scans acquired in H_2SO_4 solutions. We attribute the reduced electroactive surface area to irregularities on the PS substrate surface, which is rougher than the flat polished glass, and to the fabrication conditions where the sputtering of the gold film onto the PS substrates heats the polymer enough that it can partially mix with the metal being deposited. CV curves from PS devices were also obtained in solutions containing the redox complex potassium ferrocyanide. The CV curves taken from unshrunken PS devices exhibited well-defined oxidation and reduction peaks associated with the redox couple ferrocyanide/ferricyanide, which also compared favorably to the voltammograms obtained from devices fabricated on glass (Supplemental Figure 4c). Analysis of the CV curve characteristics showed that PS devices exhibit redox potentials and peak shapes that closely match those of glass devices and do not display any undesired background electrochemical activity. In addition, PS devices demonstrated exceptional device-to-device reproducibility as the variations in peak potentials and peak currents observed were less than 1% and 8% respectively (Supplemental Figure 4d). Altogether these experiments show that devices fabricated on PS substrates exhibit electrochemical behavior that closely resembles that of devices fabricated on glass, making them suitable for electrochemical device fabrication.

4.3.4 Electrical and Electrochemical Properties of Crumple-Structured Electrodes (CSEs)

Tunable high surface area inorganic materials are important to many scientific and industrial applications including catalysis, sensing, separations, and energy storage.[3839] The ability to fabricate micro- and nanostructured surfaces through bench top techniques is an attractive route for the rapid development of high surface area electrodes with tunable characteristics. To demonstrate the suitability of CSEs fabricated through bench top techniques as functional, high surface area electrodes, we conducted a series of measurements of their electrical and electrochemical properties. The continuity and integrity of CSE devices were first evaluated by measuring the sheet resistance of the patterned gold films through the van der Pauw method.[40] The sheet resistance measured for PS devices before shrinking showed decreasing values for increasing gold film thicknesses, with the sheet resistance values tending towards an asymptotic value of 0.28 ohms/square (Supplemental Figure 5). The sheet resistance for the PS devices after shrinking exhibited a similar trend, with CSEs made from thinner films showing higher sheet resistance than those made with thicker films (Supplemental Figure 5). In addition, shrunken devices displayed a significantly lower sheet resistance than their unshrunken counterparts. We hypothesize that the decrease in sheet resistance in CSEs arises from the contact between adjacent creases and folds present on the wrinkled films, which yields a shorter path length for current to travel through and results in a lower effective sheet resistance. The observation that the decrease in sheet resistance after shrinking is more significant for thinner films supports this hypothesis, since SEM images (Figure 4-2) show that wrinkles are more closely packed in thinner films and have a higher probability of contacting adjacent structures. The ability to successfully and reproducibly measure sheet resistance values from devices fabricated on PS substrates demonstrates that the gold films before and after shrinking are continuous and suitable for electrical measurements.

An attractive feature of the wrinkled topography of CSEs is that these devices could present significantly larger active surfaces per projected geometrical area than flat electrodes. To measure the active surface area of CSEs, we quantified the total charge involved in the electrochemical formation of a monolayer of gold oxide (Figure 4-4a). The active areas of PS devices fabricated with different film thicknesses were compared before and after shrinking at temperatures of 130 and 160°C (Figure 4-4 a-b). All unshrunken devices, regardless of film thickness, showed the same electroactive surface area, which was expected as no surface structuring is present and all devices present the same geometrical area. On the other hand, all shrunken devices exhibited significantly larger electroactive surface areas, with enhancements as high as 665% of the area presented by unshrunken devices. This result is readily explained, as the shrinking process crumples the original film into a geometrical area that is ~16% of the original device. Figure 4-4b also shows that the measured electroactive surface area enhancement for shrunken devices is larger for thicker than for thinner film devices processed using identical methods. This supports our hypothesis that coalescence of adjacent wrinkles is more frequent in CSEs fabricated out of thinner films where the wrinkles are more closely packed. Additionally, we observed that the temperature at which the devices were shrunk could influence the resulting electroactive surface area. Figure 4-4b shows that shrinking of 20 nm thick devices at 160°C yielded lower enhancements than shrinking at 130°C, while the enhancement was not statistically different for all other film thicknesses. This observation can be explained by the faster shrinking kinetics at higher temperature, which results in secondary wrinkles (seen in Figure 4-2) that leave some of the primary wrinkles inaccessible to the oxidation process. This effect is more pronounced in thin film devices because the wrinkles formed are more closely packed, and are more easily shielded by secondary wrinkling than in thicker film devices. The results from the characterization of the electroactive surface area of CSEs

demonstrate that the shrinking process is a facile method to create high surface area electrodes where the surface area enhancement can be tuned through experimental parameters such as film thickness and shrinking temperature.

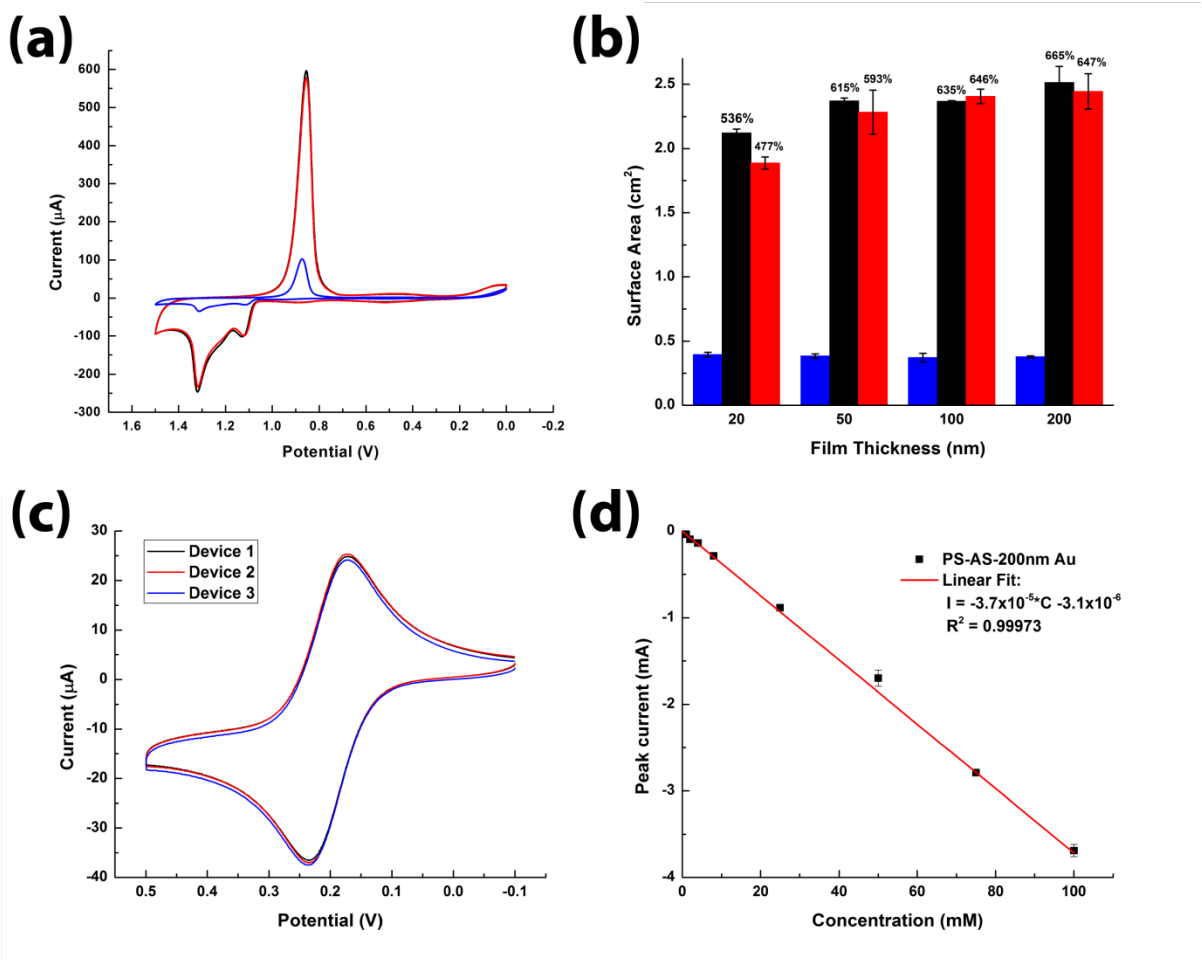

Figure 4-4 Crumple-structured electrodes are suitable devices for electrochemical measurements. (a) A comparison of cyclic voltammograms obtained in dilute acid solutions for electrodes before (blue line) and after shrinking at 130 (black line) and 160°C (red line). (b) Quantification of the charge transferred during the formation of a monolayer of gold oxide reveals significant enhancement of electroactive surface area after shrinking at 130 (black) and 160°C (red), as compared to that of the unshrunken electrodes (blue). (c) Cyclic voltammograms obtained from three different 200 nm CSE devices immersed into a potassium ferrocyanide solution demonstrate the high device-to-device reproducibility. (d) Chronoamperometric measurements performed with 200 nm CSEs immersed into solutions

containing various concentrations of potassium ferrocyanide demonstrate exceptional linearity in sensing the redox complex.

To investigate the possibility of using high surface area CSEs in electrical and electrochemical devices, we assessed their performance and device-to-device reproducibility in electrochemical measurements. CV measurements were conducted with 200 nm thick CSE devices immersed in a 2 mM solution of potassium ferrocyanide. The CV curves generated from these devices showed peak oxidation/reduction currents and reduction/oxidation potentials (Figure 4-4c) that compared favorably with those measured from devices fabricated on glass and unshrunken PS substrates (Supplemental Figure 4 c-d). Furthermore, the CV for three CSE devices tested displayed close to identical curves, with variations in peak redox currents and potentials that were < 1%. Thus, CSEs are suitable for electrochemical measurements and display an extraordinary device-to-device reproducibility, which translates in highly reliable electrodes for electrochemical device applications. Because electrochemical sensing relies on the accurate and quantifiable detection of redox analytes, we further tested the suitability of CSEs fabricated from 200 nm thick films as electrochemical amperometric sensors. The CSEs were used as working electrodes in a three-electrode electrochemical cell and were used to detect increasing concentrations of potassium ferrocyanide. Chrono-amperometric measurements were used to characterize the electrodes' response to the analyte concentration in solution. Figure 4-4d shows that the peak current response is linear and highly reproducible for potassium ferrocyanide concentrations in the 50 μM to 100 mM range, which is in accordance with the Cottrell equation for changes in current due to the diffusion limited oxidation of the target analyte. These electrochemical measurements show that CSEs are suitable for the fabrication of electrochemical devices because they exhibit properties that mimic those of electrodes fabricated on traditional substrates, high device-to-device

reproducibility, and linearity in sensing of electroactive species. CSEs could thus present an attractive alternative for the fabrication of highly sensitive electrochemical sensing devices with applications ranging from toxic gas to biomolecular detection.

4.3.5 Hierarchical Nanostructuring of CSEs through Electrodeposition

Three-dimensional nanostructured electrodes with features in the 10-50 nm range have demonstrated superior sensitivity in detection of biomolecular analytes (*e.g.* nucleic acids and proteins) than materials comprised of larger grains.[11] In an attempt to develop electrodes suitable for biosensing applications, we sought to bring another level of hierarchical structuring to CSEs through electrodeposition. To this end, gold was electrodeposited from a solution containing $HAuCl_4$ and HCl onto flat electrodes and CSE devices fabricated out of 50 nm thick gold films. Our hypothesis was that the folds and creases present on the CSEs would present regions of local electric field enhancement where electrodeposition would occur preferentially. The resulting nanostructures would increase the electrode surface area, making CSEs even more sensitive and suitable for biosensing applications.

Systematic sampling of the electrodeposition parameter space, allowed the controlled formation of sub-50 nm structures on patterned electrode surfaces. Electrodeposition tests were performed on unshrunken devices to compare the effect of variations in the applied potential and in the concentration of $HAuCl_4$ on the shape and size of the electrodeposited gold structures. SEM images of electrodeposition on flat, unshrunken electrodes (Figure 4-5a) show that as the cathodic potential is decreased from -0.2 to -0.3 V, the resulting electrodeposited gold structures shift from hemispherical and cylindrical grains to two-dimensional leaf-like structures, where the leaf's plane lies perpendicular to the electrode. This difference in grain morphology can be explained as a shift from kinetically-controlled to diffusion-controlled electrodeposition. Previously, the

electrodeposition of gold has been categorized as: kinetically controlled at small nucleation overpotentials, mixed kinetically/diffusion controlled at moderate nucleation overpotentials, and diffusion controlled at large nucleation overpotentials.[35] Images of electrodes where the deposition was performed at -0.2 V show hemispherical structures, which are indicative of the radial transport of metal ions associated with mixed kinetically-diffusion controlled electrodeposition. On the other hand, for samples where electrodeposition was performed at -0.3 V the faster reaction kinetics shifted the deposition towards a diffusion-limited regime, where growth instabilities resulted in the formation of irregularly shaped vertical dendrites that coalesced into leaf-like structures as they grew. Furthermore, increasing the concentration of $HAuCl_4$ translated into an increased deposition rate (Supplemental Figure 6), which increased the size of the structures. However, changing the $HAuCl_4$ concentration did not affect the morphology of the deposited structures.

Having established specific electrodeposition parameters for precisely tuning the size and morphology of the deposited structures on flat electrodes, we proceeded to use these conditions to integrate nanostructured morphologies onto CSE devices fabricated from 50 nm thick gold films. To understand the role of the micro/nanostructuring of the CSE materials on the morphology of the electrodeposited gold structures, we compared the SEM images obtained from electrodeposition experiments on un-shrunken and shrunken substrates (Figures 4-5 a-c). Analysis of high magnification images (Figure 4-5b) showed that deposition on CSE devices yielded structures with similar morphology to those deposited on their unshrunken counterparts. However, the structures formed on CSE devices were significantly larger than structures formed on flat substrates under similar electrodeposition conditions. This indicates that although deposition on CSE devices does not change the electrodeposition regime, it influences the growth kinetics of the

deposited structures. Local electric field enhancement[36] along with increased heterogeneous electron transfer kinetics[37] have been previously observed on nanostructured metallic films and are likely responsible for the enhanced deposition rate on CSE devices. The analysis of low-magnification SEM images showed that the deposition of nanostructures on CSE devices was not as homogeneous as the deposition on unshrunken devices. Under all deposition conditions, CSE substrates exhibited regions of nanostructure formation alternating with regions where no significant deposition occurred. The reasons for these differences are unclear, but might be related to the existence of regions that are inaccessible due to poor wetting of the surface by the electrolyte solution.

Nanostructures formed through electrodeposition on the electrode surfaces increased the electroactive surface area of CSE devices. This process is schematically depicted in Figure 4-5d. To quantify the change in surface area induced by the electrodeposited structures, we measured the charge transferred by the electrochemical formation of a monolayer of gold oxide on the modified electrodes. Figure 4-5e summarizes the measured electroactive surface area for devices where electrodeposition was performed under the four conditions pictured in Figures 4-5 a-c. Significant surface area enhancement was only observed for conditions where large structures were formed, namely electrodeposition experiments conducted at 10 mM $HAuCl_4$. The largest enhancement was observed for devices where electrodeposition was performed at -0.3 V and 10 mM $HAuCl_4$, where the final electroactive surface area was ~200% of the surface corresponding to the bare shrunken device and ~1000% of the unshrunken device. The results presented demonstrate that it is possible to increase the electroactive surface area of CSE devices by the controlled growth of nanostructures with different morphologies through electrodeposition.

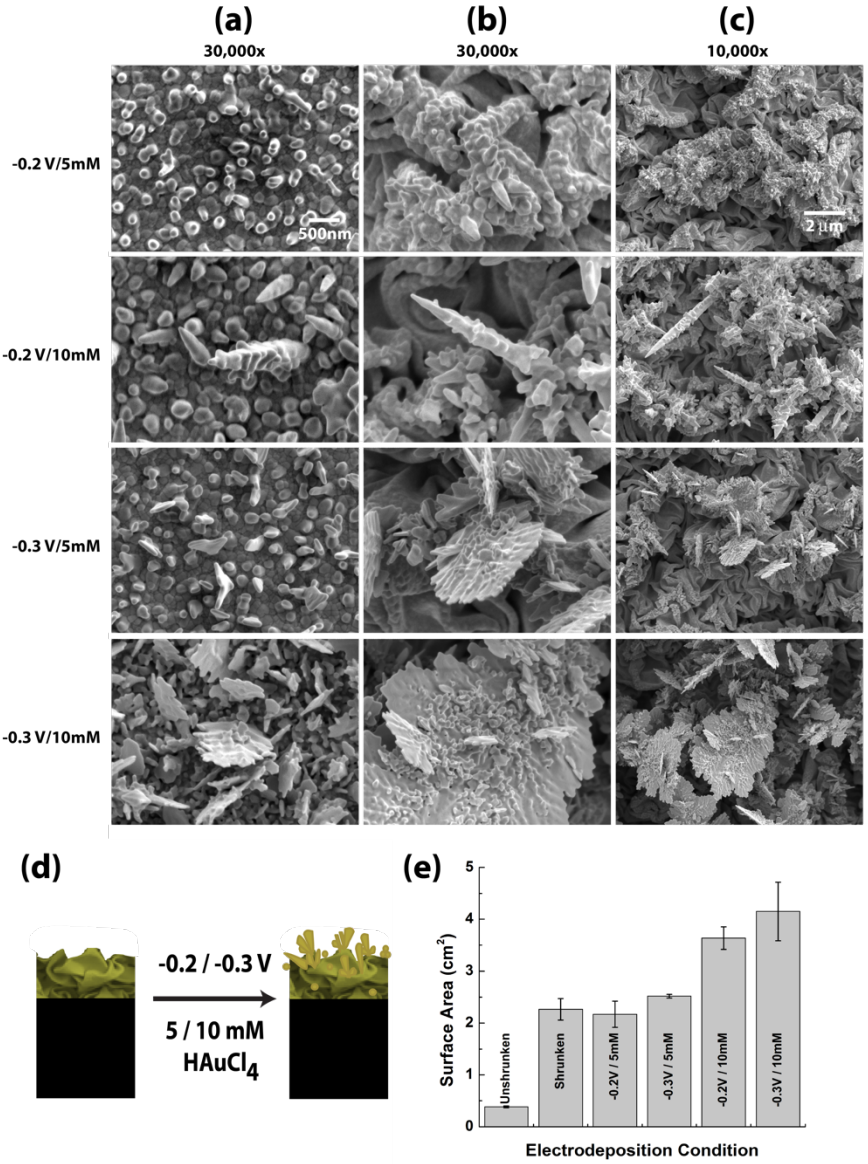

Figure 4-5 Electrodeposition of gold nanostructures enhances the electroactive surface area of CSEs. A comparison of Scanning Electron Microscopy images of the nanostructures formed through electrodeposition on unshrunken flat (a) and shrunken electrodes (b-c) shows that CSEs enhance the electrodeposition process. The deposition potential and metallic salt concentration control the morphology and size of the deposited nanostructures. (d) Schematic depiction of the electrodeposition process on CSEs. (e) The comparison of the electroactive surface area for unshrunken, shrunken, and electrodeposited devices shows that through shrinking and electrodeposition, surface area enhancements of up to 1000% of the flat electrode can be achieved.

4.4 Conclusions

A rapid, facile and inexpensive bench top approach has been developed for fabricating electrodes with hierarchical structures spanning from the millimeter to the nanometer range. The use of self-adhesive vinyl as masking material and a craft cutter allowed prototyping of electrodes with critical dimensions in the sub-millimeter range in timeframes of minutes to hours. Furthermore, the use of a PS shrinkable substrate allowed the reduction of the patterned feature dimensions to sub-100 μm sizes. The shrinking of the PS substrates induced stress-driven wrinkling of the gold films, and it was observed that the size of the topographical features and surface roughness could be tailored from the micrometer to the nanometer scale by adjusting the thickness of the gold film deposited. We characterized the behavior of these crumple-structured electrodes (CSEs) and found that they exhibit electrical and electrochemical properties that compare favorably with electrodes fabricated on traditional substrates such as glass. We also found that the CSEs exhibited high device-to-device reproducibility and robustness. The most attractive feature of CSEs, however, is that they exhibit significantly enhanced electroactive surface areas per geometric area (665% compared to flat electrodes). Further controllable nanostructuring was produced on CSEs through the tuned electrodeposition of gold nanostructures. We observed that the electrodeposition was improved on CSEs (compared to flat electrodes) due to the field enhancement offered by the structured surface. Devices with electrodeposited nanostructures exhibited further electroactive surface area enhancements (up to 1000% compared to flat electrodes). Thus, we have shown that it is possible to produce hierarchically structured electrodes, with features spanning the sub-millimeter to nanometer scales, through inexpensive, easy to implement and rapid bench top techniques in timeframes less than one hour. We anticipate that such materials will find wide application in the development of highly sensitive point-of-care

devices, where high surface area materials can offer enhanced signal to noise ratios and bioprocessing capability towards target analytes.

4.5 Experimental Section

4.5.1 Reagents

Potassium hexacyanoferrate(II) trihydrate ($K_4Fe(CN)_6 \cdot 3H2O$, >98.5%), potassium chloride (KCl, ≥99.0%), hydrogen tetrachloroaurate(III) trihydrate ($HAuCl_4 \cdot 3H2O$, >99.9%), hydrochloric acid (HCl ACS reagent, 37%) were purchased from Sigma-Aldrich (St. Louis, Missouri). Sulfuric acid (H_2SO_4, 98%) was purchased from Calden (Georgetown, Ontario). All reagents were of analytical grade and were used without further purification. Milli-Q grade water (18.2 MΩ) was used to prepare all solutions.

4.5.2 Device Fabrication

All devices were fabricated on pre-stressed polystyrene shrink films (Graphix Shrink Film, Graphix, Maple Heights, Ohio). Shrink film sheets were cleaned under orbital agitation (50 rpm) for 5 minutes in isopropanol, ethanol, and water baths, and were dried using a dry nitrogen stream. Self-adhesive vinyl sheets (FDC-4300, FDC graphic films, South Bend, Indiana) were laid over the cleaned shrink film sheets and evenly flattened with a hand roller. The desired gold film shapes were cut into the self-adhesive vinyl using a Robo Pro CE5000-40-CRP vinyl cutter (Graphtec America Inc., Irvine, CA) equipped with a CB09UA supersteel blade, with force, quality and speed set at 10, 1, and 1 respectively. The cut out shapes were peeled off from the shrink film using tweezers. The remaining self-adhesive vinyl was used as a mask during gold sputtering. Gold was deposited from a 99.999% purity gold target (LTS Chemical Inc., Chestnut Ridge, New York) using a Torr Compact Research Coater CRC-600 manual planar magnetron sputtering system

(New Windsor, New York) onto the masked shrink film. The argon (>99.999% purity, AlphaGaz, Air Liquide, Montreal, Quebec) plasma was created by a DC current of 37 A, which allowed for a typical gold deposition rate, monitored by the Quartz Crystal Thickness Sensor, of 1.1 Å/s. The sputtered thickness of the gold was estimated according to the deposition rate and the deposition time. After sputtering the vinyl mask was removed manually using tweezers. Gold coated shrink film devices were shrunk on aluminum boats at 130 and 160°C in an Isotemp Vacuum oven (Fisher Scientific, Ottawa, Ontario). The use of an aluminum boat as a carrier for the PS substrates provided uniform heat transfer, which ensured that there was no distortion in the shrunken devices. Self-adhesive vinyl masks were used to expose a small region of the devices used for electrochemical characterization.

4.5.3 SEM Characterization

SEM images of the gold films before and after shrinking were obtained using a JEOL JSM-7000S Scanning Electron Microscope with an accelerating voltage of 3 kV, working distance of 6 mm, and low probe current.

4.5.4 Surface roughness characterization

The roughness of shrunken device surfaces was measured for gold coating thicknesses of 0, 20, 50, 100 and 200 nm using a Zygo NewView 5000 white light interferometer (Zygo Corporation, Middlefield, CT). The root mean square (RMS) and peak-to-valley (PV) values were obtained in 3-5 device areas and compared across devices. Measurements were taken with 10x and 50x interferometric objectives and both were with a 2×image zoom setting, which resulted in fields of view of 360×270 μm and 70×50 μm, respectively. Data was collected from a CCD camera with an imaging pixel size of 11.2 μm. The built in software, MetroPro, was used for data analysis. A Fast Fourier Transform (FFT) band pass filter was applied, using cutoff frequencies of 183.35 and

558.79 mm^{-1}. Spikes with height values above 10*RMS were removed from the analysis of the imaged area to eliminate any contribution from contaminants (dust particles or defects on the films) to the roughness values.

4.5.5 Electrochemical Characterization

Cyclic voltammetry was performed using a CHI 660D Electrochemical Workstation (CH Instrument, Austin, Texas) and a standard three-electrode set-up. The electrochemical system consisted of an Ag/AgCl reference electrode, a platinum wire counter electrode, and gold sputtered on polystyrene as the working electrode. To ensure that the planar geometric surface area of the working electrode was the same for samples before and after shrinking (0.25 cm^2), a vinyl mask was placed over the gold with a single 0.5 cm by 0.5 cm square cut out to expose the electrochemically active surface. To determine the electrochemically active surface area of the samples, a solution of 0.1 M H_2SO_4 was used to perform 10 cyclic voltammetry scans at a scan rate of 0.05 V s^{-1} and a voltage range between 0 and 1.5 V. The reduction section of the resulting cyclic voltammograms were integrated using OriginPro 8 software to determine the charge and the electrochemically active surface area was calculated (Surface area = charge/surface charge density) using the surface charge density of a monolayer of gold, 386 μC cm^{-2}. To test the ability to conduct electrochemical measurements, a solution of 2 mM $K_4Fe(CN)_6$ in 0.1 M KCl was used to cycle between -0.1 and 0.5 V at the following scan rates: 0.01, 0.02, 0.04, and 0.08 V s^{-1}. Also, chronoamperometry was performed using solutions ranging from 50 μM to 100 mM $K_4Fe(CN)_6$ in 1 M KCl at a potential of 0.5V for 1 second.

4.5.6 Electrical Characterization

Sheet resistance(R_s) measurements were taken using the HL5500PC- Hall Effect Measurement System with HL5500 Buffer Amplifier (Nanometrics, Milpitas, California). Four gold probe tips

were used to take R_s measurements of the samples in a standard van der Pauw configuration. The sheet resistance was calculated according to:

$$R_s = \frac{2.2662(V_{43}+V_{23})}{I} \times F \times Q R_s = \frac{2.2662(V_{43}+V_{23})}{I} \times F \times Q \quad (1)$$

where I is the applied current, V_{43} and V_{23} are the potentials measured perpendicular to each other on the film in response to the current, Q is the symmetry factor and is calculated by $Q = \frac{V_{43}}{V_{23}}$, and F is a correction factor for any asymmetry and is calculated by: $F = 1 - 0.34657A - 0.09236A^2$, where $A = \left[\frac{Q-1}{Q+1}\right]^2$. In order to cancel thermoelectric and other effects, the currents were applied in both directions between two tips, and then the measured potentials were averaged.

4.5.7 Electrodeposition

The CHI 660D Electrochemical Workstation (CH Instrument, Austin, Texas) was used for electrodeposition with the standard three-electrode set-up described above. To ensure the planar geometric surface area of the working electrode was the same for samples before and after shrinking (0.25 cm^2), a vinyl mask was placed over the gold with a single 0.5 cm by 0.5 cm square cut out to expose the electrochemically active surface. Gold nanostructures were grown by electrodeposition on the gold-polystyrene substrate using solutions containing 5 and 10 mM $HAuCl_4$ in 0.5 M HCl at potentials of -0.2 or -0.3 V for 900 seconds.

4.6 Acknowledgements

We thank Laura Dodge for help with the measurement of contact angles, and Dr. Maneesh Khanna for help with white light interferometry. This research made use of facilities at the McMaster Manufacturing Research Institute. JMM acknowledges funding through the Science and Engineering Research Board at McMaster University.

4.7 References

(1) Lakes, R. Materials with Structural Hierarchy. *Nature* **1993**, *361* (6412), 511–515.

(2) Fratzl, P.; Weinkamer, R. Nature's Hierarchical Materials. *Prog. Mater. Sci.* **2007**, *52* (8), 1263–1334.

(3) Tsakalakos, L.; Balch, J.; Fronheiser, J.; Korevaar, B. A.; Sulima, O.; Rand, J. Silicon Nanowire Solar Cells. *Appl. Phys. Lett.* **2007**, *91* (23), 233117.

(4) Bierman, M. J.; Jin, S. Potential Applications of Hierarchical Branching Nanowires in Solar Energy Conversion. *Energy Environ. Sci.* **2009**, *2* (10), 1050.

(5) Chen, A.; Lieu, D. K.; Freschauf, L.; Lew, V.; Sharma, H.; Wang, J.; Nguyen, D.; Karakikes, I.; Hajjar, R. J.; Gopinathan, A.; et al. Shrink-Film Configurable Multiscale Wrinkles for Functional Alignment of Human Embryonic Stem Cells and Their Cardiac Derivatives. *Adv. Mater.* **2011**, *23* (48), 5785–5791.

(6) Dalby, M. J.; Gadegaard, N.; Tare, R.; Andar, A.; Riehle, M. O.; Herzyk, P.; Wilkinson, C. D.; Oreffo, R. O. The Control of Human Mesenchymal Cell Differentiation Using Nanoscale Symmetry and Disorder. *Nat. Mater.* **2007**, *6* (5), 407–413.

(7) Stevens, M. M.; George, J. H. Exploring and Engineering the Cell Surface Interface. *Science* **2005**, *310* (18), 1135–1138.

(8) Frechet, J. M. J. Dendrimers and Other Dendritic Macromolecules: From Building Blocks to Functional Assemblies in Nanoscience and Nanotechnology. *J. Polym. Sci. Part A Polym. Chem.* **2003**, *41* (23), 3713–3725.

(9) Goldberg, M.; Langer, R.; Jia, X. Nanostructured Materials for Applications in Drug Delivery and Tissue Engineering. *J. Biomater. Sci. Polym. Ed.* **2007**, *18* (3), 241–268.

(10) Soleymani, L.; Fang, Z.; Sargent, E. H.; Kelley, S. O. Programming the Detection Limits of Biosensors through Controlled Nanostructuring. *Nat. Nanotechnol.* **2009**, *4*, 844–848.

(11) Soleymani, L.; Fang, Z.; Lam, B.; Bin, X.; Vasilyeva, E.; Ross, A. J.; Sargent, E. H.; Kelley, S. O. Hierarchical Nanotextured Microelectrodes Overcome the Molecular Transport Barrier to Achieve Rapid, Direct Bacterial Detection. *ACS Nano* **2011**, *5* (4), 3360–3366.

(12) Lu, X.; Xiao, Y.; Lei, Z.; Chen, J. Graphitized Macroporous Carbon Microarray with Hierarchical Mesopores as Host for the Fabrication of Electrochemical Biosensor. *Biosens. Bioelectron.* **2009**, *25* (1), 244–247.

(13) Wen, Z.; Ci, S.; Li, J. Pt Nanoparticles Inserting in Carbon Nanotube Arrays: Nanocomposites for Glucose Biosensors. *J. Phys. Chem. C* **2009**, *113* (31), 13482–13487.

(14) Luo, Y.; Misra, V. Large-Area Long-Range Ordered Anisotropic Magnetic Nanostructure Fabrication by Photolithography. *Nanotechnology* **2006**, *17* (19), 4909–4911.

(15) Duan, H.; Zhao, J.; Zhang, Y.; Xie, E.; Han, L. Preparing Patterned Carbonaceous

Nanostructures Directly by Overexposure of PMMA Using Electron-Beam Lithography. *Nanotechnology* **2009**, *20* (13), 135306.

(16) Inguanta, R.; Piazza, S.; Sunseri, C. Template Electrosynthesis of CeO 2 Nanotubes. *Nanotechnology* **2007**, *18* (48), 485605.

(17) Xia, Y.; Whitesides, G. M. SOFT LITHOGRAPHY. *Annu. Rev. Mater. Sci.* **1998**, *28*, 153–184.

(18) Fu, C.-C.; Grimes, A.; Long, M.; Ferri, C. G. L.; Rich, B. D.; Ghosh, S.; Ghosh, S.; Lee, L. P.; Gopinathan, A.; Khine, M. Tunable Nanowrinkles on Shape Memory Polymer Sheets. *Adv. Mater.* **2009**, *21* (44), 4472–4476.

(19) Nguyen, D.; Taylor, D.; Qian, K.; Norouzi, N.; Rasmussen, J.; Botzet, S.; Lehmann, M.; Halverson, K.; Khine, M. Better Shrinkage than Shrinky-Dinks. *Lab Chip* **2010**, *10* (12), 1623–1626.

(20) Grimes, A.; Breslauer, D. N.; Long, M.; Pegan, J.; Lee, L. P.; Khine, M. Shrinky-Dink Microfluidics: Rapid Generation of Deep and Rounded Patterns. *Lab Chip* **2008**, *8* (1), 170–172.

(21) Haynes, W. M. *CRC Handbook of Chemistry and Physics.*; CRC ; Taylor & Francis: Boca Raton, FL, 2011.

(22) Shao, Y.; Brook, M. a. Structured Metal Films on Silicone Elastomers. *J. Mater. Chem.* **2010**, *20* (39), 8548.

(23) Stafford, C. M.; Harrison, C.; Beers, K. L.; Karim, A.; Amis, E. J.; VanLandingham, M. R.; Kim, H. C.; Volksen, W.; Miller, R. D.; Simonyi, E. E. A Buckling-Based Metrology for Measuring the Elastic Moduli of Polymeric Thin Films. *Nat. Mater.* **2004**, *3* (8), 545–550.

(24) Yoo, P. J.; Lee, H. H. Evolution of a Stress-Driven Pattern in Thin Bilayer Films: Spinodal Wrinkling. *Phys. Rev. Lett.* **2003**, *91* (15), 154502.

(25) Yoo, P. J.; Suh, K. Y.; Kang, H.; Lee, H. H. Polymer Elasticity-Driven Wrinkling, and Coarsening in High Temperature Buckling of Metal-Capped Polymer Thin Films. *Phys. Rev. Lett.* **2004**, *93* (3), 034301.

(26) Sharp, J. S.; Vader, D.; Forrest, J. A.; Smith, M. I.; Khomenko, M.; Dalnoki-Veress, K. Spinodal Wrinkling in Thin-Film Poly(ethylene Oxide)/polystyrene Bilayers. *Eur. Phys. J. E* **2006**, *19* (4), 423–432.

(27) Fu, C.-C.; Ossato, G.; Long, M.; Digman, M. a.; Gopinathan, A.; Lee, L. P.; Gratton, E.; Khine, M. Bimetallic Nanopetals for Thousand-Fold Fluorescence Enhancements. *Appl. Phys. Lett.* **2010**, *97* (20), 203101.

(28) Groenewold, J. Wrinkling of Plates Coupled with Soft Elastic Media. *Phys. A Stat. Mech. its Appl.* **2001**, *298* (1), 32–45.

(29) Huang, Z.; Hong, W.; Suo, Z. Evolution of Wrinkles in Hard Films on Soft Substrates. *Phys.*

Rev. E **2004**, *70* (3), 030601.

(30) Chung, J. Y.; Nolte, A. J.; Stafford, C. M. Surface Wrinkling: A Versatile Platform for Measuring Thin-Film Properties. *Adv. Mater.* **2011**, *23* (3), 349–368.

(31) Shahraz, A.; Borhan, A.; Fichthorn, K. A. A Theory for the Morphological Dependence of Wetting on a Physically Patterned Solid Surface. *Langmuir* **2012**, *28*, 14227–14237.

(32) Choi, M. C.; Kim, Y.; Ha, C. S. Polymers for Flexible Displays: From Material Selection to Device Applications. *Prog. Polym. Sci.* **2008**, *33* (6), 581–630.

(33) McAlpine, M. C.; Ahmad, H.; Wang, D.; Heath, J. R. Highly Ordered Nanowire Arrays on Plastic Substrates for Ultrasensitive Flexible Chemical Sensors. *Nat. Mater.* **2007**, *6* (5), 379–384.

(34) Söderström, T.; Haug, F.-J.; Terrazzoni-Daudrix, V.; Ballif, C. Optimization of Amorphous Silicon Thin Film Solar Cells for Flexible Photovoltaics. *J. Appl. Phys.* **2008**, *103* (11), 114509.

(35) Osório, W. R.; Peixoto, L. C.; Canté, M. V.; Garcia, A. Electrochemical Corrosion Characterization of Al–Ni Alloys in a Dilute Sodium Chloride Solution. *Electrochim. Acta* **2010**, *55* (13), 4078–4085.

(36) Sriram, S.; Bhaskaran, M.; Ahluwalia, R.; Nguyen, T. G.; Ng, N.; Srolovitz, D. J.; Kalantar-Zadeh, K.; Mitchell, A. Surface Morphology Induced Localized Electric Field and Piezoresponse Enhancement in Nanostructured Thin Films. *ACS Nano* **2011**, *5* (2), 1067–1072.

(37) Bharathi, S.; Nogami, M.; Ikeda, S. Novel Electrochemical Interfaces with a Tunable Kinetic Barrier by Self-Assembling Organically Modified Silica Gel and Gold Nanoparticles. *Langmuir* **2001**, *17* (1), 1–4.

Chapter 5 Highly Bendable and Stretchable Electrodes Based on Micro/Nanostructured Gold Films for Flexible Sensors and Electronics

Yujie Zhu and Jose M. Moran-Mirabal designed the experiments. Yujie Zhu conducted all the experiments. Yujie Zhu and Jose M. Moran-Mirabal analyzed the data and wrote the manuscript.

5.1 Abstract

Building sensors or electronic components on flexible, stretchable materials requires retention of conductivity under strain. Various nanostructured materials (e.g. carbon nanotubes and metal films) have been used to make flexible conductors. However, most materials are limited in applicability due to instability under high strain, low conductivity or high cost. Here, we present a simple, inexpensive method to fabricate stretchable electrodes with excellent conductive properties. The unique feature allowing the fabricated electrodes to withstand high strains is their micro/nanostructures generated by stress-driven wrinkling of thin gold films on carrier shape memory polymer. The structured electrodes were transferred onto elastomeric substrates via a lift-off process. The structured surfaces displayed similar topography and electroactive surface area before and after transfer. The stretchability of electrodes on both PDMS and Ecoflex was investigated by measuring the change in resistance under tensile strain. The relative resistance remained close to unity for Au-on-PDMS electrodes until the substrate broke at ~105% strain; whereas it progressively increased for Au-on-Ecoflex electrodes until the conductivity was lost at 130% strain. Great mechanical stability of the electrodes was demonstrated by the fact that the initial resistance was recovered after releasing the devices from stretching strains up to 100% and bending strains up to 60% over 100 cycles. Finally, a 3-electrode electrochemical cell was implemented from structured electrodes and used for sensing ferrocyanide and ascorbic acid. The devices under bending strain displayed very similar

electrochemical properties as the unstrained ones. We anticipate wide applicability of the micro/nanostructured electrodes for flexible, stretchable electronics or sensors.

5.2 Introduction

Simple and inexpensive ways of fabricating electronics on flexible substrates are in high-demand for wearable devices,[1] sensors,[2,3] and actuators,[4] where conductive materials need to perform consistently under strain. To date, various nanomaterials, such as polymers,[5] carbon nanotubes,[6] graphene,[7,8] metal films,[9] and nanoparticles,[10,11] have been used as flexible conductors. However, most of these materials are limited in their applicability due to instability, low conductivity, or high material cost.[12] Thus, simple and cost-effective methods to make stretchable electrodes from metal films are highly desirable. Metal films can be structured to achieve stretchability through: (1) patterning thin films into spring-shape wire[13] or filament networks;[14] (2) introducing roughness at a metal/elastomer interface to produce non-percolating cracks during stretching;[15] (3) using pre-stressed elastomeric substrates during thin film deposition followed by strain release.[9] The first strategy involves expensive and complex fabrication processes, while the other methods are limited in the maximum strain that the electrodes can withstand. In this manuscript, by combining shape-memory polymer shrinking[16–18] with patterning through xurography[19,20] and lift-off, we introduce a simple and inexpensive method for fabricating structured metal electrodes. Such electrodes exhibit excellent conductivity, electrochemical sensing stability and great resiliency to stretching and bending strain on poly(dimethylsiloxane) (PDMS) and Ecoflex® elastomeric substrates.

5.2 Results and Discussion

The bench-top fabrication of stretchable conductive films is illustrated in Figure 5-1A.

Adhesive vinyl served as a mask during gold deposition to create centimeter to sub-millimeter patterned electrodes. After vinyl lift-off, the polystyrene substrate (PS) was shrunk down to ~16% of its original size, resulting in micrometer size electrodes. Additionally, the shrinking process buckled and wrinkled the gold films, resulting in micro/nanostructured surfaces. The structured films were lifted-off by dissolving an intermediate photoresist layer, whose thickness was optimized to yield small micro/nanostructures on the gold film and to allow it to be readily lifted-off (Figure S1). The last fabrication step involved transferring the gold film to the receiving substrate. Figure 5-1 B-C show photos of structured gold films (200 nm-thick) transferred onto PDMS and SiO_2 substrates respectively. To achieve the best adhesion on the receiving elastomers (PDMS/Ecoflex), they were partially cured prior to the transfer of the structured metal films. It was observed that the presence of bubbles or contaminants at the gold/elastomer interface led to film delamination, resulting in low electrode stretchability. Using the optimized conditions, this simple and inexpensive benchtop method allowed the patterning, structuring and transferring of thin gold films.

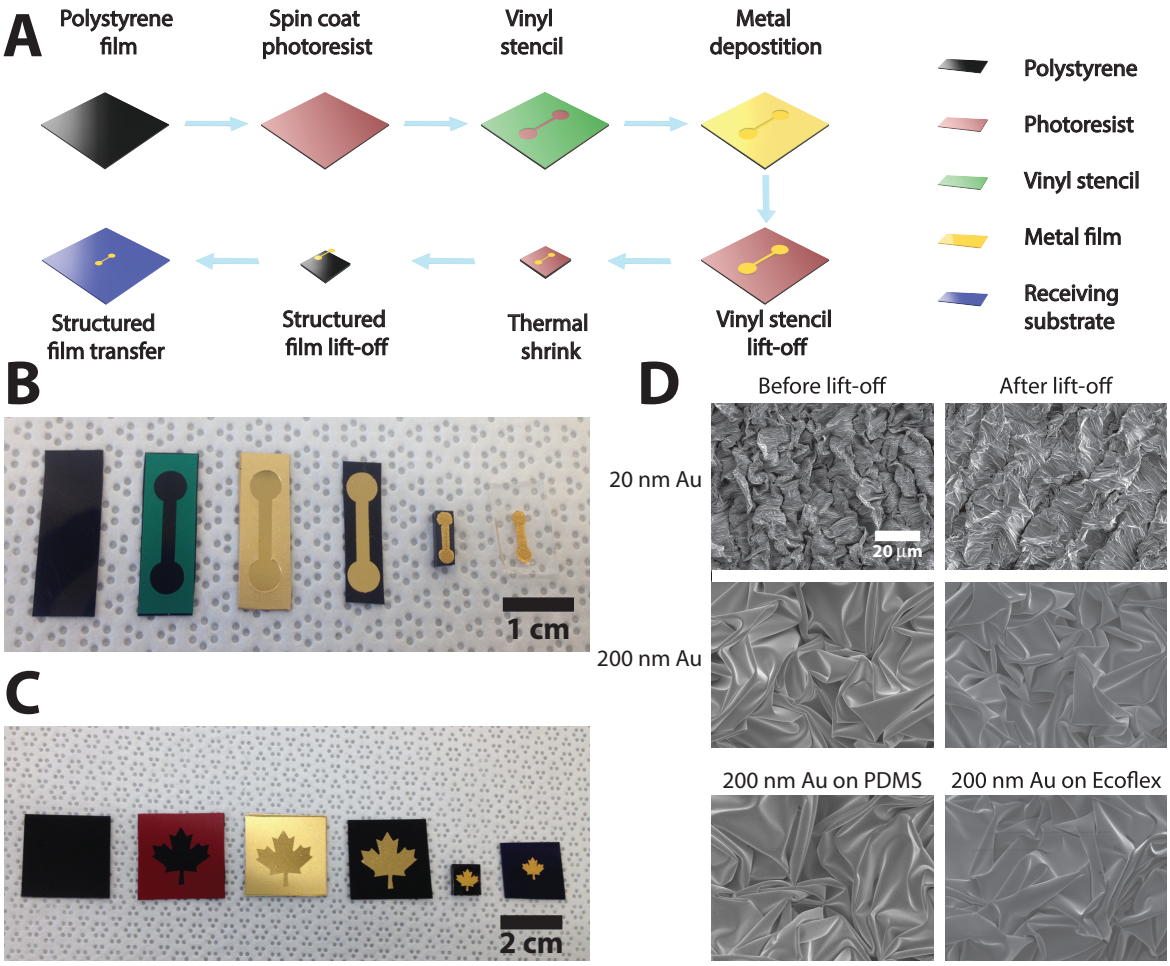

Figure 5-1 Fabrication of structured electrodes. A) Schematic of the bench-top micro/nanostructured metal thin film fabrication and transfer. B) Depiction of the fabrication process of gold electrode transferred on to PDMS. C) Depiction of the fabrication of patterned maple leaf-shaped Au film and the transfer onto a silicon wafer. D) SEM images of 200 nm Au films before and after lift-off, and after transfer to PDMS. SEM images were taken with accelerating voltage of 2.5 kV, working distance of 6 mm, and low probe current. All images taken at the same magnification.

The structured films were characterized through electron and optical microscopy before and after lift-off and transfer to the receiving substrates. Scanning electron microscopy (Figure 5-1D) showed that 20 nm-thick films presented smaller structures than 200 nm ones, because thinner films buckled more readily during shrinking.[21] Little difference was observed in the morphology

for the structured films before lift-off, after lift-off, and after transfer onto elastomer substrates. To confirm this observation, the surface roughness of the structured films was measured through optical profilometry. The surface root mean squared roughness was measured to be statistically equal before lift-off, after lift-off, and after transfer to the receiving substrates (Figure S2). This shows that the fabrication process does not change the physical attributes of the structured films.

To test the stretchability of structured Au/PDMS electrodes, their conductivity was tested under strain. The structured electrode resistance was measured in a two-probe setup (Figure 5-2A, bottom inset) at 5% strain increments. Typical I-V curves at 0, 50 and 100% strain are shown in the top inset of Figure 5-2A. All electrodes remained conductive until the PDMS mechanically failed (110-130% strain), suggesting that they are excellent candidates for PDMS-based devices. The effect of electrode shape on stretchability was assessed by measuring the conductivity under strain for electrodes with different form factors (defined as length-to-width ratio, L/W, Figure 5-2A). As L/W increased, the resistance at comparable strains also increased. This is explained by film cracking perpendicular to the stretching axis, which reduces the number of available conductive paths. For electrodes with high L/W, the number of cracks necessary to span the width of the electrode, resulting in total loss of conductivity, is smaller than for electrodes with low L/W. This is exemplified by Figure 5-2A, where the resistance for electrodes with W = 2, 0.8, and 0.8 mm and L/W = 3, 5 and 7.5 at 100% strain is on average ~10, 30 and 100% higher than their initial (relaxed) resistance. Thus, electrodes with large form factors could be useful as strain sensors, while those with small form factors would be robust conductive elements for applications where a constant resistance is required.

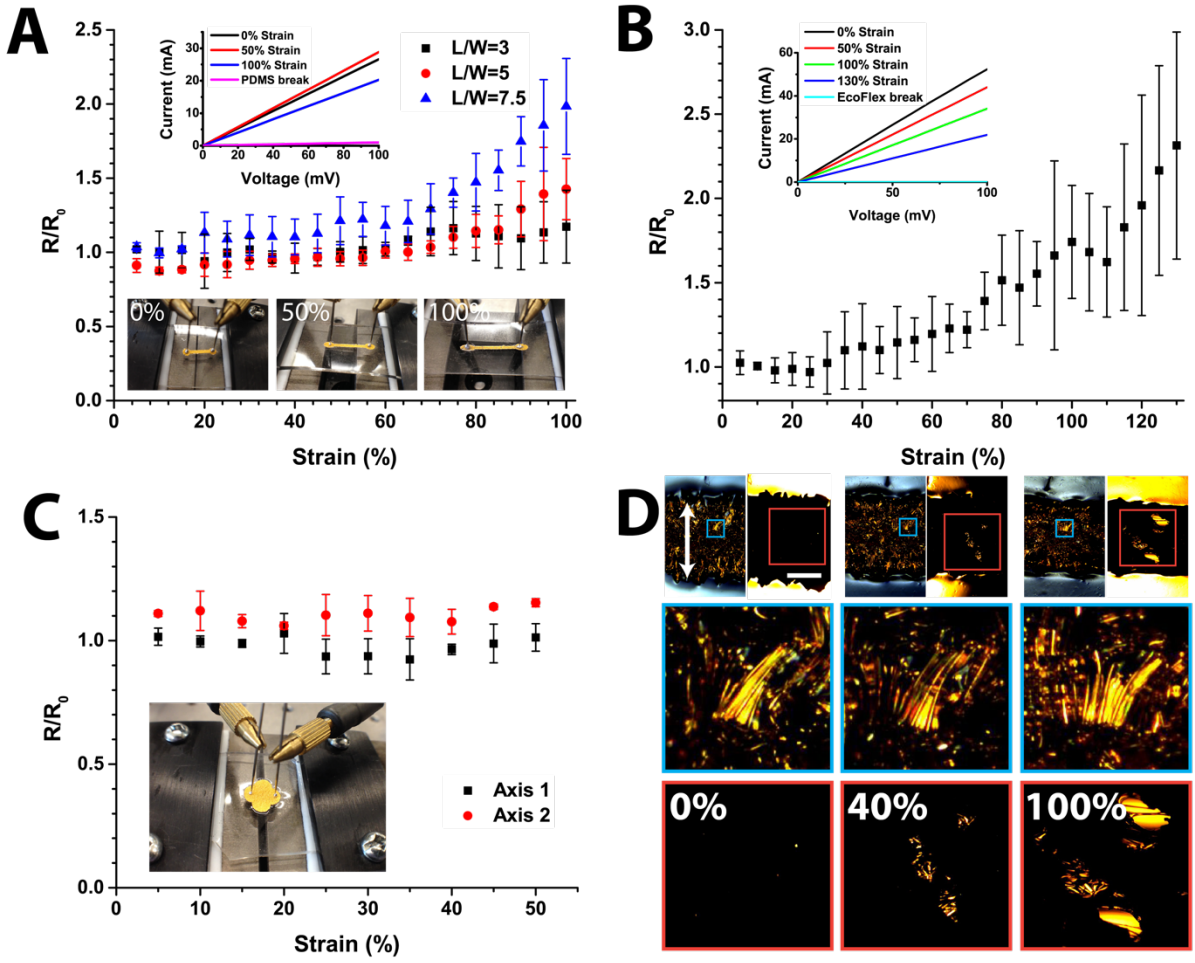

Figure 5-2 Stretchability and mechanism. A) Relative resistance change measurement under various strains for stretchable electrodes on PDMS substrates with L/W=3 (black square, W = 2 mm), 5 (red circle, W = 0.8 mm) and 7.5 (blue triangle, W = 0.8 mm). Top inset graph shows typical I-V curves where resistance was extracted for gold electrodes (L/W=5) under 0%, 50%, 100% strains and when PDMS broke. Bottom inset photos show the two-probe measurement for a gold electrode/PDMS device under 0%, 50% and 100% stretching strain, respectively. B) Relative resistance change measurement under various strains for gold electrode (L/W=3, W = 2 mm) on Ecoflex® substrate. The electrode lost conductivity at 135% strain. Inset are representative I-V curves for gold electrode stretched on Ecoflex® at 0%, 50%, 100%, 130% and 135% strain (conductivity broke). C) Biaxial stretchability. The relative resistance change shows the same trend when Au/PDMS device was stretched along two orthogonal axes, indicating similar electric properties of both axes. Inset is a photo of flower-shaped Au film on PDMS at 0% strain for biaxial stretching measurement. D) Optical images show gold film morphology change during the stretching process. The top row shows reflected (left panels) and transmitted light (right panels) images that reveal the unwrinkling and cracking

process of the gold film. The scale bar in this image is 500 μm. The areas confined with blue (reflected light) and red (transmitted light) squares were zoomed into for clearer observation. The reflected light images (middle row, blue) reveal the unwrinkling of surface features when tensile stress (0, 40, 100%) is applied. On the other hand, the transmitted light images (bottom row, red) show the evolution of defects or cracks in the gold film as tensile stress (0, 40, 100%) is applied.

To overcome the limitations of PDMS-based devices and explore the maximum stretchability of micro/nanostructured electrodes, we used Ecoflex® elastomer as the receiving substrate (~800% elongation at break). Resistance measurements under strain for Au/Ecoflex® electrodes (L/W = 7.5, Figure 5-2B) showed higher inter-device variability than those on PDMS. This is a result of the variability in adhesion between the film and elastomer, where areas of the film that did not adhere well delaminated more easily. The measured strain at conductivity break was 135%, with the relative resistance remaining in the range of 1-2.5 for strains up to 130% (Figure 5-2B). As controls, we tested the conductivity of planar gold electrodes fabricated directly on the elastomer surfaces. The flat Au/elastomer films cracked and delaminated much more readily (Figure S3), losing conductivity with little applied strain (< 5%). These results highlight the need for a structured film and proper adhesion to obtain highly stretchable and conductive electrodes.

Biaxial stretchability is required for conductive elements that can be draped over arbitrary surfaces. Various materials with such properties have been explored in the past, including silver nanowires,[22] gold,[9] and graphene films.[23] To test the biaxial stretchability of structured Au/PDMS electrodes, their conductivity was evaluated under strains along two orthogonal axes. For a design with L/W = 1 (Figure 5-2C), the relative resistance experienced little variation when 0-50% strain was applied along orthogonal axes. The uniform behavior when the micro/nanostructured gold films are stretched biaxially suggests that they could be attractive as electrodes attached to the

surface of inflatable devices (e.g. balloon catheters).[24]

To understand the stretching mechanics of micro/nanostructured Au/PDMS electrodes, their surfaces were imaged under strain. From reflected and transmitted light microscopy images (Figure 5-2D), it can be seen that the wrinkles on the structured gold films contribute to their enhanced stretchability in two ways. First, the wrinkles unfold as the film is stretched, which maintains the integrity of the film by keeping the tensile stress low. Second, the cracks that originate from the weakest points or defects on the film extend along the wrinkles as the strain increases. The random orientation of the wrinkles prevents cracks from propagating across the film and minimizes the loss of conductivity. Finally, micro/nanostructure size and periodicity does not impact film stretchability and conductivity, as shown by electrodes fabricated from films with different thicknesses (Figure S4). These experiments show that the stretchability of structured electrodes derives from features produced during the shrinking process, and hints at alternative methods that exploit surface structuring for the fabrication of flexible devices.

The implementation of flexible electronics also requires that the conductivity be reproducible under stretching and bending. To assess reproducibility, changes in resistance were measured for Au/elastomer devices (W = 0.8 mm, L/W=7.5) over 100 stretching and bending cycles. On PDMS, the resistance measurements were done at 0 and 50% strain (Figure 5-3A). Over the first two cycles resistance increased slightly at 50% strain, which was attributed to the development of the necessary cracks to relieve tensile strain. After the initial "conditioning" of the electrodes, resistance remained constant for the stretched and relaxed states. Similarly, Ecoflex® devices were tested at 0 and 100% strain (Figure 5-3B), where the relative resistance under strain remained constant at 1.4 for the first 20 cycles, and increased to 2.1 over the next 80 cycles. This increase is attributed to partial delamination due to the weaker adhesion of the structured film to Ecoflex®. It

must be noted however that the increase is among the lowest reported in the literature for metallic film or nanostructure-based stretchable conductors.[25,26] To determine if electrodes stretched beyond their break point could recover conductivity upon relaxation, we measured the resistance for Au/Ecoflex® devices released from 150% strain (beyond conductivity break point, Figure 5-3C). No significant change occurred until after the 80th cycle and the relative resistance only increased to 1.45 through the 100th cycle. Similar behavior was observed for a device stretched to 100% strain (Figure 5-3B), which indicates that the Au/Ecoflex® electrodes remain conductive but exhibit slight degradation after ~80 cycles.

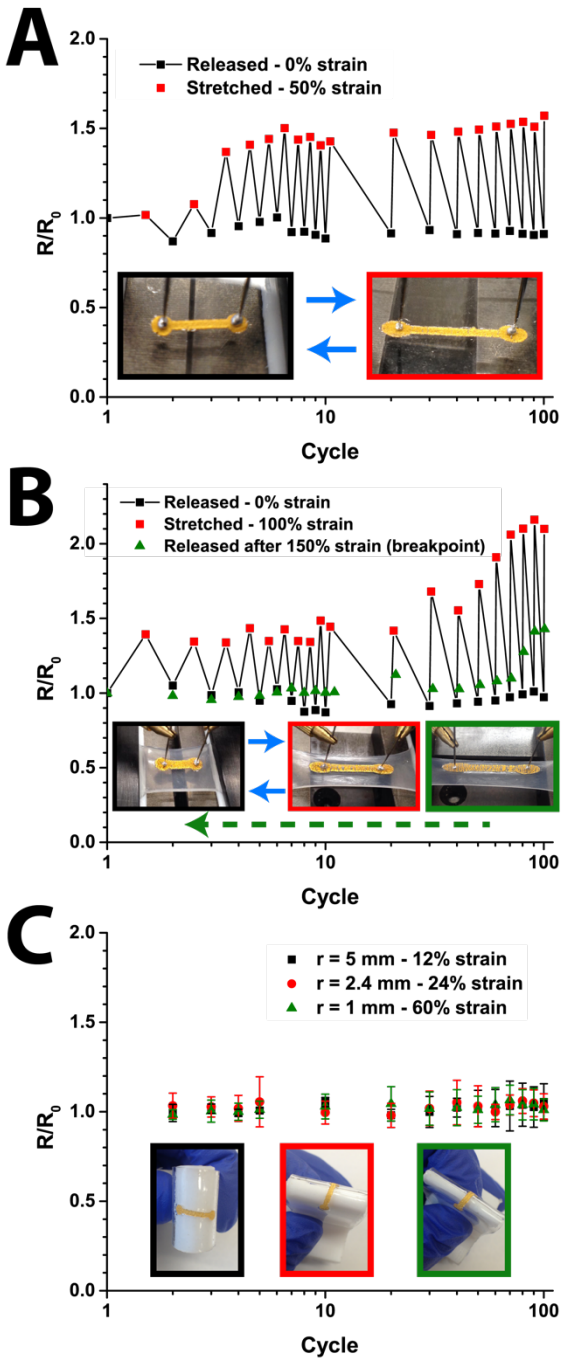

Figure 5-3 Stretching and bending reproducibility. A) Relative resistance of an Au/PDMS electrode (W = 0.8 mm, L/W=7.5) stretched from 0% to 50% strain over 100 stretching cycles. Inset photos show the device at 0% (black, left inset photo) and 50% strain (red, right inset photo). B) Relative resistance of Au/Ecoflex electrode (W = 2 mm, L/W=3) over 100 stretching cycles from 0% (black, left inset photo) to 100% (red, middle inset photo) strain, as well as relative resistance of devices after being stretched beyond their conductivity break point (~150% strain) and

released back to 0% strain (green, right inset photo). C) Relative resistance of Au/PDMS electrodes (W = 0.8 mm, L/W=7.5) released after being bent to 12% (black, left inset photo), 24% (red, middle inset photo) and 60% (green, right inset photo) bending strains. Inset photos show the electrode bent along holders with radii of 5 mm (black), 2.5 mm (red) and 1 mm (green). Each stretching and bending test was performed with three replicate electrodes.

The reproducibility in conductivity of Au/PDMS structured electrodes after bending was also investigated. Bending was performed by wrapping the Au/PDMS device around a Teflon mold with known radius of curvature (Figure 5-3C, r = 5, 2.5 or 1 mm, corresponding to tensile strains at the film of 12, 24 or 60% respectively) and releasing it, after which the resistance was measured. Figure 5-3C shows the relative resistance of Au/PDMS electrodes (W = 0.8 mm, L/W=7.5) over 100 bend and release cycles. Even for the highest strain (60%, r = 1 mm) the conductivity fully recovered after the release, and remained unchanged over 100 cycles. These results coupled to those from stretching experiments showcase the robustness of the micro/nanostructured electrodes, which retain excellent conductivity over repeated stretching and bending cycles.

As proof-of-concept of the use of structured gold films as conductive elements in functional devices, they were used as flexible electrodes for electrochemical sensing. First, cyclic voltammetry (CV) was used to measure the electroactive surface area (ESA) of devices at different fabrication stages: planar films on PS, structured films after shrinking, free-standing structured films after lift-off and structured films transferred onto PDMS (Figure 5-4A). CV was performed using the films as the working electrode in a 3-electrode electrochemical cell (Figure 5-4B, inset). The voltammograms displayed well-defined peaks associated with the oxidation/reduction of the gold surface. By quantifying the total charge transferred, the ESA of each film was assessed. Structured films on PS exhibited an increase in ESA (~520%) that is consistent with the reduction in the device footprint produced through shrinking. After lift-off, the ESA of the free standing

films increased by 80%. This was less than the 100% increase expected, which was attributed to photoresist or polystyrene residues left on the backside of the film after lift-off (Figure S5). Conversely, the ESA of films transferred onto PDMS was statistically equal to that of the films before lift-off. This showed that the surface of the structured films transferred onto PDMS substrates was not damaged by the fabrication procedure and could be suitable for electrochemical measurements.

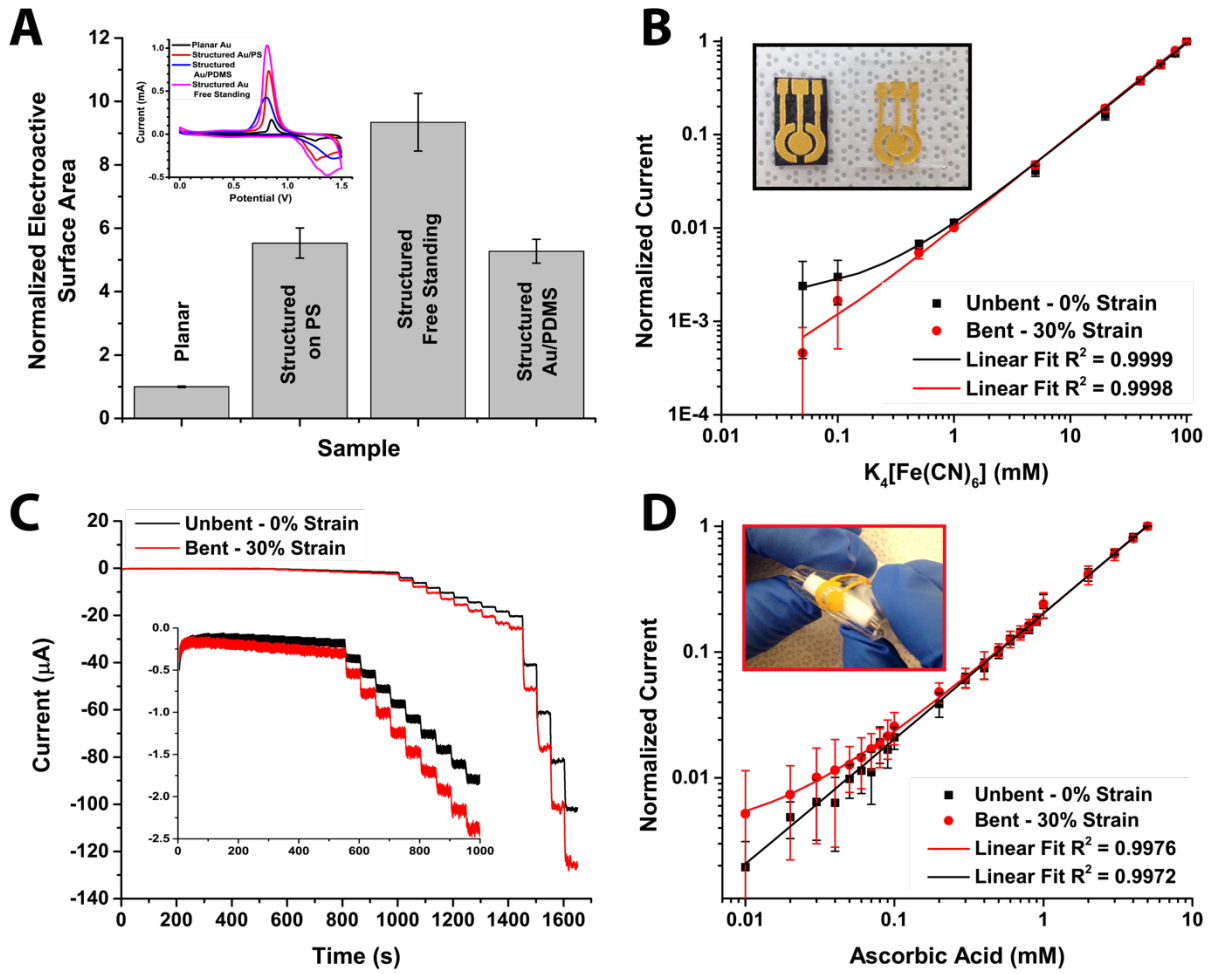

Figure 5-4 Electrochemical characterization and sensing. Electroactive surface area measurement through cyclic voltammetry for planar gold films, structured gold films on polystyrene, structured gold films after transfer onto PDMS and structured free-standing gold films. Inset graph is a comparison of cyclic voltammograms of each type of samples obtained in 0.05 M acid solutions. B) Calibration curves of response current over potassium ferrocyanide

concentration in chronoamperometric measurements performed with unbent (0% strain) and bent (30% strain) Au/PDMS sensing device. C) Typical amperometric curves of unbent (0% strain) and bent (30% strain) sensors to successive addition of ascorbic acid (final concentrations from 1 μm to 5 mM) in 0.02 M phosphate buffer solution (pH 7.0) at a constant applied potential of 0.4 V. D) Calibration curves of the current response over ascorbic acid concentration for both unbent and bent (30% strain) devices. Error bars represent the standard deviation of measurements performed on a minimum of at least three using different devices.

Structured Au/PDMS electrodes were used for electrochemical sensing with and without external bending strain. A circular working electrode and two arc-shaped counter electrodes were fabricated on PDMS (Figure 5-4B, inset photo) and an external Ag/AgCl electrode was used as reference. Chronoamperometry was used to assess the electrodes' response to different concentrations of redox-active molecules (ferrocyanide and ascorbic acid (AA)) in aqueous solutions. In all electrochemical-sensing experiments, the current was normalized to the current measured for the highest concentration, to account for any device-to-device variability. Figure 5-4B shows that current is linearly proportional to ferrocyanide concentrations from 50 μM to 100 mM for electrodes under 0 and 30% bending strain, where they also exhibited similar performance and limit of detection (50 μM). With a geometric area of the structured electrode of 0.196 cm^2, the sensitivity was calculated to be 0.05 $mM^{-1}cm^{-2}$ for relaxed and strained sensors. We further investigated the electrode response to temporal changes in AA concentration. Figure 5-4C shows typical chronoamperograms for structured gold electrodes (held at a constat potential of 0.4 V) in response to temporal increases of AA concentration. AA calibration curves constructed from three replicate devices show excellent linearity in the 10 μM - 5 mM concentration range for relaxed ($I/I_{max} = 0.2027 \times C_{AA} + 5 \times 10^{-5}$, $R^2 = 0.9999$) and strained electrodes ($I/I_{max} = 0.2007 \times C_{AA} + 0.0034$, $R^2 = 0.9994$). Furthermore, the relaxed and bent devices had identical limit of detection (20 μM),

while strain caused only a 1% decrease in sensitivity (from 1.03 $mM^{-1}cm^{-2}$ for relaxed to 1.02 $mM^{-1}cm^{-2}$ for strained devices). These results show that the structured electrodes are suitable for applications where flexibility or stretchability of the conductive elements are required, such as in flexible electrochemical sensors.

5.3 Conclusions

In conclusion, we have demonstrated a simple, rapid and inexpensive technique to fabricate highly stretchable micro/nanostructured metal electrodes. By combining shape-memory polymer shrinking and thin film lift-off, we successfully fabricated and transferred micro/nanostructured gold electrodes onto stretchable elastomeric substrates. Little change was observed in the conductive properties of Au/PDMS devices under strain until the substrate mechanically failed, while the Au/Ecoflex® devices remained conductive up to 135% strain. Furthermore, the structured electrodes showed uniform properties when stretched along two orthogonal axes. It was observed that the micro/nanostructured surface contributed to the stretchability of the electrodes in two ways: releasing tensile stress by unfolding of the wrinkles and preventing crack propagation by the random orientation of the wrinkles. The structured electrodes also displayed resilience to bending strains, as demonstrated by the complete recovery of their initial conductivity from tensile strains of up to 60%. Finally, the structured electrodes also proved to be candidates for flexible electrochemical sensors, as they performed very similarly in the detection of redox active molecules with and without applied strain. We anticipate that such micro/nanostructured electrodes could find use as conductive elements in flexible, stretchable, and/or inflatable electronics and sensors.

5.4 Experimental Section

Pre-stressed polystyrene films (Graphix Shrink Film, Graphix, Maple Heights, Ohio) were cleaned and spin coated with positive photo-resist of thicknesses ranging from 100 nm to 1.8 μm. After being heated at 90℃ for 3 min to remove residual solvent, the sheets were covered with self-adhesive vinyl (FDC-4300, FDC graphic films, South Bend, Indiana), and the desired shapes were cut out using a vinyl cutter (Robo Pro CE5000-40-CRP, Graphtec America Inc., Irvine, California). Gold was deposited from 99.999% purity gold target (LTS Chemical Inc., Chestnut Ridge, New York) using a Torr Compact Research Coater CRC-600 manual planar magnetron sputtering system (New Windsor, New York) onto the masked shrink film. After removing the vinyl mask, gold coated polystyrene films were shrunk at 160 °C. The metal films were lifted off from the substrates by dissolving the photoresist in acetone. The lifted-off gold films were then washed and transferred onto partially cured silicone elastomers, Sylgard-184 polydimethylsiloxane (PDMS) and Ecoflex® rubber, which were then cured to completion. Addition of methanol helped to overcome the electrostatic repulsion between PDMS and gold surfaces, thus making it easier to lay down the structured gold films.

The surface morphology of the gold thin films before and after lift-off was characterized using a JEOL JSM-7000S Scanning Electron Microscope with an accelerating voltage of 2.5 kV, working distance of 6 mm, and low probe current. An estimate of surface roughness by the root mean square (RMS) and peak-to-valley (PV) values was obtained using a Zygo NewView 5000 white light interferometry microscope (Zygo Corporation, Middlefield, Connecticut). The electrochemically active surface area of the gold films before shrinking, after shrinking on polystyrene, and transferred onto PDMS, was measured by cyclic voltammetry (CV) using a CHI 660D Electrochemical Workstation (CH Instrument, Austin, Texas). A standard three-electrode

set-up was used for electrochemical sensing, with the fabricated structured electrodes as working and counter electrodes, and an Ag/AgCl electrode as reference electrode. CV scans were performed in 0.05 M H_2SO_4 at a scan rate of 0.1 V s^{-1} and a voltage range between 0 and 1.5 V. Self-adhesive vinyl films with a single 0.5 cm by 0.5 cm square cut out were used as masks to expose the same geometric surface area (0.25 cm^2) of the gold films. The reduction peak of the resulting cyclic voltammograms was integrated to determine the charge and the electrochemically active surface area was calculated (Surface area = charge/surface charge density) using the surface charge density of a monolayer of gold, 386 μC cm^{-2}.

2-probe resistance measurements were performed on gold film electrodes using a source picoammeter (Model 2450, Keithley Instruments, Cleveland, Ohio). A droplet of eutectic gallium-indium (EGAIn, Sigma-Aldrich, St. Louis, Missouri) was used to create better contact between the Pt-wire probes and the structured gold films. The source voltage was swept linearly from 0 to 100 mV in 10 mV steps, and the resulting current was measured. I-V curves were recorded, and resistance R was extracted using $R = \Delta V/\Delta I$. The Au/PDMS and Au/Ecoflex electrodes were stretched on a home-built stretcher in 5% strain increments and resistance was measured at each strain level. The film resistance was obtained at 3-6 probe positions and compared across a minimum of three replicate devices. Bending measurements were carried out using custom machined Teflon holders with radii of 5, 2.5, and 1mm. Resistance was measured over 100 cycles of stretching and bending. The stretching process of micro/nanostructured gold film was imaged using Nikon Eclipse LV100N POL epifluorescence microscope (Nikon Instruments, Mississauga, Ontario) equipped with a Nikon 4×/0.10NA objective. Reflected and transmitted light images were taken from the gold electrode while it was being stretched from 0% to 100% strain at a 10% strain

interval. All these images were acquired with an Infinity 1 color camera (Lumenera, Ottawa, Ontario) and recorded with Infinity Capture software (Lumenera).

The flexible electrodes were used as working and counter electrodes to detect concentrations of potassium ferrocyanide and ascorbic acid electrochemically. An Ag/AgCl electrode was used as reference electrode in a three-electrode system. $K_4Fe(CN)_6$ solutions from 50 μM to 100 mM were measured by chronoamperometry at a fixed potential of 0.5 V for 1 s. 1M KCl was used as the supporting electrolyte. For ascorbic acid (AA) detection, all chronoamperometric measurements were performed at 0.4 V in 1×PBS (100 mM, pH=7.4). The transient background current was allowed to decay to a steady-state value before the addition of AA from 1 μM to 5 mM. The solution was stirred to provide convective transport.

5.5 Acknowledgements

This research was supported through the Natural Sciences and Engineering Research Council (NSERC, RGPIN/418326) and a Canada Foundation for Innovation Leaders Opportunity Fund. Y.Z. is partially supported by an NSERC IDEM CREATE grant. J.M.M. is the recipient of an Early Researcher Award through the Ontario Ministry of Research and Innovation. This research made use of instrumentation available through the BioInterfaces Institute and Canadian Centre for Electron Microscopy at McMaster University.

5.6 References

(1) Stoppa, M.; Chiolerio, A. Wearable Electronics and Smart Textiles: A Critical Review. *Sensors* **2014**, *14* (7), 11957–11992.

(2) Chortos, A.; Bao, Z. Skin-Inspired Electronic Devices. *Mater. Today* **2014**, *17* (7), 321–331.

(3) Cai, W.; Lai, T.; Du, H.; Ye, J. Electrochemical Determination of Ascorbic Acid, Dopamine and Uric Acid Based on an Exfoliated Graphite Paper Electrode: A High

Performance Flexible Sensor. *Sensors Actuators, B Chem*. **2014**, *193*, 492–500.

(4) Kim, U.; Kang, J.; Lee, C.; Kwon, H. Y.; Hwang, S.; Moon, H.; Koo, J. C.; Nam, J.-D.; Hong, B. H.; Choi, J.-B.; et al. A Transparent and Stretchable Graphene-Based Actuator for Tactile Display. *Nanotechnology* **2013**, *24* (14), 145501.

(5) Blattmann, C. O.; Sotiriou, G. A; Pratsinis, S. E. Rapid Synthesis of Multi-Layered & Multi-Functional Polymer Nanocomposite Films. *Nanotechnology* **2013**, *26* (12), 8092.

(6) Kim, T.; Song, H.; Ha, J.; Kim, S.; Kim, D.; Chung, S.; Lee, J.; Hong, Y. Inkjet-Printed Stretchable Single-Walled Carbon Nanotube Electrodes with Excellent Mechanical Properties. *Appl. Phys. Lett.* **2014**, *104* (11), 113103.

(7) Lim, S.; Son, D.; Kim, J.; Lee, Y. B.; Song, J.-K.; Choi, S.; Lee, D. J.; Kim, J. H.; Lee, M.; Hyeon, T.; et al. Transparent and Stretchable Interactive Human Machine Interface Based on Patterned Graphene Heterostructures. *Adv. Funct. Mater.* **2015**, *25* (3), 375–383.

(8) Kim, K. S.; Zhao, Y.; Jang, H.; Lee, S. Y.; Kim, J. M.; Kim, K. S.; Ahn, J.-H.; Kim, P.; Choi, J.-Y.; Hong, B. H. Large-Scale Pattern Growth of Graphene Films for Stretchable Transparent Electrodes. *Nature* **2009**, *457* (7230), 706–710.

(9) Görrn, P.; Cao, W.; Wagner, S. Isotropically Stretchable Gold Conductors on Elastomeric Substrates. *Soft Matter* **2011**, *7* (16), 7177.

(10) Wu, H.; Kong, D.; Ruan, Z.; Hsu, P.-C.; Wang, S.; Yu, Z.; Carney, T. J.; Hu, L.; Fan, S.; Cui, Y. A Transparent Electrode Based on a Metal Nanotrough Network. *Nat Nano* **2013**, *8* (6), 421–425.

(11) Amjadi, M.; Pichitpajongkit, A.; Lee, S.; Ryu, S.; Park, I. Highly Stretchable and Sensitive Strain Sensor Based on Silver Nanowire-Elastomer Nanocomposite. *ACS Nano* **2014**, *8* (5), 5154–5163.

(12) Hecht, D. S.; Hu, L.; Irvin, G. Emerging Transparent Electrodes Based on Thin Films of Carbon Nanotubes, Graphene, and Metallic Nanostructures. *Adv. Mater.* **2011**, *23* (13), 1482–1513.

(13) Gray, D. S.; Tien, J.; Chen, C. S. High-Conductivity Elastomeric Electronics. *Adv. Mater.* **2004**, *16* (5), 393–397.

(14) Guo, C. F.; Sun, T.; Liu, Q.; Suo, Z.; Ren, Z. Highly Stretchable and Transparent Nanomesh Electrodes Made by Grain Boundary Lithography. *Nat. Commun.* **2014**, *5*, 3121.

(15) Robinson, A. P.; Minev, I.; Graz, I. M.; Lacour, S. P. Microstructured Silicone Substrate for Printable and Stretchable Metallic Films. *Langmuir* **2011**, *27* (8), 4279–4284.

(16) Lin, S.; Lee, E. K.; Nguyen, N.; Khine, M. Thermally-Induced Miniaturization for Micro- and Nanofabrication: Progress and Updates. *Lab Chip* **2014**, *14* (18), 3475–3488.

(17) Nguyen, D.; Taylor, D.; Qian, K.; Norouzi, N.; Rasmussen, J.; Botzet, S.; Lehmann, M.;

Halverson, K.; Khine, M. Better Shrinkage than Shrinky-Dinks. *Lab Chip* **2010**, *10* (12), 1623–1626.

(18) Gabardo, C. M.; Zhu, Y.; Soleymani, L.; Moran-Mirabal, J. M. Bench-Top Fabrication of Hierarchically Structured High-Surface-Area Electrodes. *Adv. Funct. Mater.* **2013**, *23* (24), 3030–3039.

(19) de Santana, P. P.; de Oliveira, I. M. F.; Piccin, E. Evaluation of Using Xurography as a New Technique for the Fabrication of Disposable Gold Electrodes with Highly Reproducible Areas. *Electrochem. commun.* **2012**, *16* (1), 96–99.

(20) Sonney, S.; Shek, N.; Moran-Mirabal, J. M. Rapid Bench-Top Fabrication of Poly(dimethylsiloxane)/polystyrene Microfluidic Devices Incorporating High-Surface-Area Sensing Electrodes. *Biomicrofluidics* **2015**, *9* (2), 026501.

(21) Khang, D. Y.; Rogers, J. a.; Lee, H. H. Mechanical Buckling: Mechanics, Metrology, and Stretchable Electronics. *Adv. Funct. Mater.* **2009**, *19* (10), 1526–1536.

(22) Ho, X.; Nie Tey, J.; Liu, W.; Kweng Cheng, C.; Wei, J. Biaxially Stretchable Silver Nanowire Transparent Conductors. *J. Appl. Phys.* **2013**, *113*, 044311.

(23) Zang, J.; Ryu, S.; Pugno, N.; Wang, Q.; Tu, Q.; Buehler, M. J.; Zhao, X. Multifunctionality and Control of the Crumpling and Unfolding of Large-Area Graphene. *Nat. Mater.* **2013**, *12* (4), 321–325.

(24) Rogers, J. a; Someya, T.; Huang, Y. Materials and Mechanics for Stretchable Electronics. *Science* **2010**, *327* (5973), 1603–1607.

(25) Polywka, A.; Jakob, T.; Stegers, L.; Riedl, T.; Görrn, P. Facile Preparation of High-Performance Elastically Stretchable Interconnects. *Adv. Mater.* **2015**, *27*, 3755–3759.

(26) Lee, J.; Lee, P.; Lee, H.; Lee, D.; Lee, S. S.; Ko, S. H. Very Long Ag Nanowire Synthesis and Its Application in a Highly Transparent, Conductive and Flexible Metal Electrode Touch Panel. *Nanoscale* **2012**, *4* (20), 6408.

Chapter 6 Micro/nanostructured SiO_2 and TiO_2 Films Fabricated through Polymer Shrinking as Tunable Topography Substrates for Cell Studies

Yujie Zhu and Jose M. Moran-Mirabal designed the experiments. Yujie Zhu fabricated the glassy film substrates and characterized the surfaces with SEM. Yujie Zhu and Katija Bonin characterized the surface roughness with white light microscopy. Yujie Zhu, Justin Boyle, and Katija Bonin conducted the cell viability assays. Katija Bonin and Tanzina Chowdhury did the AFM imaging. Yujie and Justin Boyle cultured the cells on each type of substrate and conducted fractal analysis with the fluorescence images for cell morphology study. Yujie Zhu, Justin Boyle, Katija Bonin, and Jose M. Moran-Mirabal analyzed the data. Yujie Zhu, Justin Boyle and Jose M. Moran-Mirabal wrote the manuscript.

6.1 Abstract

The extracellular matrix plays a crucial role in the life of a cell because it influences numerous cellular interactions and functions. The fabrication of materials and structures that can mimic the ECM is of interest because they can control cell behaviour *in vitro*. Micro- to nanoscale topographies can provide physical cues to stimulate cells and lead to changes in cell morphology, migration, adhesion, proliferation, and differentiation. Numerous techniques have been utilized to generate various geometrical features to study cell response, including laser inference lithography, electrochemical/chemical etching, nano-imprinting lithography, and electrospinning. However, there is still a lack of techniques that can produce nanotopographic features that are easily tunable with low cost and high efficiency. In this work, we utilized micro/nanostructured SiO_2 and TiO_2

films fabricated through shrinking of a shape-memory polymer to investigate their impact on cell viability and morphology. The size of surface structures was easily tuned from the nano- to microscale by varying the thickness of the deposited glassy films. Fibroblasts were plated onto the substrates and showed excellent viability. Fractal analysis was used to quantitatively assess the cell morphology on the structured surfaces, and it was observed that larger surface structures induced cell elongation, while smaller structures stimulated the growth of cellular protrusions or filipodia. Such structured glassy surfaces are anticipated to provide *in vitro* platforms for the investigation of other cell behaviour such as cell adhesion and stem cell differentiation, and thus facilitate the reconstitution of tissue-like environments. It is further envisioned that these surfaces will find application in the fabrication of biosensing devices for circulating tumor cell isolation, and rare cell detection.

6.2 Introduction

The extracellular matrix (ECM) is a highly complex environment comprised of diverse physical and biochemical cues which direct cell function and determine cell fate.[1–3] As such, the ECM plays a crucial role in the initiation and maintenance of essential cell processes. Specifically, micro- and nano-sized topographical features encountered in natural microenvironments (*e.g.* in the bone marrow niche) can provide cues to stimulate cells, which lead to changes in cell properties such as contractility and morphology,[4–6] as well as different cellular behavior such as migration,[7,8] adhesion,[9,10] proliferation,[11] and differentiation.[12,13] Despite the pivotal role the ECM plays in the life cycle of a cell, it is underrepresented in traditional tissue culture techniques. As a result, there has been much research into the fabrication of tissue culture substrates that replicate the micro- and nanostructured cellular microenvironments observed *in vivo*. Furthermore, fabricating substrates that mimic the physical components of the ECM allows for the investigation of the

effects of surface topography on cell morphology and function, independent of any biochemical cues. In the past, a variety of techniques have been explored to generate micro/nanostructures, such as electron-beam lithography,[14–16] laser inference lithography,[17] electrochemical and chemical etching,[18–20] nano-imprint lithography,[21] electrospinning,[22,23] stencil lift-off,[24] and microfluidics.[25] Using these techniques, a variety of features (*e.g.* pits,[14,18] pillars,[15,21] grooves,[16,17,25] wells,[24] roughened surfaces[19,20], fibers,[22,23] etc.) have been fabricated for cell studies.

Numerous materials have been used to fabricate biomimetic substrates, such as metals or oxides,[26–28] molded thermoset elastomers (*e.g.* poly(dimethyl siloxane), PDMS),[28–30] polymer sheets (*e.g.* polyethylene and polystyrene), and electrospun polymeric and hydrogel scaffolds.[31–33] While elastomers such as PDMS are valuable for their ease of fabrication, they possess a softness and hydrophobicity that is not observed physiologically and may interfere with potential biomimetic applications. For structuring metallic and glassy materials, the main problems associated with traditional micro/nanofabrication techniques include the efficiency, economy, and ease of the fabrication. Moreover, the resulting structure sizes cannot be tuned easily and efficiently, as optimization of parameters and redesign of masks are frequently involved. As an alternative, shape-memory polymers have been employed to structure various thin film materials (*e.g.* gold, silver, platinum, ITO[34–37]) in a quick and inexpensive manner. Micro- and nanostructured surfaces can be generated through the stress mismatch between the thin film and the shape memory polymer substrate during thermal shrinking process. Although glass substrates have been used as conventional cell culture materials, the effect of continuous micro/nanostructured glassy films on cell behavior has not been explored. Taking advantage of thermal shrinking of pre-stressed polystyrene, in this work we present a simple, fast, and low-cost method to fabricate structured glassy surfaces with features whose length scale can mimic the

topographies encountered in natural cellular microenvironments. The structure sizes created on SiO_2 and TiO_2 surfaces through this approach can easily be controlled by varying the film thickness. Such surfaces are shown to be suitable for studying the effect of topography on murine fibroblast morphology.

Previous work has shown that one-dimensional features (*e.g.*, nanofibers,[38] grooves[25]) can induce cell elongation and alignment along the structures, but the effect of two-dimensional structures on cell morphology has not been well studied. Wang et al[30] compared the macrophage cell morphology on 1D and 2D wrinkled polymer surface, and found that 1D wrinkles induce cell elongation while cells on 2D wrinkles remained circular. Yet, this research explored only the aspect ratio of the cell morphology, which does not quantify the complexity of the cell shape and ignores the contribution of dynamic cytoplasmic protrusions. Fractal geometry is a mathematical tool that offers a quantitative description of pattern complexity in biological systems (*e.g.*, lipid bilayers,[39] cells,[40] neurons and brains[42]), and thus is ideally suited for the study of cell response to microenvironments with topographies in the micro- to nanoscale. However, to the best of our knowledge, it has not been used to characterize cellular morphology on structured surfaces, as most work has focused on measuring cell area, aspect ratio, circularity, and angular deviation. In this work, fractal analysis of individual cells has been explored, which provides a wealth of information on how cell shape complexity changes on structured surfaces.

6.3 Experimental Section

6.3.1 Micro/nanostructured glassy surface fabrication

Structured glassy films were fabricated using pre-stressed polystyrene shrink films as substrates (Graphix Shrink Film, Graphix, Maple Heights, OH). The polystyrene sheets were

washed under agitation at 50 rpm for 5 min in successive isopropanol, ethanol, and water baths, and dried with a nitrogen stream. The clean shrink films were then cut into 2x2 cm squares using a Robo Pro CE5000-40-CRP cutter (Graphtec America Inc., Irvine, CA) equipped with a CB09UB super steel blade. Three passes were required to cut through the film with force, quality and speed set at 30, 1, and 1, respectively. TiO_2 and SiO_2 were then deposited onto the polystyrene films using a Torr Compact Research Coater CRC-600 manual planar magnetron sputtering system (New Windsor, NY). The argon (>99.999% purity, AlphaGaz, Air Liquide, Montreal, QC, Canada) plasma was created by RF power of 100 W for SiO_2 and 60 W for TiO_2, which resulted in deposition rates of 0.2 and 0.3 Å/s respectively. 1-100 nm glassy films were deposited using both materials. The coated shrink films were shrunk on parchment paper covered aluminum boats at 115°C and 160°C in an Isotemp vacuum oven (Fisher Scientific, Ottawa, ON, Canada).

6.3.2 Glassy film surface characterization

Scanning Electron Microscopy (SEM) images of the glassy films shrunk at 115°C and 160°C were obtained using a JEOL JSM-7000S SEM with an accelerating voltage of 2.5 kV, working distance of 6 mm, and low probe current. The surface roughness was measured for glassy film coatings of all thicknesses using a Zygo NewView 5000 white light interferometer (Zygo Corporation, Middlefield, CT). The root mean square (RMS) and peak-to-valley (PV) values were obtained in 3-5 device areas and compared across a minimum of 3 replicate devices. Measurements were taken with 10× and 50× interferometric objectives with additional 2× optical magnification, which resulted in fields of view of 360×270 μm and 70×50 μm, respectively. Data was collected from a CCD camera with an imaging pixel size of 11.2 μm. The built in software, MetroPro, was used for data analysis. A Fast Fourier Transform (FFT) band pass filter was applied, using cutoff frequencies of 183.35 and 558.79 mm^{-1}. Spikes with height values above 10*RMS were removed

from the analysis of the imaged area to eliminate any contribution from contaminants (dust particles or defects on the films) to the roughness values.

6.3.3 Cell culturing

DMEM media (supplemented with 10% FCS, 1% L-glutamine, 1% penicillin/streptomycin [Invitrogen, Life Technologies, Burlington, ON, Canada]) was heated to 37°C. 30 mL of supplemented DMEM was pipetted into a 50 mL conical tube and kept warm at 37°C. A cryovial of frozen murine 3T3 fibroblasts (ATCC, Manassas, VA) was thawed as quickly as possible by swirling vial in a 37°C water bath. The contents were poured into the warm media and centrifuged at 500g for 5 minutes to remove the DMSO (Caledon Laboratory Chemicals, Georgetown, ON) from the cryovial contents. The cell pellet was resuspended in 15 mL of supplemented DMEM media and incubated overnight in a T25 tissue culture flask (Sigma-aldrich, Oakville, ON, Canada). When cells had grown to 80% confluency, they were sub-cultured on the glassy substrates. To subculture the murine 3T3 fibroblasts, the media from the T25 tissue culture flask was discarded, with the flask being subsequently washed with 1x PBS buffer. Following this, the buffer was removed and 10 mL Trypsin-EDTA (Invitrogen) was added to the culture flask. The flask was incubated at 37°C for 15 minutes and once all the cells were lifted, the cell/enzyme suspension was removed and transferred to a conical tube containing 20 mL of DMEM. The conical tube was then centrifuged at 500g for 5 minutes. The supernatant was removed and the cell pellet was resuspended in 10 mL of fresh DMEM. The cell concentration was estimated using a hemocytometer to which 10 μL of trypan blue (Invitrogen) and 10 μL of the cell suspension were added. Approximately 500 cells were added per substrate for the morphology assessments (*i.e.* fractal analysis, epifluorescence) and incubated at 37°C for 24 hours prior to fixation.

6.3.4 Cell viability assay

To test cell viability, a 0.4 mg/mL solution of dimethylthiazol-2-yl)-2,5-diphenyltetrazolium bromide (MTT, Sigma-Aldrich) was prepared in DMEM medium. 300 μL of the MTT solution was added to each sample in the well plate. The samples were then incubated at 37°C for a period of 4 hours, after which 500 μL of dimethyl sulfoxide (DMSO) was added to each sample to dissolve the formazan precipitate that forms when the cells are viable. Samples were run in triplicate. The absorbance for each sample was measured at both 570 nm and 600 nm using a multi-well SpectraMax i3 plate reader (Molecular Devices, Sunnyvale, CA).

6.3.5 Cell Fixation

Following the 24-hour incubation period, the old media was removed from each substrate. The samples were washed 3x with 1x PBS. A fixation solution comprised of 0.4% p-formaldehyde and 0.1% glutaraldehyde (Sigma-Aldrich) was added to each substrate in the well plate. The samples were then incubated at room temperature for 15 minutes in a dark environment. The substrates were washed 3x PBS once again and a 25 mM solution of glycine (Sigma-Aldrich) in 1x PBS was incubated on each sample for 10 minutes to quench the fixation process. Then, the glycine solution was replaced with a blocking solution (0.2% BSA and 0.2% Fish Gelatin in 1x PBS, Sigma-Aldrich) and incubated for 15 minutes at room temperature. The blocking solution was then removed and 1x PBS was added to each sample in the well plate. The substrates were refrigerated until further needed.

6.3.6 Fluorescence staining

The fluorescent dye DAPI (4',6-diamidino-2-phenylindole, dihydrochloride) (Invitrogen) was used to visualize the cell nuclei. The substrates were stained by adding 500 μL of a 600 nM a DAPI

stock solution in 1x PBS to each sample and incubating for 5 minutes. The DAPI staining solution was removed and the substrate was washed with 1x PBS. To stain the actin filaments, the cell membranes of the fibroblasts were first permeabilized using a 0.2% Triton-X 100 solution in 1x PBS with an incubation of 5 minutes. The substrates were then washed with 1x PBS, and 5 μL of stock AlexaFluor 488-phalloidin (Invitrogen) in 200 μL of 1x PBS were added and incubated for 20 minutes at room temperature to stain the actin filaments. Then, the staining solution was washed with 1x PBS and the samples were imaged using a Nikon Eclipse LV100N POL epifluorescence microscope (Nikon Instruments, Mississauga, ON) equipped with a physiological 60x/0.9NA objective, and a Retiga 200R camera. NIS software (Nikon Instruments, Mississauga, ON) was used to capture the fluorescence images.

6.3.7 Fractal Analysis

The box counting method[288] was used to quantitatively analyse the changes in macrophage morphology when cultured on structured glassy films. Briefly, the box counting method involves using boxes of different sizes and determining how many boxes are needed to cover the area or perimeter of the cell. The images used in the fractal analysis were fluorescence images of cells converted to binary maps, which were then used as input for a box counting program written on MATLAB (MathWorks). Specifically, the binary maps were generated using an intensity threshold of 2σ above the mean background (defined manually in an area devoid of cells). For each image processed, the fractal analysis program generated a plot of $ln(1/N)$ *vs*. $ln(s)$, where N represents the number of boxes, and s the size of the boxes (in pixels or pixels^2, for perimeter and area respectively). When there is a scaling law represented by the shape of the cell, the resulting graph is linear, with the slope representing the fractal dimension (F_D). Fractal dimensions were generated

for the area and the perimeter of the cell, as shown in Fig. S1. A sample size of n ≥ 30 cells from each type of substrate was used for the fractal analysis.

6.3.8 Statistical Analysis

All the data are reported as the sample average and the standard deviation. Comparisons between multiple samples were performed with one-way analysis of variance (ANOVA). Tukey's post-test was performed to a significance level of $P<0.05$. The Asterisks indicate **p- value <0.01, and ***p-value <0.001, and the same for dots where $^{\bullet\bullet}p<0.01$, $^{\bullet\bullet\bullet}p<0.001$, $^{\bullet\bullet\bullet\bullet}p<0.0001$.

6.4 Results and Discussion

6.4.1 Structured glassy surface characterization

The structured glassy films were fabricated by shrinking the SiO_2 and TiO_2 coated pre-stressed polystyrene films above their glass transition temperature (~100°C), as illustrated in Figure 6-1a. The two different conditions tested for shrinking were 115°C for 30 min and 160°C for 3 min, which controlled the rate of compression of the glassy films. The area of the films decreased by 84% under both conditions, and the compressive stress induced micro/nanostructures on the film surfaces, as revealed by SEM (Figure 6-1b). Structures formed with various film thicknesses (1-100 nm) were compared. Similar to what has been previously observed for gold films,[38,39] the thicker glassy films generated larger structures. However, unlike metal films, the glassy films started to crack on the wrinkle folds at a 20 nm film thickness, and fractured for films with thickness > 50 nm, due to the low fracture toughness of SiO_2 and TiO_2.

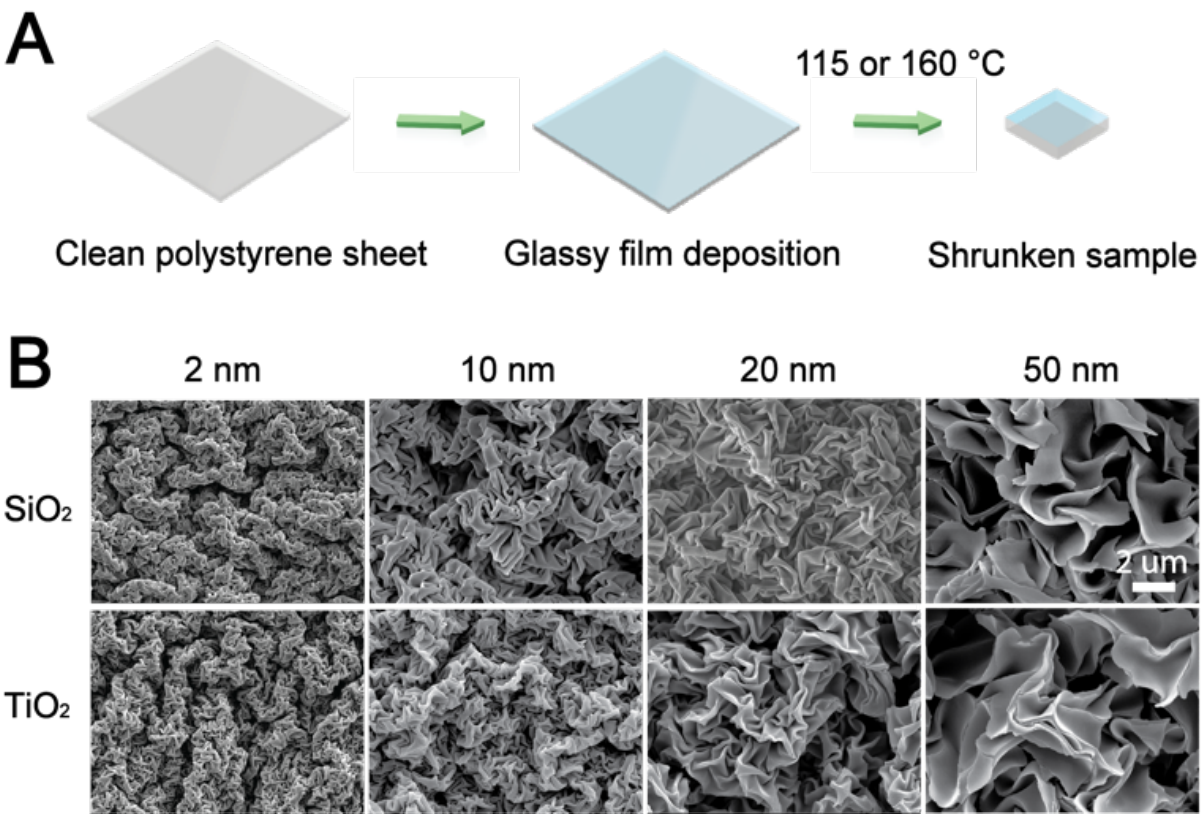

Figure 6-1 Compressive stress induced structuring of glassy films. (a) Schematic of micro/nanostructured glassy film fabrication. (b) SEM images show the topography of micro/nanostructured SiO_2 and TiO_2 surfaces of films with thicknesses of 2 - 50 nm that were shrunk at 160°C.

White light interferometry microscopy (WLIM) was used to quantitatively assess the root mean square (RMS) roughness and peak-to-valley (PV) values of the structured surfaces. Both RMS roughness and PV values initially increased with increasing film thickness and plateaued for thick films as they fractured during structuring, which was in good agreement with the observation from SEM images (Figure 6-2). It was also found that the shrinking conditions had some impact on the surface roughness: the higher temperature (160°C) resulted in higher surface roughness due to faster shrinking, compared to the lower temperature (115°C), as shown in Figures S2 and S3. Due to the small size of the structures of the thinnest films, atomic force microscopy (AFM) was

used to characterize 1 and 2 nm films, and the results corroborated the roughness value obtained by WLIM (Figure S4).

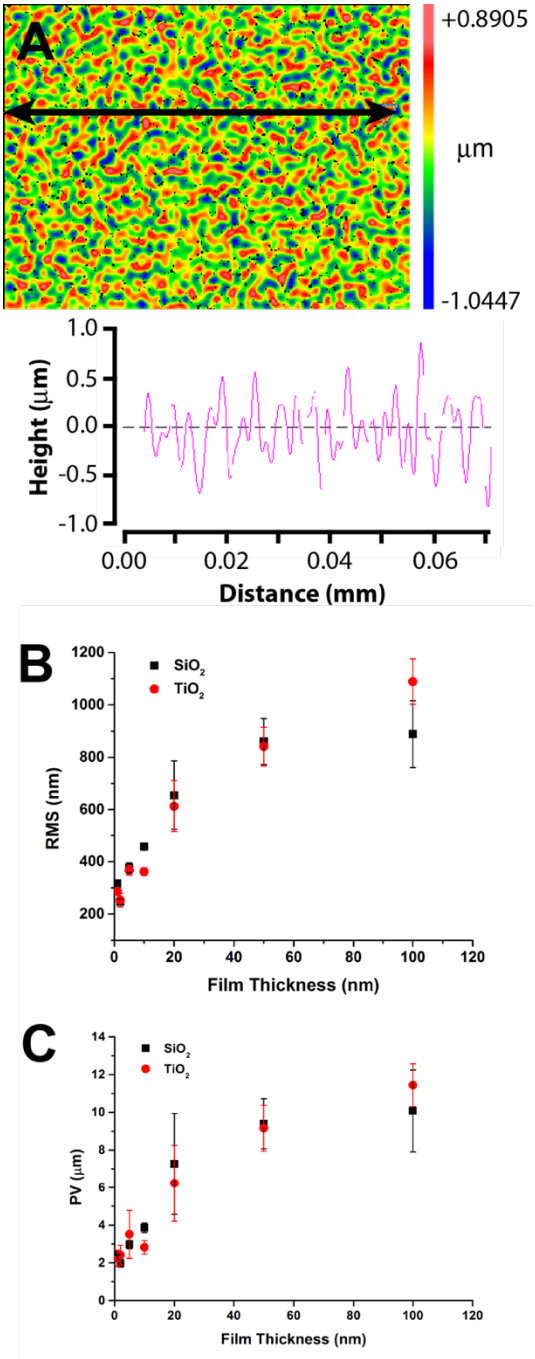

Figure 6-2 The surface roughness of the structured substrates was characterized via white light interferometry microscopy. (A) Typical topographical map and height profile obtained for a 1 nm SiO_2 film shrunk at 160°C. (B) RMS roughness and (C) peak-to-valley (range of height data) of structured SiO_2 and TiO_2 films of varying thickness.

6.4.2 Cell viability on glassy films

To investigate the effect of surface roughness on cell behaviour, 2, 10, and 50 nm SiO_2 and TiO_2 substrates were selected as films with structures of representative sizes. Murine 3T3 fibroblast cells were plated and on both flat and structured glassy films of different thicknesses, as well as bare polystyrene substrates, and were cultured at 37 °C for 24 hours. The MTT assay was then performed to assess their viability on these substrates. The results showed that for all the structured SiO_2 and TiO_2 substrates, the relative viability normalized to the polystyrene was *ca.* 100% (Figure 6-3), indicating that the structured substrates are suitable for continued cell culture.

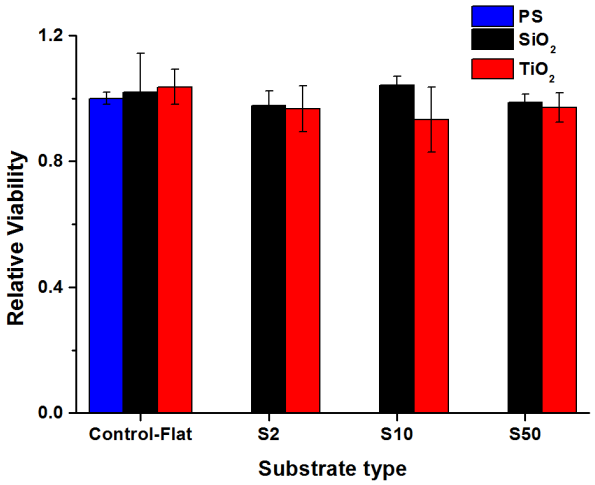

Figure 6-3 Relative viability of murine 3T3 fibroblasts on polystyrene (blue), flat (control), and 2, 10, and 50 nm structured SiO_2 (black) and TiO_2 (red) surfaces. Viability was normalized to polystyrene control.

6.4.3 Fibroblast cell morphology analysis

The effect of substrate topography on cell morphology was investigated by fixing the cells grown on the flat and structured substrates and imaging them using epifluorescence microscopy. Cell morphology was visualized by staining with two dyes: DAPI for the nuclei and Alexa Fluor 488 labelled phalloidin to tag the actin filaments. Figure 6-4a shows representative images of

murine 3T3 fibroblasts on polystyrene, and flat and structured glassy surfaces. Qualitatively, it was observed that cells were more elongated and spread out on structured surfaces, and more cellular protrusions (filipodia) were generated on surfaces with finer topography.

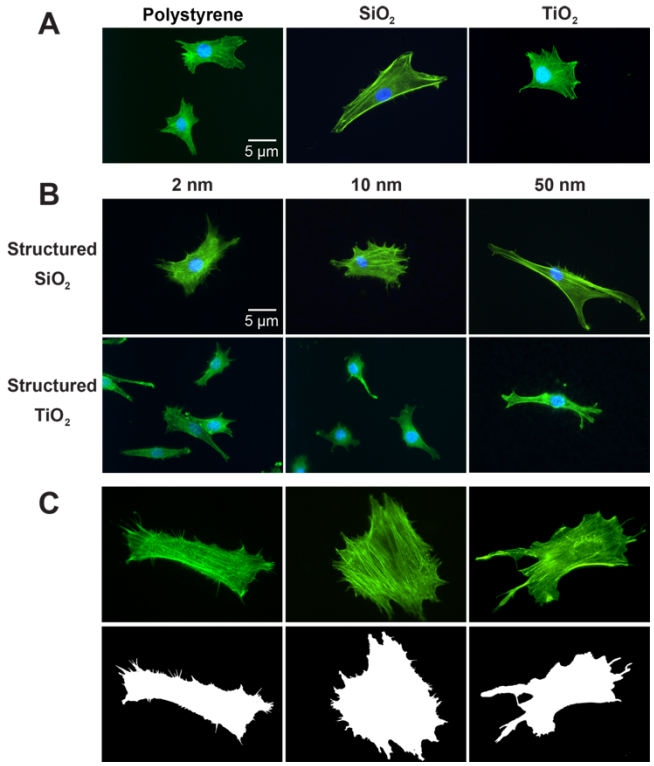

Figure 6-4 Representative fluorescence images of 3T3 murine fibroblasts grown on flat (a) and structured (b) surfaces. Blue shows the nuclei of cells stained with DAPI, and green indicates the actin filaments labelled with Alexa Fluor 488 phalloidin. (c) Comparison of the fluorescence images and the binary images generated for fractal analysis of a cell. All images taken at the same magnification, except zoomed in images in panel (c).

Quantitative evaluation of cell morphologies was carried out through fractal analysis for cells grown on each type of substrate. Fractal analysis was first proposed by Mandelbrot *et al*.[45] in the 1980s and later was applied for cell image analysis.[46,47] In our study, the box counting method was used to generate fractal dimensions for the cell area (FDA) and perimeter (FDP). To interpret the values obtained and gain insight into the way cells change in response to topographical features, it

is useful to keep in mind that a larger fractal dimension value means that the object (cell) becomes more complex as the box size decreases. A smaller value means that the amount of detail of the cell does not increase as rapidly with smaller pixel sizes. For a two-dimensional image, the fractal dimension of area will lie between 1 and 2, with the value of 1 corresponding to a line and the value of 2 corresponding to a square shape.

Comparing the FDA values obtained from fibroblasts (Figure 5a), we found that that cells grown on flat SiO_2 and TiO_2 surfaces had significantly lower FDA values than cells grown on polystyrene, meaning that they were more elongated. We attributed this to the higher stiffness of the glassy films, since previous work has shown that fibroblasts spread more readily and display elongated morphologies on stiffer surfaces.[48,49] We then compared the structured surfaces to the flat ones and observed that only the cells grown on wrinkled surfaces produced from 50 nm-thick films showed a decrease in FDA value, making the cells even less square-like. Such elongation behaviour has been demonstrated with 1D nano-topographical features such as nanofibers,[51,52] gratings,[52] and grooves[30], but not with randomly oriented structured surfaces like the ones used in this study.

Although the FDA values for wrinkled surfaces produced from 2 and 10 nm-thick films did not significantly differ from the unstructured ones, we observed that a larger amount of filipodia were generated by cells cultured on these surfaces. Therefore, fractal analysis on the cell boundary (perimeter) was performed, as the FDP value would provide more information about the fine details of the cellular morphology. A higher FDP value indicates more complex boundary of the cell shapes. From Figure 5b, it is observed that cells grown on structured surfaces made from 2 and 10 nm-thick SiO_2 films had more complex boundary structures than those grown on flat

surfaces. With this analysis, the structured surfaces made from 50 nm-thick surfaces did not have much impact in the number of filipodia that the cells produce.

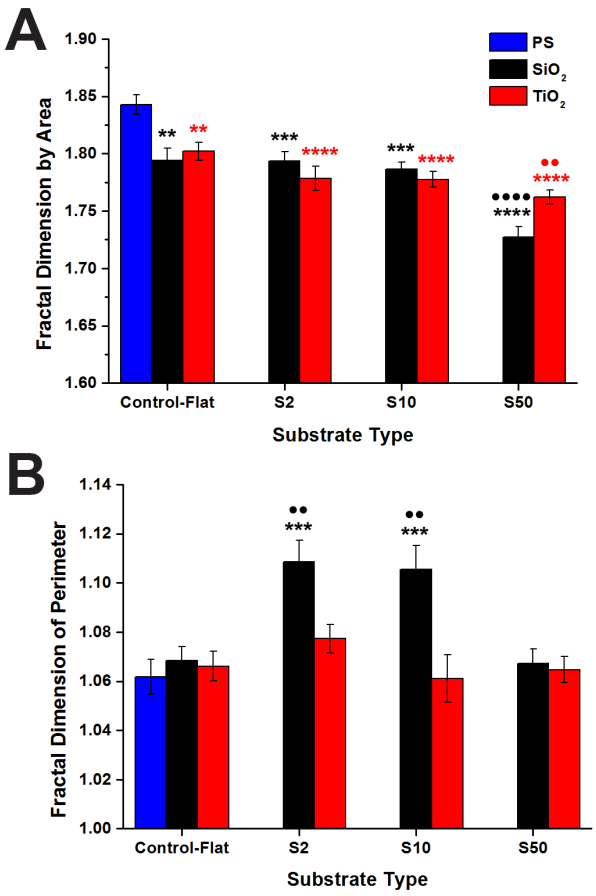

Figure 6-5 Quantitative fibroblast morphology assessment through fractal analysis. (a) Fractal dimension for area and (b) perimeter of fibroblasts grown on polystyrene (blue), flat (control), and 2, 10, and 50 nm structured SiO_2 (black) and TiO_2 (red) surfaces. Statistical significance: **p<0.01, ***p<0.001, ****p<0.0001 when compared against polystyrene control, and $^{••}$p<0.01, $^{••••}$p<0.0001 when compared against flat SiO_2 or TiO_2 control, n = 30 cells.

The different effects of the rougher and finer surfaces on cell morphology can be interpreted by the structure size scales. The structures generated with the 2 and 10 nm- thick glassy films are in the range of a few hundred nanometers, which is similar to filopodium-size (100-300 nm).[53] These fine structures are too small to stimulate a change in the overall cell shape, but provide

enough roughness to promote filopodia growth. This results implies that filopodia are able to sense nanotopographies of a comparable size range, which has been previously suggested by Kang et al. who reported that developmental acceleration of hippocampal neurons occurred on filopodium-size nanotopographies.[54] In contrast, the wrinkle sizes obtained with 50-nm-thick glassy surfaces are in the micron range, which is comparable to the fibroblast cell size (10-15 μm). As a result, they did not promote filopodia generation, but introduce cell elongation. The width of the wrinkles are in nanometer scale, which provided the suitable size range for contact guidance, as proposed in some other work.[38,55] The morphology of cells cultured on TiO_2 substrates follow similar trend to those on SiO_2, but with subtler differences. This observation suggested that the material properties of the substrate are also an essential factor for changing cell morphology, beyond surface topography.

6.5 Conclusions

In conclusion, we have demonstrated a quick and cost-efficient way of fabricating tuneable micro/nanostructured glassy surfaces for cell morphology studies. This bench top fabrication method involves only two steps which are SiO_2 and TiO_2 thin film deposition and thermal shrinking of pre-stressed polystyrene. The surface structure size can be easily tuned by varying the thickness of the glassy film deposited prior to shrinking. Such surfaces are suitable for murine 3T3 fibroblast culture, as the relative viability of cells was *ca*. 100% when compared to polystyrene. According to the results obtained through qualitative and quantitative analysis of fibroblast cells, it can be concluded that cell growth on micro/nanostructured glassy substrates can induce changes in cell morphology. Specifically, the larger surface structures generated by 50 nm-thick glassy films contributed more to changes in the general cell shape, while the smaller structures generated by 2 and 10 nm-thick films did not significantly change the general shape, but stimulated the

growth of cellular protrusions. These structured glassy films could be further used to investigate how the morphological changes observed in cells influence any of their functional characteristics. We anticipate that the ability of the structured glassy films to selectively influence cell morphology could be used to enhance *in vitro* assays by mimicking the micro- and nanostructural components of the cellular microenvironment.

6.6 Acknowledgements

This work was supported through the Natural Sciences and Engineering Research Council (RGPIN/418326) and the Canada Foundation for Innovation Leaders Opportunity Fund. JMM is the recipient of an Early Researcher Award through the Ontario Ministry of Research and Innovation. YZ, JB and KT were partially supported by the Interdisciplinary Development of Extracellular Matrices Collaborative Research Training Program. We thank Dr. Peter Kruse for access to Atomic Force Microscopy Equipment and Dr. Todd Hoare for the donation of fibroblast cells. This research made use of facilities at the Centre for Emerging Device Technology and the Canadian Centre for Electron microscopy at McMaster University.

6.7 References

(1) Watt, F. M.; Huck, W. T. S. Role of the Extracellular Matrix in Regulating Stem Cell Fate. *Nat. Rev. Mol. Cell Biol.* **2013**, *14* (8), 467–473.

(2) Berthiaume, F.; Moghe, P. V; Toner, M.; Yarmush, M. L. Effect of Extracellular Matrix Topology on Cell Structure, Function, and Physiological Responsiveness: Hepatocytes Cultured in a Sandwich Configuration. *FASEB J.* **1996**, *10* (13), 1471–1484.

(3) Gattazzo, F.; Urciuolo, A.; Bonaldo, P. Extracellular Matrix: A Dynamic Microenvironment for Stem Cell Niche. *Biochim. Biophys. Acta - Gen. Subj.* **2014**, *1840* (8), 2506–2519.

(4) Huang, N. F.; Lai, E. S.; Ribeiro, A. J. S.; Pan, S.; Pruitt, B. L.; Fuller, G. G.; Cooke, J. P. Spatial Patterning of Endothelium Modulates Cell Morphology, Adhesiveness and Transcriptional Signature. *Biomaterials* **2013**, *34* (12), 2928–2937.

(5) Andersson, A.-S.; Bäckhed, F.; von Euler, A.; Richter-Dahlfors, A.; Sutherland, D.;

Kasemo, B. Nanoscale Features Influence Epithelial Cell Morphology and Cytokine Production. *Biomaterials* **2003**, *24* (20), 3427–3436.

(6) Tsimbouri, P.; Gadegaard, N.; Burgess, K.; White, K.; Reynolds, P.; Herzyk, P.; Oreffo, R.; Dalby, M. J. Nanotopographical Effects on Mesenchymal Stem Cell Morphology and Phenotype. *J. Cell. Biochem.* **2014**, *115* (2), 380–390.

(7) Charras, G.; Sahai, E. Physical Influences of the Extracellular Environment on Cell Migration. *Nat. Rev. Mol. Cell Biol.* **2014**, *15* (12), 813–824.

(8) Hadjizadeh, A.; Doillon, C. J. Directional Migration of Endothelial Cells towards Angiogenesis Using Polymer Fibres in a 3D Co-Culture System. *J. Tissue Eng. Regen. Med.* **2010**, *4* (7), 524–531.

(9) Kasputis, T.; Pieper, A.; Rodenhausen, K. B.; Schmidt, D.; Sekora, D.; Rice, C.; Schubert, E.; Schubert, M.; Pannier, A. K. Use of Precisely Sculptured Thin Film (STF) Substrates with Generalized Ellipsometry to Determine Spatial Distribution of Adsorbed Fibronectin to Nanostructured Columnar Topographies and Effect on Cell Adhesion. *Acta Biomater.* **2015**, *18*, 88–99.

(10) Groves, J. T.; Dustin, M. L. Supported Planar Bilayers in Studies on Immune Cell Adhesion and Communication. *J. Immunol. Methods* **2003**, *278*, 19–32.

(11) Chaudhuri, P. K.; Pan, C. Q.; Low, B. C.; Lim, C. T. Topography Induces Differential Sensitivity on Cancer Cell Proliferation via Rho-ROCK-Myosin Contractility. *Sci. Rep.* **2016**, *6*, 19672.

(12) Lu, D.; Luo, C.; Zhang, C.; Li, Z.; Long, M. Differential Regulation of Morphology and Stemness of Mouse Embryonic Stem Cells by Substrate Stiffness and Topography. *Biomaterials* **2014**, *35* (13), 3945–3955.

(13) Qi, L.; Li, N.; Huang, R.; Song, Q.; Wang, L.; Zhang, Q.; Su, R.; Kong, T.; Tang, M.; Cheng, G. The Effects of Topographical Patterns and Sizes on Neural Stem Cell Behavior. *PLoS One* **2013**, *8* (3), 2–9.

(14) Dalby, M. J.; Gadegaard, N.; Tare, R.; Andar, A.; Riehle, M. O.; Herzyk, P.; Wilkinson, C. D.; Oreffo, R. O. The Control of Human Mesenchymal Cell Differentiation Using Nanoscale Symmetry and Disorder. *Nat. Mater.* **2007**, *6* (5), 407–413.

(15) Padmanabhan, J.; Kinser, E. R.; Stalter, M. A.; Duncan-lewis, C.; Balestrini, J. L.; Sawyer, A. J.; Schroers, J.; Kyriakides, T. R. Engineering Cellular Response Using Nanopatterned Bulk Metallic Glass. *ACS Nano* **2014**, *8* (5), 4366–4375.

(16) Klymov, A.; Bronkhorst, E. M.; Te Riet, J.; Jansen, J. A.; Walboomers, X. F. Bone Marrow-Derived Mesenchymal Cells Feature Selective Migration Behavior on Submicro- and Nano-Dimensional Multi-Patterned Substrates. *Acta Biomater.* **2015**, *16* (1), 117–125.

(17) Pan, F.; Zhang, M.; Wu, G.; Lai, Y.; Greber, B.; Schöler, H. R.; Chi, L. Topographic Effect on Human Induced Pluripotent Stem Cells Differentiation towards Neuronal Lineage. *Biomaterials* **2013**, *34* (33), 8131–8139.

(18) Zinger, O.; Anselme, K.; Denzer, A.; Habersetzer, P.; Wieland, M.; Jeanfils, J.; Hardouin, P.; Landolt, D. Time-Dependent Morphology and Adhesion of Osteoblastic Cells on Titanium Model Surfaces Featuring Scale-Resolved Topography. *Biomaterials* **2004**, *25* (14), 2695–2711.

(19) Anselme, K.; Bigerelle, M. Topography Effects of Pure Titanium Substrates on Human Osteoblast Long-Term Adhesion. *Acta Biomater.* **2005**, *1* (2), 211–222.

(20) Gentile, F.; Medda, R.; Cheng, L.; Battista, E.; Scopelliti, P. E.; Milani, P.; Cavalcanti-Adam, E. a; Decuzzi, P. Selective Modulation of Cell Response on Engineered Fractal Silicon Substrates. *Sci. Rep.* **2013**, *3*, 1461.

(21) Moe, A. A. K.; Suryana, M.; Marcy, G.; Lim, S. K.; Ankam, S.; Goh, J. Z. W.; Jin, J.; Teo, B. K. K.; Law, J. B. K.; Low, H. Y.; Goh, E. L. K.; Sheetz, M. P.; Yim, E. K. F. Microarray with Micro- and Nano-Topographies Enables Identification of the Optimal Topography for Directing the Differentiation of Primary Murine Neural Progenitor Cells. *Small* **2012**, *8* (19), 3050–3061.

(22) Nathan, A. S.; Baker, B. M.; Nerurkar, N. L.; Mauck, R. L. Mechano-Topographic Modulation of Stem Cell Nuclear Shape on Nanofibrous Scaffolds. *Acta Biomater.* **2011**, *7* (1), 57–66.

(23) Jhala, D.; Rather, H.; Vasita, R. Polycaprolactone–chitosan Nanofibers Influence Cell Morphology to Induce Early Osteogenic Differentiation. *Biomater. Sci.* **2016**, *4* (11), 1584–1595.

(24) Myers, F. B.; Silver, J. S.; Zhuge, Y.; Beygui, R. E.; Zarins, C. K.; Lee, L. P.; Abilez, O. J. Robust Pluripotent Stem Cell Expansion and Cardiomyocyte Differentiation via Geometric Patterning. *Integr. Biol.* **2013**, *5* (12), 1495–1506.

(25) Hwang, S. Y.; Kwon, K. W.; Jang, K.-J.; Park, M. C.; Lee, J. S.; Suh, K. Y. Adhesion Assays of Endothelial Cells on Nanopatterned Surfaces within a Microfluidic Channel. *Anal. Chem.* **2010**, *82* (7), 3016–3022.

(26) Jahed, Z.; Molladavoodi, S.; Seo, B. B.; Gorbet, M.; Tsui, T. Y.; Mofrad, M. R. K. Cell Responses to Metallic Nanostructure Arrays with Complex Geometries. *Biomaterials* **2014**, *35* (34), 9363–9371.

(27) Dhawan, U.; Pan, H. A.; Lee, C. H.; Chu, Y. H.; Huang, G. S. Spatial Control of Cell-Nanosurface Interactions by Tantalum Oxide Nanodots for Improved Implant Geometry. **2016**, 1–17.

(28) Ankam, S.; Suryana, M.; Chan, L. Y.; Moe, A. A. K.; Teo, B. K. K.; Law, J. B. K.; Sheetz, M. P.; Low, H. Y.; Yim, E. K. F. Substrate Topography and Size Determine the Fate of Human Embryonic Stem Cells to Neuronal or Glial Lineage. *Acta Biomater.* **2013**, *9* (1), 4535–4545.

(29) Viswanathan, P.; Guvendiren, M.; Chua, W.; Telerman, S. B.; Liakath-Ali, K.; Burdick, J. A.; Watt, F. M. Mimicking the Topography of the Epidermal-Dermal Interface with

Elastomer Substrates. *Integr. Biol. (Camb).* **2016**, *8* (1), 21–29.

(30) Wang, T.; Luu, T. U.; Chen, A.; Khine, M.; Liu, W. F. Topographical Modulation of Macrophage Phenotype by Shrink-Film Multi-Scale Wrinkles. *Biomater. Sci.* **2016**, 0–4.

(31) Kim, I. L.; Khetan, S.; Baker, B. M.; Chen, C. S.; Burdick, J. A. Fibrous Hyaluronic Acid Hydrogels That Direct MSC Chondrogenesis through Mechanical and Adhesive Cues. *Biomaterials* **2013**, *34* (22), 5571–5580.

(32) Low, W. C.; Rujitanaroj, P. O.; Lee, D. K.; Messersmith, P. B.; Stanton, L. W.; Goh, E.; Chew, S. Y. Nanofibrous Scaffold-Mediated REST Knockdown to Enhance Neuronal Differentiation of Stem Cells. *Biomaterials* **2013**, *34* (14), 3581–3590.

(33) Tian, L.; Prabhakaran, M. P.; Hu, J.; Chen, M.; Besenbacher, F.; Ramakrishna, S. Synergistic Effect of Topography, Surface Chemistry and Conductivity of the Electrospun Nanofibrous Scaffold on Cellular Response of PC12 Cells. *Colloids Surf B Biointerfaces* **2016**, *145*, 420–429.

(34) Lin, S.; Lee, E. K.; Nguyen, N.; Khine, M. Thermally-Induced Miniaturization for Micro- and Nanofabrication: Progress and Updates. *Lab Chip* **2014**, *14* (18), 3475–3488.

(35) Nguyen, D.; Taylor, D.; Qian, K.; Norouzi, N.; Rasmussen, J.; Botzet, S.; Lehmann, M.; Halverson, K.; Khine, M. Better Shrinkage than Shrinky-Dinks. *Lab Chip* **2010**, *10* (12), 1623–1626.

(36) Sonney, S.; Shek, N.; Moran-Mirabal, J. M. Rapid Bench-Top Fabrication of Poly(dimethylsiloxane)/polystyrene Microfluidic Devices Incorporating High-Surface-Area Sensing Electrodes. *Biomicrofluidics* **2015**, *9* (2), 26501.

(37) Zhang, B.; Zhang, M.; Song, K.; Li, Q.; Cui, T. Shrink Induced Nanostructures for Energy Conversion Efficiency Enhancement in Photovoltaic Devices. *Appl. Phys. Lett.* **2013**, *103*, 23104.

(38) Chaurey, V.; Block, F.; Su, Y. H.; Chiang, P. C.; Botchwey, E.; Chou, C. F.; Swami, N. S. Nanofiber Size-Dependent Sensitivity of Fibroblast Directionality to the Methodology for Scaffold Alignment. *Acta Biomater.* **2012**, *8* (11), 3982–3990.

(39) Moran-Mirabal, J. M.; Aubrecht, D. M.; Craighead, H. G. Phase Separation and Fractal Domain Formation in Phospholipid/diacetylene-Supported Lipid Bilayers. *Langmuir* **2007**, *23* (21), 10661–10671.

(40) Behar, T. N. Analysis of Fractal Dimension of O2A Glial Cells Differentiating in Vitro. *Methods* **2001**, *24* (4), 331–339.

(41) Di Ieva, A.; Grizzi, F.; Jelinek, H.; Pellionisz, A. J.; Losa, G. A. Fractals in the Neurosciences, Part I: General Principles and Basic Neurosciences. *Neuroscientist* **2013**, *20* (4), 403–417.

(42) Dewey, T. G. *Fractals in Molecular Biophysics*.; Oxford University Press: New York, **1997**.

(43) Gabardo, C. M.; Zhu, Y.; Soleymani, L.; Moran-Mirabal, J. M. Bench-Top Fabrication of Hierarchically Structured High-Surface-Area Electrodes. *Adv. Funct. Mater.* **2013**, *23* (24), 3030–3039.

(44) Zhu, Y.; Moran-Mirabal, J. Highly Bendable and Stretchable Electrodes Based on Micro/Nanostructured Gold Films for Flexible Sensors and Electronics. *Adv. Electron. Mater.* **2016**, *2*, 1500345.

(45) Mandelbrot, B. B.; Passoja, D. E.; Paullay, A. J. Fractal Character of Fracture Surfaces of Metals. *Nature* **1984**, *308*, 721–722.

(46) Smith, T. G.; Marks, W. B.; Lange, G. D.; Sheriff, W. H.; Neale, E. A. A Fractal Analysis of Cell Images. *J. Neurosci. Methods* **1989**, *27* (2), 173–180.

(47) Smith, T. G.; Lange, G. D.; Marks, W. B. Fractal Methods and Results in Cellular Morphology - Dimensions, Lacunarity and Multifractals. *J. Neurosci. Methods* **1996**, *69* (2), 123–136.

(48) Hopp, I.; Michelmore, A.; Smith, L. E.; Robinson, D. E.; Bachhuka, A.; Mierczynska, A.; Vasilev, K. The Influence of Substrate Stiffness Gradients on Primary Human Dermal Fibroblasts. *Biomaterials* **2013**, *34* (21), 5070–5077.

(49) Yeung, T.; Georges, P. C.; Flanagan, L. A.; Marg, B.; Ortiz, M.; Funaki, M.; Zahir, N.; Ming, W.; Weaver, V.; Janmey, P. A. Effects of Substrate Stiffness on Cell Morphology, Cytoskeletal Structure, and Adhesion. *Cell Motil. Cytoskeleton* **2005**, *60* (1), 24–34.

(50) Han, J.; Wu, Q.; Xia, Y.; Wagner, M. B.; Xu, C. Cell Alignment Induced by Anisotropic Electrospun Fibrous Scaffolds Alone Has Limited Effect on Cardiomyocyte Maturation. *Stem Cell Res.* **2016**, *16* (3), 740–750.

(51) Tseng, L. F.; Mather, P. T.; Henderson, J. H. Shape-Memory-Actuated Change in Scaffold Fiber Alignment Directs Stem Cell Morphology. *Acta Biomater.* **2013**, *9* (11), 8790–8801.

(52) Pholpabu, P.; Kustra, S.; Wu, H.; Balasubramanian, A.; Bettinger, C. J. Lithography-Free Fabrication of Reconfigurable Substrate Topography for Contact Guidance. *Biomaterials* **2015**, *39*, 164–172.

(53) Mattila, P. K.; Lappalainen, P. Filopodia: Molecular Architecture and Cellular Functions. *Nat. Rev. Mol. Cell Biol.* **2008**, *9* (6), 446–454.

(54) Kang, K.; Choi, S. E.; Jang, H. S.; Cho, W. K.; Nam, Y.; Choi, I. S.; Lee, J. S. In Vitro Developmental Acceleration of Hippocampal Neurons on Nanostructures of Self-Assembled Silica Beads in Filopodium-Size Ranges. *Angew. Chemie - Int. Ed.* **2012**, *51* (12), 2855–2858.

(55) Loesberg, W. A.; te Riet, J.; van Delft, F. C. M. J. M.; Schön, P.; Figdor, C. G.; Speller, S.; van Loon, J. J. W. A.; Walboomers, X. F.; Jansen, J. A. The Threshold at Which Substrate Nanogroove Dimensions May Influence Fibroblast Alignment and Adhesion. *Biomaterials* **2007**, *28* (27), 3944–3951.

Chapter 7 Conclusions and Future Outlook

7.1 Conclusions

The development of fabrication techniques has made it possible to tailor material attributes and thus micro/nanostructured surfaces are becoming increasingly important for a variety of applications, such as electronics, photonics, sensing devices, tissue engineering, bio-diagnostics, etc.[1–6] The demand for fabrication techniques that can be easily scaled up in a time and cost-efficient manner is one of the major driving forces in the development of micro/nanotechnology. In this dissertation, we have presented the application of thin film lift-off to pattern multi-component and multi-stacked supported lipid bilayers (SLB) and the use of pre-stressed polystyrene film shrinking to structure and pattern thin film materials for high surface area electrodes, stretchable electronics, and tissue engineering.

We have shown improvements to the polymer stencil lift-off (PSLO) technique and its implementation in creating complex supported lipid bilayer (SLB) micropatterns. PSLO is a relatively new patterning method that enables the formation of arrays of micro- to nanometre-sized biomaterial domains over large surface areas.[7–11] In Chapter 2, we used bovine serum albumin (BSA) during the stencil lift-off process to prevent SLB spreading on the patterned feature edges, as BSA molecules adhered to the substrate and compete efficiently with the lipid lateral diffusion. It was also demonstrated that an optimized UV/O_3 and base treatment could effectively remove residual Parylene in the openings, and result in a cleaner and smoother surface for SLB formation with higher mobility. The improved PSLO has been used to produce phase-segregated SLBs with patterned feature size down to 2 μm. In addition, the effect of patterned feature size effect on lipid phase separation was studied for the first time: the percent area of gel phase and the average gel

phase area size decreases with patterned feature sizes and gel phase nucleation is suppressed along the patterned feature edges.

In Chapter 3, we further utilized the improved PSLO protocol to pattern multi-stacked supported lipid bilayers. Through electrostatic interactions between the SLBs, the lipid bilayers were successfully stacked within the micron-sized openings of the polymer stencils, and up to four layer of homogeneous SLB were formed. The stacking of phase-segregated SLB was also achieved, showing that the gel-phase domains of subsequent added layers register with each other. The ability to pattern stacked SLBs with easy control of their components and layer orders, provides a new approach for creating cushioned SLB micropatterns. Such elevated SLBs patterns also have the potential advantage of being able to accommodate transmembrane proteins by preventing their direct contact with the substrate. We believe that these facile and robust strategies are easily transferrable to pattern other type of SLBs of interest, and thus can help in the design of biosensing platforms.[12–15]

In addition to using polymer films as stencils, in this thesis we have also explored the use of self-adhesive vinyl film lift-off to pattern various thin film materials.[16] With the use of a computer-aided design-driven cutter, accurate control of the feature shape and dimensions could be achieved in the sub-millimeter range on timeframes of minutes to hours. Through thermal shrinking of pre-stressed polystyrene substrate, we could further reduce the patterned feature dimensions to sub-100 μm sizes. Moreover, thermal shrinking of the polystyrene substrates induced stress-driven wrinkling of the thin films deposited on top, ranging from micrometer to the nanometer scale depending on the thickness of the film deposited.[17–19] Combining vinyl stencil lift-off and shape memory polymer shrinking, this inexpensive, rapid and easy bench top fabrication approach allowed the creation of micron scale thin film patterns with micro/nano structured topographies.

In this dissertation, we have presented three different applications of the micro/nanostructured surfaces produced through the above techniques. In Chapters 4 and 5, we have reported the patterning and structuring strategies of gold thin films, and further built them into high-surface-area electrodes and stretchable electrodes on elastomer substrates. These micro/nanostructured electrodes have been found to exhibit over 665% enhancement in the electroactive surface area over the electrode footprint, high device-to-device reproducibility and robustness. In Chapter 4, we characterized micro/nanostructured gold surfaces of thicknesses ranging from 20 to 200 nm, and further added nanostructures through electrodeposition of gold to further increase electrode surface area. Due to the field enhancement effect from the tips of the wrinkled films, electrodeposition was greatly improved, and the devices with electrodeposited structures exhibited increased electroactive surface areas of up to 1000% compared to flat electrodes. The electrochemical analysis has proved that the structured electrodes exhibit properties that mimic those of electrodes fabricated on traditional substrates, high device-to-device reproducibility, and linearity in sensing of redox-active species. Such structured surfaces could provide an attractive alternative for highly sensitive electrochemical devices.

In Chapter 5, we developed a technique to lift-off and transfer the micro/nanostructured gold films onto elastomeric substrates. Lift-off was achieved through the addition of a sacrificial layer before gold deposition, which was then dissolved after shrinking. As the lifted off films retained the wrinkled morphologies after lift-off and transfer onto the elastomeric substrates, we explored their use as stretchable electrodes. The structured gold films exhibited excellent stretching and bending ability, contributed by the micro/nanostructures on gold surface which released tensile stress by unfolding of the wrinkles and prevented crack propagation through the random orientation of the wrinkles. We also demonstrated the electrochemical sensing ability of the

stretchable electrodes through sensing of redox-active molecules with and without applied strain. We anticipate that our strategy of flexible electrode fabrication could find use in flexible electronic or sensing devices. The two cases presented in Chapters 4 and 5 have demonstrated that micro/nanostructured gold electrodes are promising candidates for next generation of low-cost electrochemical sensing devices for detecting various analytes such as toxic gas, biomolecules, and cells.

To explore the possibility of using the thin film patterning and PS shrinking techniques for other materials, we structured glassy thin films (SiO_2 and TiO_2) and used them for cell culturing studies. Wrinkled and buckled structures similar to those obtained with gold films were observed. However, the glassy films started to crack at thicknesses > 20 nm due to the lower fracture toughness of the materials compared to gold films. In Chapter 6, we presented the fabrication and characterization of SiO_2 and TiO_2 micro/nanostructured films, as well as studied their effect on murine fibroblast cell morphology. 100% relative viability of fibroblast cells was observed on both structured and unstructured glassy films. Using fractal analysis, quantitative analysis of cell morphology was performed. It was found that larger surface structure sizes contributed more to the general cell shape, causing fibroblasts to elongate. On the other hand, cells grown on finer structures with nanometer scales did not change the cell shape much, but the smaller topographies were found to stimulate the growth of cellular protrusions, leading to more complex cell outlines. The ability of the structured glassy films to selectively influence cell morphology could be used to direct cell behaviour and enhance in vitro assays by mimicking the micro and nanostructured components of the cellular microenvironment.[20–23]

The objective of the work presented in this dissertation has been to explore facile, rapid, and inexpensive ways to fabricate micro/nanostructured surfaces, and to further build functional

platforms and devices for biological and sensing applications. We believe that the thin film lift-off and shape memory polymer shrinking approaches for making micro/nanostructured surfaces can find applications in many other areas, and such techniques can be extended to structure other materials of interest, such as polymers, nanocomposites, and alloys.

7.2 Future Outlook

With the increasing demand for understanding more complex biological phenomena as well as the need for highly sensitive diagnostic techniques, micro and nanostructured materials will play a preponderant role in the study of biomolecular interactions and the development of novel sensing devices. Not only the ability to create more complex micro/nanostructures is important, but also the ability to achieve this with low cost and high throughput. As has been shown in this dissertation, polymer stencil lift-off and shape-memory polymer shrinking are two facile, robust and versatile techniques that are easily adaptable for different systems. It is expected that in the near future, these fabrication strategies will expand the range of biological systems that can be studied and monitored in vitro, and further extend their application for patterning and structuring many other materials.

There has been great interest in study biological systems under controlled environmental conditions at micro/nano scales. In this manuscript, it has been shown that SLB pattern feature size has an effect on phase separation at micro scale, and that the stacked gel phase domains register. It can be foreseen that more research will be carried out either experimentally or theoretically how to understand how confined area or physical boundary affect lipid diffusion and gel phase formation. The SLB patterns should also be integrated into diagnostic platforms based on membrane-binding analytes and drug screening systems that target membrane associated proteins.

Reconstruction of tissue-like environments for *in vitro* cell culture and behaviour study has been a popular research topic. We have shown that thermal shrinking induced micro/nanotopography by itself changes fibroblast morphology. Further study of interest will be to look into the substrate effect on other cellular properties (e.g. adhesion, migration, and phenotypes, etc.) and potentially on stem cell differentiation. Moreover, by selectively integrating proteins into the phase-segregated SLB micropatterns, this system can be modified into a platform that can provide both dynamic and geometric properties to better mimic the extracellular matrix for cell studies.

With the increasing demand for point-of-care devices, sensitive and inexpensive biosensing platforms are of great interest. Our manuscripts have demonstrated the use of the simple polymer shrinking technique for the fabrication of high-surface-area gold electrodes for electrochemical sensing. Through further surface modification, the functionality of such electrode can be easily tailored for specific species detection. The electrode lift-off and transfer techniques reported in this dissertation have enabled fabrication of stretchable and flexible sensing platform. Such electrode could then be integrated into microfluidic devices and further be development into functional devices that is portable and disposable. In addition, the use of pre-stressed polymer shrinking techniques have great potentials to structure various other thin film materials. Considering the ease of fabrication and low material cost, we believe that it will find a wide range of applications in photonics, tissue engineering, biodiagnostics, and electrochemical sensing.

As a final word, micro and nanotechnology has evolved for decades with numerous techniques being developed, nowadays increasing attention has been placed on improving efficiency and lowering the cost of fabrication. We believe that the thin film stencil lift-off and shape memory

polymer shrinking techniques are attractive tools to add into micro/nanofabrication toolbox, for their easy accessibility and versatility.

7.3 References

(1) Zhang, B.; Zhang, M.; Song, K.; Li, Q.; Cui, T. Shrink Induced Nanostructures for Energy Conversion Efficiency Enhancement in Photovoltaic Devices. *Appl. Phys. Lett.* **2013**, *103*, 023104.

(2) Hecht, D. S.; Hu, L.; Irvin, G. Emerging Transparent Electrodes Based on Thin Films of Carbon Nanotubes, Graphene, and Metallic Nanostructures. *Adv. Mater.* **2011**, *23* (13), 1482–1513.

(3) Nikkhah, M.; Edalat, F.; Manoucheri, S.; Khademhosseini, A. Engineering Microscale Topographies to Control the Cell-Substrate Interface. *Biomaterials* **2012**, *33* (21), 5230–5246.

(4) Nathan, A. S.; Baker, B. M.; Nerurkar, N. L.; Mauck, R. L. Mechano-Topographic Modulation of Stem Cell Nuclear Shape on Nanofibrous Scaffolds. *Acta Biomater.* **2011**, *7* (1), 57–66.

(5) Nguyen, A. T.; Sathe, S. R.; Yim, E. K. F. From Nano to Micro: Topographical Scale and Its Impact on Cell Adhesion, Morphology and Contact Guidance. *J. Phys. Condens. Matter* **2016**, *28* (18), 183001.

(6) Moran-Mirabal, J. M.; Aubrecht, D. M.; Craighead, H. G. Phase Separation and Fractal Domain Formation in Phospholipid/diacetylene-Supported Lipid Bilayers. *Langmuir* **2007**, *23* (21), 10661–10671.

(7) Jinno, S.; Moeller, H.-C.; Chen, C.-L.; Rajalingam, B.; Chung, B. G.; Dokmeci, M. R.; Khademhosseini, A. Microfabricated Multilayer Parylene-C Stencils for the Generation of Patterned Dynamic Co-Cultures. *J. Biomed. Mater. Res. A* **2008**, *86* (1), 278–288.

(8) Atsuta, K.; Suzuki, H.; Takeuchi, S. A Parylene Lift-off Process with Microfluidic Channels for Selective Protein Patterning. *J. Micromechanics Microengineering* **2007**, *17* (3), 496–500.

(9) Moran-Mirabal, J. M.; Tan, C. P.; Orth, R. N.; Williams, E. O.; Craighead, H. G.; Lin, D. M. Controlling Microarray Spot Morphology with Polymer Liftoff Arrays. *Anal. Chem.* **2007**, *79* (3), 1109–1114.

(10) Tan, C. P.; Seo, B. R.; Brooks, D. J.; Chandler, E. M.; Craighead, H. G.; Fischbach, C. Parylene Peel-off Arrays to Probe the Role of Cell-Cell Interactions in Tumour Angiogenesis. *Integr. Biol.* **2009**, *1* (10), 587–594.

(11) Goddard, J. M.; Mandal, S.; Nugen, S. R.; Baeumner, A. J.; Erickson, D. Biopatterning for Label-Free Detection. *Colloids Surf. B. Biointerfaces* **2010**, *76* (1), 375–380.

(12) Bally, M.; Bailey, K.; Sugihara, K.; Grieshaber, D.; Vörös, J.; Städler, B. Liposome and Lipid Bilayer Arrays towards Biosensing Applications. *Small* **2010**, *6* (22), 2481–2497.

(13) Lowry, T.; Prommapan, P.; Rainer, Q.; van Winkle, D.; Lenhert, S. Lipid Multilayer Grating Arrays Integrated by Nanointaglio for Vapor Sensing by an Optical Nose. *Sensors* **2015**, *15* (8), 20863–20872.

(14) Malmstadt, N.; Nash, M. a.; Purnell, R. F.; Schmidt, J. J. Automated Formation of Lipid-Bilayer Membranes in a Microfluidic Device. *Nano Lett.* **2006**, *6* (9), 1961–1965.

(15) Moran-Mirabal, J. M.; Edel, J. B.; Meyer, G. D.; Throckmorton, D.; Singh, A. K.; Craighead, H. G. Micrometer-Sized Supported Lipid Bilayer Arrays for Bacterial Toxin Binding Studies through Total Internal Reflection Fluorescence Microscopy. *Biophys. J.* **2005**, *89* (1), 296–305.

(16) Taylor, D.; Dyer, D.; Lew, V.; Khine, M. Shrink Film Patterning by Craft Cutter: Complete Plastic Chips with High Resolution/high-Aspect Ratio Channel. *Lab Chip* **2010**, *10* (18), 2472–2475.

(17) Nguyen, D.; Taylor, D.; Qian, K.; Norouzi, N.; Rasmussen, J.; Botzet, S.; Lehmann, M.; Halverson, K.; Khine, M. Better Shrinkage than Shrinky-Dinks. *Lab Chip* **2010**, *10* (12), 1623–1626.

(18) Pegan, J. D.; Ho, A. Y.; Bachman, M.; Khine, M. Flexible Shrink-Induced High Surface Area Electrodes for Electrochemiluminescent Sensing. *Lab Chip* **2013**, *13* (21), 4205–4209.

(19) Lin, S.; Lee, E. K.; Nguyen, N.; Khine, M. Thermally-Induced Miniaturization for Micro- and Nanofabrication: Progress and Updates. *Lab Chip* **2014**, *14* (18), 3475–3488.

(20) Chaudhuri, P. K.; Pan, C. Q.; Low, B. C.; Lim, C. T. Topography Induces Differential Sensitivity on Cancer Cell Proliferation via Rho-ROCK-Myosin Contractility. *Sci. Rep.* **2016**, *6*, 19672.

(21) Sonam, S.; Sathe, S. R.; Yim, E. K. F.; Sheetz, M. P.; Lim, C. T. Cell Contractility Arising from Topography and Shear Flow Determines Human Mesenchymal Stem Cell Fate. *Sci. Rep.* **2016**, *6*, 20415.

(22) Pan, F.; Zhang, M.; Wu, G.; Lai, Y.; Greber, B.; Sch??ler, H. R.; Chi, L. Topographic Effect on Human Induced Pluripotent Stem Cells Differentiation towards Neuronal Lineage. *Biomaterials* **2013**, *34* (33), 8131–8139.

(23) Watt, F. M.; Huck, W. T. S. Role of the Extracellular Matrix in Regulating Stem Cell Fate. *Nat. Rev. Mol. Cell Biol.* **2013**, *14* (8), 467–473.

Appendix A Supplementary Figures for Chapter 2

Micropatterning of Phase-Segregated Supported Lipid Bilayers and Binary Lipid Phases through Polymer Stencil Lift-Off

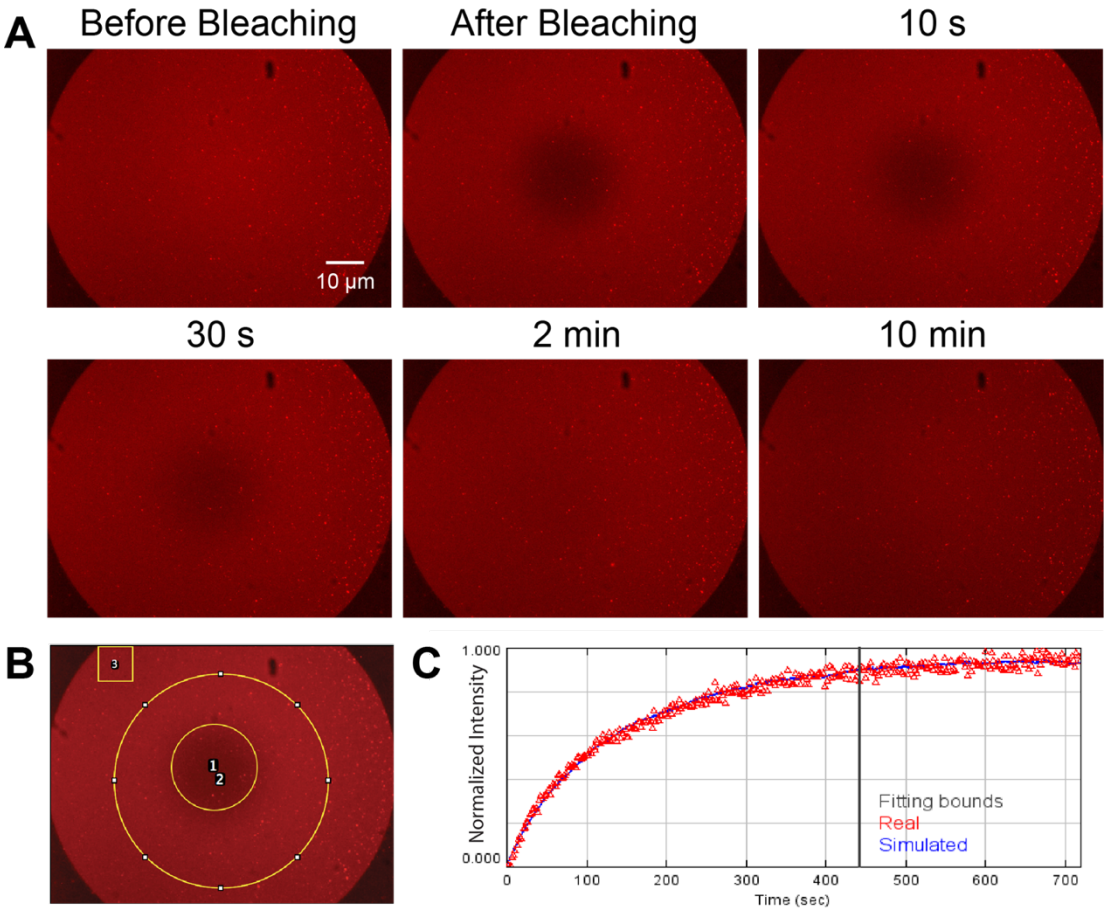

Figure S1. FRAP analysis of homogeneous SLB patterns. (A) Fluorescence images of DOPC:DHPE-LR (99:0.1) SLB pattern shows the center of a circular area being bleached, and the fluorescence recovery over time. (B) The selection of regions of interest are shown for simFRAP analysis using ImageJ software. Area 1 indicates the bleached area, area 2 is the "cell" around the bleached area and area 3 is the reference section used to correct for bleaching. (C) Typical output of the the simFRAP plugin, which gives information of the normalized intensity of the bleached area that is used to calculate the diffusion coefficient. All the images were acquired at the same magnification.

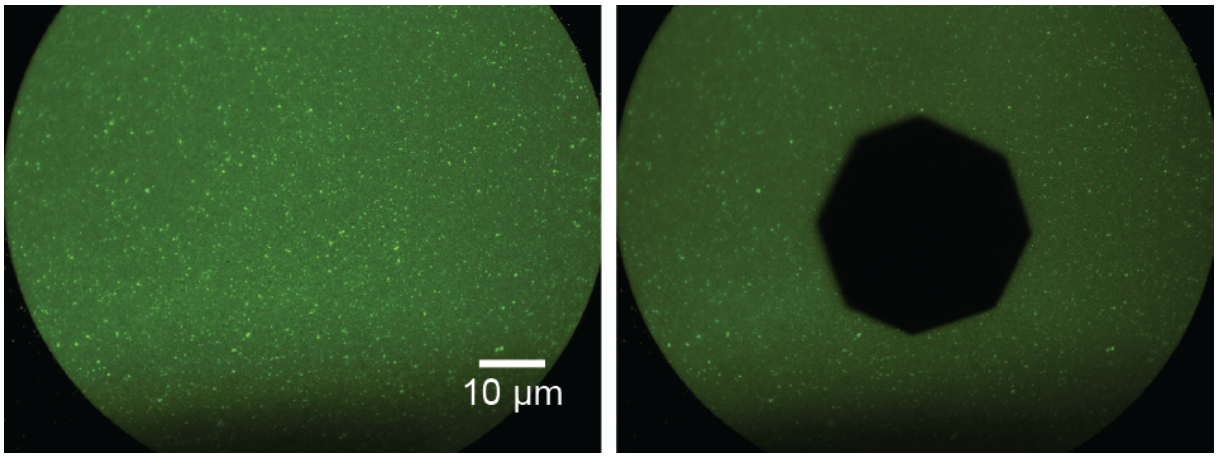

Figure S2. FRAP test of homogeneous DSPC SLB patterns. The DSPC:DHPE-OG (99:1) patterns did not recover after photobleaching at room temperature (picture taken 5 minutes after bleaching). Both images were acquired at the same magnification.

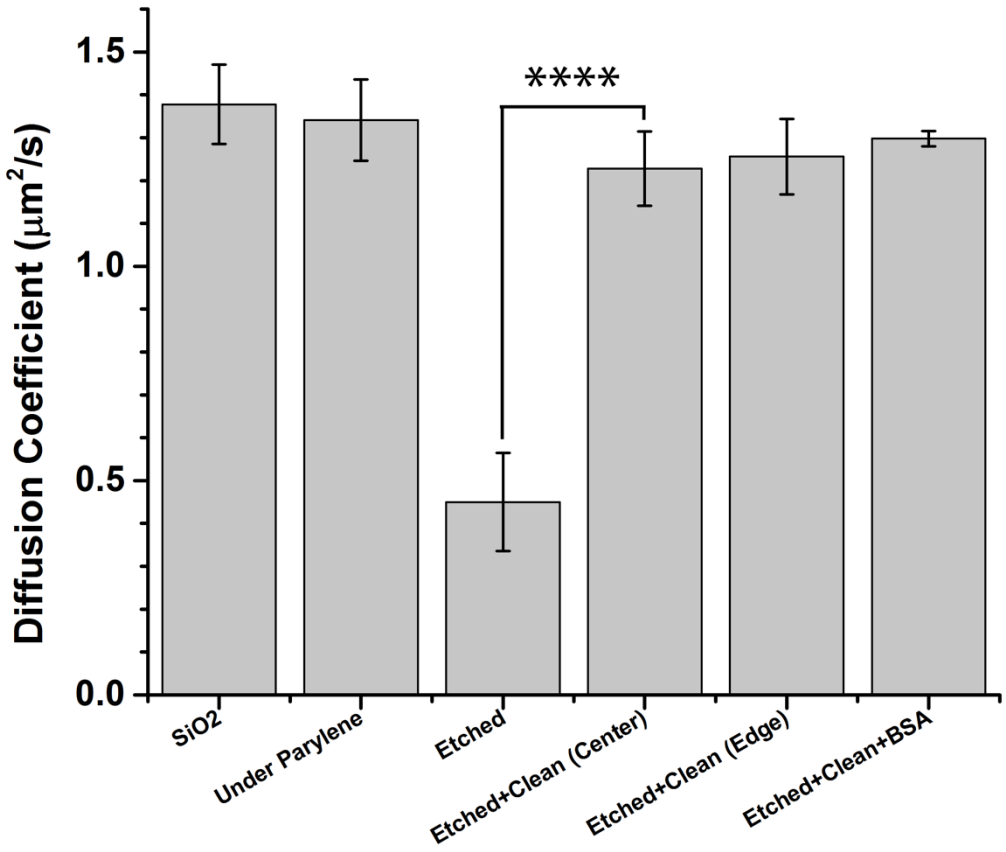

Figure S3. Diffusion coefficients extracted from FRAP measurements on SLBs formed on different substrates. The substrates tested were bare clean SiO_2 wafers, wafers where Parylene coating was deposited and then lifted off (Under Parylene), wafers where features were etched into the Parylene and the SLB was formed in the openings before (Etched) and after the UV/O_3+base cleaning (Etched+Clean), and wafers where the lift-off was performed in buffer containing BSA (Etched+Clean+BSA). The key observations in these experiments were: (1) SLBs formed in the substrates after etching only showed diminished mobility, (2) the UV/O_3+base cleaning removed any polymer residue and afforded SLBs with high mobility, comparable to that of piranha cleaned SiO_2 substrates (SiO_2), (3) the mobility at the center and edge of the patterned features is statistically equal, and (4) using BSA during lift-off does not alter the bilayer mobility. Statistical significance evaluated through ANOVA: ****$p<0.0001$.

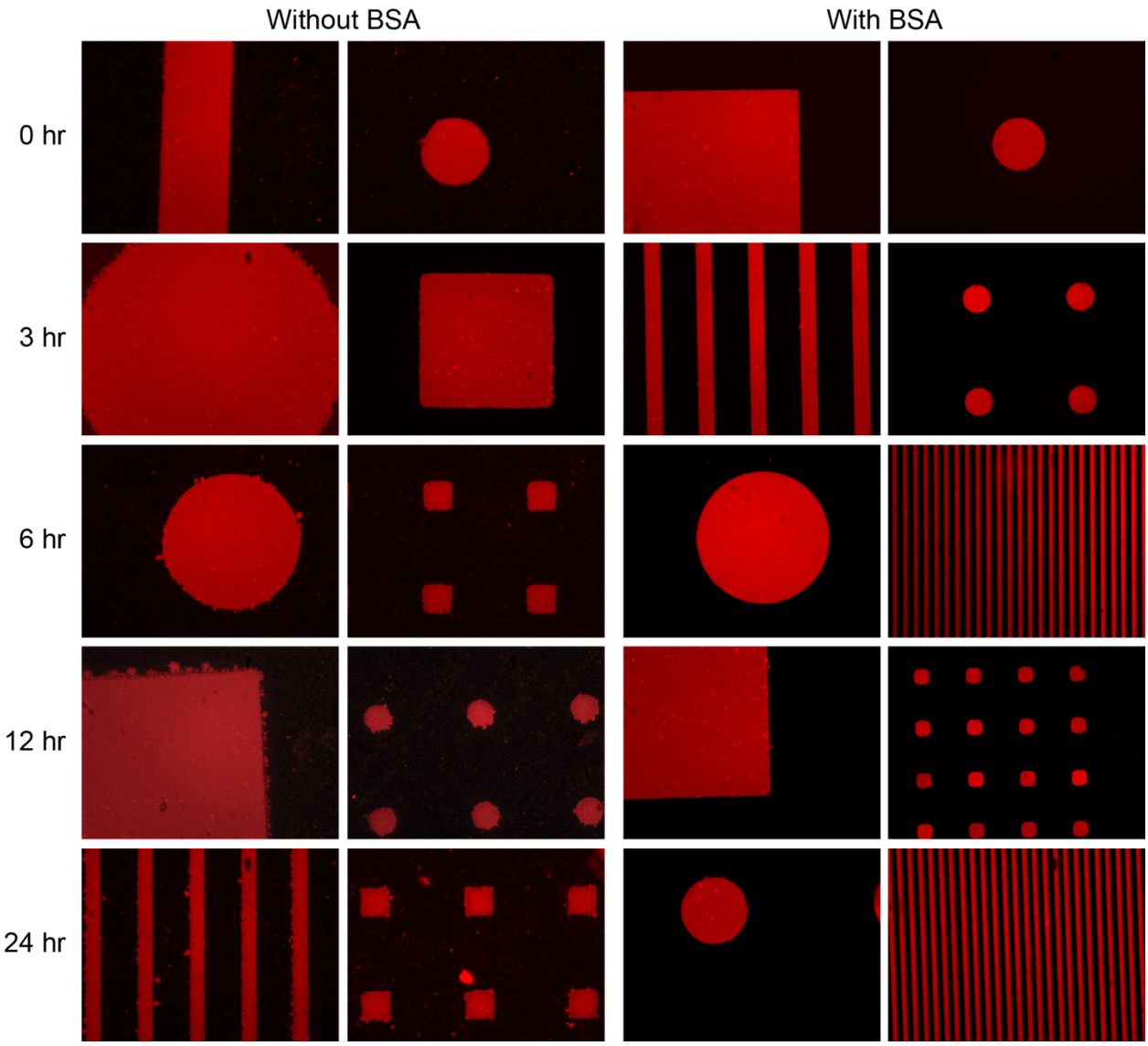

Figure S4. Evaluation of the effect of BSA blocking treatment during polymer lift-off on pattern fidelity. Epifluorescence images show homogeneous DOPC:DHPE-LR (99: 0.1) SLB patterns without (left two columns) and with BSA treatment (right two columns) during lift-off. The SLB patterns were imaged immediately after lift-off, and at 3, 6, 12, and 24 hr after lift-off. It can be seen that without the BSA blocking treatment, the lipid spreads at the edges of the patterned features, while this does not occur when BSA is used. Thus, the BSA blocking treatment during lift-off produces faithful pattern transfer and prevents feature shape degradation due to bilayer spreading. All the images were acquired at the same magnification using the same acquiring settings.

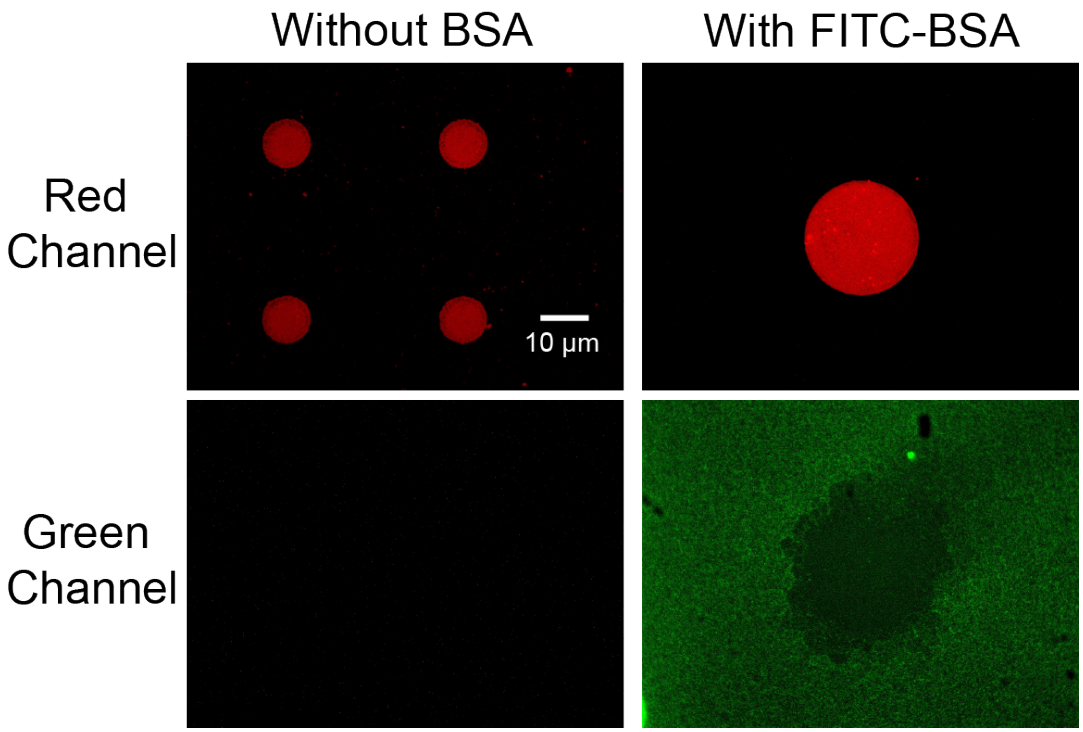

Figure S5. BSA binding on the substrate after polymer lift-off. Epifluorescence images of both Rhodamine and FITC channels were taken for homogeneous DOPC:DHPE-LR (99:0.1) SLB patterns without (left) and with (right) fluorescein labeled BSA used in the blocking treatment. Increased fluorescein intensity in the FITC channel was observed on area outside of the patterns containing the SLBs. The images for same channel were acquired at the same magnification using the same acquisition settings.

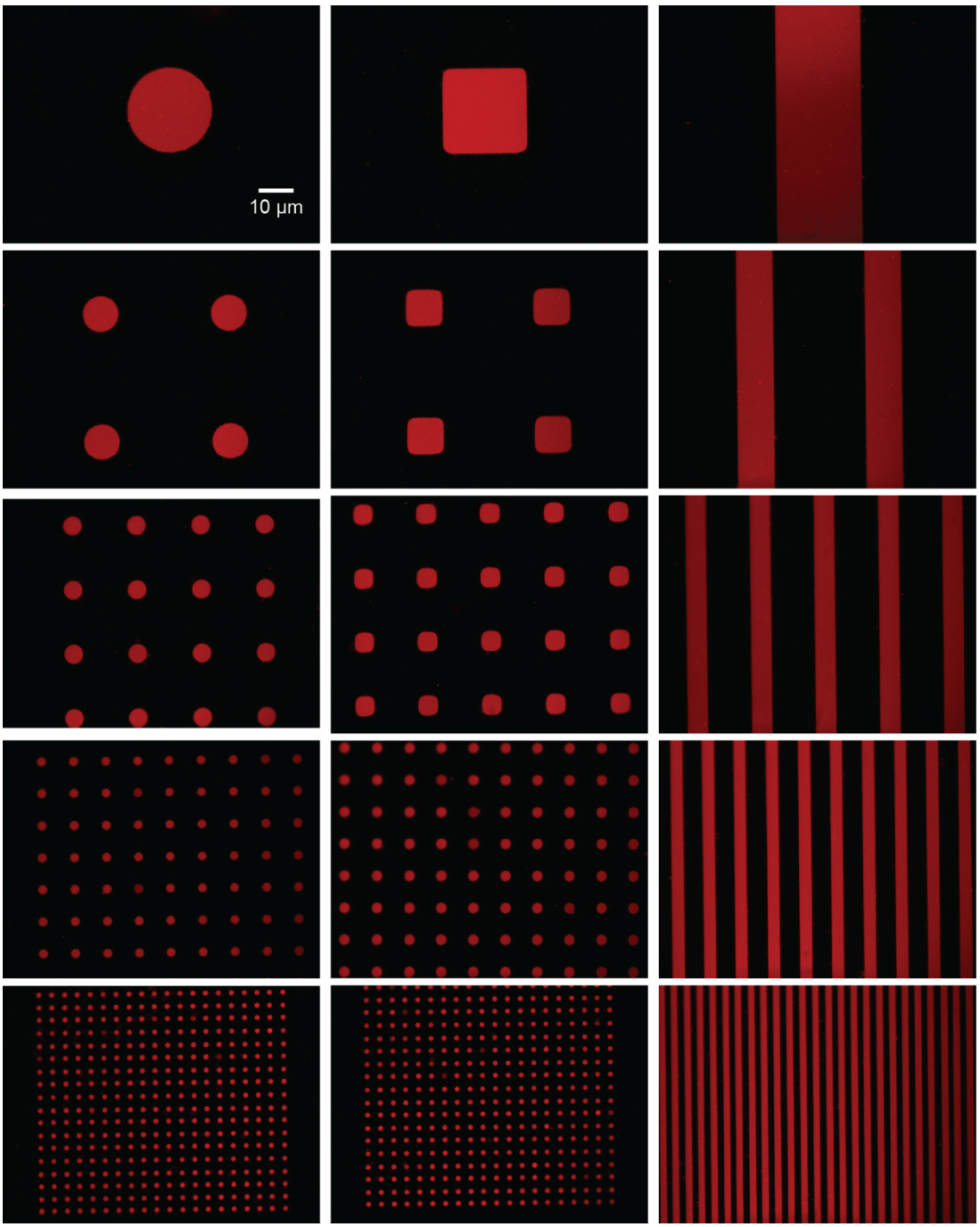

Figure S6. Epifluorescence images show homogeneous DOPC:DHPE-LR (99:1) SLB patterns of various shapes and sizes produced through the polymer stencil lift-off technique using BSA blocking treatment. All images were obtained at the same magnification.

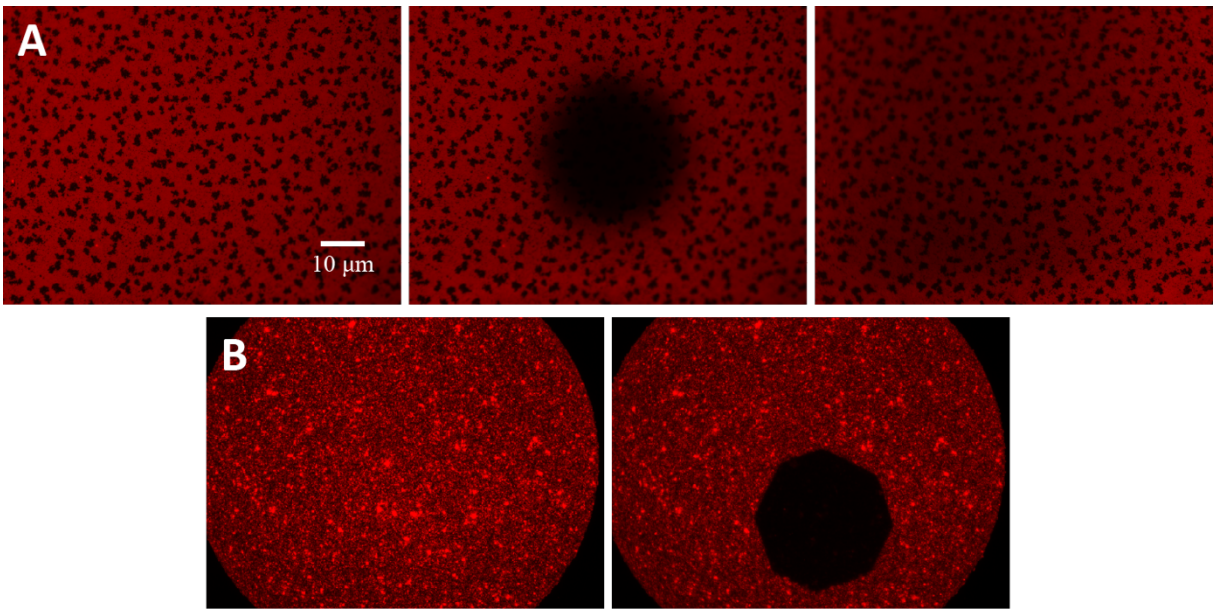

Figure S7. Qualitative bleaching tests of phase-segregating DOPC:DSPC SLB bilayers: (A) Quick fluorescence recovery was observed on DOPC:DSPC:DHPE-LR (49.5:49.5:1) SLBs formed on piranha-cleaned SiO_2 wafers; (B) No fluorescence recovery was observed on patterned SLBs with the same composition in substrates where there was no UV/O_3 and base treatment after patterning. All the images were acquired at the same magnification.

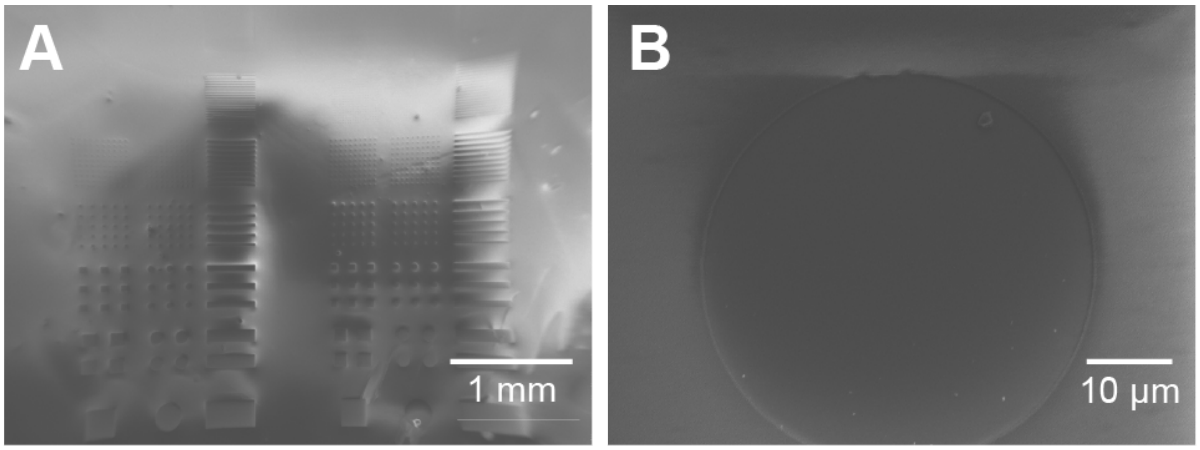

Figure S8. Scanning electron micrographs of SiO_2 wafers after Parylene film was patterned and lifted off. (A) Patterned features were visible with SEM. (B) Image obtained within the etched openings show some residual Parylene.

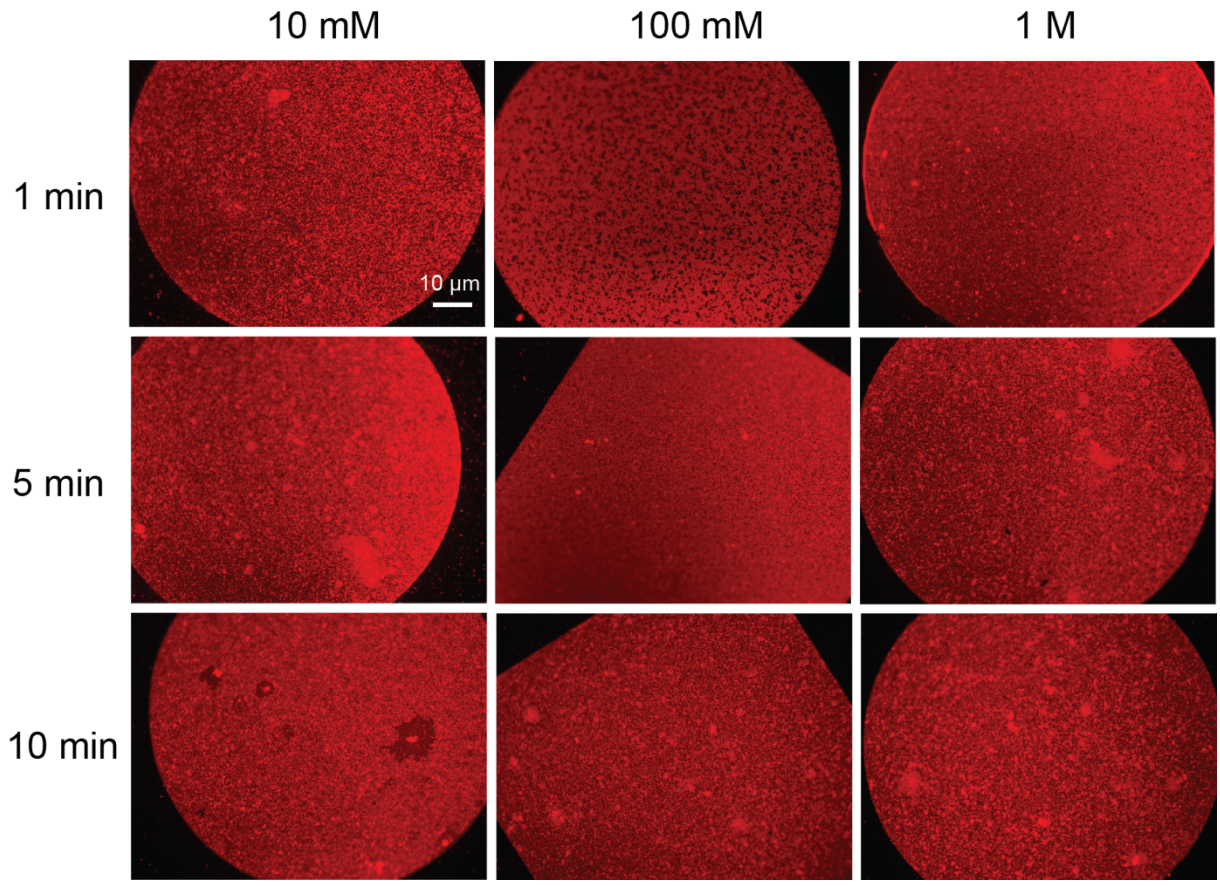

Figure S9. Epifluorescence images showing the phase-segregating SLB (DOPC:DSPC:DHPE-LR) patterns on substrates cleaned with a range of UV/O_3 cleaning times (1-10 min) and NaOH concentrations (0.01-1 M).

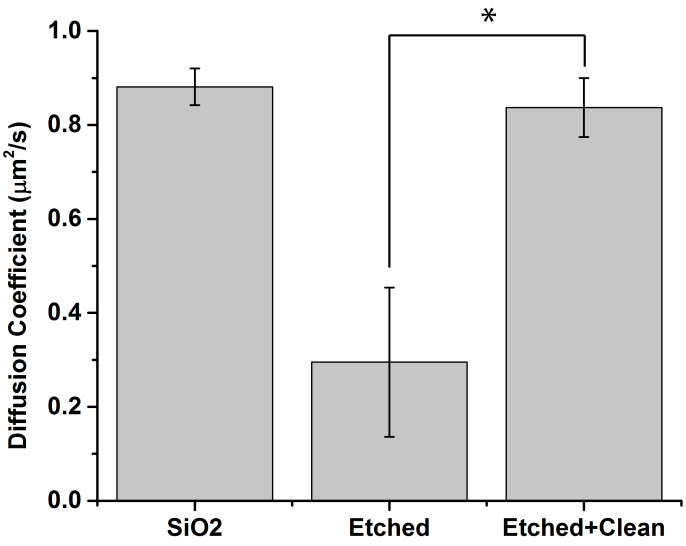

Figure S10. Diffusion coefficients for the lower leaflet of SLBs formed on different substrates were extracted from FRAP measurements performed in the presence of 100 mM $CoCl_2$. The substrates tested were bare clean SiO_2 wafers, and wafers where features were etched into the Parylene and the SLB was formed in the openings before (Etched) and after the UV/O_3+base cleaning (Etched+Clean). The key observations in these experiments were: (1) The lower leaflet of SLBs formed in the substrates after etching only showed diminished mobility, (2) the UV/O_3+base cleaning removed any polymer residue and afforded SLBs where the lower leaflet mobility was comparable to that of piranha cleaned SiO_2 substrates (SiO_2). Statistical significance evaluated through ANOVA: *$p<0.05$.

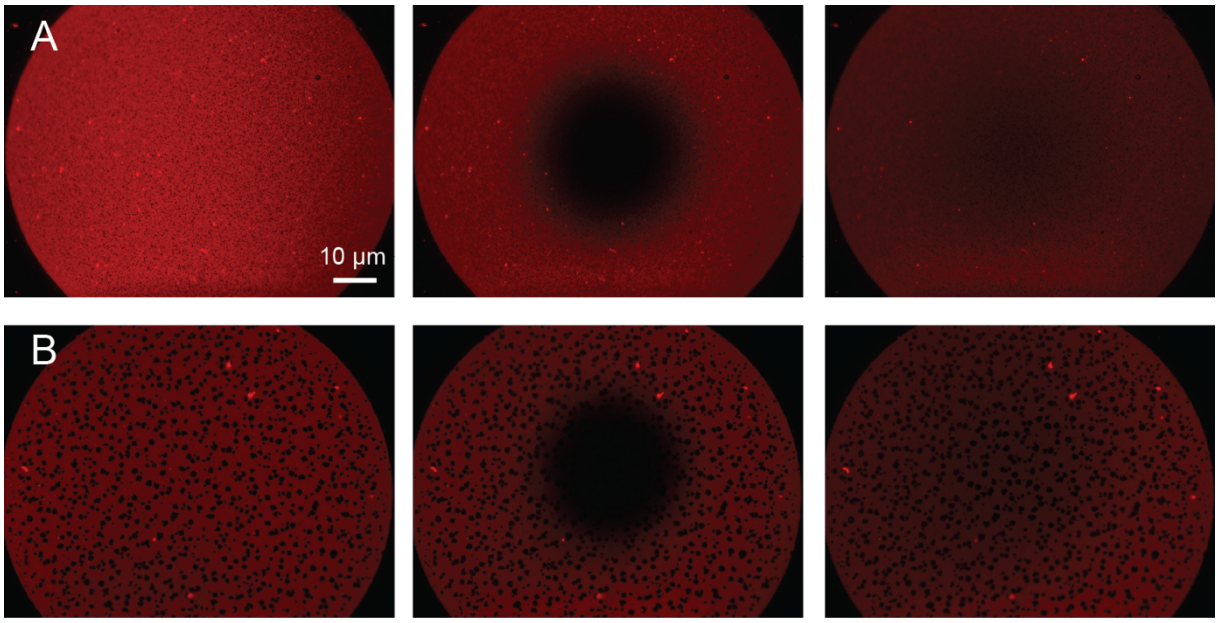

Figure S11. Epifluorescence images showing the cooling effect on phase segregation of patterned DOPC:DSPC:DHPE-LR (49.5:49.5:1) SLBs. Larger gel phase domains were formed when the SLBs were cooled down slowly (B) than when cooled down fast (A). Rapid recovery was observed 5 minutes after bleaching for both cooling conditions, demonstrating that both bilayers were mobile. All the images were acquired at the same **magnification**.

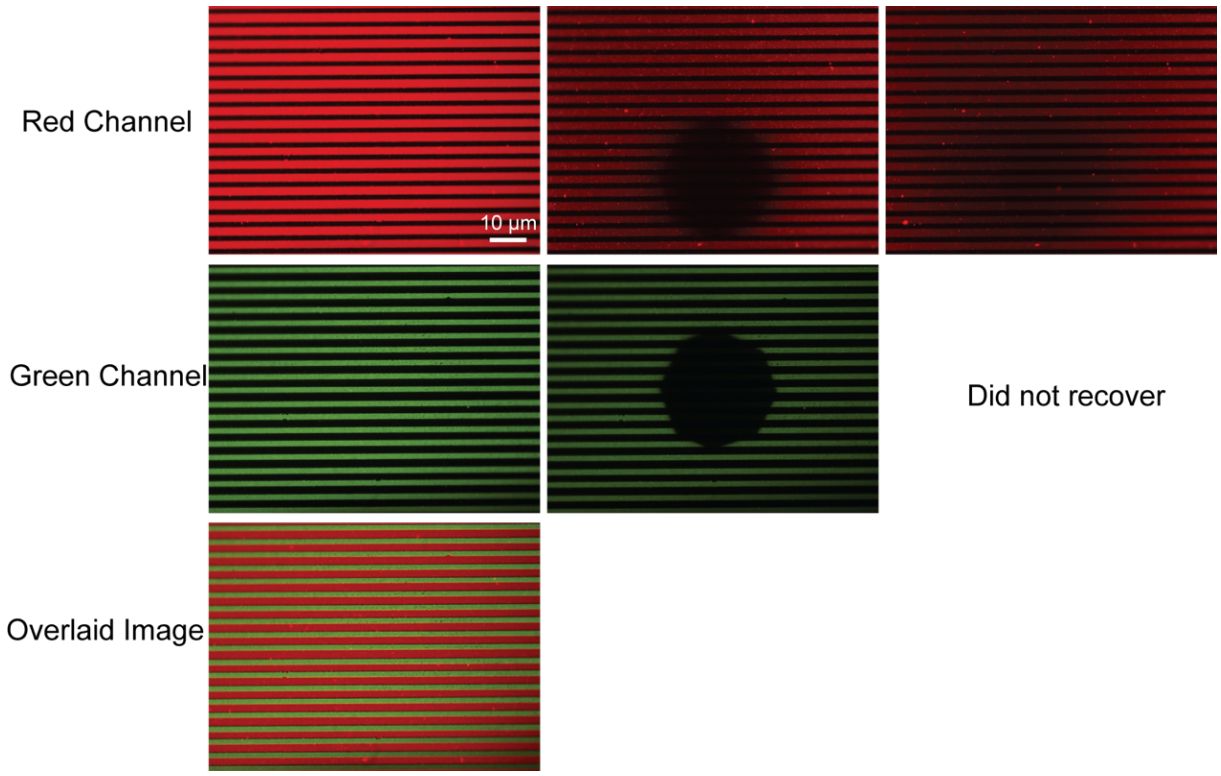

Figure S12. Qualitative fluorescence recovery after bleaching test on binary lipid bilayer patterns with DSPC (green) and DOPC (red) using DHPC-OG and DHPE-LR fluorescent probes, respectively. Overlay image is shown to demonstrate the perfect registration of the two lipid phases. All images were obtained at the same magnification.

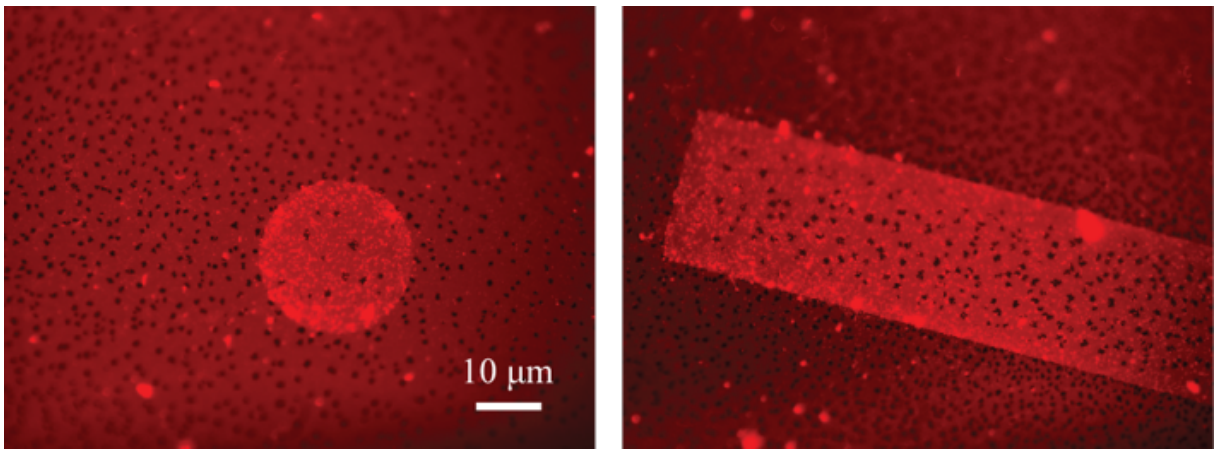

Figure S13. Epifluorescence images of spontaneously phase-segregating SLBs (DOPC:DSPC:DHPE-LR) after the binary lipid bilayers patterns were heated up to 60 °C and cooled down. Both images taken at the same magnification.

Appendix B Supplementary Figures for Chapter 3

Multi-Stacked Supported Lipid Micropatterning through Polymer Stencil Lift-Off

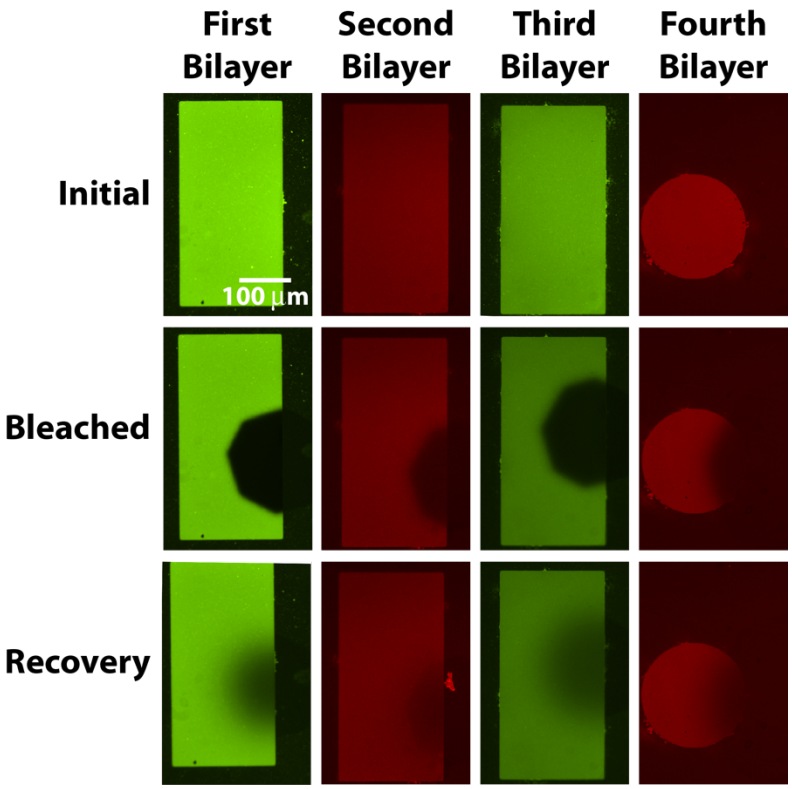

Figure S1 Fluorescence recovery after photobleaching (FRAP) test for four homogeneous bilayer stack SLB micropatterns. Epifluoresence images of each layer were taken before photobleaching, after photobleaching and after partial fluorescence recovery. All images were acquired at the same magnification.

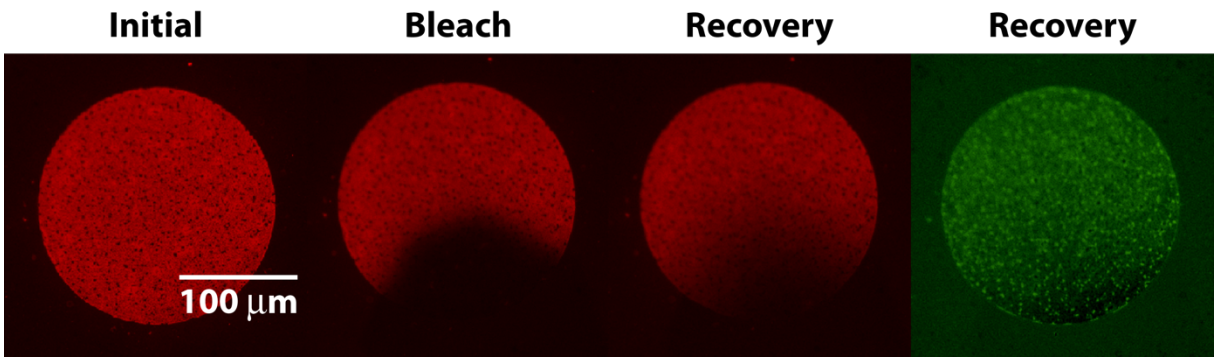

Figure S2 Epifluorescence images of fluorescence recovery after photobleaching (FRAP) test for a two-bilayer SLB stack composed of a phase-segregated bilayer (red labeled with DHPE-LR) deposited on a homogeneous bilayer (green labeled with DHPE-OG). Epifluoresence images of each layer were taken before photobleaching, after photobleaching and after partial fluorescence recovery.

Appendix C Supplementary Figures for Chapter 4

Bench top fabrication of hierarchically structured high surface area electrodes

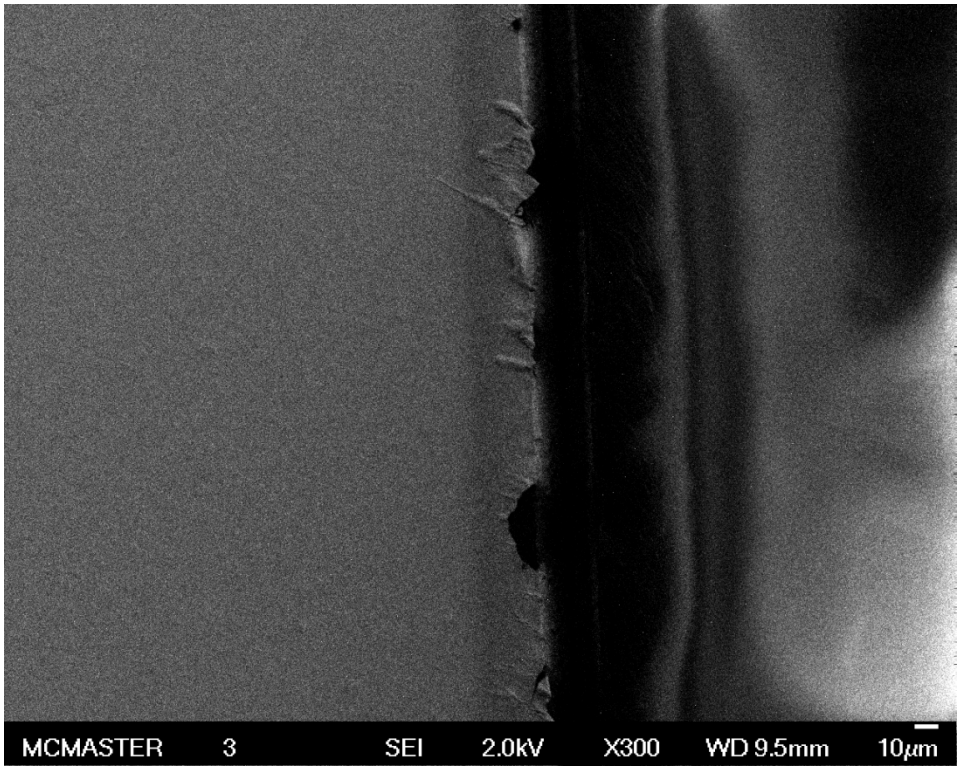

Supplemental Figure 1. Scanning electron microscopy image depicting tearing of gold film at pattern edges after vinyl lift-off. Tearing was more evident in thick gold films (100-200 nm).

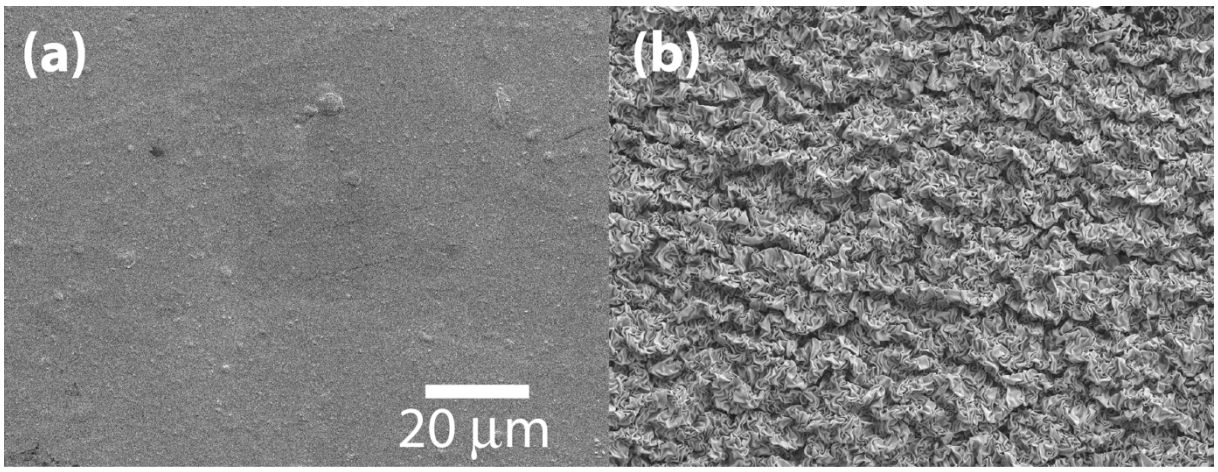

Supplemental Figure 2. Sample SEM images of pristine and shrunken gold films reveal a striking difference in surface structuring. Images were taken from devices coated with 100 nm thick gold films.

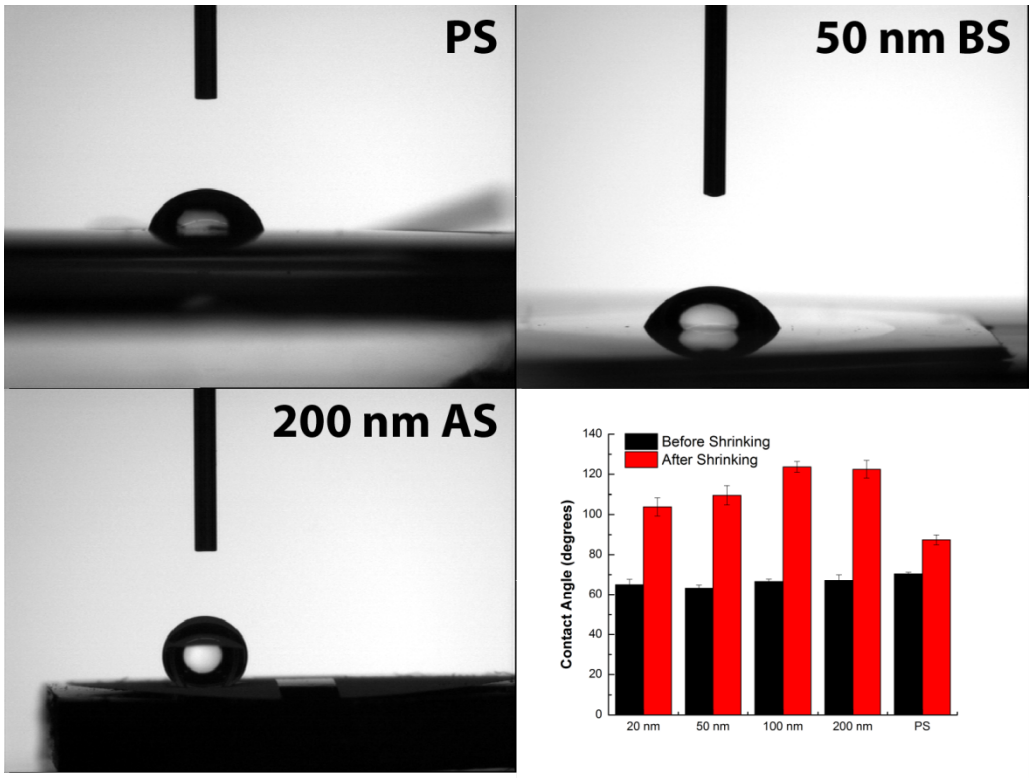

Supplemental Figure 3. The contact angle for water droplets placed on the polystyrene (PS) and gold films before (BS) and after shrinking (AS) was measured to assess the change in surface wettability due surface structuring. The contact angles were measured for all gold film thicknesses in four different areas on three different devices. Error bars represent standard deviations of the measurements ($n > 36$).

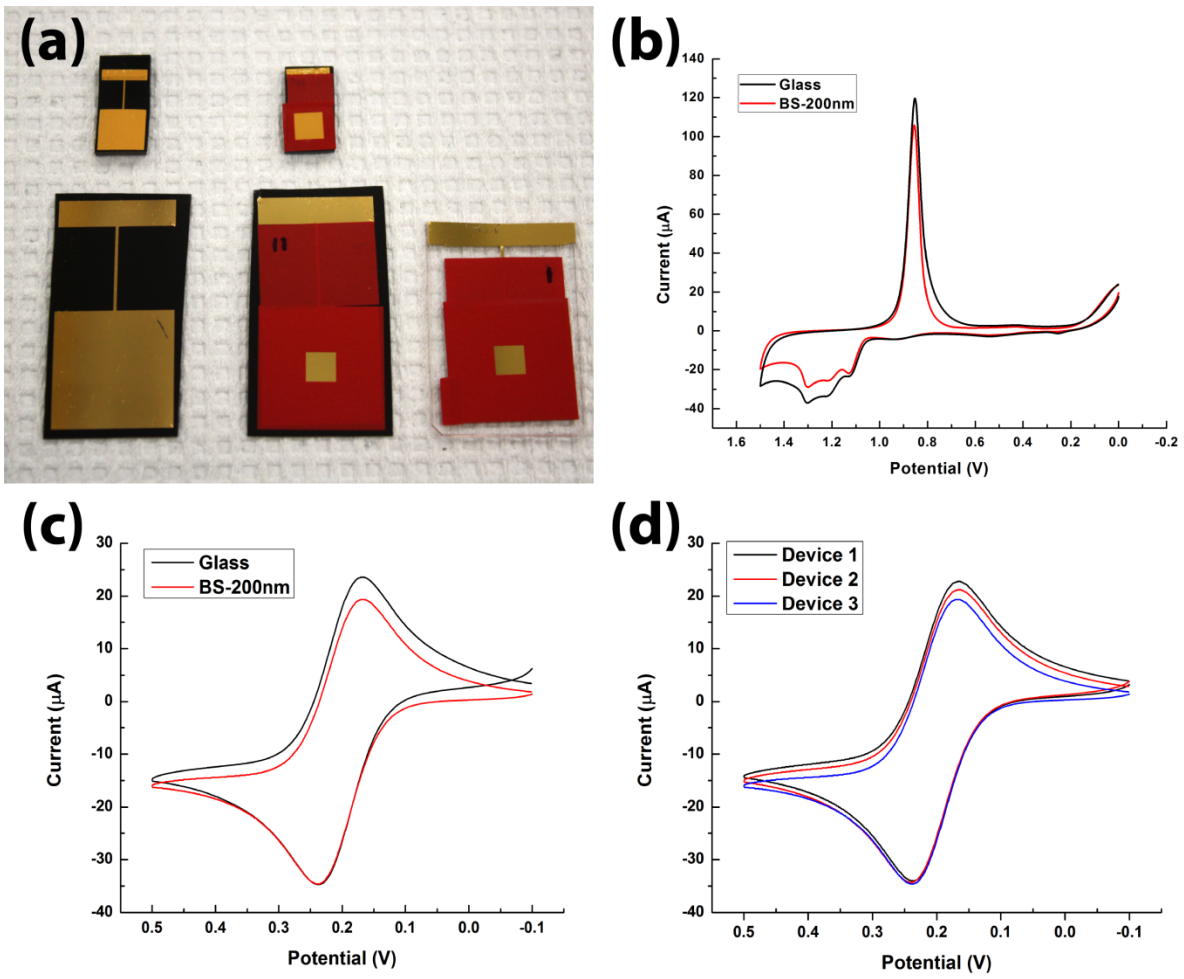

Supplemental Figure 4. Comparison of the performance of devices fabricated on polystyrene and glass substrates. (a) Representative devices (and their shrunken counterparts) designed for electrochemical measurements. From left to right: device layout as fabricated on polystyrene substrate, polystyrene device with area masked by self-adhesive vinyl film, glass device with area masked by vinyl film. (b) Comparison of the cyclic voltammograms obtained from glass and unshrunken polystyrene devices (200 nm gold film) immersed in 0.1 M H_2SO_4. (c) Comparison of the cyclic voltammograms obtained from glass and unshrunken polystyrene devices (200 nm gold film) immersed in 0.1 M KCl solution containing 2 mM $K_4Fe(CN)_6$. (d) Comparison of the cyclic voltammograms obtained from three different unshrunken polystyrene devices (200 nm gold film)

immersed in 0.1 M KCl solution containing 2 mM $K_4Fe(CN)_6$. The polystyrene devices show high device-to-device reproducibility.

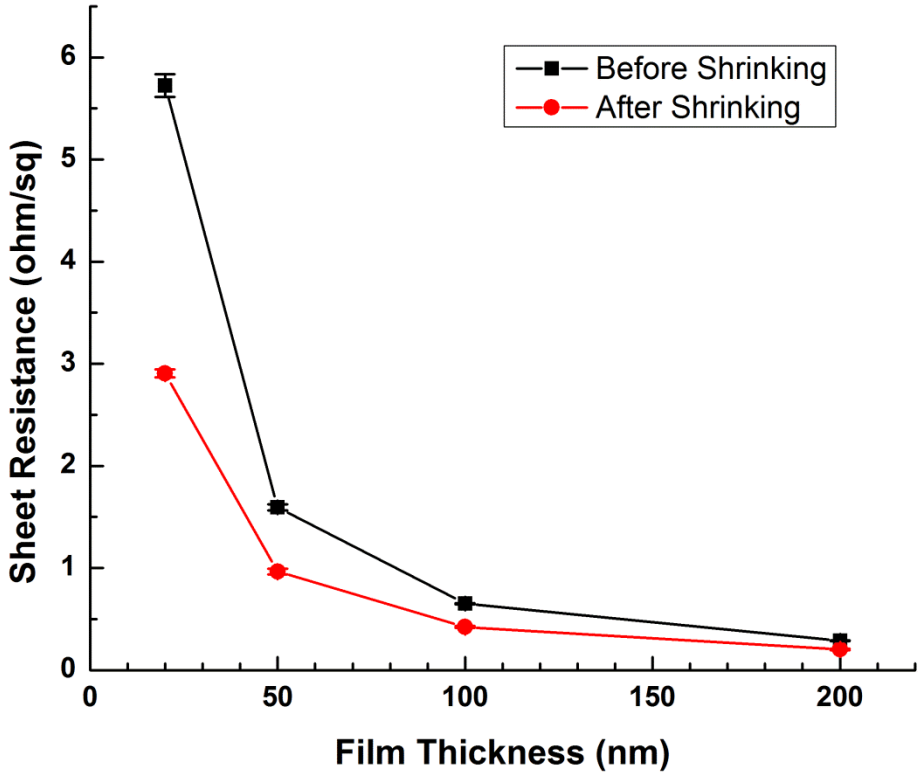

Supplemental Figure 5. Sheet resistance measured using the van der Pauw method for devices fabricated on polystyrene substrates before and after shrinking. Film thickness reported is the nominal film thickness measured during gold sputtering. Error bars represent the standard deviation of measurements performed on three different devices (n > 9).

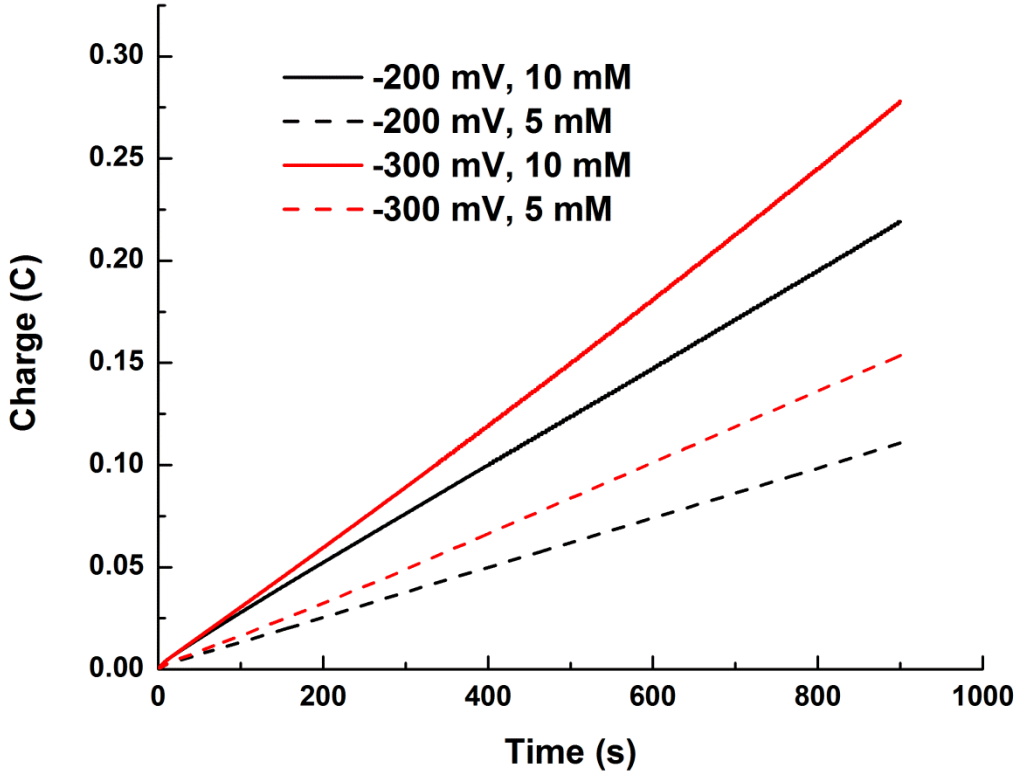

Supplemental Figure 6. Effect of change in $HAuCl_4$ concentration on electrodeposition rate at -200 and -300 mV. Increase in charge transfer correlates with faster deposition rate.

Appendix D Supplementary Figures for Chapter 5

Highly Bendable and Stretchable Gold Electrodes Based on Micro/Nanostructured Films for Flexible Sensors and Electronics

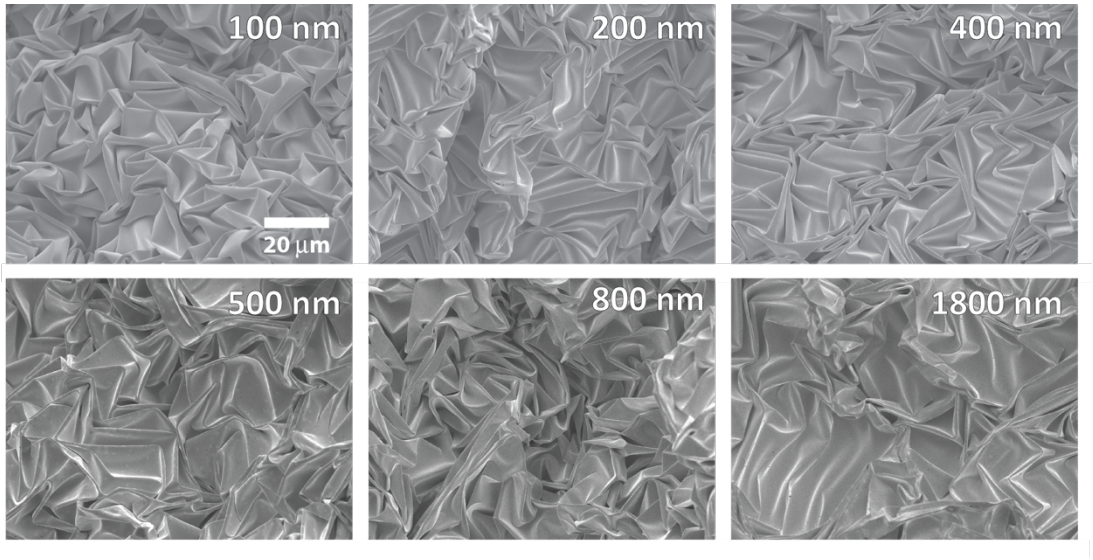

Figure S1. Comparison of the surface morphology for wrinkled gold films fabricated with an intermediate photoresist layer of various thicknesses. Scanning electron microscopy images of 200 nm Au films fabricated using with photoresist thicknesses ranging from 100 nm to 1800 nm.

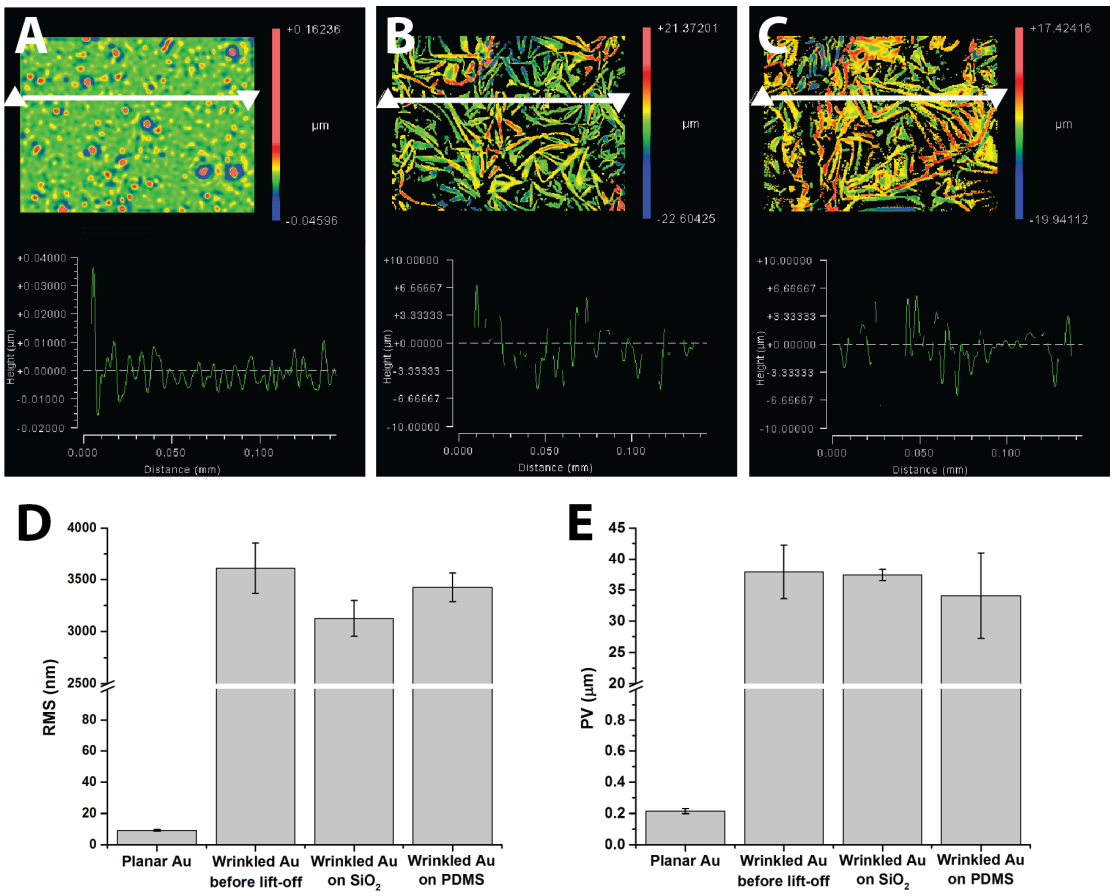

Figure S2. Characterization of the surface roughness for mirco/nanostructured gold films was carried out by white light interferometry microscopy. Typical interferometry topographical images and line profiles are shown for (a) 200 nm thick gold film before shrinking (planar), (b) after shrinking (wrinkled), and (c) after being transferred onto a silicon wafer. The line of the profile is discontinuous because of missing data points form areas that scattered light. Comparison of (d) RMS roughness and (e) peak to valley (PV) ranges for planar gold films, structured gold films before lift off, and after transfer to SiO_2 and PDMS substrates. Error bars represent the standard deviation of measurements performed on replicate films (n 4).

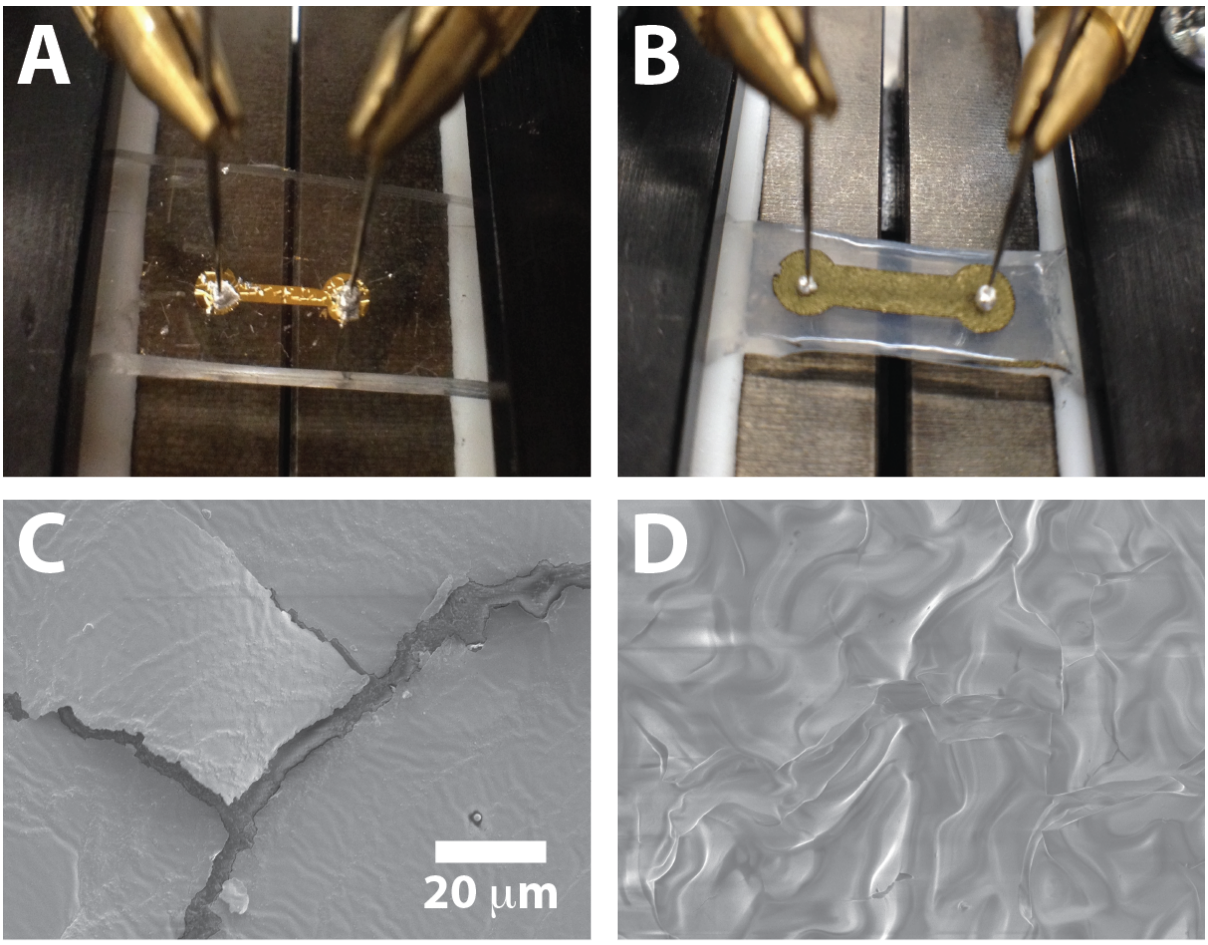

Figure S3. Resistance measurements were performed for 200 nm gold films deposited directly on PDMS (a) and Ecoflex (b). Even without stretching, the films were not conductive. (c) The SEM image reveals that the planar gold cracks easily across the whole film on PDMS. Gold-coated Ecoflex surface is very rough and also presents cracks, which leads to the discontinuity and lack of conductivity of the gold film. Both images were obtained at the same magnification.

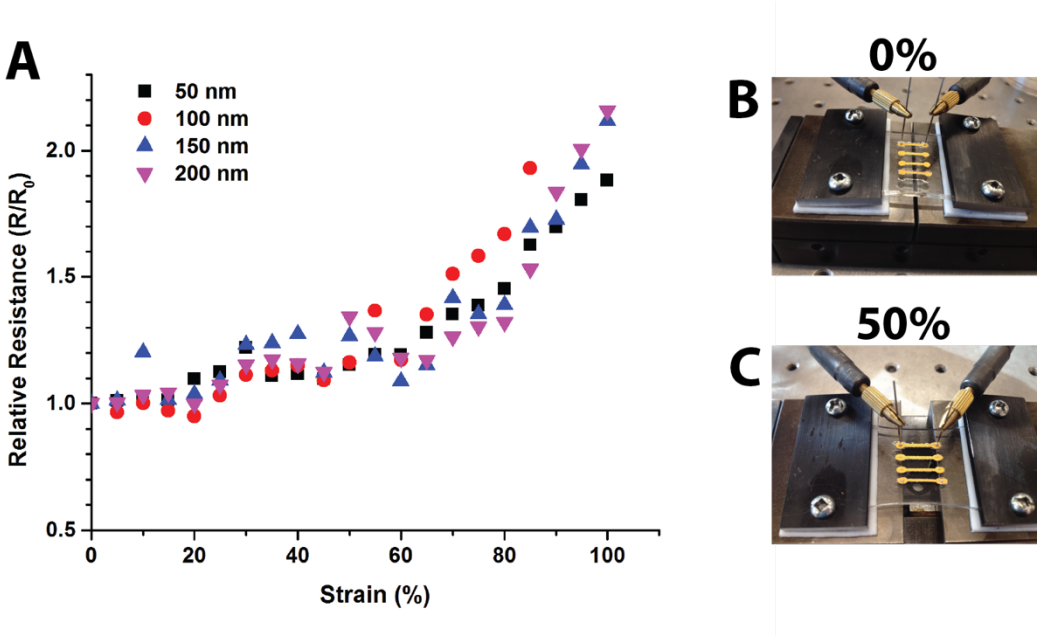

Figure S4. The stretchability of 50, 100, 150 and 200 nm-thick structured gold electrodes was compared on PDMS substrate. (a) Relative resistance change measurements over 0 to 100% strain show similar trends for electrodes of all thicknesses, indicating that the stretchability is independent of film thickness. Photos show the setup used for comparable resistance measurements at 0% strain (b) and 50% strain (c).

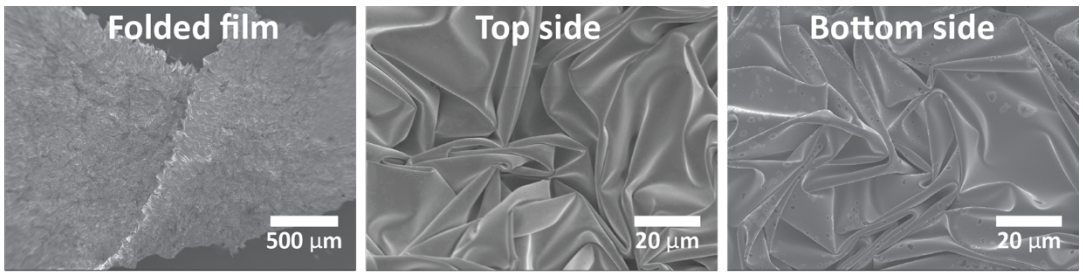

Figure S5. Scanning electron microscopy images show that a 200 nm-thick lifted-off structured gold film displays similar structures on both the top and bottom sides of the film. Closer examination reveals that photoresist or polystyrene residue on the bottom side of the film, which led to a lower electroactive surface area than that for the top side of the film.

Appendix E Supplementary Figures for Chapter 6

Micro/nanostructured SiO_2 and TiO_2 Films Fabricated through Polymer Shrinking as Tunable Topography Substrates for Cell Studies

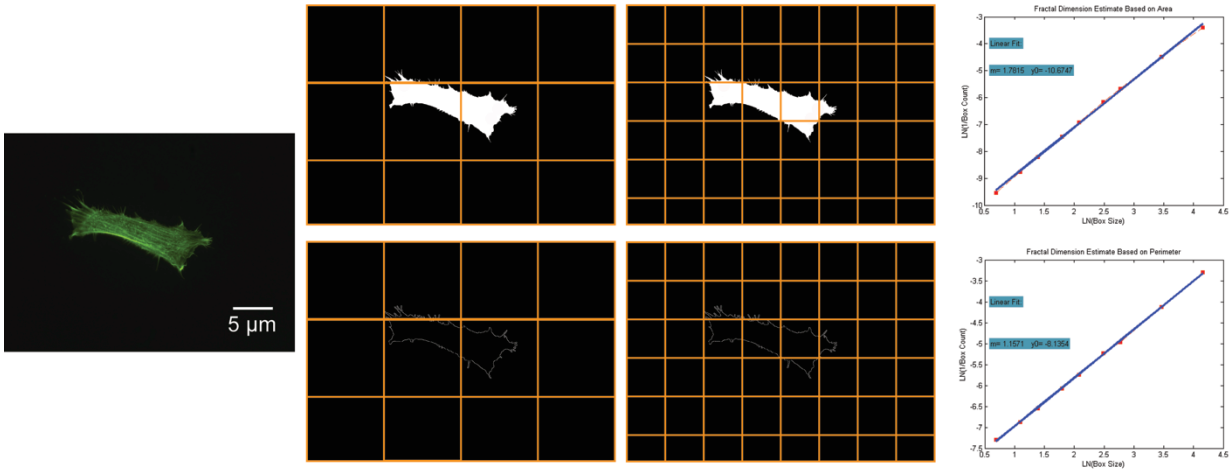

Fig. S1 Illustration of box counting method for fractal analysis of cell area (top row) and boundary (bottom row). The images show a fibroblast grown 2 nm structured SiO_2 surface.

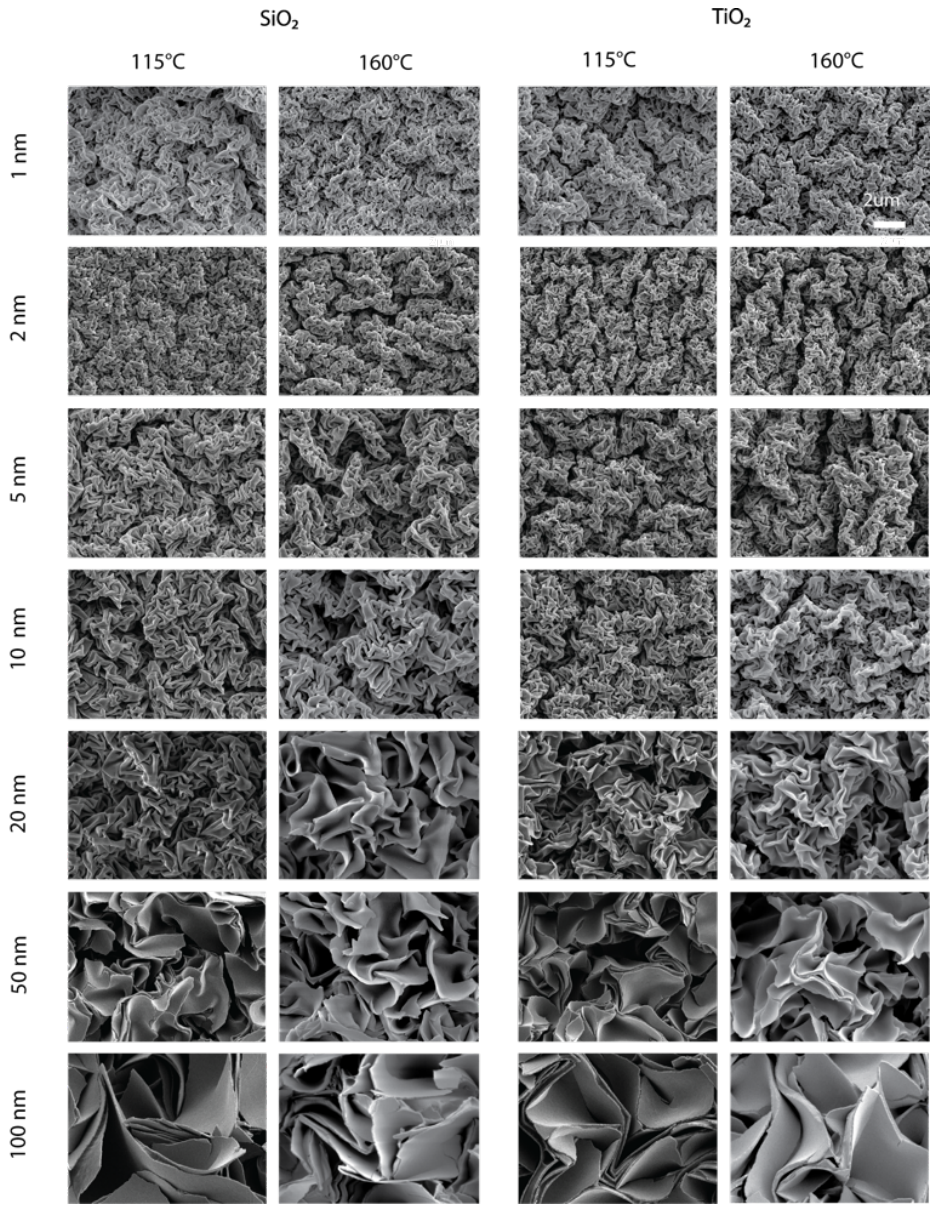

Fig. S2 SEM images of micro/nanostructured SiO_2 and TiO_2 surfaces of 1, 2, 5, 10, 20, 50, and 100 nm thicknesses shrunk at 160 °C.

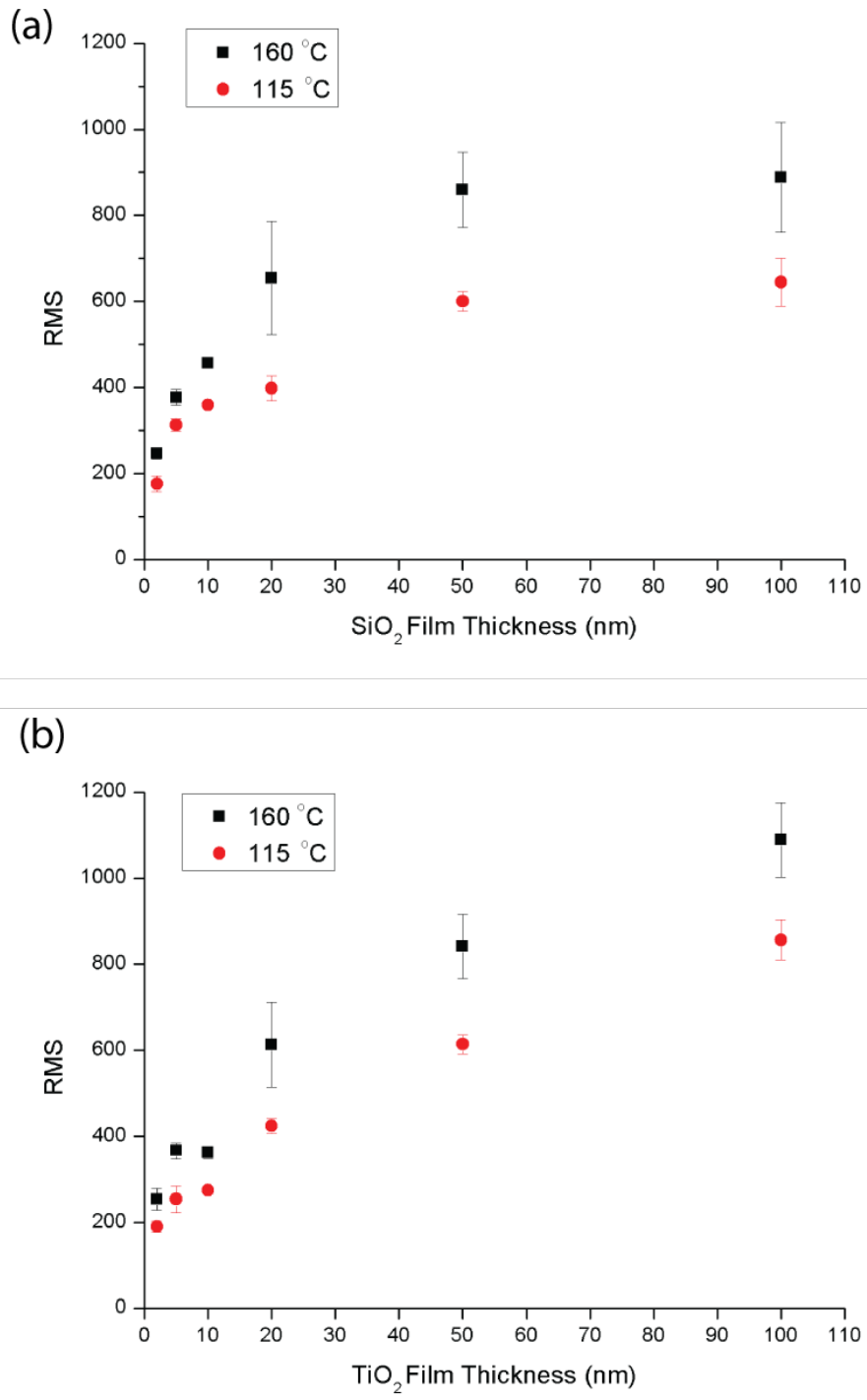

Fig. S3 Surface roughness characterized by RMS of the structured (a) SiO2 and (b) TiO2 of different film thicknesses at 115°C and 160°C.

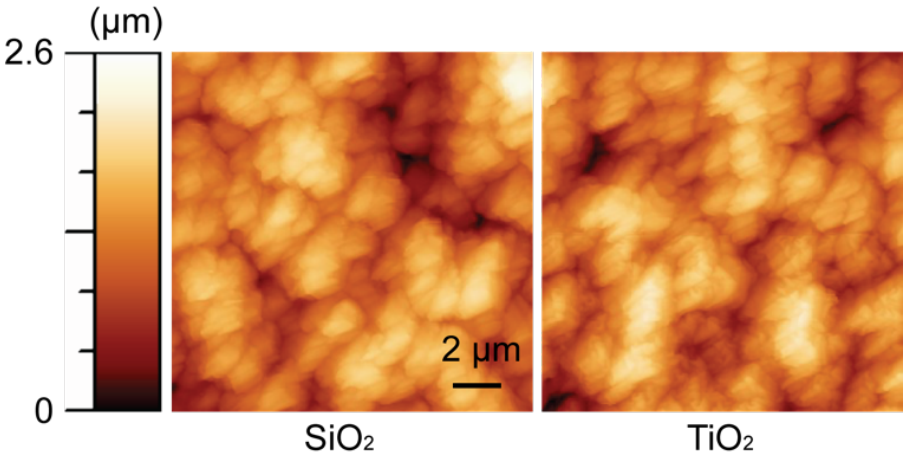

Fig. S4 AFM images of structured 2 nm SiO_2 (left) and TiO_2 (right) thin films